



A University of Sussex DPhil thesis

Available online via Sussex Research Online:

<http://sro.sussex.ac.uk/>

This thesis is protected by copyright which belongs to the author.

This thesis cannot be reproduced or quoted extensively from without first obtaining permission in writing from the Author

The content must not be changed in any way or sold commercially in any format or medium without the formal permission of the Author

When referring to this work, full bibliographic details including the author, title, awarding institution and date of the thesis must be given

Please visit Sussex Research Online for more information and further details



The development of microfabricated ion traps towards quantum information and simulation

Marcus D. Hughes

Submitted for the degree of Doctor of Philosophy
University of Sussex, Brighton, United Kingdom
November 2012

Declaration

I hereby declare that this thesis has not been and will not be submitted in whole or in part to another University for the award of any other degree.

Signature:

Marcus D. Hughes

UNIVERSITY OF SUSSEX

MARCUS D. HUGHES, DOCTOR OF PHILOSOPHY

THE DEVELOPMENT OF MICROFABRICATED ION TRAPS
TOWARDS QUANTUM INFORMATION AND SIMULATION

Abstract

Trapped ions within Paul traps have shown to be a promising architecture in the realisation of a quantum information processor together with the ability of providing quantum simulations. Linear Paul traps have demonstrated long coherence times with ions being well isolated from the environment, single and multi-qubit gates and the high fidelity detection of states. The scalability to large number of qubits, incorporating all the previous achievements requires an array of linear ion traps. Microfabrication techniques allow for fabrication and micron level accuracy of the trap electrode dimensions through photolithography techniques.

The first part of this thesis presents the experiential setup and trapping of Yb^+ ions needed to test large ion trap arrays. This include vacuum systems that can host advanced symmetric and asymmetric ion traps with up to 90 static voltage control electrodes. Demonstration of a single trapped Yb^+ ion within a two-layer macroscopic ion trap is presented. with an ion-electrode distance of $310(10) \mu\text{m}$. The anomalous heating rate and spectral noise density of the trap was measured, a main form of decoherence within ion traps.

The second half of this thesis presents the design and fabrication of multi-layer asymmetric ion traps. This allows for isolated electrodes that cannot be accessed via surface pathways, allowing for higher density of electrodes as well as creating novel trap designs that allow for the potential of quantum simulations to be demonstrated. These include two-dimensional lattices and ring trap designs in which the isolated electrodes provide more control in the ion position.

For the microfabrication of these traps I present a novel high-aspect ratio electroplated electrode design that provides shielding of the dielectric layer. This provides a means to mitigate stray electric field due to charge build up on the dielectric surfaces. Electrical testing of the trap structures was performed to test bulk breakdown and surface flashover of the ion trap architectures. Results showed sufficient isolation between electrodes for both radio frequency and static breakdown. Surface flashover voltage measurements over the dielectric layer showed an improvement of more than double over previous results using a new fabrication technique. This will allow for more powerful ion trap chips needed for the next generation of microfabricated ion trap arrays for scalable quantum technologies.

Acknowledgements

The last four years of my PhD has been extremely enjoyable and engaging but would not have been possible with the support of the people around me. I would firstly like to thank my supervisor Winfried Hensinger for giving me the opportunity to undertake a PhD within his group. I really admire his constant drive and enthusiasm within research. You were always available for support and I always enjoyed the celebration dips in the sea even if it was December.

A huge appreciation goes out to the fellow PhD students when I first joined the group for being extremely welcoming and helpful. James Siverns for initial supervision during my undergraduate project and help with understanding the imaging and resonator design. Altaf Nizamani for always been available for any questions I had with the designs of the ion traps. Robin Sterling your support with initial simulations and ion trap designs as well as the locking setup. James McLoughlin for helping me understand laser laser setup and many hours aligning the Toptica system. Bjoern Lekitsch your support and determination during the first experiments and useful guidance in the initial fabrication designs and not forgetting the support in writing the microfab paper. Seb Weidt your constant drive and entertainment has proved a great support. Kim Lake your dedication and enthusiasm with every physical topic. I would also like to thank the other members of the group in particular Jiddu Broersma, Darren De Motte, Joe Randall, Gouri Giri and Simon Webster.

During my time fabricating at Nottingham it would not have been possible without the input and support from the people around me. Chris Mellor your support, patience and knowledge has been invaluable during my time fabricating. Jessica Maclean you have provided great assistance and expertise when performing many a fabrication trial and questioning all aspects of the process has been priceless in achieving the final traps. Jas Chauhan and Dave Taylor for your support with the cleanroom facilities. The people at Nottingham lifesaving club who provide a warm welcome and great entertainment during my stay.

I would also like to thank people within the department, Barry Garraway, Matthias Keller and the other members next door who has provided useful guidance during my research.

A massive thank you to my family, mum, dad and Laurie your constant support and interest has provided to be extremely motivational and also a release which has helped me push on during some long days.

I would also like to thank my close friends, your support has been a pleasure to have and much needed entertainment during my hardest yet rewarding years of my life.

Contributions

With the nature of experimental physics, the work presented in this thesis would not be possible without the input and contributions from the other members of the group and the people at Nottingham during the fabrication of the traps. I have outline the individual contributions made by each person below.

Chapter 2: Ion trapping

The investigation of power dissipation and loss tangent within an ion trap circuit was performed by myself and Jiddu Broersma.

Chapter 3: Experimental Setup

The construction of the lasers was performed by James McLoughlin and Robin Sterling. The laser locking setup was designed and constructed by Robin Sterling, James Siversns, James McLoughlin and Altaf Nizamani. The first generation vacuum system was designed by Altaf Nizamani and constructed by Altaf Nizamani with assistance from James McLoughlin, Robin Sterling and Philippa Young. The second generation vacuum system was designed by Robin Sterling with assistance from James Sayers and constructed by Robin Sterling, Seb Weidt and Kim Lake. The design and construction of the helical resonator was performed by James Siversns. The imaging system was designed and constructed by James Siversns and myself. The macroscopic linear Paul trap was designed by Robin Sterling and assembled by myself, James McLoughlin, James Siversns, Robin Sterling and Altaf Nizamani.

The ionisation wavelengths were measured by Altaf Nizamani and James McLoughlin. The cooling laser wavelengths for each Yb isotope were determined and measured by Robin Sterling, James Siversns, Altaf Nizamani, James McLoughlin, Seb Weidt, Bjoern Lekitsch

and myself. The characterisation of the ion trap by a heating measurement was performed by myself, Bjoern Lekitsch, Seb Weidt, James McLoughlin, James Siverns, Altaf Nizamani and Robin Sterling. The theoretical model was reproduced by Bjoern Lekitsch with assistance from James McLoughlin.

Chapter 4: Asymmetric ion trap designs

The optimisation of the surface geometries carried out by Altaf Nizamani, was used to design the ion traps presented within this thesis. The y-junction design was provided by Robin Sterling. A Mathematica Notebook provided by Altaf Nizamani was used to theoretically shuttle an ion within a y-junction. The optimisation of two-dimensional ion trap arrays was carried out by James Siverns with help from Kim Lake, Seb Weidt, Bjoern Lekitsch and myself. Analytical calculations of the ring ion traps was performed with C++ program provided by James Siverns. The final layout of the mask was done by Chris Mellor.

Chapter 6: Microfabrication process

All of the fabrication trials were performed by myself with assistance from Jessica Maclean and Chris Mellor. The PECVD growth of the dielectric layers was performed by Chris Mellor. The dry etches was performed by Chris Mellor with assistance from Jessica Maclean. The electroplating step was performed by Jessica Maclean.

Chapter 7: Characterisation and testing of microfabricated ion traps

The breakdown measurements were performed by myself and Robin Sterling. The theory of surface flashover was produced by Robin Sterling. The design of the recessed window was done by Bjoern Lekitsch. The construction of the third vacuum system was done by Seb Weidt and myself.

Publications

Journal publications

Increased surface flashover voltage in microfabricated devices,

Robin C. Sterling, Marcus D. Hughes, Chris J. Mellor and Winfried K. Hensinger,
arXiv:1208.5672v1 (2012).

Optimization of two-dimensional ion trap arrays for quantum simulation,

James D Siverns, Seb Weidt, Kim Lake, Bjoern Lekitsch, Marcus D Hughes and Winfried
K Hensinger,
New J. Phys. 14, 085009 (2012).

Microfabricated ion traps,

Marcus D. Hughes, Bjoern Lekitsch, Jiddu Broersma and Winfried K. Hensinger,
Contemporary Physics 52:6, 505-529 (2011).

Versatile ytterbium ion trap experiment for operation of scalable ion-trap chips with motional heating and transition-frequency measurements,

James J. McLoughlin, Altaf H. Nizamani, James D. Siverns, Robin C. Sterling, Marcus
D. Hughes, Bjoern Lekitsch, Björn Stein, Seb Weidt, and Winfried K. Hensinger,
Phys. Rev. A 83, 013406 (2011).

Conference contributions

Trapped ytterbium ions for scalable quantum technology,

M. D. Hughes, J. J. McLoughlin, A. H. Nizamani, J. D. Siverns, R. C. Sterling, B. Lek-
itsch, B. Stein, S. Weidt and W. K. Hensinger.

Poster at ICAP 2010 - 22nd International Conference on Atomic Physics, 25-30 July 2010,

at Cairns, Australia.

Microfabricated asymmetric ion traps for quantum information and simulation,

R. C. Sterling, P. Srinivasan, J. D. Sivers, H. Rattanasonti, M. D. Hughes, M. Kraft and W. K. Hensinger.

Poster at ICAP 2010 - 22nd International Conference on Atomic Physics, 25-30 July 2010, at Cairns, Australia.

Design of optimum electrode configuration for fast ion separation and the development of junctions within ion trap arrays,

A. H. Nizamani, B. Stein, M. D. Hughes and W. K. Hensinger.

Poster at ICAP 2010 - 22nd International Conference on Atomic Physics, 25-30 July 2010, at Cairns, Australia.

Design and set up of an ytterbium ion trap experiment for quantum information processing,

Marcus D. Hughes, James J. McLoughlin, Altaf H. Nizamani, James D. Sivers, Robin C. Sterling and Winfried K. Hensinger.

Poster at SCALA Summer School, 17-29 August 2009, at Cargèse, Corsica (France).

Contents

List of Tables	xv
List of Figures	xxiv
1 Introduction	2
2 Ion trapping	6
2.1 Radio frequency ion traps	6
2.1.1 Ion trap dynamics	6
2.1.2 Motional and internal states of the ion.	11
2.1.3 Laser cooling	12
2.1.4 Operation of microfabricated ion traps	13
2.2 Linear ion traps	14
2.2.1 Linear ion trap geometries	15
2.2.2 From linear ion traps to arrays	17
2.3 Simulating the electric potentials of ion trap arrays	17
2.4 Electrical characteristics	19
2.4.1 Voltage breakdown and surface flashover	19
2.4.2 Power dissipation and loss tangent	20
2.5 Anomalous heating	23
3 Experimental setup	26
3.1 Ytterbium ions	26
3.1.1 Photoionisation	27
3.1.2 Doppler cooling	28
3.1.3 Destabilisation of dark states	30
3.2 Lasers and locking	30
3.2.1 External cavity laser diodes (ECLD)	31

3.2.2	369 nm Doppler cooling laser	32
3.2.3	Laser locking	33
3.3	Vacuum systems	37
3.3.1	Vacuum System I	37
3.3.2	Vacuum System II	39
3.3.3	Vacuum operation	39
3.4	Helical resonator	39
3.5	Imaging system	42
3.6	Macroscopic ion trap	44
3.6.1	Trap operation	46
3.6.2	Heating measurement	49
4	Asymmetric ion trap designs	55
4.1	Multi-layered structures	55
4.2	Design limitations	56
4.2.1	Electrical characteristics	58
4.3	Trap modelling	59
4.3.1	Numerical simulations	59
4.3.2	Analytical simulations	61
4.4	Asymmetric geometries	61
4.4.1	Ion separation	64
4.4.2	Alternative geometry	66
4.5	Y-junction ion trap	68
4.5.1	Electrical characteristics	70
4.5.2	Shuttling within the junction region	70
4.6	Two-dimensional ion trap arrays	77
4.6.1	Ion-ion interactions and lattice geometry	77
4.6.2	Simulation	79
4.6.3	Optimisation method	80
4.6.4	Lattice design	82
4.7	Ring ion traps	85
4.7.1	Ring designs	86
4.8	Linear ion trap	91
4.9	Photolithography mask design	91

5	Microfabrication techniques	96
5.1	Introduction	96
5.2	Photolithography	97
5.3	Deposition	99
5.3.1	Thin film deposition	99
5.3.2	Thick film deposition	101
5.3.3	Chemical vapor deposition (CVD)	103
5.4	Etching	105
5.4.1	Wet etching	105
5.4.2	Dry etching	106
6	Microfabrication process	108
6.1	Wafer preparation	108
6.2	Underlying conducting layer	110
6.2.1	Lift-off resist	110
6.2.2	Thermal deposition	111
6.2.3	Resist removal	112
6.3	Insulating Layer and vias	113
6.3.1	Plasma enhanced CVD	113
6.3.2	ICP etch resist	114
6.3.3	ICP etch	115
6.3.4	Resist removal	116
6.4	Electrode layer	116
6.4.1	Seed and adhesion layer	116
6.4.2	Electroplating resist	116
6.4.3	Removal of exposed adhesion layer	120
6.4.4	Electroplating	120
6.4.5	Resist removal	121
6.4.6	Etching of the seed and adhesion layer	122
6.4.7	Wafer dicing	125
6.5	Process sequence for multi-layered ion traps	126
6.6	Conclusion	130
7	Characterisation and testing of microfabricated ion traps	131
7.1	Voltage breakdown measurements	131

7.1.1	Bulk breakdown	133
7.1.2	Surface flashover	135
7.2	Vacuum System	137
7.2.1	Assembly	138
7.3	Trap packaging	140
7.4	Further work	142
8	Conclusion	143
	Bibliography	145
A	Mask set	165
A.1	First layer ‘buried wires’ mask	165
A.2	Second layer ‘vias’ mask	166
A.3	Third layer ‘electrodes’ mask	167
A.4	Y-junction ion trap	168
A.5	Lattice ion trap	171
A.6	‘Big’ ring ion trap	174
A.7	‘Small’ ring ion trap	177
A.8	Linear ion trap	180
A.9	Characterisation area	183
B	Electrical feedthrough map	186

List of Tables

3.1	Yb ionisation and Yb^+ transition wavelengths	30
3.2	Specifications of the resonator	42
3.3	Rf and static control volatges	47
4.1	List of parameters for the hexagonal ion trap lattice	83
5.1	List of properties and parameters during the thermal evaporation of thin metal layers	101
7.1	Bulk breakdown measurements	134
B.1	Mapping of bond pad number to corresponding D-type electrical feedthrough pin	186

List of Figures

2.1	Hyperbolic electrodes where an rf voltage of $V_0 \cos(\Omega_T t)$ together with a static voltage of U_0 is applied to two opposite electrodes. The polarity of this voltage is reversed and applied to the other set of electrodes.	7
2.2	Principles of confinement with a pseudopotential. (a) A saddle potential created by a static electric field from a hyperbolic electrode geometry. (b) The saddle potential acquiring an inversion from a change in polarity. (c) The effective potential the ion sees resulting from the oscillating electric potential.	8
2.3	Stability regions in which the motion of the ion is stable and can be trapped. a) By solving the Mathieu equations for both the x and y -axes of the trap, the overlap within both axes is obtained, shaded grey. b) The lowest region of stability.	9
2.4	Motion of the ion as given by equation 2.6, characterised by high amplitude slow frequency secular motion, $\omega_x/(2\pi) = 1$ MHz and small amplitude high frequency micromotion at a drive frequency of $\Omega_T/(2\pi) = 30$ MHz, with q parameter of 0.2 and a parameter of 0.	10
2.5	Wire bonding a microfabricated chip to a chip carrier providing external electrical connections.	14
2.6	Different linear trap geometries. (a) A two-layer design in which the rf electrodes (yellow) are diagonally opposite and the dc electrodes (grey) are segmented. (b) A three-layer design in which the rf electrodes are surrounded by the dc electrodes. (c) A five-wire asymmetric design where all the electrodes lie in the same plane.	15
2.7	for two-layer traps the aspect ratio is defined as w/d	16

2.8	Cross-section in the x - y plane of the different types of asymmetric designs, (a) Four-wire design in which the principal axes are naturally non-perpendicular with respect to the plane of the electrodes. (b) Five-wire design where the electrodes are symmetric and one principal axis is perpendicular to the surface. (c) Five-wire design with different widths rf electrodes, this allows the principal axes to be rotated.	16
2.9	First junction designs that have been used to successfully shuttle ions. . . .	18
2.10	The rf electrode modelled with resistance R , capacitance C , inductance L and conductance G	20
2.11	Approximation of power dissipated in the limit where $\tan \delta$ and $\Omega_T CR \ll 1$, the dissipated power can be simplified as $P_d = \frac{1}{2}V_0^2\Omega_T^2C^2R$ shown by the dashed line. When $\tan \delta \approx 0.22$ there is a 10% error within the approximation and equation 2.16	22
2.12	Previously published measurements of motional heating plotted as the product of electric field noise spectral density $S_E(\omega)$ and the secular frequency ω , versus ion-electrode distance d . A $1/d^4$ trend line is also shown. Each label shows both the ion species and the electrode material used and the electrode temperature is also noted if the measurement is performed below room temperature.	24
3.1	A partial energy level diagram for neutral ytterbium atoms showing the photoionisation process. A two-step process is used with one photon at 398nm and another at 369.5nm.	27
3.2	A partial energy level diagram for ytterbium ions. The driven transitions are shown in solid lines whilst the decays are dashed Due to background collisions the ion can be knocked into the $^2D_{5/2}$ state in which it decays into the long lived low lying $^2F_{7/2}$ state.	28
3.3	Partial Energy level diagram for $^{171}Yb^+$ atom with the addition hyperfine levels compared to neutral isotopes.	29
3.4	External cavity diode laser setup. (a) Schematic of the Littrow ECDL configuration. An aspheric lens is used to collimate the beam. A diffraction grating is then used to provide feedback and light to the experiment through the zeroth order beam. (b) A picture of the 399 nm ECDL system within our experiment.	31

3.5	Hyperfine structure of the ^{87}Rb D_2 transition line and saturation absorption signal	34
3.6	Schematic of the optical table setup providing locking of the lasers and alignment of the beams to the individual vacuum systems.	36
3.7	Picture of the first vacuum system hemisphere and octagon arrangement. (a) Front view. (b) Rear view. (c) Complete vacuum system.	38
3.8	Picture of the second vacuum system hemisphere and octagon arrangement. (a) Front view. (b) Rear view. (c) Complete vacuum system.	40
3.9	(a) Cap of the resonator with an antenna coil attached to impedance match the source frequency to ion trap circuit. Inside the coil and shield arrangement of the quarter wave helical resonator. (b) Complete construction of the resonator.	41
3.10	Schematic of the Imaging setup.	44
3.11	Design of the Blade trap.	45
3.12	Assembled Blade trap.	46
3.13	Simulated Pseudopotential of the trap electrodes after mechanical alignment. The first turning point within the trapping potential occurring at $\{x(\mu\text{m}), y(\mu\text{m})\} \approx \{330, 80\}$ has a potential of $4.9(2)\text{eV}$	47
3.14	Schematic of the laser alignment for trapping within the blade trap.	48
3.15	Ion chains produced within the Blade trap. (a) Chain of three $^{174}\text{Yb}^+$ ions. (b) Chain of 10 Yb^+ ions with a different isotope trapped and sympathetically cooled, shown by dark space. (c) By adjusting the rf voltage and thus varying the ratio between the radial and axial frequencies, a zigzag configuration can be achieved.	50
3.16	Probability density function of the ion showing the overlap with the linewidth of the transition. (a) Hot ion. (b) Cold ion.	51
3.17	The control sequence for turning the 369 nm laser on and off via the AOM and data collection from the PMT.	52
3.18	Averaged ion fluorescence from 500 runs for a 5 second delay at a secular frequency of $\omega_z/2\pi = 178(1)\text{ KHz}$	53
3.19	Motional quanta of the ion after various delay times, for an ion with secular frequency of $\omega_z/2\pi = 178(1)\text{ KHz}$	53
3.20	Heating rate as a function of secular frequency showing the expected $1/\omega^2$ dependency.	54

4.1	Multi-layered structure with buried wires to realise isolated control electrodes.	56
4.2	General process sequence for the construction of a multi-layered asymmetric trap. 1) A low loss tangent $\tan \delta$ wafer provides the foundation of the ion traps. 2) Deposition of patterned conducting layer for the buried wires. 3) Blanket deposition of an insulator layer. 4) Etching vertical interconnect access (vias) to gain access to the underlying conducting layer. 5) Deposition of the electrode structure.	57
4.3	Modelled ion trap circuit to provide an estimate on the dissipated power. .	58
4.4	Trap electrodes drawn in AutoCAD with four sided polygons with 3D polylines. The file is then exported as a .dxf file and is used to simulate the corresponding electric fields. (a) A linear segmented section, (b) a y-junction.	60
4.5	rf pseudopotential field created from an asymmetric electrode arrangement. To rotate the principal axis the symmetry of rf electrodes is broken with even rf widths having a ratio of 2:1.	61
4.6	Five wire asymmetric ion trap designs with inner segmented W_i and outer segmented W_o static control electrodes. (a) Equal rf electrode widths where $b = c$. (b) Unequal electrode widths where $c = b/2$. This provides rotation of the principal axes allowing for efficient laser cooling. To provide easier compensation of the ion position a ground wire is inserted such that the outer control electrodes are symmetric about the ion position.	63
4.7	Profile of the potential for different values of α . When $\alpha < 0$ a double well potential is created.	65
4.8	Five wire asymmetric ion trap design with equal rf electrode widths and additional static control rails to provide rotation of the principal axes allowing for efficient laser cooling. Alternating polarity of the voltages are applied to the rotation rails.	67
4.9	Complete design of the whole y-junction trap, the rf electrode is shaded blue and the buried wires yellow. The trap consists of 81 individual control electrodes combining both optimised inner and outer segmented electrodes for fast ion separation. A linear section and the y-junction are shown within the inserts. The geometry of the buried wires, shown in the insert tapers down to reduce the capacitance.	69

4.10	A plot of the rf pseudopotential together with the physical electrode geometry. With an applied voltage of 400 V at $\Omega_{rf}/2\pi = 30$ MHz the rf <i>barrier</i> has a maximum amplitude of ≈ 16 meV.	71
4.11	(a) Variations within the ion's radial position as a function of axial position. (b) Variation within the radial secular frequencies $\omega_x/2\pi$ (purple) and $\omega_y/2\pi$ (blue).	72
4.12	(a) Applied static voltages as a function of ion position $V_i(z)$ along the axial direction. The voltage on electrode 5 (centre of junction) is ramped to a negative value to 'pull' the ion over the rf <i>barrier</i> . (b) Variations in the axial secular frequency ω_z within the junction region from the applied voltages. .	73
4.13	Various ion velocity profiles, hyperbolic tangent, linear and sinusoidal. The hyperbolic tangent N-parameter can be varied to achieve different profiles. .	73
4.14	Voltage functions to shuttle the ion along path <i>a-c-d</i> . A hyperbolic tangent velocity profile with N-parameter of 4 was selected.	75
4.15	Simulated gain in kinetic energy of the ion during transport through the junction with a total shuttling time of $T = 300 \mu s$	75
4.16	Gain in kinetic energy of the ion for various shuttling times T using an $N=4$ hyperbolic tangent velocity profile. The red dashed curve represents the gain in motional quanta from anomalous heating during the shuttling process. The crossing point between the best fit of the data and anomalous heating determines the speed of shuttling whilst minimising the total gain in motional quanta.	76
4.17	A hexagonal arrangement of an ion trap lattice. Each site is defined by a polygon of radii R , the separation between the centres of the polygons A , and g the distance to the edge of the rf from the outer ion site.	79
4.18	Example contour plot of K_{sim} values for various polygon separations and radii. As the polygon radius and separation increase, so does α and K_{sim} . The lower bounded impossible region describe geometries in which the individual trapping sites start to merge into a singular trapping zone. This region describes when the polygon radius, R is greater than or equal to a third of the polygon separation, A	81

4.19	Hexagonal lattice with 22 individual trapping sites. The rf electrode is shaded blue and the buried wires yellow. Each lattice site has 4 control electrodes and is arranged such that the ion is not in direct sight of the dielectric layer. The buried wires providing electrical connections are $3\ \mu\text{m}$ and $\approx 1\ \text{mm}$ in length.	84
4.20	Pseudopotential of the lattice trap. (a) Cut through the trap at $z = -335\ \mu\text{m}$ at the ion height $r = 182\ \mu\text{m}$. (b) The trap depth of each lattice site is set to a minimum $\approx 0.1\ \text{eV}$ to maximise K_{sim}	84
4.21	A ring arrangement of 18 ions, a is defined as the ion-ion spacing and S the spacing to the next nearest ion.	85
4.22	Complete design of the ‘big’ ring ion trap, the rf electrode is shaded blue and the buried wires yellow. An ion height of $\sim 250\ \mu\text{m}$ is selected together with a radius of $1688\ \mu\text{m}$. Shown in the insert the rf electrodes are connected via a buried wire of dimensions $(1300\ \text{by}\ 50)\ \mu\text{m}^2$	88
4.23	Pseudopotential minimum as a function of ion position C , around the circumference of the ring trap. An rf <i>barrier</i> is present from the outer rf wire.	89
4.24	Complete design of the ‘small’ ring ion trap, the rf electrode is shaded blue and the buried wires yellow. An ion height of $\sim 98\ \mu\text{m}$ and a radius of $486\ \mu\text{m}$ is selected. Shown in the insert the rf electrodes are connected via a buried wire of dimensions $\approx (900\ \text{by}\ 25)\ \mu\text{m}^2$	90
4.25	Full design of the linear ion trap, the rf electrode is shaded blue and the buried wires yellow. An ion height of $\sim 220\ \mu\text{m}$ is selected to reduce the affects of anomalous heating, 70 individual control electrodes provide control of the ion in 41 individual trapping zones.	92
4.26	Finalised mask set. All three masks superimposed onto each other, each ion trap design is repeated twice, a characterisation area for voltage breakdown tests and a square frame for cleaving the ion traps is also included.	94
5.1	General process sequence for the use of a photoresist. A wafer is cleaned and dried before a photoresist layer is spin coated. After a soft bake the sample is then exposed to a UV light source through a patterned mask. Depending on whether the resist is positive or negative the exposed area can be removed or kept during development.	98
5.2	Spin coating a resist onto a wafer. An edge bead can develop	99

5.3	Schematic diagram of a thermal evaporator for the deposition of thin metallised films.	100
5.4	Au electroplating process, the sample is placed into an electrolyte solution and a current is created between the anode and cathode through the transport of ions allowing for the deposition of a metallic layer. The insert displays a connection pad, together with a seed layer provides a means to electrically connect all the trap electrodes.	102
5.5	Schematic of the Corial D250 PECVD chamber used to deposit the dielectric layer.	104
5.6	Conformality of CVD grown films. The deposited PECVD films were non-conformal transferring the underlying topography of the buried wires. . . .	105
5.7	Etch profiles obtain through wet and dry etching techniques.	105
6.1	Process flow showing all the main steps involved in the realisation of the trap structures. The sequence is classified into three general steps with the intermediate steps shown.	109
6.2	Negative profile of a resist for lift-off process. The deposited gold layer on the substrate remains separated making the process of lift-off possible. . . .	111
6.3	Microscope image showing a spit of gold shorting adjacent electrodes. . . .	112
6.4	Microscope image showing detaching of two underlying wires during the lift-off process.	113
6.5	Finalised insulating structure after performing breakdown measurements. .	114
6.6	Bubbling of the AZ 6632 resist due to insufficient evaporation of the solvents during the soft bake step.	114
6.7	(a) SEM picture showing delamination of the resist during electroplating. (b) Electroplating occurred within the gaps due to delamination.	117
6.8	Spin program of the KMPR 1025 resist to achieve a thickness of $\approx 18 \mu\text{m}$. .	118
6.9	Soft bake profile	118
6.10	(a) Nibbling of the resist structure from one continuous exposure. (b) Segmenting the exposure and adding in time delays between exposures improved the resolution.	119
6.11	Post exposure bake (PEB) profile	120
6.12	Electroplating of big ring design to a thickness of $18 \mu\text{m}$	121

6.13	Au etch trail on an electroplated structure. (a) Microscope focused on the quartz wafer showing residual Au remaining after an initial etch. (b) Microscope focused on the tracks showing seed layer still present after the initial etch. (c) After a second etch step the Au seed layer was removed in the tracks.	124
6.14	Picture of a ‘Big’ ring ion trap after the whole process sequence.	125
7.1	(a) Optical microscope image of two test samples. The sample on the left has two overlapping wires from different conducting layers to test bulk breakdown. The sample on the right has a gap of 20 μm to test surface flashover. (b) Side view schematic of a bulk breakdown sample.	132
7.2	(a) Circuit diagram for voltage breakdown measurements, the breakdown voltage is measured from an in built voltage divider. (b) The test samples are mounted to a chip carrier and wire bonded before being placed under vacuum in a glass belljar.	132
7.3	(a) SEM image of surface flashover over a 20 μm gap. (a) SEM image of bulk breakdown over a 2 μm SiO_2 layer showing the formation of a hot spot.	133
7.4	Dielectric structures of the samples used for bulk breakdown measurements. Sample A consists of 2.0 μm of SiO_2 . Sample B has the addition of two 80 nm Si_3N_4 layers. Sample C the addition of six ~ 80 nm alternating SiO_2 and Si_3N_4 layers totalling 0.5 μm	134
7.5	Comparison between Au on PECVD nitride and Au on quartz flashover measurements.	137
7.6	Custom recessed viewport designed by Bjoern Lekitsch. (a) Atmosphere side (b) Vacuum side (c) Side view.	138
7.7	Layout and pin arrangement of the frontside and backside ovens.	140
7.8	(a) Picture of the assembled vacuum system (b) Front view of the hemisphere and custom recessed window.	141
7.9	Photo of a ‘Big’ ring ion trap before being wire bonded.	142
A.1	Mask layout to pattern the first conducting layer.	165
A.2	Mask layout to create vias to the buried conducting wires.	166
A.3	Mask layout for the electrode layer of the trap designs.	167
A.4	Y-junction first layer mask.	168
A.5	Y-junction second layer mask.	169

A.6	Y-junction third layer mask.	170
A.7	Lattice first layer mask.	171
A.8	Lattice second layer mask.	172
A.9	Lattice third layer mask.	173
A.10	‘Big’ ring first layer mask.	174
A.11	‘Big’ ring second layer mask.	175
A.12	‘Big’ ring third layer mask.	176
A.13	‘Small’ ring first layer mask.	177
A.14	‘Small’ ring second layer mask.	178
A.15	‘Small’ ring third layer mask.	179
A.16	Linear first layer mask.	180
A.17	Linear second layer mask.	181
A.18	Linear third layer mask.	182
A.19	Characterisation first layer mask.	183
A.20	Characterisation second layer mask.	184
A.21	Characterisation third layer mask.	185
B.1	Mapping of the chip bracket pins to the corresponding pins on the 2×50 D-type electrical feedthroughs.	187
B.2	Schematic of the ceramic pin grad array (CPGA) chip carrier from Global Chip Materials (pt No. PGA20855101). 102 of the 208 pins on the chip are connected via the chip bracket. The bond pads are numbered from the bottom left corner in a anticlockwise direction. The rf and ground pins are highlighted. A mapping of the bond pad to feedthrough pin number is presented in table B.1.	188

“The way to deal with an impossible task was to chop it down into a number of merely very difficult tasks, and break each one of them into a group of horribly hard tasks, and each of them into tricky jobs, and each of them...”

Terry Pratchett, Truckers

Chapter 1

Introduction

The constant development of classical computers with the ever decreasing size of individual components has allowed for faster and more complex computations to be performed. Quantum mechanics opens up a new direction in solving particular problems. Extremely non-intuitive phenomena exist, including the superposition of a particles internal states and the entanglement between particles. These quantum features have lead to the idea and development of a quantum computer, allowing for exponential improvement over a classical computer when dealing with certain tasks such as Grover’s search algorithm [1] and Shor’s algorithm [2] for factorising large numbers. Many physical systems are being pursued to realise a quantum computer from photons [3], NMR [4, 5], superconducting circuits [6–8], solid state devices such as impurities in silicon [9] and diamond [10], neutral trapped atoms [11, 12] and trapped atomic ions [13, 14]. In general, ion traps compare well to other physical systems with good isolation from the environment and long coherence times.

Ion trapping was developed by Wolfgang Paul [15] and Hans Dehmelt [16] in the 1950’s and 60’s and has lead to studies of fundamental physics [17–19], spectroscopy [20], and coherent control [21], as well as becoming an important tool to study important physical systems such as ion cavity QED [22, 23], quantum simulators [24–28], determine frequency standards [29–32] and then the development towards a quantum information processor. First proposed in 1995 by Cirac and Zoller [33] the scheme developed uses the motional modes as a quantum bus between a string of ions. Since then there has been ongoing development [21, 34] with the extension of this scheme by D. Kielpinski *et al.* in 2002 [14], introducing the idea of a ”quantum CCD” in which ions can be shuttled through an array of various regions, including storage, transport and interaction regions, together with the

coupling of a small collection of ions through the Coulomb-Coulomb interaction.

Two types of ion traps exist, Paul traps, also known as radio frequency (rf) ion traps and Penning traps [35]. Rf traps employ a combination of static and oscillating electric fields to create a potential minimum. Penning traps use static electric and magnetic fields to produce confinement. Paul traps are more practical in the development of a quantum information processor and they are the focus of this thesis. Advances in fabrication of Penning traps have been discussed by Castrejón-Pita *et al.* [36] and will not be discussed within my thesis.

In 1995, David DiVincenzo set out criteria which determine how well a system can be used for quantum computing [37]. Most of these criteria have been demonstrated with an ion trap: Qubit initialization [38, 39], a set of universal quantum gates creating entanglement between ions [33, 40–42], long coherence times [43], detection of states [44, 45] and a scalable architecture to host a large number of qubits [46–49]. An important research area is the development of a scalable architecture which can incorporate all of the DiVincenzo criteria. A realistic architecture has been proposed consisting of an ion trap array incorporating storage and gate regions [13, 14, 50] and could be implemented using microfabricated ion traps. Microfabricated ion traps hold the possibility of small trap dimensions on the order of tens of micrometers and more importantly fabrication methods like photolithography that allow the fabrication of very large scale arrays. Electrodes with precise shape, size and geometry can be created through a number of process steps when fabricating the trap.

Quantum simulators present an important stepping stone in the pursuit of a quantum computer. Richard Feynman and David Deutsch in 1980's described how a quantum system can be simulated using another quantum system which is easier to control giving rise to the idea of the quantum simulator [51]. This becomes important as the number of particles increases, the entanglement between these particles becomes increasingly difficult to classically simulate even for tens of particles [52, 53]. Trapped ions have been used to study quantum simulations of spin systems, spin frustration of three ions in a linear chain was performed [28], then extended to studying the emergence of magnetism within an 9 ion chain [54] and the adiabatic evolution of paramagnetic into ferromagnetic order of two spin system [25]. The focus is now extending to more complex systems such as two-dimensional arrays of ions [27, 55, 56] allowing for the time evolution of spin lattice

structures to be studied.

Microfabrication techniques allow for a new generation of ion traps with the ion - electrode distance on the order of tens of micrometers, together with the availability of versatile and scalable fabrication methods. Micro-electromechanical systems (MEMS) and other micro-fabrication technologies will become important in the development of more sophisticated ion traps. Although there have been many advances in the development of ion trap architectures, there are still many technical problems. Within my thesis I will focus on the design and development of microfabricated ion traps with the goal of producing architectures capable of demonstrating elements of a quantum information processor and provide ion trap simulator array structures. A fabrication process is created that can be extended to more advanced arrays.

Within chapter 2 an introduction to ion trapping is presented, with important considerations with regards to microfabrication highlighted. This provides a foundation in the design and operation of such traps.

Chapter 3 describes an overview of the experimental setup in the initial trapping of Yb ions. This includes the atomic structure Yb and the laser setup needed to ionise and Doppler cool Yb ions. The vacuum systems which are capable of housing symmetric and asymmetric ion trap arrays and the imaging system used to accommodate both vacuum systems are also presented. A description of the macroscopic two-layer symmetric ion trap is presented, this provided the initial trapping of Yb ions, allowing for more precise measurements of the transition wavelengths of the different Yb isotopes and the characterisation of the trap through heating measurements.

Chapter 4 describes the design of asymmetric ion traps incorporating isolated electrodes. A general fabrication process to realise such structures is considered, providing estimates for the electrical characteristics of the ion traps. We make sure these do not pose a problem for the operation of the traps. The geometry of the electrodes is then investigated. Electrode arrangements are calculated to maximise trap depth for a given ion height. Optimised electrodes for fast separation and recombination of ions are then incorporated into the designs to obtain more control of the ions, a key requirements when determining shuttling protocols. This is then applied to theoretical shuttling within a y-junction. New

ion trap architectures are considered with the availability of isolated electrodes including an ion-trap lattice and ring trap designs.

Chapter 5 outlines microfabrication techniques involved in creating the ion trap arrays. Basic photolithography, deposition and etching techniques are presented highlighting their capabilities as well as their limitations. The exact fabrication process is then discussed in more detail within chapter 6, highlighting the important techniques that were unique to the fabrication process.

Chapter 7 describes the characterisation and testing of the fabricated ion traps before they can be used within the experimental setup. Voltage breakdown measurements of trap structures were performed to ensure sufficient voltage could be supplied for designed operation of the traps. A new experimental setup is presented to accommodate the ion trap chips building on the experiences with the previous experiments.

Chapter 2

Ion trapping

This chapter provides a general introduction to ion trapping¹, highlighting important aspects when considering the design and operation of microfabricated ion traps. First I will discuss basic principles of ion traps and their operation in section 2.1. Section 2.2.1 discusses linear ion trap geometries as a foundation of most ion trap arrays. The methodology of efficient simulation of electric fields within ion trap arrays is discussed in Section 2.3. Section 2.4 discusses some material characteristics that have to be considered when designing microfabricated ion traps including electric breakdown and rf dissipation. Section 2.5 discusses motional heating of the ion due to fluctuating voltage patches on surfaces and its implications for the design and fabrication of microfabricated ion traps.

2.1 Radio frequency ion traps

Static electric fields alone cannot confine charged particles, this is a consequence of Earnshaw's theorem [57] which is analogous to Maxwell's equation $\nabla \cdot E = 0$. To overcome this, Penning traps use a combination of static electric and magnetic fields to confine the ion [35, 58]. Radio frequency (rf) Paul traps use a combination of static and oscillating electric fields to achieve confinement. We begin with an introduction into the operation of radio frequency ion traps, highlighting important factors when considering the design of microfabricated ion traps.

2.1.1 Ion trap dynamics

First we consider a quadrupole potential within the radial directions, x and y -axes, which is created from hyperbolic electrodes as shown in Fig. 2.1, whilst there is no confinement

¹Adapted from article; **Microfabricated ion traps**, Marcus D. Hughes, Bjoern Lekitsch, Jiddu Broersma and Winfried K. Hensinger, Contemporary Physics 52:6, 505-529 (2011).

within the axial (z) direction. By considering a static voltage V_0 applied to two opposite electrodes, the resultant electric potential will produce a saddle as depicted in Fig. 2.2 (a). With the ion present within this potential, the ion will feel an inward force in one direction and outward force in the direction perpendicular to the first. Reversing the polarity of the applied voltage the saddle potential will undergo an inversion as shown in Fig. 2.2 (b). As the force acting on the ion is proportional to the gradient of the potential, the magnitude of the force is less when the ion is closer to the centre. The initial inward force will move the ion towards the centre where the resultant outward force half a cycle later will be smaller. Over one oscillation the ion experiences a greater force towards the centre of the trap than outwards resulting in confinement. The effective potential the ion sees when in an oscillating electric field is shown in Fig. 2.2 (c). If the frequency of the oscillating voltage is too small then the ion will not be confined long enough in one direction. For the case where a high frequency is chosen then the effective difference between the inward and outward forces decreases and the resultant potential is minimal. By selecting the appropriate frequency Ω_T of this oscillating voltage together with the amplitude V_0 which is dependent on the mass of the charged particle, confinement of the particle can be achieved within the radial directions.

There are two ways to calculate the dynamics of an ion within a Paul trap, firstly a com-

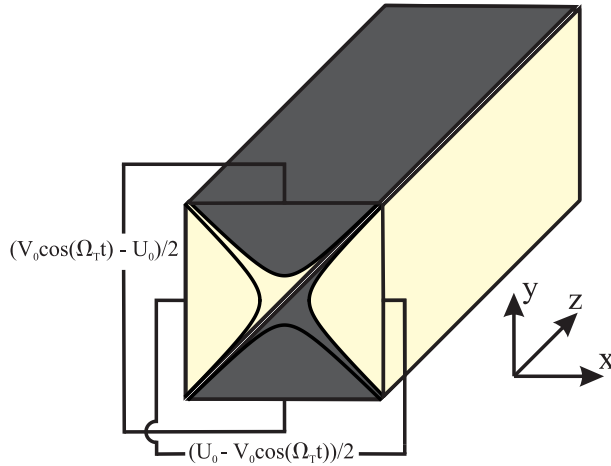


Figure 2.1: Hyperbolic electrodes where an rf voltage of $V_0 \cos(\Omega_T t)$ together with a static voltage of U_0 is applied to two opposite electrodes. The polarity of this voltage is reversed and applied to the other set of electrodes.

prehensive treatment can be given using the Mathieu equation. The Mathieu equation provides a complete solution for the dynamics of the ion. It also allows for the determination of parameter regions of stability where the ion can be trapped. These regions of stability are determined by trap parameters such as voltage amplitude and rf drive

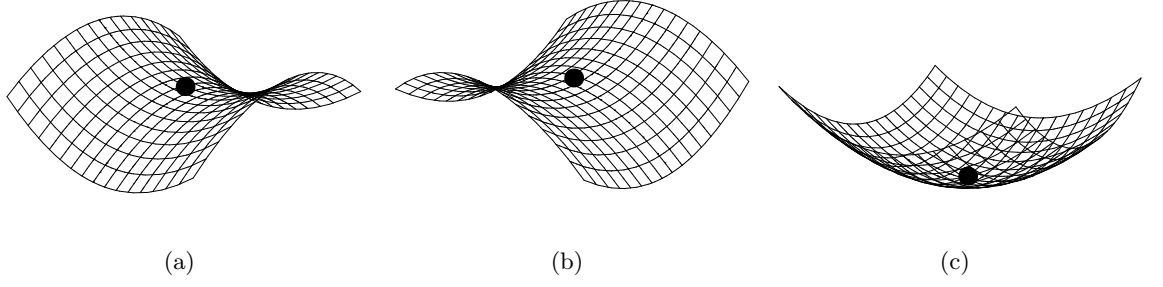


Figure 2.2: Principles of confinement with a pseudopotential. (a) A saddle potential created by a static electric field from a hyperbolic electrode geometry. (b) The saddle potential acquiring an inversion from a change in polarity. (c) The effective potential the ion sees resulting from the oscillating electric potential.

frequency. Here we outline the process involved in solving the equation of motion via the Mathieu equation approach. By applying an oscillating potential together with a static potential, the total potential for the geometry in Fig. 2.1 can be expressed as [18]

$$\phi(x, y, t) = (U_0 - V_0 \cos(\Omega_T t)) \left(\frac{x^2 - y^2}{2r_0^2} \right) \quad (2.1)$$

where r_0 is defined as the ion-electrode distance. This is from the centre of the trap to the nearest electrode and Ω_T is the drive frequency of the applied time varying voltage. The equations of motion of the ion due to the above potential are then given by [18]

$$\frac{d^2x}{dt^2} = -\frac{e}{m} \frac{\partial \phi(x, y, t)}{\partial x} = -\frac{e}{mr_0^2} (U_0 - V_0 \cos \Omega_T t) x \quad (2.2)$$

$$\frac{d^2y}{dt^2} = -\frac{e}{m} \frac{\partial \phi(x, y, t)}{\partial y} = \frac{e}{mr_0^2} (U_0 - V_0 \cos \Omega_T t) y \quad (2.3)$$

$$\frac{d^2z}{dt^2} = 0 \quad (2.4)$$

Later it will be shown that the confinement in the z -axis will be produced from the addition of a static potential. Making the following substitution

$$a_x = -a_y = \frac{4eU_0}{mr_0^2\Omega_T^2}, \quad q_x = -q_y = \frac{2eV_0}{mr_0^2\Omega_T^2}, \quad \zeta = \Omega_T t/2$$

equations 2.2 and 2.3 can be written in the form of the Mathieu equation.

$$\frac{d^2i}{d\zeta^2} + (a_i - 2q_i \cos 2\zeta)i = 0, \quad i = [x, y] \quad (2.5)$$

The general Mathieu equation given by equation 2.5 is periodic due to the $2q_i \cos 2\zeta$ term. The Floquet theorem [59] can be used as a method for obtaining a solution. Stability regions for certain values of the a and q parameters exist in which the ion motion is stable. By considering the overlap of both the stability regions for the x and y -axes of the trap, the parameter region where stable trapping can be accomplished is obtained. This is shown in Fig. 2.3. For the case when $a = 0$, $q \ll 1$ then the motion of the ion in the x -axis can be described as follows,

$$x(t) = x_0 \cos(\omega_x t) \left[1 + \frac{q_x}{2} \cos(\Omega_T t) \right] \quad (2.6)$$

with the equation of motion in the y -axis of the same form. The motion of the ion is composed of secular motion ω_x (high amplitude slow frequency) and micromotion at the drive frequency Ω_T (small amplitude high frequency) shown in Fig 2.4.

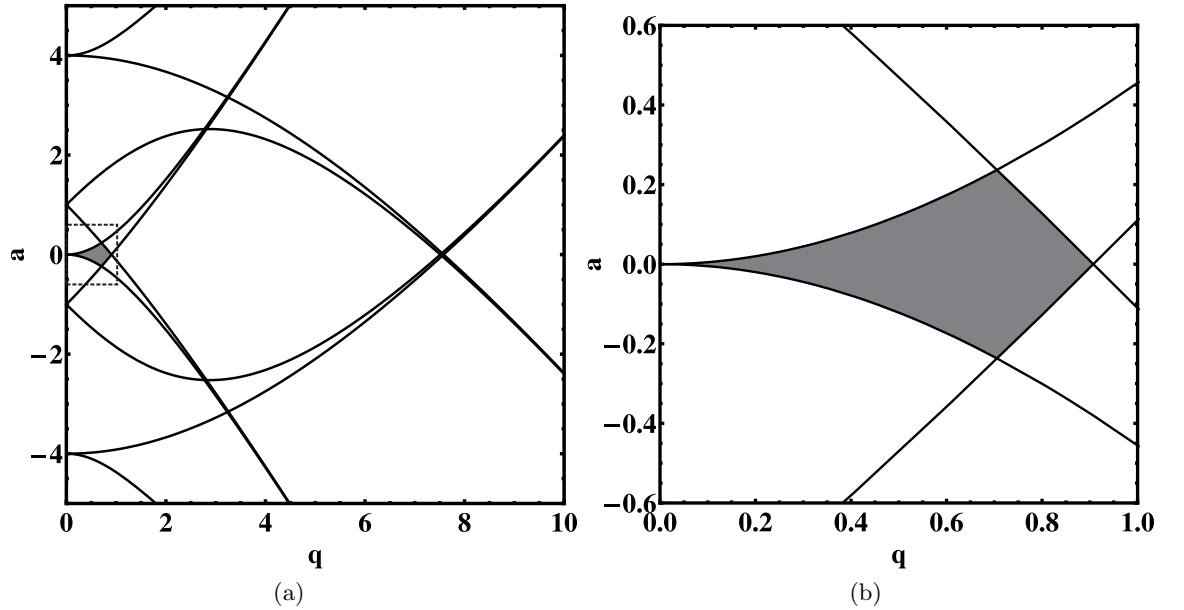


Figure 2.3: Stability regions in which the motion of the ion is stable and can be trapped. a) By solving the Mathieu equations for both the x and y -axes of the trap, the overlap within both axes is obtained, shaded grey. b) The lowest region of stability.

The second way to calculate motion is the pseudopotential approximation [16]. This considers the time averaged force experienced by the ion in an inhomogeneous field. With an rf voltage of $V_0 \cos \Omega_T t$ applied to the trap a solution for the pseudopotential approximation is given by [16]

$$\psi(x, y, z) = \frac{e^2}{4m\Omega_T^2} |\nabla V(x, y, z)|^2 \quad (2.7)$$

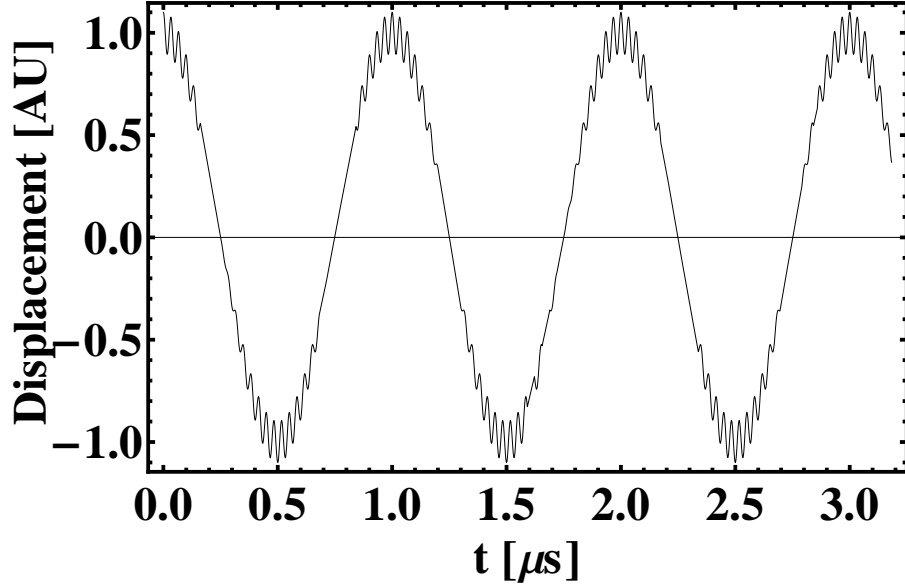


Figure 2.4: Motion of the ion as given by equation 2.6, characterised by high amplitude slow frequency secular motion, $\omega_x/(2\pi) = 1$ MHz and small amplitude high frequency micromotion at a drive frequency of $\Omega_T/(2\pi) = 30$ MHz, with q parameter of 0.2 and a parameter of 0.

where m is the mass of the ion, $\nabla V(x, y, z)$ is the gradient of the potential. The motion of the ion in a rf potential can be described just by the secular motion in the limit where $q_i/2 \equiv \sqrt{2}\omega_i/\Omega_T \ll 1$. The secular frequency of the ion is given by [60].

$$\omega_i^2(x, y, z) = \frac{e^2}{4m^2\Omega_T^2} \frac{\partial^2}{\partial x^2} (|\nabla V(x, y, z)|^2) \quad (2.8)$$

The pseudopotential approximation provides a means to treat the rf potential in terms of electrostatics only, leading to simpler analysis of electrode geometries.

Micromotion can be divided into intrinsic and extrinsic micromotion. Intrinsic micromotion refers to the driven motion of the ion when displaced from the rf nil position due to the secular oscillation within the trap. Extrinsic micromotion describes an offset of the ion's position from the rf nil from stray electric fields, this can be due to imperfections of the symmetry in the construction of the trap electrodes or the build up of charge on dielectric surfaces. Micromotion can cause a problem with the widening of atomic transition linewidth, second-order Doppler shifts and reduced lifetimes without cooling [61]. It is therefore important when designing ion traps that compensation of stray electric fields can occur in all directions of motion. Another important factor is the occurrence of a possible phase difference φ between the rf voltages on different rf electrodes within the ion

trap. This will result in micromotion that cannot be compensated for. A phase difference of $\varphi = 1^\circ$ can lead to an increase in the equivalent temperature for the kinetic energy due to the excess micromotion of 0.41 K [61], well above the Doppler limit of a few milli-kelvin.

The trap depth of an ion trap is the potential difference between pseudopotential at the minimum of the ion trap and the lowest turning point of the potential well. For hyperbolic geometries this is at the surface of the electrodes, for linear geometries (see section 2.2.1) it can be obtained through electric field simulations. Higher trap depths are preferable as they allow the ion to remain trapped longer without cooling. Typical trap depths are on the order of a few eV. The speed of optical qubit gates for quantum information processing [62] and shuttling within arrays [63] is dependent on the secular frequency of the ion trap. Secular frequencies and trap depth are a function of applied voltage, drive frequency Ω_T , the mass of the ion m and the particular geometry (the ion - electrode distance). Since the variation of the drive frequency is limited by the stability parameters, it is important to achieve large maximal rf voltages for the design of microfabricated ion traps, which is typically limited by bulk breakdown and surface flashover (see section 2.4). It is also important to note that the secular frequency also increases whilst scaling down trap dimensions for a given applied voltage allowing for large secular frequencies at relatively small applied voltages.

2.1.2 Motional and internal states of the ion.

Single ions can be considered to be trapped within a three-dimensional harmonic well with the three directions of motion uncoupled. Considering the motion of the ion along one of the axes, the Hamiltonian describing this model can be represented as

$$H = \hbar\omega \left(a^\dagger a + \frac{1}{2} \right) \quad (2.9)$$

with ω the secular frequency, a^\dagger and a the raising and lowering operators respectively, these operators have the following properties $a^\dagger|n\rangle = \sqrt{n+1}|n+1\rangle$, $a|n\rangle = \sqrt{n}|n-1\rangle$. When an ion moves up one motional level, it is said to have gained one motional quantum of kinetic energy. For most quantum gates with trapped ions, the ion must reside within the Lamb-Dicke regime. This is where the ion's wave function spread is much less than the optical wavelength of the photons interacting with the ion. The original proposed gates [13] required the ion to be in the ground state motional energy level, but more robust schemes [41] do not have such stringent requirements anymore.

Another requirement for many quantum technology applications is the availability of a two-level system which will act as the qubit, such that the ion's internal states can be used for encoding. The qubit can then be initialised into the state $|1\rangle$, $|0\rangle$ or a superposition of both. Typical ion species used are hydrogenic ions, which are left with one orbiting electron in the outer shell and are similar in structure to hydrogen once ionised. These have the simplest lower level energy diagrams. Candidates for ions to be used as qubits can be subdivided into two categories. Hyperfine qubits, $^{171}\text{Yb}^+$ [64–67], $^{43}\text{Ca}^+$ [68], $^9\text{Be}^+$ [69], $^{111}\text{Cd}^+$ [70], $^{25}\text{Mg}^+$ [71] [72] use the hyperfine levels of the ground state and have lifetimes on the order of thousands of years, whilst optical qubits, $^{40}\text{Ca}^+$ [68, 73], $^{137}\text{Ba}^+$ [74], $^{88}\text{Sr}^+$ [75], $^{172}\text{Yb}^+$ [76] use a ground state and a metastable state as the two level system. These metastable states typically have lifetimes on the order of seconds and are connected via optical transitions to the other qubit state.

2.1.3 Laser cooling

For most applications, the ion has to be cooled to a state of sufficiently low motional quanta, which can be achieved via laser cooling. For a two level system, when a laser field with a frequency equivalent to the spacing between the two energy levels is applied to the ion, photons will be absorbed resulting in a momentum “kick” onto the ion. The photon is then spontaneously emitted which leads to another momentum kick onto the ion in a completely random direction so the net effect of many photon emissions averages to zero. Due to the motion of the ion within the harmonic potential the laser frequency will undergo a Doppler shift. By red detuning (lower frequency) the laser frequency by δ from resonance, Doppler cooling can be achieved. When the ion moves towards the laser, the ion will experience a Doppler shift towards the resonant transition frequency and more scattering events will occur with the net momentum transfer slowing the ion down. Less scattering events will occur when travelling away from the Doppler shifted laser creating a net cooling of the ion's motion. Doppler cooling can typically only achieve an average motional energy state $\bar{n} > 1$. In order to cool to the ground state of motion, resolved sideband cooling can be utilised. This can be achieved with stimulated Raman transitions [77, 78].

For effective cooling of the ion, the \vec{k} -vector of the laser needs a component in all three directions of uncoupled motion. These directions depend on the trap potential and they

are called the principal axes. For a convenient choice of directions for the laser beam, the principal axes can be rotated by an angle θ by application of appropriate voltages on compensation electrodes [60, 79] or asymmetries in the geometry about the ion's position [80–82]. The angle of rotation of the principal axes can be obtained through the Hessian matrix of the electric field. This angle describes a linear transformation of the electric potential that eliminates any cross terms between the axes creating uncoupled equations of motion. The eigenvectors of the matrix signify the direction of the principal axes.

2.1.4 Operation of microfabricated ion traps

In order to successfully operate a microfabricated ion trap a certain experimental infrastructure needs to be in place, from the ultra high vacuum (UHV) system apparatus to the radio-frequency source. More specific details to our experimental setup can be found in Chapter 3. A description of experimental considerations for the operation of microfabricated ion traps was given by McLoughlin *et al.* [83]. For long storage times of trapped ions and performing gate operations, the collision with background particles must not be a limiting factor. Ion traps are therefore typically operated under ultra high vacuum (UHV) (pressures of $10^{-9} - 10^{-12}$ mbar). The materials used need to be chosen carefully such that outgassing does not pose a problem.

To generate the high rf voltage (~ 100 - 1000 V) a resonator [84] is commonly used. Typical resonator designs include helical and coaxial resonators. The advantage of using a resonator, is that it provides a frequency source with a narrow bandpass, defined by the quality factor Q of the combined resonator - ion trap circuit. This provides a means of filtering out frequencies that couple to the motion of the ion leading to motional heating of the trapped ion. A resonator also fulfills the function of impedance matching the frequency source to the ion trap. The total resistance and capacitance of the trap lowers the Q factor. It is therefore important to minimise the resistance and capacitance of the ion trap array if a high Q value is desired.

To provide electrical connections, ion traps are typically mounted on a chip carrier with electrical connections provided by wire bonding individual electrodes to an associated connection on the chip carrier. Bond pads on the chip are used to provide a surface on

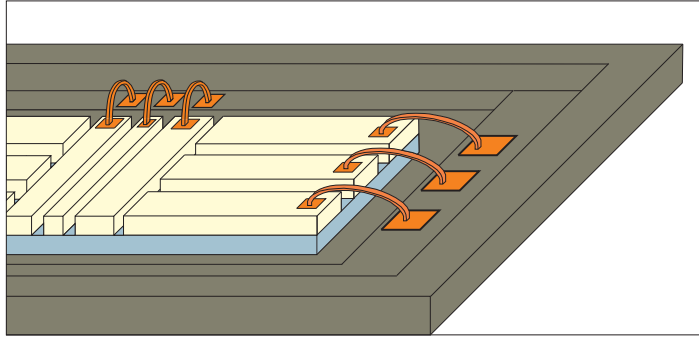


Figure 2.5: Wire bonding a microfabricated chip to a chip carrier providing external electrical connections.

which the wire can be connected to, see Fig. 2.5. The pins of the chip carrier are connected to wires which pass to external voltage supplies outside the vacuum system.

The loading of atomic ions within Paul traps is performed utilising a beam of neutral atoms typically originating from an atomic oven consisting of a resistively heated metallic tube filled with the appropriate atomic species or its oxide. The atomic flux is directed to the trapping region where atoms can be ionised via electron bombardment or more commonly by photoionisation, see for example refs. [83, 85]. The latter has the advantage of faster loading rates requiring lower neutral atom pressures and results in less charge build up resulting from electron bombardment. For asymmetric traps in which all the electrodes lie in the same plane, see Fig. 2.6, a hole within the electrode structure can be used for the atomic flux to pass through the trap structure, this is defined as backside loading [80]. The motivation behind this method is to reduce the coating of the electrodes and more importantly reduce coating of the notches between the electrodes from the atomic beam reducing charge build up and the possibility of shorting between electrodes. However, the atomic flux can also be directed parallel to the surface in an asymmetric ion trap due to the low atomic flux required for photoionisation loading.

2.2 Linear ion traps

The previously mentioned ideal linear hyperbolic trap only provides confinement within the radial directions and does not allow for optical access. By modifying the geometry as depicted in Fig. 2.6 linear ion traps are created. To create an effective static potential for the confinement in the axial (z -axis) direction, the associated electrodes are segmented. This allows for the creation of a saddle potential and when superimposed onto the rf

pseudopotential, it provides trapping in three dimensions. By selecting the appropriate amplitudes for the rf and static potentials such that the radial secular frequencies ω_x, ω_y are significantly larger than the axial frequency ω_z , multiple ions will form a linear chain along the z -axis. The motion of the ion near the centre of the trap can be considered to be harmonic as a very good approximation. The radial secular frequency of a linear trap is on the order of that of a hyperbolic ion trap of the same ion - electrode distance but different by a geometric factor η [60].

2.2.1 Linear ion trap geometries

Linear ion trap geometries can be realised in a symmetric or asymmetric design as depicted in Fig. 2.6. In symmetric designs the ions are trapped between the electrodes, as

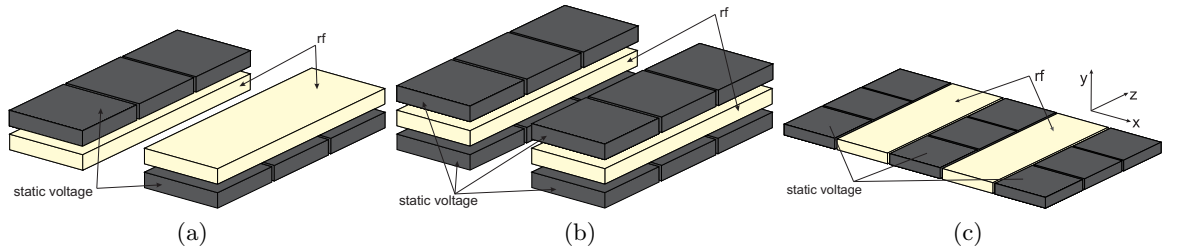


Figure 2.6: Different linear trap geometries. (a) A two-layer design in which the rf electrodes (yellow) are diagonally opposite and the dc electrodes (grey) are segmented. (b) A three-layer design in which the rf electrodes are surrounded by the dc electrodes. (c) A five-wire asymmetric design where all the electrodes lie in the same plane.

shown for two- and three-layer designs in Fig. 2.6 (a) and (b) respectively. These types of designs offer higher trap depths and secular frequencies compared to asymmetric traps of the same trap parameters. Two-layer designs offer the highest secular frequencies and trap depths whilst three-layer designs offer more control of the ions position for micromotion compensation and shuttling.

The aspect ratio for symmetric designs is defined as the ratio of the separation between the two sets of electrodes w and the separation of the layers d depicted in Fig. 2.7. As the aspect ratio rises, the geometric efficiency factor η decreases and approaches asymptotically $1/\pi$ for two-layer designs. [60]. Another advantage of symmetric traps is more freedom of optical laser access, allowing laser beams to enter the trapping zone in various angles. In asymmetric trap structures the laser beams typically have to enter the trapping zone parallel to the trap surface. Asymmetric designs offer the possibility of simpler fabrication processes. Buried wires [81] and vertical interconnect access (vias) can provide electrical

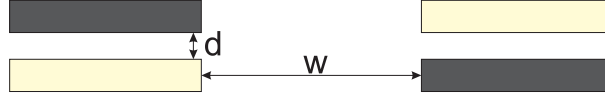


Figure 2.7: for two-layer traps the aspect ratio is defined as w/d

connections to electrodes which cannot be connected via surface pathways. Traps depths are typically smaller than for symmetric ion traps, therefore higher voltages need to be applied to obtain the same trap depth and secular frequencies of an equivalent symmetric ion trap. The widths of the individual electrodes can be optimised to maximise trap depth [82].

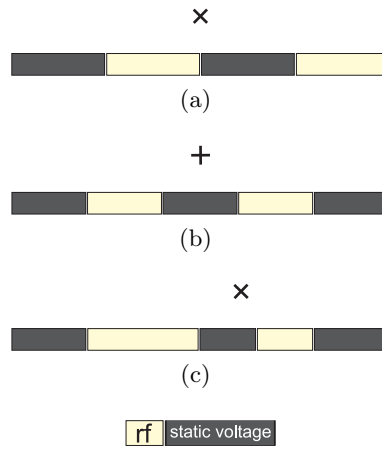


Figure 2.8: Cross-section in the x - y plane of the different types of asymmetric designs, (a) Four-wire design in which the principal axes are naturally non-perpendicular with respect to the plane of the electrodes. (b) Five-wire design where the electrodes are symmetric and one principal axis is perpendicular to the surface. (c) Five-wire design with different widths rf electrodes, this allows the principal axes to be rotated.

In order to successfully cool ions, Doppler cooling needs to occur along all three principal axes therefore the \vec{k} -vector of the laser needs to have a component along all the principal axes. Due to the limitation of the laser running parallel to the surface it is important that all principal axes have a component along the \vec{k} -vector of the Doppler cooling laser beam. Five-wire designs (Fig. 2.8(b) and (c)) have a static voltage electrode below the ions position, surrounded by rf electrodes and additional static voltage electrodes, with the rf electrodes of equal width (Fig. 2.8(b)) one of the principal axes is perpendicular to the surface of the trap. However, it can be rotated via utilising two rf electrodes of different width (Fig. 2.8(c)) or via splitting the central electrodes [79]. A four-wire design shown in Fig. 2.8(a) has the principal axes naturally rotated but the ion is in direct sight of the dielectric layer below since the ion is located exactly above the trench separating two

electrodes. Deep trenches have been implemented [80, 86] to reduce the effect of exposed dielectrics.

2.2.2 From linear ion traps to arrays

For ions stored in microfabricated ion traps to become viable for quantum information processing, thousands or even millions of ions need to be stored and interact with each other. This likely requires a number of individual trapping regions that is on the same order as the number of ions and furthermore, the ability for the ions to interact with each other so that quantum information can be exchanged. This could be achieved via arrays of trapping zones that are connected via junctions. To scale up to such an array requires fabrication methods that are capable of producing large scale arrays without requiring an unreasonable overhead in fabrication difficulty. This makes some fabrication methods more viable for scalability than other techniques.

The transport of ions through junctions has first been demonstrated within a three-layer symmetric design [48] and later near-adiabatically in a two-layer symmetric trap array [49], shown in Fig. 2.9 (a) and (b) respectively. Both ion trap arrays were made from laser machined alumina substrates incorporating mechanical alignment. The necessity of mechanical alignment and laser machining limit the opportunity to scale up to much larger numbers of electrodes making other microfabrication methods more suitable in the long term. Transport through an asymmetric ion trap junction (Fig. 7 (c)) was then demonstrated by Amini *et al.* [81], however, this non adiabatic transport required continuous laser cooling. Wesenberg carried out a theoretical study [87] how one can implement optimal ion trap array intersections. Splatt *et al.* demonstrated reordering of ions within a linear trap [88].

2.3 Simulating the electric potentials of ion trap arrays

Accurate simulations of the electric potentials are important for determining trap depths, secular frequencies and to simulate adiabatic transport including the separation of multiple ions and shuttling through corners [63, 89]. Various methods can be used in determining the electric potentials from the trap electrodes, with both analytical and numerical methods available. Numerical simulations using the finite element method (FEM) and the boundary element method (BEM) [63, 90] provide means to obtain the full 3D potential

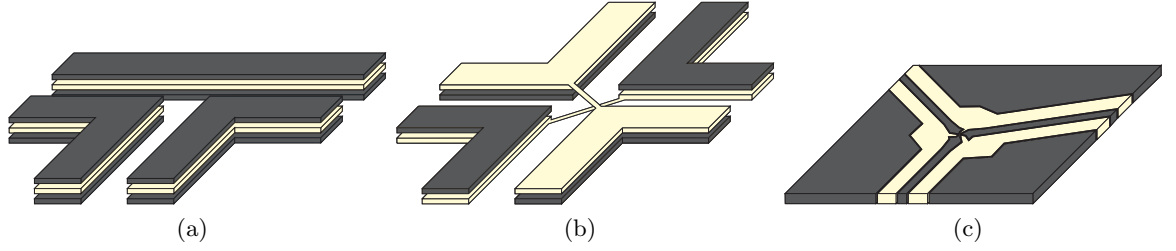


Figure 2.9: First junction designs that have been used to successfully shuttle ions. The yellow parts represent the rf electrodes. No segmentation of the static voltage electrodes (grey) is shown. (a) T-junction design [48] where corner shuttling and swapping of two ions were demonstrated for the first time. While the transport was reliable the ion gained a significant amount of kinetic energy during a corner-turning operation. (b) A two-layer X-junction [49] was used to demonstrate highly reliable transport through a junction with a kinetic energy gain of only a few motional quanta. (c) A Y-junction [81] was used to demonstrate transport through an asymmetric junction design, however, requiring continuous laser cooling during the shuttling process.

of the trap array. FEM works by dividing the region of interest into a mesh of nodes and vertices, an iterative process then finds a solution which connects the nodes whilst satisfying the boundary conditions and a potential can be found for each node. BEM starts with the integral equation formulation of Laplace's equation resulting in only surface integrals being non-zero in an empty ion trap. Due to BEM solving surface integrals, this is a dimensional order less than FEM thus providing a more efficient numerical solution than FEM [63]. To obtain the total potential the basis function method is used [63]. A basis function for a particular electrode is obtained by applying 1V to one particular electrode whilst holding the other electrodes at ground. By summing all the basis functions (with each basis function multiplied by the actual voltage for the particular electrode) the total trapping potential can be obtained.

For the case of asymmetric ion traps, analytical methods provide means to calculate the trapping potential significantly faster allowing for optimisation of the electrode structures. A Biot-Savart-like law [91] can be used and is related to the Biot-Savart law for magnetic fields in which the magnetic field at a point of interest is obtained by solving the line integral of an electrical current around a closed loop. This analogy is then applied to electric fields in the case of asymmetric ion traps [92]. One limitation for these analytical methods is the fact that all the electrodes must lie in a single plane, with no gaps, which is referred to as the gapless plane approximation. House [93] has obtained analytical solutions to the electrostatic potential of asymmetric ion trap geometries with the electrodes located

on a single plane within a gapless plane approximation. Microfabrication typically requires gaps of a few micrometers [80] which need to be created to allow for different voltages on neighboring electrodes. The approximation is suggested to be reasonable for gaps much smaller than the electrode widths and studies into the effect of gapped and finite electrodes have been conducted [94]. However, within the junction region where electrodes can be very small and high accuracy is required, the gapless plane approximation may not necessarily be sufficient.

2.4 Electrical characteristics

2.4.1 Voltage breakdown and surface flashover

Miniaturisation of ion traps is not only limited by the increasing motional heating of the ion (see section 2.5), but also by the maximum applied voltages allowed by the dielectrics and gaps separating the electrodes. Both secular frequency and trap depth depend on the applied voltage. Therefore it is important to highlight important aspects involved in electrical breakdown. Breakdown can occur either through the bulk material, a vacuum gap between electrodes, or across an insulator surface (surface flashover). There are many factors which contribute to the breakdown of a trap, from the specific dielectric material used and its deposition process, residues on insulating materials to the geometry of the electrodes itself and the frequency of the applied voltage.

Bulk breakdown describes the process of breakdown via the dielectric layer between two independent electrodes. An important variable which has been modelled and measured is the dielectric strength. This is the maximum field that can be applied before breakdown occurs. The breakdown voltage V_c is related to the dielectric strength for an ideal capacitor by $V_c = dE_c$, where d is the thickness of the dielectric. There have been many studies into dielectric strengths showing an inverse power law relation $E_c \propto d^{-n}$ [95–101]. The results show a typical range of values $(0.5 - 1)$ for the scaling parameter n . Although decreasing the thickness will increase the dielectric strength this will not increase the breakdown voltage if the scaling parameter lies below one.

Surface flashover occurs over the surface of the dielectric material between two adjacent electrodes. The topic has been reviewed [102] with studies showing a similar trend with a distance dependency on the breakdown voltage with $V_b \propto d^\alpha$ where $\alpha \approx 0.5$ [101, 103].

Surface flashover usually starts from electron emission from the interface of the electrode, dielectric and vacuum known as the triple point. Imperfections at this point increase the electric field locally and will reduce the breakdown voltage. The electric field strength for surface breakdown has been measured to be a factor of 2.5 less than that for bulk breakdown of the same material, dimensions and deposition process [101], with thicknesses ranging from 1-3.9 μm for substrate breakdown and lengths of 5-600 μm considered.

The range of parameters that can affect breakdown from the difference between rf and applied static voltages [46, 103, 104] includes the dielectric material, deposition process and the geometry of the electrodes [102]. Therefore it is most advisable to carry out experimental tests on a particular ion trap fabrication design to determine reliable breakdown parameters. In a particular design it is very important to avoid sharp corners or similar features as they will give rise to large local electric fields at a given applied voltage.

2.4.2 Power dissipation and loss tangent

When scaling to large trap arrays the finite resistance R and capacitance C of the electrodes as well as the dielectric materials within the trap structure result in losses and therefore have to be taken into account when designing an ion trap. The power dissipation, which results from rf losses, is highly dependent on the materials used and the dimensions of the trap structure and can result in heating and destruction of trap structures. To calculate the power dissipated in a trap a simple lumped circuit model, as shown in Fig. 2.10 can be utilised.

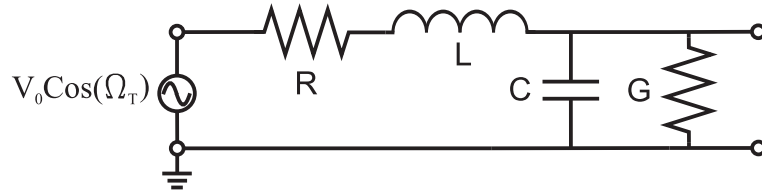


Figure 2.10: The rf electrode modelled with resistance R , capacitance C , inductance L and conductance G .

The dielectric material insulating the electrodes cannot be considered a perfect insulator resulting in a complex permittivity ϵ , with $\epsilon = \epsilon' + i\epsilon''$. Lossless parts are represented by ϵ' and lossy parts by ϵ'' . Substituting this into Ampère's circuital law and by rearranging

one obtains [105]

$$\nabla \times \mathbf{H} = [(\sigma + \omega\epsilon'') - i\omega\epsilon'] \mathbf{E} \quad (2.10)$$

σ is the conductivity of the dielectric for an applied alternating current, and ω is the angular frequency of the applied field. The effective conductance is often referred to as $\sigma' = \sigma + \omega\epsilon''$. The ratio of the conduction to displacement current densities is commonly defined as loss tangent $\tan \delta$

$$\tan \delta = \frac{\sigma + \omega\epsilon''}{\omega\epsilon'} \quad (2.11)$$

For a good dielectric the conductivity σ is much smaller than $\omega\epsilon''$ and we can then make the following approximation $\tan \delta = \epsilon''/\epsilon'$. For a parallel plate capacitor the real and imaginary parts of the permittivity can be expressed as [106]

$$\epsilon' = \frac{Cd}{\epsilon_0 A}, \quad \epsilon'' = \frac{Gd}{\epsilon_0 \omega A} \quad (2.12)$$

Substituting this into the approximated loss tangent expression, the conductance G can be expressed as

$$G = \omega C \tan \delta \quad (2.13)$$

Now we can calculate the power dissipated through the rf electrodes driven by frequency $\omega = \Omega_T$, with $I_{rms} = V_{rms}/Z$. The total impedance for this circuit is

$$Z = R - i\omega L + \frac{G + i\omega C}{G^2 + \omega^2 C^2} \quad (2.14)$$

The second term of the impedance represents the inductance L of the electrodes, which we approximate with the inductance of two parallel plates separated by a dielectric with $L = \mu l(d/w)$ [107]. Assuming a dielectric of thickness $d \approx 10\mu\text{m}$, electrode width $w \approx 100\mu\text{m}$, electrode length $l \approx 1\text{ mm}$, magnetic permeability of the dielectric $\mu \approx 10^{-6}\text{ H/m}$ [108], the inductance can be approximated to be $L \approx 10^{-10}\text{H}$. Comparing the imaginary impedance terms $i\omega L$ and $i\omega[C/G^2 + \omega^2 C^2]$, it becomes clear that the inductance can be neglected. The average power dissipated in a lumped circuit is given by $P_d = \text{Re}(V_{rms} I_{rms}^*)$ [109]. Using the approximation for the total impedance $Z = R + [(G + i\omega C)/(G^2 + \omega^2 C^2)]$ we obtain

$$P_d = \frac{V_0^2 R (G^2 + C^2 \omega^2)^2}{2(C^2 \omega^2 + R^2 (G^2 + C^2 \omega^2)^2)} \quad (2.15)$$

and using equation 2.13 one obtains

$$P_d = \frac{V_0^2 \Omega_T^2 C^2 R (1 + \tan^2 \delta)^2}{2(1 + \Omega_T^2 C^2 R^2 (1 + \tan^2 \delta)^2)} \quad (2.16)$$

In the limit where $\tan \delta$ and $\Omega_T C R \ll 1$, the dissipated power can be simplified as $P_d = \frac{1}{2} V_0^2 \Omega_T^2 C^2 R$. Considering equation 2.16, important factors to reduce power dissipation are an electrode material with low resistivity, a low capacitance of the electrode geometry and a dielectric material with low loss tangent at typical drive frequencies ($\Omega_T = 10\text{--}80$ MHz).

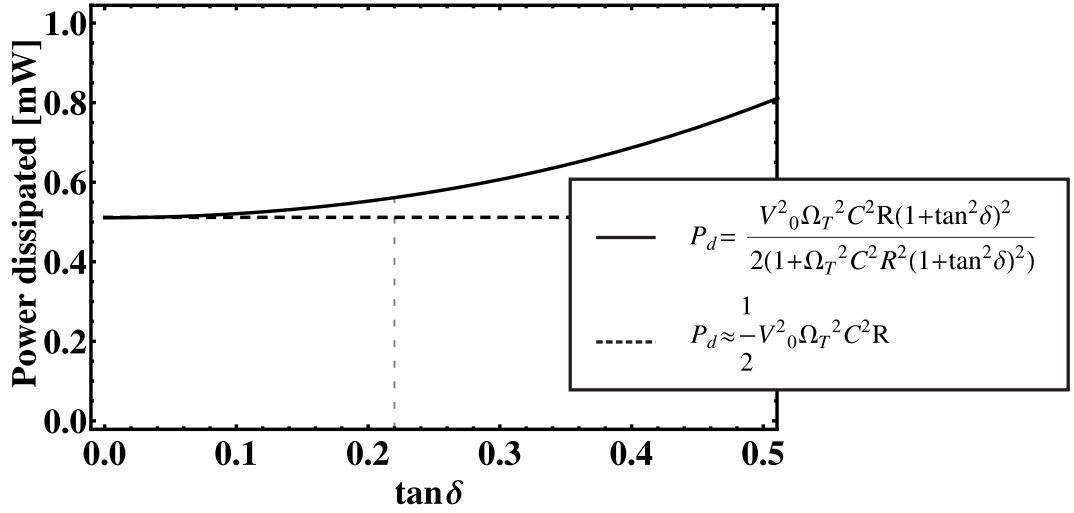


Figure 2.11: Approximation of power dissipated in the limit where $\tan \delta$ and $\Omega_T C R \ll 1$, the dissipated power can be simplified as $P_d = \frac{1}{2} V_0^2 \Omega_T^2 C^2 R$ shown by the dashed line. When $\tan \delta \approx 0.22$ there is a 10% error within the approximation and equation 2.16

Values for loss tangent have been studied in the GHz range for microwave integrated circuit applications [110] and diode structures at kHz range [106, 111, 112]. Generally the loss tangent decreases with increasing frequency [113, 114] and there has been a temperature dependence shown for specific structures [111]. Values at 1 MHz can be obtained but are dependent on the structures tested; Au/SiO₂/n-Si $\tan \delta \sim 0.05$ [106], Au/Si₃N₄/p-Si $\tan \delta \sim 0.025$, [112], Cr/SiO_{1.4}/Au $\tan \delta \sim 0.09$ [115]. The loss tangent will be dependent on the specific structure and also dependent on the doping levels. It is suggested that the loss tangent for specific materials be requested from the manufacturer or measured for the appropriate drive frequency. For optimal trap operation, careful design considerations have to be made to reduce the overall resistance and capacitance of the trap structure minimising the dissipated power.

2.5 Anomalous heating

One limiting factor in producing smaller and smaller ion traps is motional heating of trapped ions. While it only has limited impact in larger ion traps it becomes more important when scaling down to very small ion - electrode distances. The most basic constraint is to allow for laser cooling of the ion. If the motional heating rate is of similar magnitude as the photon scattering rate, laser cooling is no longer possible. Therefore for most applications, the ion - electrode distance should be chosen so the expected motional heating rate is well below the photon scattering rate. Depending on the particular application, there may be more stringent constraints. For example, in order to realise high fidelity quantum gates that rely on motional excitation for entanglement creation of internal states [116, 117], motional heating should be negligible on the time scale of the quantum gate. This timescale is typically related to the secular period $1/\omega_m$ of the ion motion, however, it can also be faster [118]. Motional heating of trapped ions in an ion trap is caused by fluctuating electric fields (typically at the secular frequency of the ion motion). These electric fields originate from voltage fluctuations on the ion trap electrodes. One would expect some voltage fluctuations from the electrodes due to the finite impedance of the trap electrodes, this effect is known as Johnson noise. Resulting heating would have a $1/d^2$ scaling [119] where d is the characteristic nearest ion-electrode distance. However, in actual experiments a much larger heating rate has been observed. In fact, heating measurements taken for a variety of ions and ion trap materials seem to loosely imply a $1/d^4$ dependence of the motional heating rate \dot{n} . A mechanism beyond Johnson noise must be responsible for this heating and this mechanism was termed 'anomalous heating'. In order to establish a more reliable scaling law, an experiment was carried out where the heating rate of an ion trapped between two needle electrodes was measured [120]. The experimental setup allowed for controlled movement of the needle electrodes. It was therefore possible to vary the ion - electrode distance and an experimental scaling law was measured $\dot{n} \sim 1/d^{3.5 \pm 0.1}$ [120]. The motional heating of the secular motion of the ion can be expressed as [119]

$$\dot{n} = \frac{q^2}{4m\hbar\omega_m} \left(S_E(\omega_m) + \frac{\omega_m^2}{2\Omega_T^2} S_E(\Omega_T \pm \omega_m) \right) \quad (2.17)$$

ω_m is the secular frequency of the mode of interest, typically along the axial direction of the trap, Ω_T is the drive frequency and the power spectrum of the electric field noise is defined as $S_E(\omega) = \int_{-\infty}^{\infty} \langle E(\tau)E(t+\tau) \rangle e^{i\omega\tau} d\tau$. The second term represents the cross

coupling between the noise and rf fields and can be neglected for axial motion in linear traps as the axial confinement is only produced via static fields [21, 119].

A model was suggested to explain the $1/d^4$ trend that considered fluctuating patch potentials; a large number of randomly distributed ‘small’ patches on the inside of a sphere, of radius d where the ion sits at the centre [119]. All patches have a power noise spectral density that influence the electric field at the ion position, over which is averaged to eventually deduce the heating rate. Figure 2.12 shows a collection of published motional heating results. Instead of plotting the actual heating rate, the spectral noise density $S_E(\omega_m)$ multiplied with the secular frequency is plotted in order to scale out the behavior from different ion mass or different secular frequencies used in individual experiments. We also plot a $1/d^4$ trend line. We note that previous experiments [83, 120] consistently showed $S_E(\omega_m) \sim 1/\omega_m$ allowing the secular frequency to be scaled out by plotting $S_E(\omega_m) \times \omega_m$ rather than just $S_E(\omega_m)$. In the experiment by Deslauriers *et al.* [120], another discovery

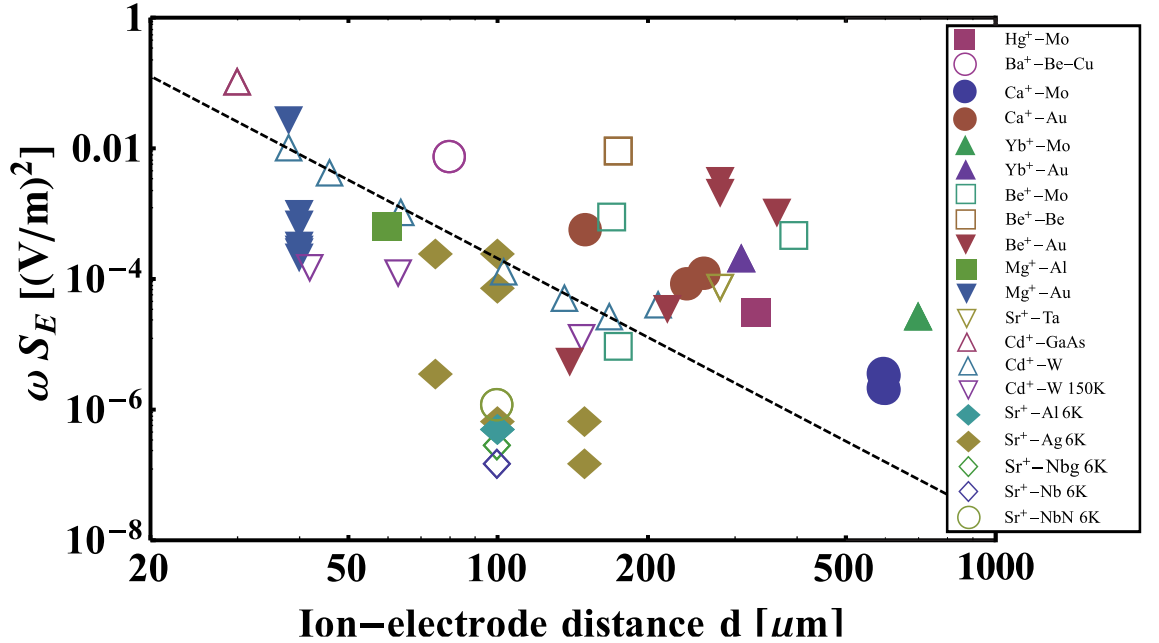


Figure 2.12: Previously published measurements of motional heating plotted as the product of electric field noise spectral density $S_E(\omega)$ and the secular frequency ω , versus ion-electrode distance d . A $1/d^4$ trend line is also shown. Each label shows both the ion species and the electrode material used and the electrode temperature is also noted if the measurement is performed below room temperature. The data point are associated with the following references. (Hg⁺–Mo [121], Ba⁺–Be-Cu [122], Ca⁺–Mo [123], Ca⁺–Au [79, 124, 125], Yb⁺–Mo [126], Yb⁺–Au [83], Be⁺–Mo [119], Be⁺–Be [119], Be⁺–Au [119, 127], Mg⁺–Al [128], Mg⁺–Au [47, 80, 81, 128, 129], Sr⁺–Ta [75], Cd⁺–GaAs [46], Cd⁺–W [120], Cd⁺–W 150K [120], Sr⁺–Al 6K [130], Sr⁺–Ag 6K [131], Sr⁺–Nbg 6K, Sr⁺–Nb 6K, Sr⁺–NbN 6K [130])

was made. The heating rate was found to be massively suppressed by mild cooling of the trap electrodes. Cooling the ion trap from 300K down to 150K reduced the heating by an order of magnitude [120]. This suggests the patches are thermally activated. Labaziewicz *et al.* [131] measured motional heating for temperatures as low as 7K and found a multiple-order-of-magnitude reduction of motional heating at low temperatures. The same group measured a scaling law for the temperature dependence of the spectral noise density for a particular ion trap as $S_E(T) = 42(1 + (T/46K)^{4.1}) \times 10^{-15} \text{ V}^2/\text{m}^2/\text{Hz}$ [132]. Superconducting ion traps consisting of niobium and niobium nitride were tested above and below the critical temperature T_c and showed no significant change in heating rate between the two states [130]. Within the same study, heating rates were reported for gold and silver trap electrodes at the same temperature (6 K) showing no significant difference between the two and superconducting electrodes. This suggests that anomalous heating is mainly caused by noise sources on the surfaces.

Safavi-Naini *et al.* [133] produced a theoretical model of adsorbed atoms with fluctuating dipole moments on the electrode surface. The resulting scaling of ion-electrode distance of $1/d^4$ was predicted together with a $1/f$ noise spectrum at typically secular frequencies of trapped ions. This suggests that surface contamination, from oxide layers to coating from atomic ovens plays a big role in the cause of anomalous heating. Allcock *et al.* [134] have shown reduction of motional heating rates by $\sim 50\%$ through pulsed-laser cleaning, whilst D. A. Hite *et al.* [135] have reported reduction of two orders of magnitude through the use of Argon-ion beam cleaning, removing any adsorbed surface contamination. While anomalous heating limits our ability to make extremely small ion traps, it does not prevent the use of slightly larger microfabricated ion traps. Learning how to mitigate anomalous heating is therefore not a prerequisite for many experiments, however, mitigating it will help to increase experimental fidelities (such as in quantum gates) and will allow for the use of smaller ion traps.

Chapter 3

Experimental setup

Outlined within this chapter is the experimental setup used to trap single Ytterbium ions for the progress towards quantum information and simulations. Many technical details need to be addressed for successful trapping of single ions. Ultra high vacuum (UHV) systems must be used that allow for sufficiently high vacuum pressures (10^{-12} mbar) reducing the background collision rate required to perform quantum operations. Laser systems provide the frequency stability needed for photoionisation and efficient Doppler cooling. A high voltage radio frequency (rf) source coupled via a resonator is required to create trapping fields.

3.1 Ytterbium ions

Among all the possible ion species available Ytterbium is particularly attractive. Firstly the relevant atomic transitions can be easily addressed directly with diode lasers. The main Doppler cooling electronic dipole transition $^2S_{1/2} \leftrightarrow ^2P_{1/2}$ being of wavelength 369.5nm can be easily accommodated with standard optics coatings available and laser can be easily coupled into optical fibers allowing for possibility of large scale integration. Also the low reflectance of quartz together with well established silicon based fabrication techniques allow for the integration of high efficiency detection schemes [136]. The spin 1/2 nucleus of $^{171}\text{Yb}^+$ allows the ground state hyperfine levels to be used for the qubit states, allowing for efficient state preparation and detection. Also, due to the high atomic mass compared to other possible ion species, collisions may not have a catastrophic impact.

3.1.1 Photoionisation

Successfully trapping ytterbium ions requires the ionisation of neutral Yb atoms through the ejection of a bound electron and hence can become charged and trapped. This can be performed by two methods. Electron bombardment can be used with the first demonstration of cooling and trapping ions using this technique [21, 137]. More commonly photoionisation is used having the advantage of more efficient loading rates [138] which can lead to lower atomic flux, reduced excess charge being deposited within the trap region and isotope selective loading through the tuning of the laser frequency. This especially becomes important when dealing with asymmetric designs with reduced trapped depths compared to symmetric designs of the same dimensions. A partial energy level diagram for neutral Yb atoms is shown in fig 3.1, a two-step photoionisation process is possible with a photon at 398.9 nm and one at <394 nm ejecting an electron into the continuum. The Doppler cooling laser at 369.5 nm is used for the two photon process. This provides the most efficient way to ionise Yb. The saturation intensity of the first transition is $I_{sat} = 60 \text{ mW/cm}^2$, so a beam focused down to a beam diameter of $50 \mu\text{m}$, will saturate the transition with $1.5 \mu\text{W}$ of power.

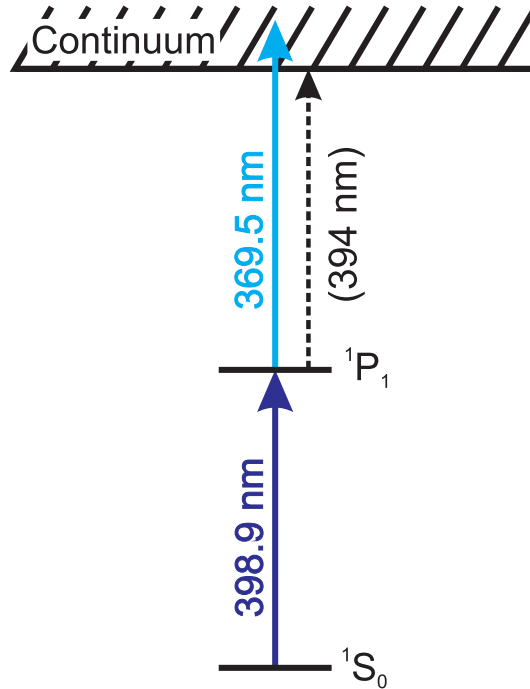


Figure 3.1: A partial energy level diagram for neutral ytterbium atoms showing the photoionisation process. A two-step process is used with one photon at 398nm and another at 369.5nm.

3.1.2 Doppler cooling

Once a Yb atom has been ionised it is then necessary to be Doppler cooled. As mentioned previously in section 2.1.3 Doppler cooling relies on the detuning Δ of the laser frequency from the transition wavelength frequency. The scattering rate of the ion is given by [139]

$$\gamma = \frac{s\Gamma/2}{1 + s + (2\Delta/\Gamma)^2} \quad (3.1)$$

where Γ is the linewidth of the transition, s is the saturation parameter defined as the ratio of the intensity of the laser beam over the saturation intensity parameter I/I_{sat} . The limit of Doppler cooling can be achieved when a detuning of $\Delta=\Gamma/2$ of the laser is selected and provides an ion energy of $E = \hbar\Gamma/2$ [139].

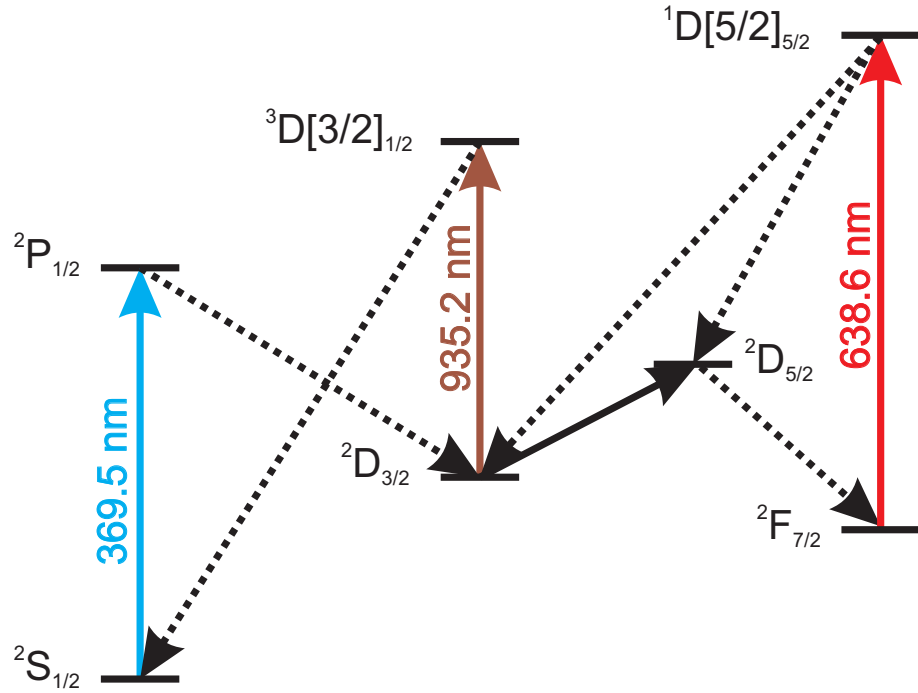


Figure 3.2: A partial energy level diagram for ytterbium ions. The driven transitions are shown in solid lines whilst the decays are dashed. Due to background collisions the ion can be knocked into the $^2D_{5/2}$ state in which it decays into the long lived low lying $^2F_{7/2}$ state.

A gross energy level diagram is shown in 3.2. This applies to all isotopes but in particular the even isotopes ($^{168}\text{Yb}^+$, $^{170}\text{Yb}^+$, $^{172}\text{Yb}^+$, $^{174}\text{Yb}^+$ and $^{176}\text{Yb}^+$) in which no more transitions need to be addressed. $^{174}\text{Yb}^+$ is used for initial trapping and detection within new

traps due to the simple cooling cycle and being the most naturally abundant [138, 140]. Three lasers are used to drive the cooling cycle. The $^2S_{1/2} \leftrightarrow ^2P_{1/2}$ is driven by a 369.5 nm laser with a natural linewidth of $\Gamma/2 = 19.6$ MHz [66]. This is the main Doppler cooling and detection cycle, however due to a metastable state the ion can decay from the $^2P_{1/2}$ into the $^2D_{3/2}$ with a branching ratio of 0.5% (once every 200 cycles) [66]. An additional laser is required at 935.2 nm to pump the ion into the $^3D[3/2]_{1/2}$ state in which it quickly decays back into the $^2S_{1/2}$ ground state. An additional laser at 638.6 nm is also required due to the presence of the low lying $^2F_{7/2}$ state. Through background collisions the ion will fall into this state via the $^2D_{5/2}$ state and which is extremely long lived and will no longer be cooled.

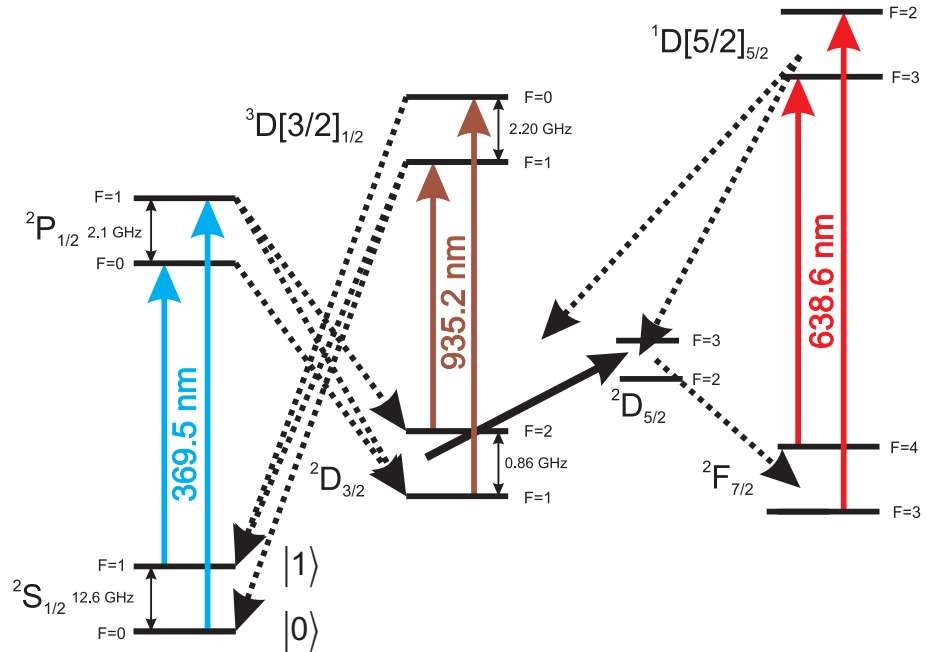


Figure 3.3: Partial Energy level diagram for $^{171}\text{Yb}^+$ atom with the addition hyperfine levels compared to neutral isotopes.

$^{171}\text{Yb}^+$ as perviously mentioned is particular suited for quantum information through accessing the $^2S_{1/2}$ hyperfine levels of the ground state for the qubit states. A partial energy level diagram for the 171 isotope is shown in fig. 3.3. The $^2S_{1/2}(F=1)$ and $^2S_{1/2}(F=0)$ states are defined as the $|1\rangle$ and $|0\rangle$ qubit states respectively. The separation between these states is 12.6 GHz. To address all cooling transitions defined by the selection rules, the 369 nm laser has sidebands added. The difference between the $^2S_{1/2}(F=1) \leftrightarrow ^2P_{1/2}(F=0)$ and the $^2S_{1/2}(F=0) \leftrightarrow ^2P_{1/2}(F=1)$ is 14.7GHz. To close the cooling cycle, the 935 nm laser also has sidebands added, with the difference between

Yb ionisation and Yb ⁺ transition wavelengths			
Isotope	¹ S ₀ ↔ ¹ P ₁ wavelength [nm]	² S _{1/2} ↔ ² P _{1/2} wavelength [nm]	² D[3/2] _{1/2} ↔ ² D _{3/2} wavelength [nm]
¹⁷⁰ Yb ⁺	399.91051(6)	369.52364(6)	935.19751(19)
¹⁷¹ Yb ⁺	399.91070(6)	369.52604(6)	935.18768(19)
¹⁷² Yb ⁺	399.91083(6)	369.52435(6)	935.18736(19)
¹⁷⁴ Yb ⁺	399.91114(6)	369.52494(6)	935.17976(19)
¹⁷⁶ Yb ⁺	399.91144(6)	369.52550(6)	935.17252(19)

Table 3.1: The ionisation and cooling wavelengths in vacuum for various Yb isotopes. The ¹S₀ ↔ ¹S₁ transition is measured at an angle of 63° between the atomic beam and the laser beam. The ¹⁷¹Yb⁺ isotope wavelengths correspond to the ²S_{1/2}(*F* = 1) ↔ ²P_{1/2}(*F* = 0) and ²D[3/2]_{1/2}(*F* = 1) ↔ ²D_{3/2}(*F* = 1) transitions respectively.

the ²D_{3/2}(*F* = 2) ↔ ³D[3/2]_{1/2}(*F* = 1) and the ²D_{3/2}(*F* = 1) ↔ ³D[3/2]_{1/2}(*F* = 0) being 3.08 GHz. The corresponding ²F_{7/2} ↔ ¹D[5/2]_{5/2} wavelengths are 638.610 and 638.616 nm in which the laser is scanned between these wavelengths to address both transitions.

After successfully trapping, more precise wavelengths for several Yb isotopes were determined from previous published values. These are shown in Table 3.1. For the neutral Yb atom ¹S₀ ↔ ¹P₁ transition, the values presented correspond to an angle of 63° between the atomic beam and the laser beam within our setup and was obtained using a fluorescence spot technique [140].

3.1.3 Destabilisation of dark states

¹⁷¹Yb⁺ atom can be optically pumped into a coherent population of the ²S_{1/2}(*F* = 1) manifold, resulting in significant reduction in fluorescence count rate. The degeneracy of the dark state can be destabilised though the Zeeman splitting of these states via an applied magnetic field [141]. Three pairs of Helmholtz coils are used to create a magnetic field, which determines the quantisation axis that can be arbitrarily rotated. A diameter of 17 cm, *N* = 80 turns and a current of 2.5 A is used to produce a magnetic fields of ≈0.8 mT at the ion position.

3.2 Lasers and locking

To drive the all the transitions within the cooling cycle, home built external cavity laser diode (ECLD) setups are used for the 399 nm, 935 nm and 638 nm transitions. For the

main Doppler cooling transition at 369 nm, a frequency doubled system from Toptica Photonics (TA-SHG 36) is used. Locking of these lasers is provided through a transverse scanning cavity locked to a reference laser at 780 nm and a wavemeter lock through LabVIEW. This provides the stability to efficiently cool to the Doppler limit as well as the control to perform initial experiments such as motional heating measurements discussed within section 3.6.2. All of these elements are discussed in more detail below.

3.2.1 External cavity laser diodes (ECLD)

The ECLD setups used within are lab are with the Littrow configuration [142], a reflective diffraction grating is used to extend to cavity length, reducing the spectral linewidth of the laser. The first order beam is fed back to the laser diode allowing us to obtain selected frequencies, whilst the zeroth order beam is used for the experiment. To tune the frequency of the laser current and temperature controllers are used. Since the frequency of laser is dependent on temperature, which changes the band gap within the junction of the laser diode, this can be adjusted to control the frequency of the laser. Also the supply of current to the laser diode will change the refractive index of the lasing medium causing heating, changing the band gap energy and hence changing the frequency of the diode as well as the output power. With the Littrow configuration the frequency is dependent on the diffraction grating angle. Through a combination of diffraction grating angle, current and temperature the frequency can be tuned to the desired value. A schematic and picture is shown in fig. 3.4 of the ECDL configuration.

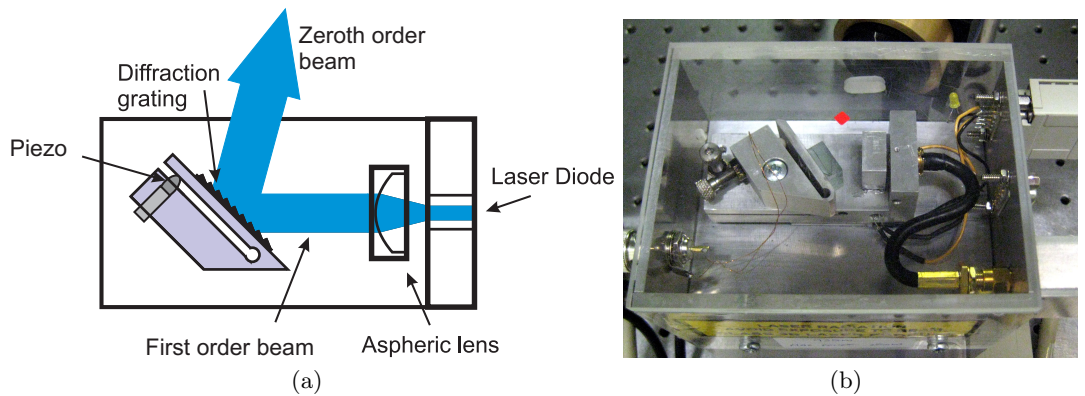


Figure 3.4: External cavity diode laser setup. (a) Schematic of the Littrow ECDL configuration. An aspheric lens is used to collimate the beam. A diffraction grating is then used to provide feedback and light to the experiment through the zeroth order beam. (b) A picture of the 399 nm ECDL system within our experiment.

399 nm Photoionisation laser

The 399 nm ECDL setup comprises of a Sanyo laser diode (pt No. DL-4146-301S), an aspheric lens and diffraction grating from Thorlabs (pt. No. A390TM-A, GH13-24V respectively). A first order efficiency of $\approx 58\%$ is achieved with an output power of ~ 4 mW.

935 nm laser

The 935 nm laser consists of a laser diode from Roithner (pt No. RLT940-100GS), together with an aspheric lens and diffraction grating from Thorlabs (pt. No. C330TM-B, GH13-1210 respectively). With 80% efficiency 20 mW of power can be obtained which is sufficient to easily saturate the transition reducing the effect of any fluctuations within the laser frequency. Sidebands needed for the hyperfine levels in $^{171}\text{Yb}^+$ are created through modulation of the laser diodes current. 3.08 GHz is combined with the DC via a bias-tee from Mini Circuits (pt. No. ZFBT-4R2G+).

638 nm laser

The 638 nm laser comprises of a Sanyo laser diode (pt. No. DL-6148-030), also an aspheric lens and diffraction grating from Thorlabs (pt. No. A390TM-B, GH13-24v respectively). This provides an efficiency of 83% and is operated at an output power of 17 mW.

3.2.2 369 nm Doppler cooling laser

A frequency doubling system from Toptica photonics (TA-SHG 36) is used to produce 369 nm laser light from a 739 nm laser diode. To access the hyperfine levels of $^{171}\text{Yb}^+$, sidebands are created by passing the 739 nm laser light externally through an electric optic modulator (EOM) modulated at 7.35 GHz before being frequency doubled to produce 14.7 GHz. Small leakage through the back of the mirrors are taken for locking and wavelength measurement purposes. The beam is passed into a bow tie cavity containing a non linear crystal Lithium Triborate (LBO) in which second harmonic generation (SHG) takes place. The output from this cavity is up to 60 mW of power.

3.2.3 Laser locking

Since the laser frequency is very sensitive to fluctuations in temperature, current and cavity length (acoustic noise), the lasers need to be locked for sufficient stabilisation. Firstly the fluctuations are reduced by placing the lasers in a isolated box to reduce temperature and acoustic variations. The 935 nm and 739 nm lasers are locked to a stable reference laser at 780 nm via a scanning cavity locking scheme using the Pound-Drever-Hall technique [143, 144]. Whilst the 398 nm and 638 nm lasers are locked via the wavemeter for sufficient stabilisation.

780 nm Reference laser lock

To obtain frequency stable lasers ~ 20 MHz, a reference laser is used as a frequency source which in turn is locked to an atomic transition within Rubidium (Rb). This provides a frequency stable laser of < 1 MHz over an hour, sufficient to run many of the initial experiments and provide a means to calibrate our wavemeter. The other lasers can then be locked to this reference laser.

The 780 nm reference laser consists of a ECDL setup, a laser diode and diffraction grating from Thorlabs (pt. No. GH0781JA2C, GR13-185 respectively) produces an output power of 80 mW. This is then locked to the $^2S_{1/2} \leftrightarrow ^2P_{3/2}$ D₂ transition line within Rb⁸⁷ (fig. 3.5(a)), with a natural linewidth $\Gamma/2\pi = 6$ MHz by Doppler free absorption spectroscopy. Two counter propagating beams called the pump and probe, with powers of 1.3 mW and 0.1 mW respectively are passed through a Rb vapour cell. These signals are then detected on individual photodiodes. The pump beam saturates the transitions within Rb whilst the probe beam, travelling in the opposite direction displays sharp peaks within the absorption spectrum shown in fig. 3.5(b).

To observe the hyperfine transitions, the laser current is modulated at 100KHz and a 10Hz triangle wave is used to scan the laser current and lock-in amplifier. By subtracting the pump (Doppler background) from the probe beam the Doppler free absorption spectrum. The output signal from the lock-in amplifier is the differential of the input absorption spectrum, a high gradient with zero crossing occurs at resonance. By turning off the 10 Hz scan and manually tuning the laser frequency to resonance, a proportional integration (PI) controller can then be used to provide feedback to lock the laser at the required

transition.

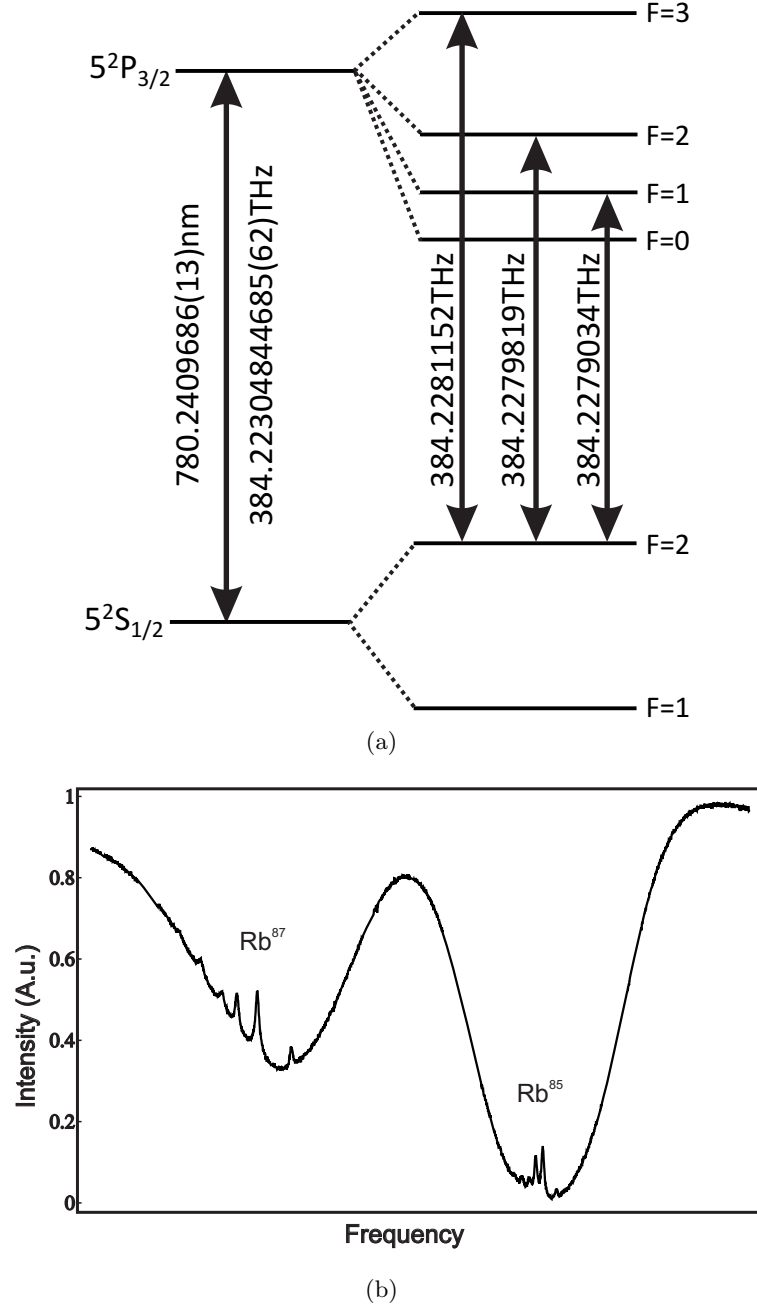


Figure 3.5: (a) Hyperfine structure of the ^{87}Rb D_2 transition line [145]. (b) Saturation absorption signal.

Transverse cavity lock

The 739 nm and 935 nm lasers are lock to the 780 nm reference laser via a transverse cavity locking scheme. Two Fabry-Pérot confocal cavities are used with high reflectivity coatings at the desired wavelengths. Polarising beam splitters are used to combine 739 nm

and 780 nm lasers into one cavity and the 935nm and 780nm lasers into the other cavity. The output laser signals from the cavities are received on respective photodiodes with polarising beam splitters and the voltage signals sent via a Data Acquisition (DAQ) card from National Instruments (NI) (pt. No. PCI-6143) to LabVIEW (graphical programming language). By scanning the cavities at 50-70Hz through applying a triangle waveform to a piezo attached to one of the mirrors of the cavity, resonant peaks are obtained.

The cavity signals received by LabVIEW can then be locked within the Real-Time mode. The distance between two locked 780 nm reference peaks is defined as a , and the distance between 780 nm reference peak and a adjacent as b . An error signal is obtained by measuring the ratio a/b . This ratio is then kept constant with the use of a proportional, integration and differential (PID) control for optimal feedback. The error signal is then converted to a voltage which can then be sent to the grating via an output card (NI PCI-6722) to compensate any drift within the laser and provide long term stability. Feedback to the cavities is used to provide thermal stability. A peaks relative position within the cavity is monitored and feedback is used to provide a dc offset to the triangle waveform scanning the cavity through a summing amplifier.

Wavemeter lock

A HighFinesse W7 wavemeter is used to measure the wavelengths of the experimental lasers. With an absolute frequency stability of ± 60 MHz and ± 120 MHz below 370 nm. Together with a relative stability of ± 10 MHz this can be used to lock the lasers in which this quoted level of accuracy is satisfactory. Light is coupled into optical fibres and then passed through a multi channel switcher unit, this allows to display all the experimental laser wavelengths simultaneously. The 399 nm ionisation laser together with the 638 nm laser are locked to the wavemeter through a LabVIEW program installed on the wavemeter computer. This sends the wavelength of the lasers to the locking program and feedback to the laser controllers is provided by comparing the desired wavelength and the measured. Care must be taken to have sufficient power coupled to the wavemeter from all the lasers thus reducing the exposure time and allowing faster feedback to the lasers being locked.

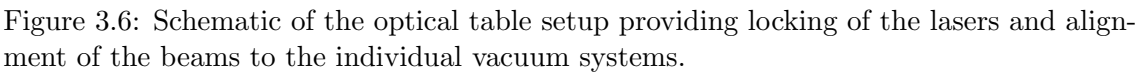


Figure 3.6: Schematic of the optical table setup providing locking of the lasers and alignment of the beams to the individual vacuum systems.

3.3 Vacuum systems

For successful loading, long storage times of ions, and the prevention of decoherence of a qubits state through background collisions, a ultra high vacuum (UHV) on the order of 10^{-12} needs to be created. The vacuum systems created are capable of housing both symmetric and asymmetric ion traps, with additional features that allow for the operation and testing of microfabricated ion traps. I will discuss both vacuum systems in more detail below.

3.3.1 Vacuum System I

The first generation vacuum system consists of a stainless steel Kimball Physics hemisphere (pt No. MCF450-MH10204/8-A) octagon and (pt No. MCF450-SO20008-C). This allows optical access for both symmetric and asymmetric ion traps, this can be seen in fig. 3.7(a) and (b). Within this arrangement a custom built chip bracket is used to supply 90 individual controls electrodes to the trap. The chip bracket is designed to house a 101-pin ceramic pin grid array (CPGA) chip carrier from Global Chip Materials (pt No. PGA10047002). The Chip bracket is made from two UHV compatible PEEK plates in which 90 gold coated pin receptacles from Mill-Max (pt No. 0672-1-15-15-30-27-10-0) are sandwich in between to provide structural stability. Insulating Kapton wires are then crimped to the back side which run to two 50 pin D-sub feedthrough connectors mounted to a 6" flange. The chip bracket is mounted with stainless steel plates and grove grabbers from Kimball Physics (Pt No. MCF450-GG-CT02-A) to the inside of the hemisphere.

Atomic ovens providing a beam of natural Yb as well as enriched $^{171}\text{Yb}^+$ are also mounted within the hemisphere. The atomic ovens are created from a stainless steel tube and are crimped and spot welded using a constantan foil. They are then filled with piece of solid Yb, with 90% enriched $^{171}\text{Yb}^+$ from Oak Ridge National Laboratory (pt No. OA0036) or a natural abundance from Goodfellow Cambridge Limited (pt No. GO0196). Four ovens are mounted within the vacuum system, Two (one of each type) for symmetric traps via the backside and two for asymmetric traps producing a beam parallel to the surface. For the symmetric ovens the atomic beam makes $\sim 60^\circ$ angle with the ionisation beam where the asymmetric ovens are at 90° .

Viewports from fused quartz silica UV-grade are used together with anti-reflection (AR)

coatings at the wavelengths used. There are six 1.33" CF flange viewports for optical access for asymmetric traps mounted on the octagon, whilst for symmetric traps two 1.33" and one 2.75" CF flange viewports are mounted to the octagon. A custom made¹ recessed window allows for the imaging optics to be placed nearer the trap whilst maintaining optical access for the exiting lasers for a higher collection efficiency. A picture of the complete vacuum is shown in fig. 3.7 (c).

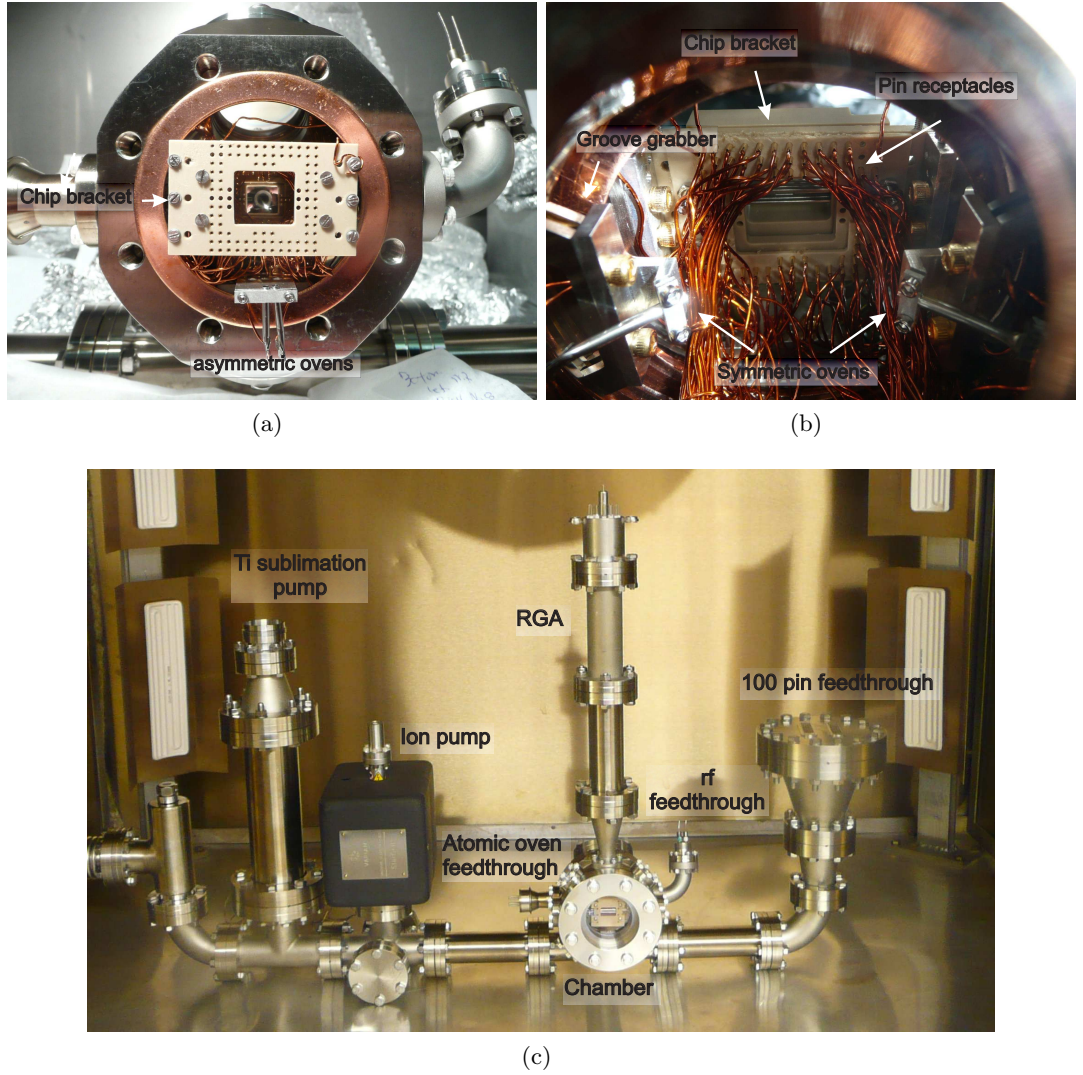


Figure 3.7: Picture of the first vacuum system hemisphere and octagon arrangement. (a) Front view. (b) Rear view. (c) Complete vacuum system.

¹Designed by Altaf Nizamani.

3.3.2 Vacuum System II

To increase the turn around time of testing traps a second vacuum was created. Notable improvements to the vacuum design include a larger hemisphere and octagon, with a redesign of the recessed window². This allowed for the laser beams to fully exit the vacuum system without clipping the imaging optics, as was apparent in the first vacuum system for the symmetric trap arrangement. Repositioning of the feedthroughs and pumps for easier alignment with asymmetric traps. A movable chip bracket was constructed to give more flexibility to the types of traps and the addition of extra flanges for microwaves and fibres. Fig. 3.8 shows the hemisphere octagon arrangement and the complete vacuum system.

3.3.3 Vacuum operation

To achieve UHV pressures within the vacuum systems care within the construction and specific procedures must take place. Firstly all the stainless steel vacuum parts are cleaned with solvents, pre baked for a week at 200°C and assembled in a clean environment with personal protective equipment. The electrical components and viewports are not pre bake but are still cleaned in solvents. After the construction of system various pumps are employed to pump down the system, a Turbo molecular pump first brings the pressure to 10^{-6} mbar, the system is then ramped to 200°C in a home built oven to outgas any absorbed particles especially water within the system. Ion pumps are then turned on and the system is typically baked for a week at 200°C. The temperature is then brought back to room temperature which produces a pressure at $\sim 10^{-10}$ mbar. A Titanium Sublimation Pump (TSP) is then cycled for 3 min at 50 A typically every couple of hours (waiting till the pressure has reduced from the previous run) to reduce the pressure below 10^{-11} mbar ready for experiments.

3.4 Helical resonator

To supply high rf voltages needed for sufficient trap depths as well as a means to filter out noise inducing heating of the ion, separated by the secular frequencies from the drive frequency ($\Omega \pm \omega_i$). A narrow bandpass source characterised by the Q-factor is required.

²Designed by Robin Sterling.

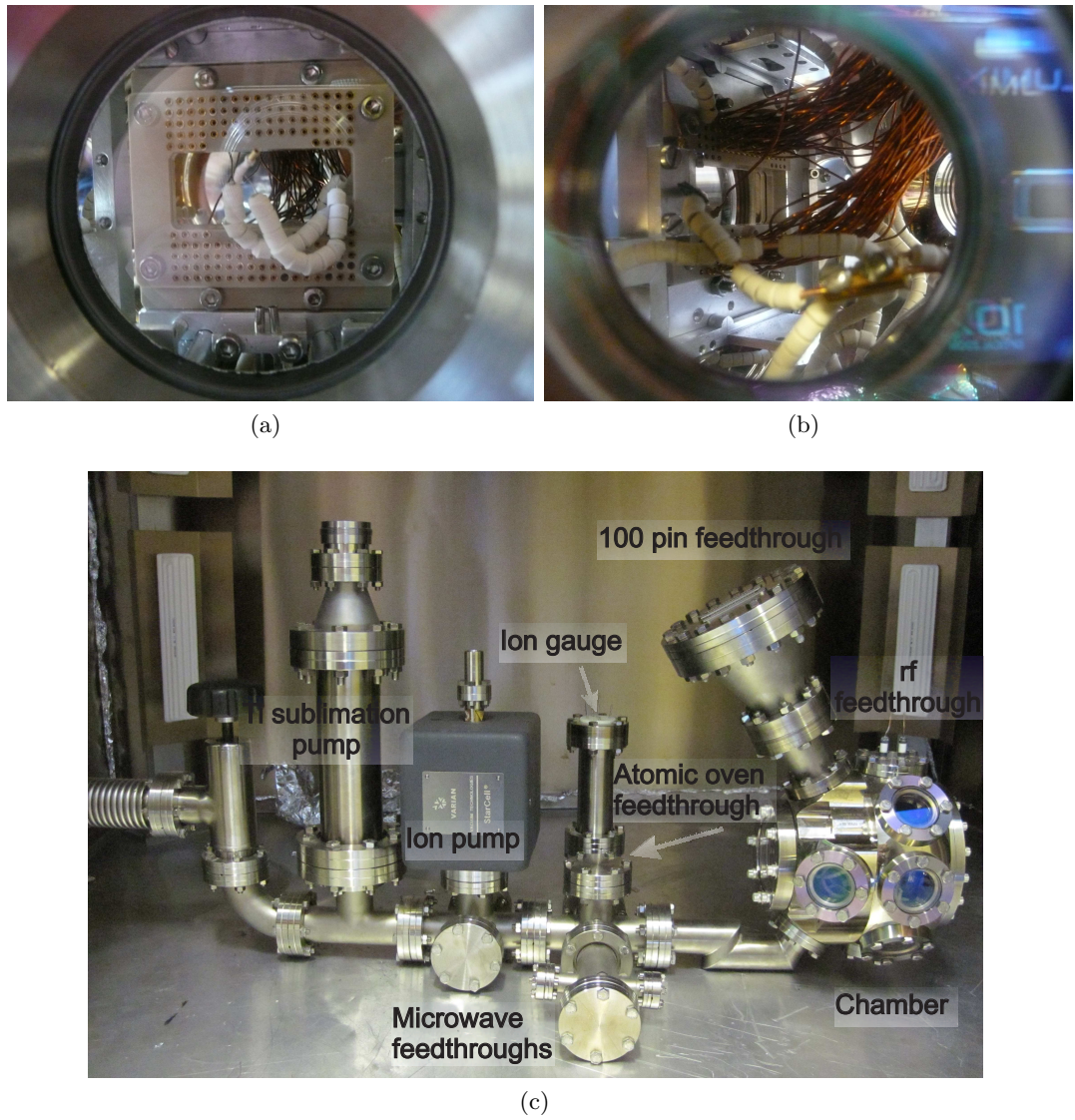


Figure 3.8: Picture of the second vacuum system hemisphere and octagon arrangement. (a) Front view. (b) Rear view. (c) Complete vacuum system.

Through the use of a helical resonator provides a convenient way to accomplish this as well as impedance matching the trap to the source frequency. A quarter wave helical resonator from Copper is constructed in which a coiled wire with length $L = \lambda/4$ is encased within a conducting shield shown in fig. 3.9. The quality factor Q and resonant frequency f_0 are defined as,

$$Q = \frac{1}{2\pi f_0 RC}, \quad f_0 = \frac{1}{2\pi\sqrt{LC}} \quad (3.2)$$

L, R and C are the Inductance, Resistance and Capacitance of the ion trap resonator circuit respectively. The peak rf voltage is defined as,

$$V_{rf} = \kappa\sqrt{2PQ} \quad (3.3)$$

where κ is defined as the geometric factor. Through careful design parameters of the resonator [84], it is possible to predict the resonant frequency and maximise the quality factor of the combined resonator ion trap circuit.

To measure the Q factor, the standard equation is used.

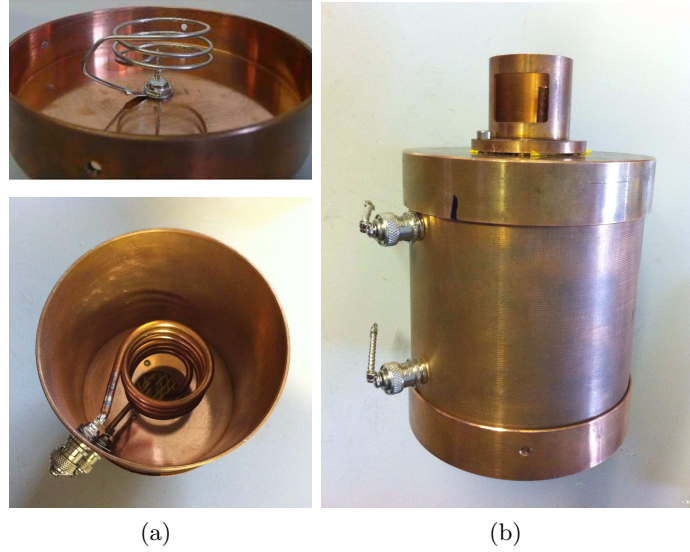


Figure 3.9: (a) Cap of the resonator with an antenna coil attached to impedance match the source frequency to ion trap circuit. Inside the coil and shield arrangement of the quarter wave helical resonator. (b) Complete construction of the resonator.

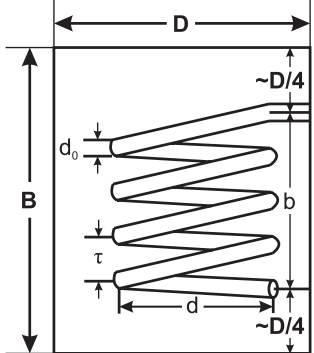
$$Q = \frac{f_0}{\Delta f} = \frac{f_0}{f_+ - f_-} \quad (3.4)$$

Where the frequencies f_+, f_- are measured above and below the resonance frequency respectively when the voltage amplitude is reduced to $V_{max}/\sqrt{2}$. The resonator is connected

to a function generator (HP 8640B) and an oscilloscope via a directional coupler such that the reflected signal from the resonator is displayed. By adjusting the source frequency the Q value can be measured. Alternatively a spectrum analyser with a tracking generator can be used.

For the experimental setup the rf voltage from the function generator is amplified with a 30W high power rf amplifier from MiniCircuits (pt No. NP-541), a directional power-meter from Rhode and Schwarz (pt No. NAUS 3) is used to measure the total and reflected power to obtain maximum coupling. The resonator used for our experiment had unloaded values of $Q = 574(46)$, $f_0 = 87.46(30)$ MHz, its design specifications are detailed in Table 3.2. When attached to the Blade ion trap circuit, loaded values of $Q = 200(20)$, $f_0 = 21.49(30)$ MHz with the macroscopic ion trap (section 3.6) having measured values of $C = 17(2)$ pF and $R \approx 0.1 \Omega$. After successfully trapping κ was measured to be $24(8)$. For microfabricated traps it is important to minimise the resistance and capacitance of the ion trap array within the design stage to maintain high Q values of the ion trap circuit.

Table 3.2: Specifications of the resonator

	Shield Diameter, D [mm]	76(1)
	Shield length, B [mm]	103(1)
	Coil Diameter, d [mm]	52(3)
	Coil Length, b [mm]	63(5)
	Coil diameter, d_0 [mm]	3.14(3)
	Winding pitch, τ [mm]	6(2)
	Number of turns, N	9.50(25)
	Resonant frequency with trap load, f_0 [MHz]	21.5(1)
	Q with trap load	200(20)

3.5 Imaging system

To detect ions and provide high detection fidelity, an efficient imaging setup is required to both reduce background noise as well as produce a high collection efficiency. This imaging system was designed to provide flexibility within the imaging area, able to be used with two vacuum systems and optimised for the collection 369 nm light from the Doppler cooling $^2S_{1/2} \leftrightarrow ^2P_{1/2}$ transition. A schematic of the imaging system is shown in fig. 3.10

The first optical element used within the imaging setup consists of an objective lens from

special optics (Pt No. 54-17-29-369) made from three elements and referred to as the triplet lens. This lens was modelled using OSLO ³ to provide the optimal position from the ion to have a diffraction limited image. The lens was calculated to be 23.54 mm from the ion including the 8 mm thickness of the vacuum window to provide 75.8% collection of photons within the central airy disc. This produces an image 549.7 mm from the focal plane resulting in a magnification from the triplet of $M_T = -23.4$. An aperture is then placed at the image position formed from the triplet to block any stray light not within the focal plane of the ion.

Next a doublet lens consisting of two plano convex lenses with the curved surface placed against each other provides a means to easily adjust the total magnification of the system whilst reducing spherical aberrations. The focal length of the doublet is defined as

$$f_D = \frac{f_1 f_2}{f_1 + f_2} \quad (3.5)$$

where f_1 and f_2 are the focal lengths of the individual lenses. The total magnification of the imaging system is then

$$M_{Total} = M_T M_D \quad (3.6)$$

By selecting lenses with the appropriate focal length the desired image area can be determined. Since the principal planes (the point at which the focal lengths of the lenses are measured) of the plano convex lenses lies on the tangent to the curved surface, the thin lens equation can be used to calculate combined focal distances and magnifications. With an object s_{0D} and image s_{iD} distance of the doublet, the focal length and magnification can be defined as

$$f_D = \frac{1}{-s_{0D}} + \frac{1}{s_{iD}}, \quad M_D = \frac{s_{iD}}{-s_{0D}} \quad (3.7)$$

Two Light tight boxes housing motorised flipper mirror mounts from Newport (pt No. 8892-K) allow the switching of imaging between the two vacuum systems, the photomultiplier tube (PMT) and electron multiplying charge coupled device (EMCCD) camera. An Andor iXon 885 EMCCD is used to align the lasers, detecting trapped ions and have the option for readout of multiple ions. A photon counting PMT module from Hamamatsu (pt No. H8259-01) is used for the collection of the ions fluorescence represented in TTL output pulses with quoted width of 30 ns. A bandpass filter from Semrock (pt No. FF01-370136) is used to filter out any scattered light from the other lasers whilst transmitting >94%

³http://www.lambdaresearch.com/software_products/oslo

light at 369 nm. Taking into account the numerical aperture of the triplet, all the optical elements and the efficiency of the EMMCCD and PMT, the overall detection efficiency of the imaging system is ≈ 0.1 . A schematic of the complete imaging system is shown in fig. 3.10.

With detection efficiencies of 99.991(1)% [44] demonstrated using external optics and a

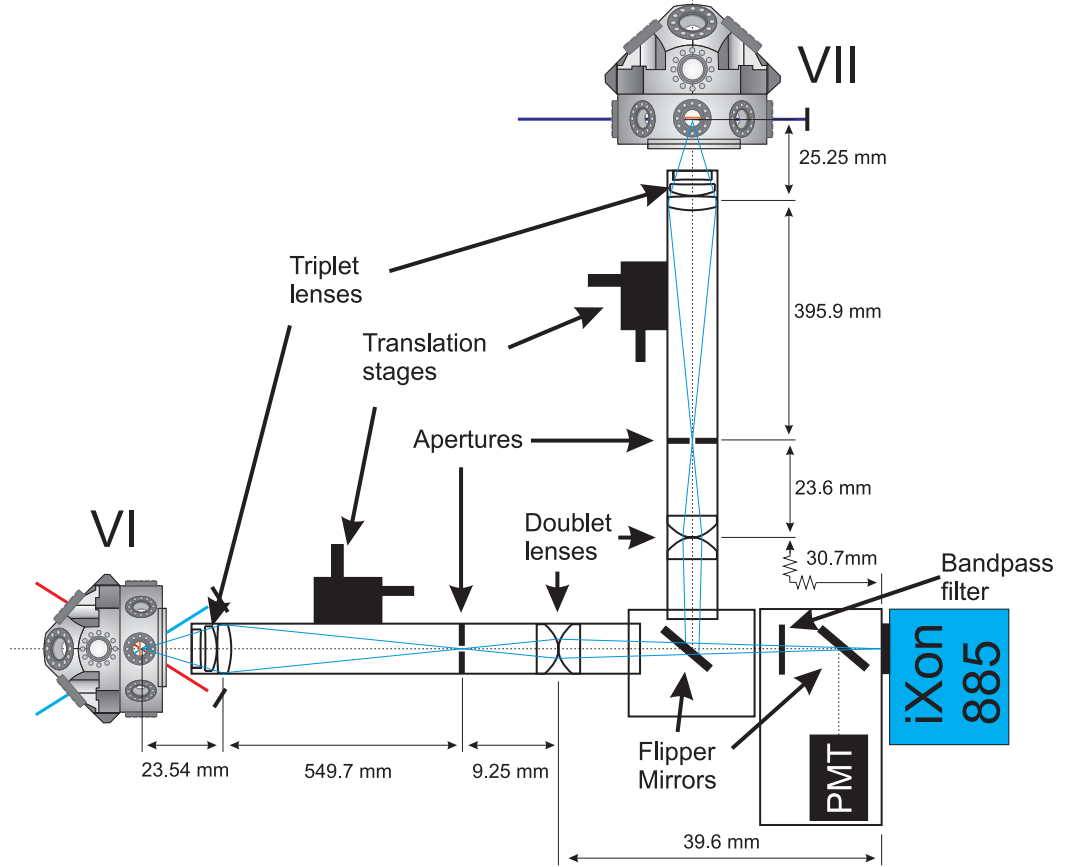


Figure 3.10: Schematic of the Imaging setup.

PMT, the area is now focused towards on chip collection [146] and detection solutions to improve the collection efficiency and reduce readout time.

3.6 Macroscopic ion trap

In order to successfully trap for the first time within our lab a key priority is to have a workable trap with as few unknown parameters as possible. The blade trap was created by Robin Sterling which consists of two layer symmetric design as shown in fig. 3.12. High trap depths ($> 1\text{eV}$) were required without any technical challenges associated with microfabricated traps, such as voltage breakdown and power dissipation previously

discussed in section 2.

The trap design shown in fig. 3.11, consists of segmented linear electrodes to provide axial confinement, rotation of the principal axes with the centre electrodes and compensation electrodes for minimisation of excess micromotion from stray electric fields due to imperfections in the geometry. The individual electrodes consist of gold coated stainless steel with the exception of the compensation electrodes being gold cylindrical wire. PEEK spacers are used to provide electrical isolation between the electrodes when mechanically assembled within the stainless steel cage. This is then mounted on top of a PEEK base to provide insulation of the vacuum ground. The stainless steel cage also provided shielding of the PEEK base reducing any unwanted stray electric fields.

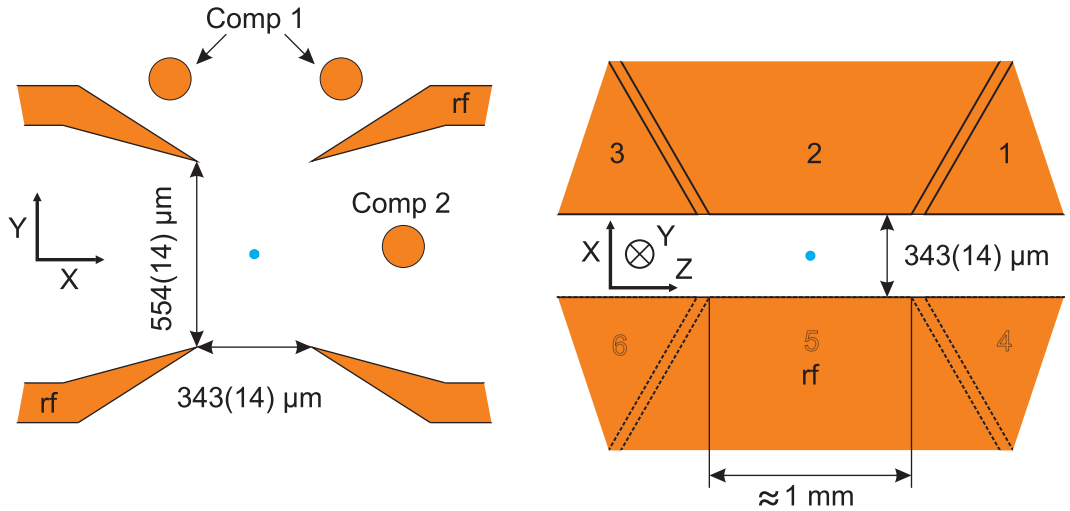


Figure 3.11: Design of the Blade trap.

After construction of the trap (fig. 3.12), the exact electrode geometry was measured using scattered laser light and the imaging system. The adjusted trap geometry was then simulated using Charge Particle Optics (CPO) software, a boundary element method (BEM) to obtain more accurate basis functions from the original design. This was performed before and after the baking of the vacuum system with movement of some electrodes observed and the grounding of dc electrode 4. The simulated Pseudopotential is shown in fig. 3.13. The electrodes are separated by 343(14) and 554(14) μm within the radial axes, producing an ion-electrode distance of 310(10) μm . A static field is calculated with the dc electrodes to overlap the rf and dc nil of the trapping fields. Table 3.3 lists the applied voltages to the trap electrodes.

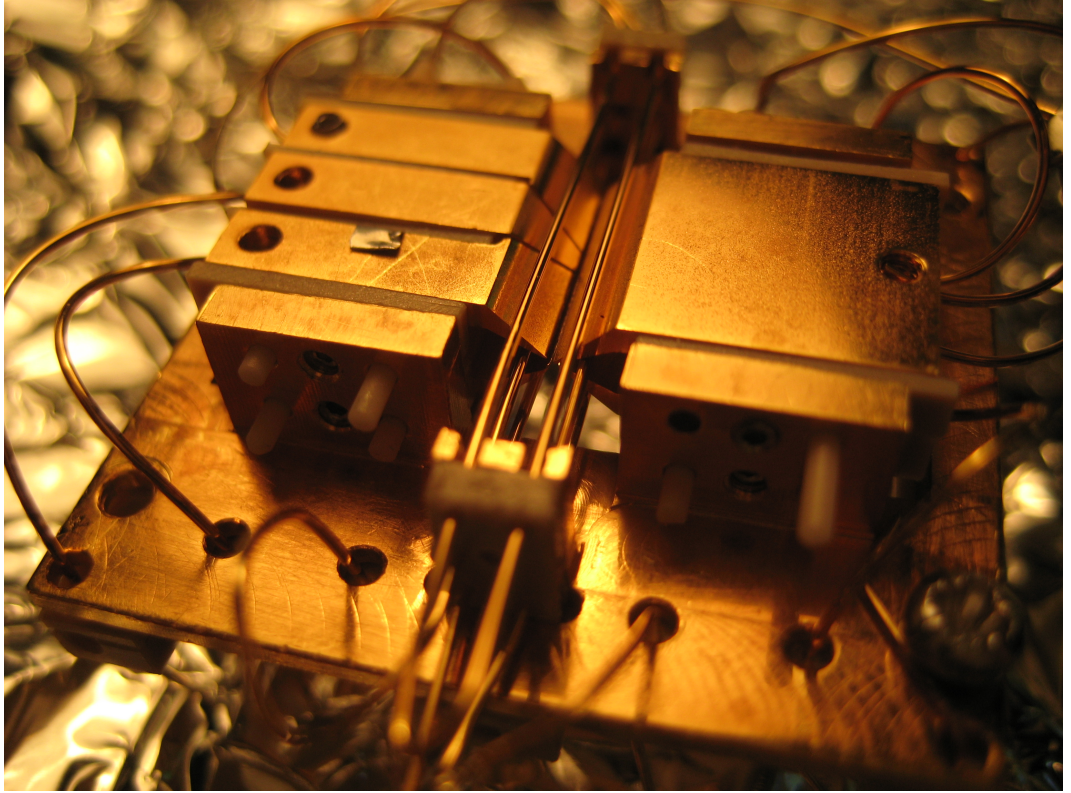


Figure 3.12: Assembled Blade trap.

3.6.1 Trap operation

In order to successfully trap ions and maintain beam stability over time a combination of optical elements are used to combine the lasers and focus them to the null position of the trap. Firstly the beams are aligned into single mode polarisation maintaining fibres, through custom made fibre couplers. This eliminates any drift in the lasers position through varying the voltage applied to the diffraction grating when adjusting the wavelength. The polarisation of the laser is matched to the long axes of the fibre through a half-wave($\lambda/2$) plate. After the fibre an additional $\lambda/2$ plate then rotates the polarisation to the desired angle with respect to the quantisation axis of the trap. An acoustic optic modulator (AOM) from Isomet (pt. No. 1212-2-949) is placed into the beam of the 369 nm laser to provide controllable blocking of the beam.

To allow for efficient photoionisation process, the 399 nm and 369 nm lasers are combined and overlapped using a narrow bandpass filter at 369 nm from Semrock (pt No. FF01-370136), these two beams are then combined with the 638 nm laser through a dichroic

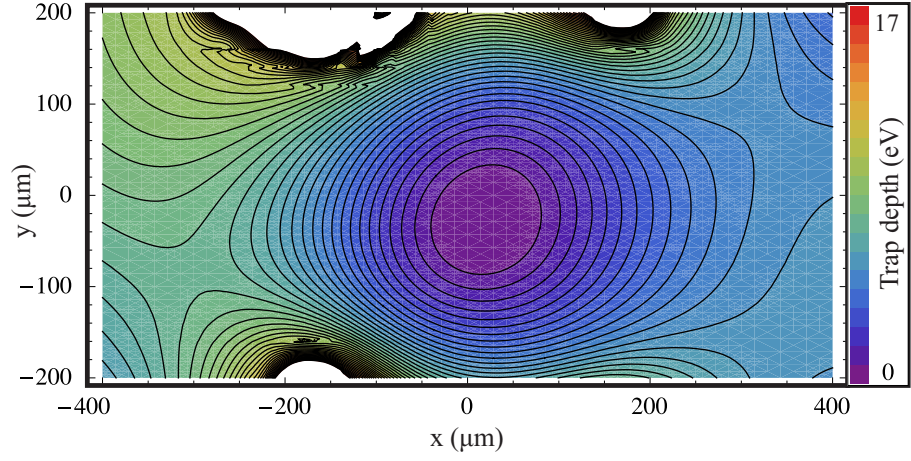


Figure 3.13: Simulated Pseudopotential of the trap electrodes after mechanical alignment. The first turning point within the trapping potential occurring at $\{x(\mu\text{m}), y(\mu\text{m})\} \approx \{330, 80\}$ has a potential of 4.9(2)eV.

Rf and static control volatges	
Electrode	Voltage (V)
rf	680(10)
1	148.88(1)
2	7.36(1)
3	25.03(1)
4	0
5	0
6	167.76(1)
comp 1	169.22(1)
comp 2	-2.70(1)

Table 3.3: rf and static voltages applied to the trap electrodes.

mirror. The three beams are then aligned and focused to the centre of the trap with beam waists $\sim 50\text{-}100\ \mu\text{m}$. Large beam waists are used to reduce the uncertainty of the overlap of the beams and centre of the trapping fields. The 935 nm laser is aligned and focused through the opposite side of the hemisphere. The 399 nm and 638 nm lasers have a telescope setup with one of the lenses attached to a translation stage allowing for individual alignment and control of the beam diameter. A schematic of the setup for combining and aligning the laser beams before passing them thorough the vacuum system is shown in fig. 3.14

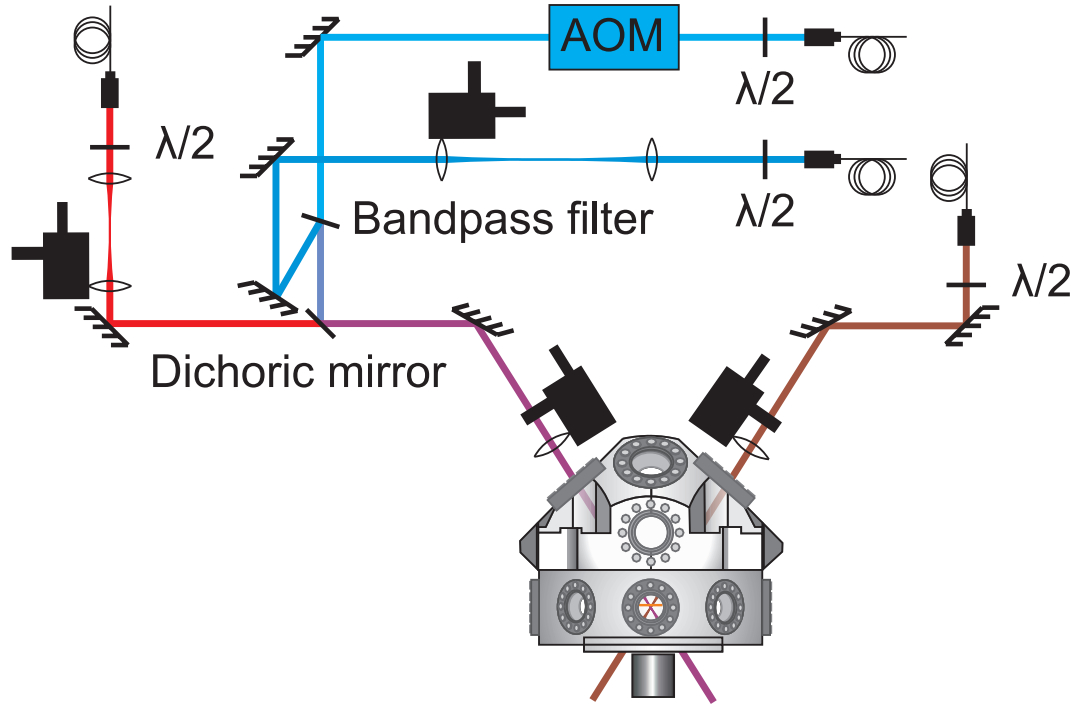


Figure 3.14: Schematic of the laser alignment for trapping within the blade trap.

The wavelengths of the lasers are adjusted to trapped the desired isotope given in table 3.1 and red detuning the $^2S_{1/2} \leftrightarrow ^2P_{1/2}$ transition for efficient Doppler cooling. To trap, a current is passed through a atomic oven producing a flux of neutral of enriched Yb. The ovens are turn off either through successful trapping or if the pressure rises above 10^{-10} mbar from a base pressure of $<1 \times 10^{-11}$ mbar.

Once able to trap single ions, the characterisation of the ion trap can take placed, the secular frequencies can be measured by applying a small ac voltage to one of the control electrodes after the low pass filters and scanning the frequency. The secular frequencies were measured to be $\omega_x/2\pi = 2.069(1)$ MHz, $\omega_y/2\pi = 2.110(1)$ MHz and $\omega_z/2\pi = 1.030(1)$

MHz. From simulations a calculated rf voltage V_{rf} of 610(10) V is applied, at a drive frequency of $\Omega_{rf}/2\pi \approx 21.48$ MHz and a trap depth is calculated to be 4.9(2) eV.

The next step after trapping is to minimise micromotion. Methods in minimising micromotion have been discussed by Berkeland *et al.* [61]. The following method was employed to reduce any excess micromotion. Firstly by observing the ions position, through checking any slow time varying stray electric fields immediately after trapping are not causing a drift in the ions position on the EMCCD camera, typically for 10 min. After this the linewidth of the transition can be measured by performing a frequency sweep of the Doppler cooling lasers frequency, the presence of micromotion can be identified in a broadened linewidth. Operating at a saturation parameter of ~ 1 and by lowering the rf voltage, compensation is carried out until no change in the ion's position is observed as the rf voltage is decreased. For the heating measurement discussed in section 3.6.2 linewidths from 38-40 MHz were achieved at a saturation parameter of $I_{sat} \approx 1.0$. This is above the expected linewidth of 30 MHz believed to be due to intrinsic micromotion via a phase mismatch between the two rf electrodes due to a path length difference. Once compensated for excess micromotion, and by lowering the axial confinement linear chains of ions can then be trapped, shown in fig. 3.15

3.6.2 Heating measurement

An important characterisation of ion trap is the heating rate experienced by trapped ions. Traditionally this is calculated by looking at the ratio between the red and blue sidebands over time requiring resolved sideband cooling techniques. Instead using a technique proposed by J. H. Wesenberg *et al.* it is possible to calculate the heating rate through the fluorescence signal during Doppler cooling. The model is based on a single trapped ion with heating dominating within one of the principal axes. By having the axial (z-direction) secular frequency less than the radial modes, heating of the ion can be dominant within this direction.

A single $^{174}\text{Yb}^+$ ion is allowed to be heated by blocking the Doppler cooling beam for a particular time delay, this increases the instantaneous Doppler shift during an oscillation defined as $\Delta_D = -\vec{k} \cdot \vec{v}$, where \vec{k} is the laser beam wave vector. By defining Δ_{max} as the maximum instantaneous Doppler shift Δ_D , then a probability density $P_D(\Delta_D)$ can be used to calculate the likelihood of the ion experiencing a specific instantaneous Doppler

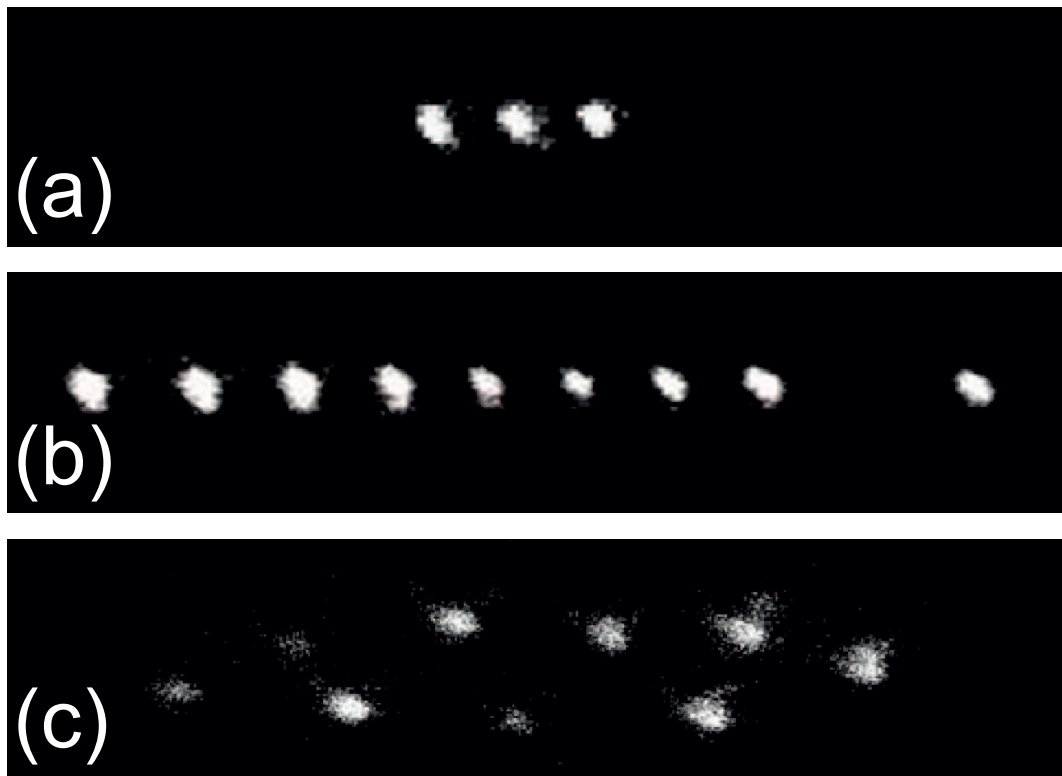


Figure 3.15: Ion chains produced within the Blade trap. (a) Chain of three $^{174}\text{Yb}^+$ ions. (b) Chain of 10 Yb^+ ions with a different isotope trapped and sympathetically cooled, shown by dark space. (c) By adjusting the rf voltage and thus varying the ratio between the radial and axial frequencies, a zigzag configuration can be achieved.

shift [147]. This can be visually understood by considering the ions motion as classical simple harmonic motion, the heating of the ion results in the increase of the ions velocity. The time in which the ion is resonant with the Doppler cooling laser decreases, resulting in a lower cooling and hence fluorescence rate. Fig. 3.16 shows the overlap between the probability density of the Doppler shift, $P_D(\Delta_D)$ and the broadened full with half maximum (FWHM) transition linewidth, L for the case of a hot and cool ion.

The overlap between the Doppler shift probability density and the transition linewidth

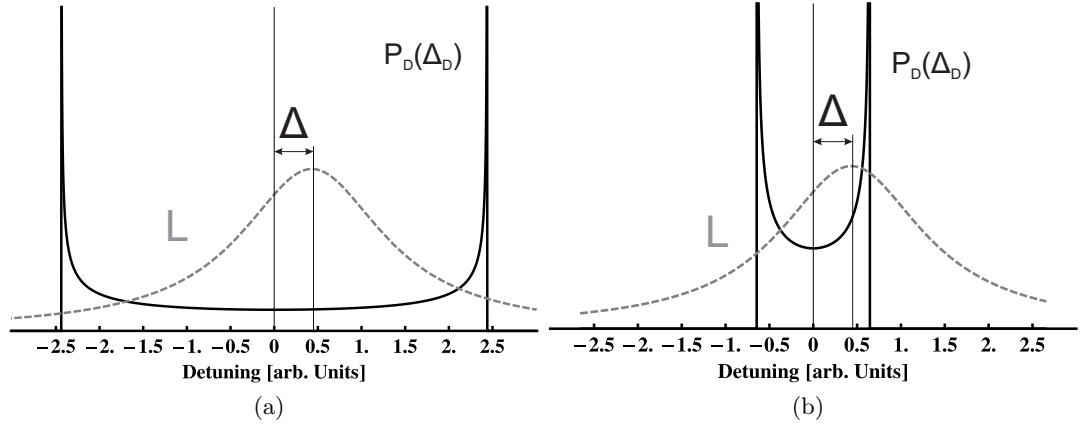


Figure 3.16: Probability density function of the ion showing the overlap with the linewidth of the transition. (a) Hot ion. (b) Cold ion.

is low as $\Delta_{max} \gg |L| + |\Delta|$ resulting in a reduced scattering rate. The case for a cool ion the overlap is good resulting in a higher scatter rate. Since the relative change in ion energy over one period oscillation is small compared to the change in total energy. The energy for one period and the scatter rate can be averaged. This leads to the average scatter rate over one oscillation can be defined as [147]

$$\left\langle \frac{dN}{dt} \right\rangle = \int \frac{dN}{dt} P_D(\Delta_D) d\Delta_D \quad (3.8)$$

where $\langle dN/dt \rangle$ is the instantaneous scatter rate.

As shown in fig. 3.16(a), The overlap of the probability density $P_D(\Delta_D)$ and the transition linewidth L can be approximated as being uniform. The scatter rate of the ion can be re-expressed as the ions energy by factoring out the probability density and can be written in terms of the following parameters. The ions energy at time t $E(E_0, t)$, the energy just before cooling E_0 , the saturation intensity parameter s , the laser \vec{k} -vector in the z-direction k_z , the ion mass m , and the broadened transition linewidth L .

$$\left\langle \frac{dN}{dt} \right\rangle (E(E_0, t)) = \frac{1}{\sqrt{E(E_0, t)}} \frac{s\Gamma^2}{2\sqrt{\frac{2}{m}k_z(1+s)^{3/2}}} \quad (3.9)$$

By defining the ion energy as a 1D Maxwell-Boltzmann thermal distribution $P_B(E_0)$, before recoiling E_0 . The average scatter rate at time t for an ion is defined as [147]

$$\left\langle \frac{dN}{dt} \right\rangle_{E_0} = \int_0^\infty P_B(E_0) \left\langle \frac{dN}{dt} \right\rangle (E(E_0, t)) dE_0 \quad (3.10)$$

For the experiment the AOM was used to block the 369 nm laser and employ delay times of 1, 3, 5 and 7 seconds. The cooling laser is then turned on and the fluorescence signal is measured in $50 \mu\text{s}$ time bins for 4 ms. The control sequence is shown in fig. 3.17.

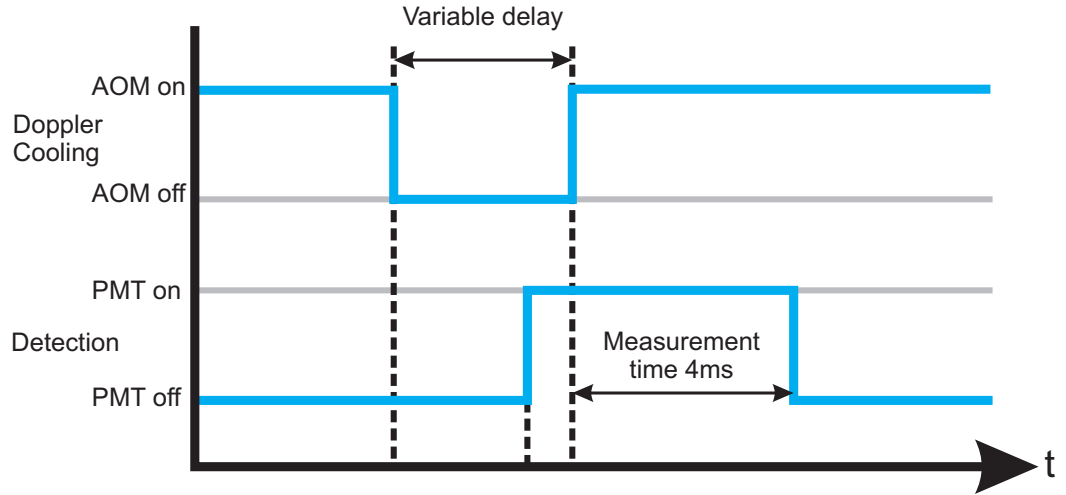


Figure 3.17: The control sequence for turning the 369 nm laser on and off via the AOM and data collection from the PMT.

By repeating this process for 500 runs a statistical average can then be taken. A $\Delta = 6(2)$ MHz, $s = 1.0(2)$ and observed transition linewidth, $L = 40(5)$ MHz were used. The small detuning from resonance compared to the natural linewidth allowed for less effective cooling and a re-coil signal to be more easily observed. Fig 3.18 shows an averaged ion fluorescence curve for a 5 second delay at a secular frequency of $\omega_z/2\pi = 178(1)$ KHz.

The ion energy was converted into motional quanta through $\bar{n} = E/\hbar\omega_z$, and plotted against the various delay times. This is shown in Fig. 3.19.

This was then repeated for the following secular frequencies $\omega_z/2\pi = (178(1), 287(1), 355(1))$ KHz, in which the expected $\dot{\bar{n}} \propto 1/\omega_z^2$ relationship is shown in Fig 3.20.

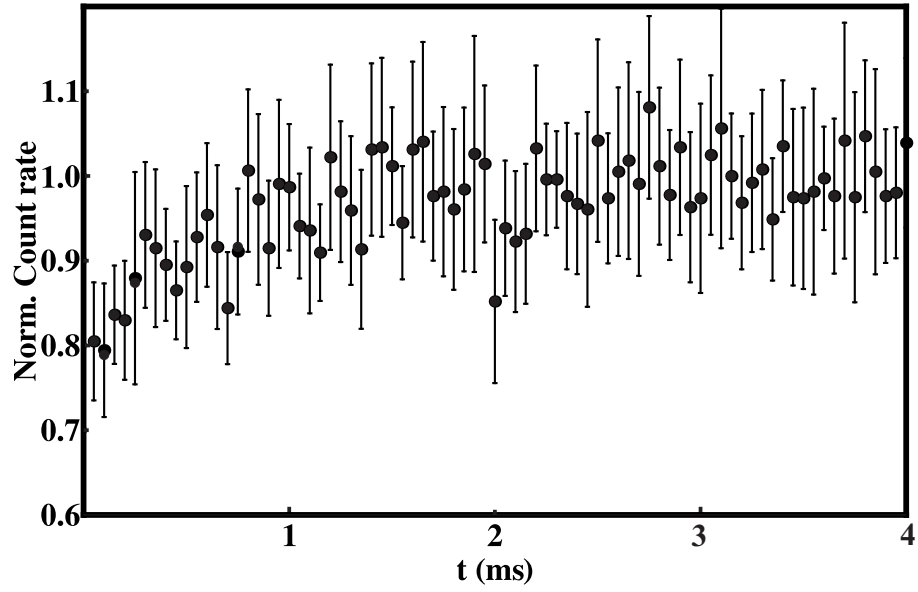


Figure 3.18: Averaged ion fluorescence from 500 runs for a 5 second delay at a secular frequency of $\omega_z/2\pi = 178(1)$ KHz.

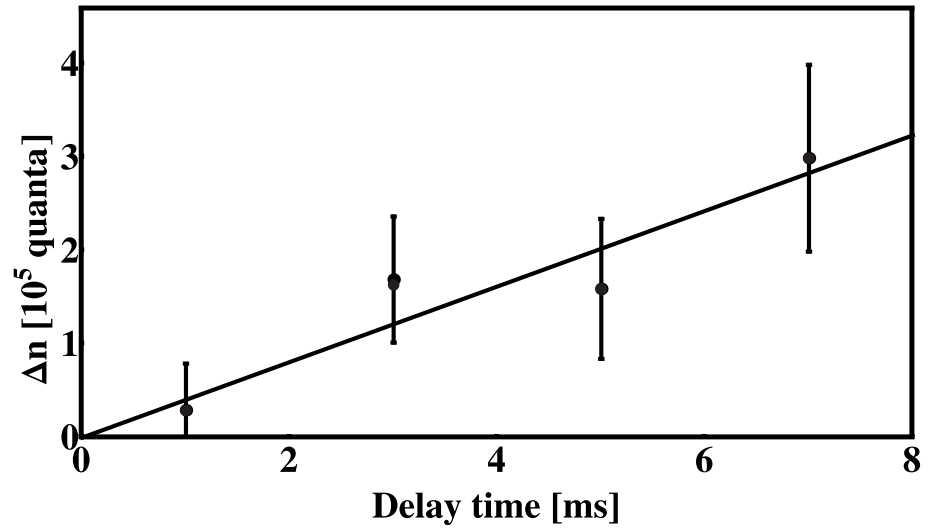


Figure 3.19: Motional quanta of the ion after various delay times, for an ion with secular frequency of $\omega_z/2\pi = 178(1)$ KHz.

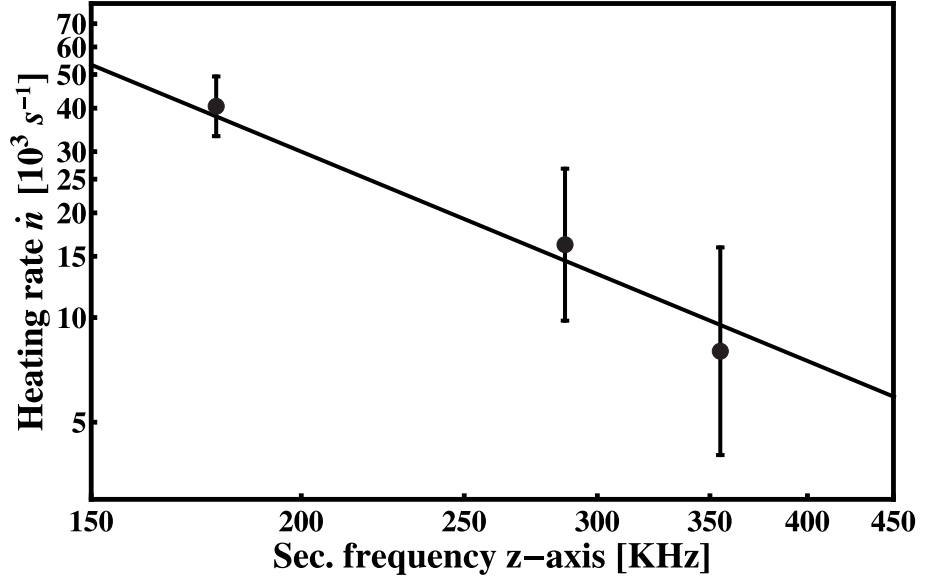


Figure 3.20: Heating rate as a function of secular frequency showing the expected $1/\omega^2$ dependency.

With the previously discussed relationship between the average change in motional quanta \dot{n} , and the electric-field noise density $S_E(\omega_z)$ within section 2.5 (equation 2.17).

$$\dot{n} = \frac{q^2}{4m\hbar\omega_z} S_E(\omega_z) \quad (3.11)$$

Through scaling out the secular frequency we obtain a value of $S_E(1\text{MHz}) = 3.6(9) \times 10^{-11} \text{ V}^2/\text{m}^2/\text{Hz}$. For a ion-electrode distance of $310(10) \text{ }\mu\text{m}$ this is consistent with previously published values shown in Fig. 2.12.

Chapter 4

Asymmetric ion trap designs

Asymmetric ion traps allows for all the electrodes to lie within one plane leading to more flexible ion trap designs. Higher density of electrodes are possible leading to a large number of individual trapping regions. Integration of optical [146, 148] and electronic elements [149] can also be implemented. These features are advantageous in the scaling of ion trap architectures. Below I will present a general fabrication processes that will provide the foundation for designing the trap structures. Optimised electrode geometries are discussed building on the results by Dr Altaf Nizamani [82] for fast ion separation and combination in the design linear asymmetric ion traps.

Five different ion trap arrays are presented, a y-junction ion trap where shuttling protocols through the junction region are presented. A hexagonal two-dimensional lattice with the ability of individual control for each ion lattice site. Two ring ion traps, where periodic boundary conditions are created by enclosing a linear section on itself. Finally a linear design with 41 individual trapping regions provides flexibility in experiments undertaken. All the designs are then transferred to a photolithography mask ready for fabrication.

4.1 Multi-layered structures

With asymmetric traps already offering particular benefits over symmetric traps, by moving towards multi-layered structures the density of electrodes can be further increased by creating isolated electrodes, shown in fig. 4.1. This allows for static control electrodes directly below the ion, providing more control in shuttling [81] and the separation and combination of ions [82, 150], without the need to apply high voltages.

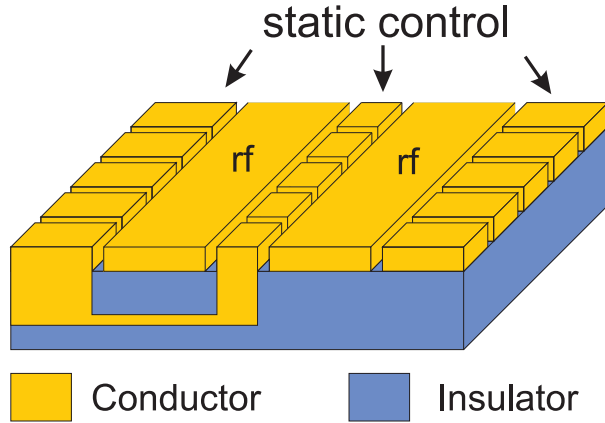


Figure 4.1: Multi-layered structure with buried wires to realise isolated control electrodes.

To produce such structures, top-down fabrication processes will be employed, depositing and etching layers placed onto a wafer. Starting with a suitable substrate that exhibits a low loss tangent $\tan \delta$ at typical radio frequency (rf) drive frequencies (15-80 MHz), a patterned conductor layer will be deposited. The geometry of the conductor layer will be designed to limit the induced resistance and capacitance. Next a blanket insulator layer is deposited onto the whole substrate. The properties of the insulator layer is also considered such that bulk breakdown doesn't limit the operation of the traps. Vertical interconnect access (vias) are then etched to gain access to the underlying conducting layer. Lastly the electrode structures are deposited, by using electroplating techniques it is possible to go to thick films that can shield dielectric, reducing the effect of stray charge. The fabrication process is shown in fig. 4.2.

4.2 Design limitations

Through collaborating with the University of Nottingham, the fabrication process was discussed in more detail to see what deposition thicknesses are possible using thier cleanroom facilities. As not to overcomplicate the fabrication process, planarisation steps were not included in the fabrication process, thus providing a quicker turn around time between traps and produce a higher yield.

With the use of thermal evaporation, depositing $0.5 \mu\text{m}$ of gold would be possible for the underlying conducting layer. This had been limited to a thickness $0.5 \mu\text{m}$ as not to

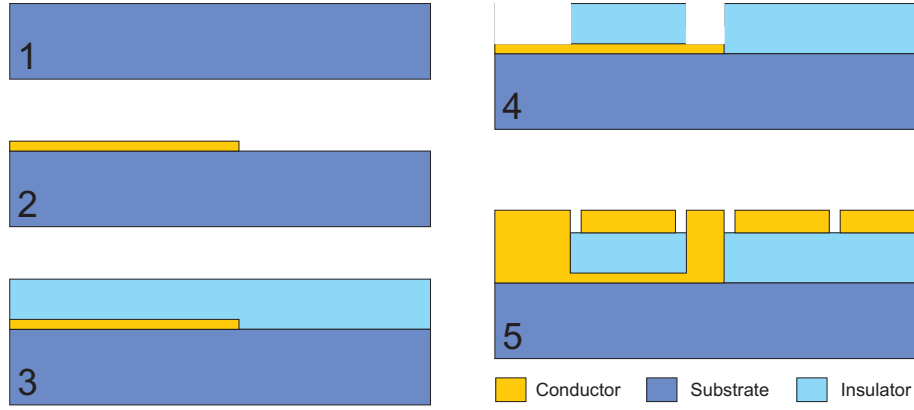


Figure 4.2: General process sequence for the construction of a multi-layered asymmetric trap. 1) A low loss tangent $\tan \delta$ wafer provides the foundation of the ion traps. 2) Deposition of patterned conducting layer for the buried wires. 3) Blanket deposition of an insulator layer. 4) Etching vertical interconnect access (vias) to gain access to the underlying conducting layer. 5) Deposition of the electrode structure.

influence the final surface profile of the electrodes. A thickness of $2\text{ }\mu\text{m}$ for the insulator layer via plasma enhanced chemical vapor deposition (PECVD) was initially estimated. Intrinsic stresses within the amorphous films will eventually cause cracking and it was determined that $2\text{ }\mu\text{m}$ would be a lower limit on the dielectric thickness without causing any problems. During fabrication thicker layers were possible, but for the ion trap designs $2\text{ }\mu\text{m}$ of SiO_2 was used.

Through the use of a high contrast, epoxy based photoresist¹, electroplating of the final electrode structures with an aspect ratio 5:1 would be possible. From initial surface flashover measurements of various gaps across quartz [151], we conclude that gaps of $5\text{ }\mu\text{m}$ would still allow the application of around 400 V. By rounding the corners of the electrodes the local electric field at the triple point (the interface of the electrode, dielectric and vacuum) can be reduced, thus allowing for potentially higher voltages to be applied. With gaps of $5\text{ }\mu\text{m}$ we would aim to have electrodes electroplated to a thickness of up to $25\text{ }\mu\text{m}$.

To be compatible with both vacuum systems, up to 90 individual control electrodes can be design into the trap arrays without the need to simultaneously connect areas together. Using the above constraints the design and simulation of various ion traps can now take place.

¹<http://www.microchem.com/Prod-KMPR.htm>

4.2.1 Electrical characteristics

When scaling up ion trap arrays to many control electrodes and individual trapping zones, the finite resistance R and capacitance C of the trap electrodes will result in losses within the ion traps. The rf losses will result in power being dissipated and if too high, will eventually cause the heating and failure of the trap. It is therefore necessary to limit and provide an estimate of the power dissipated within the ion trap structures.

Building on the discussion of the power dissipated of an ion trap circuit within section 2.4.2, in the limit where the loss tangent $\tan \delta$ and $\Omega_T CR \ll 1$, the power dissipated is given by

$$P_d = \frac{1}{2} V_0^2 \Omega_T^2 C^2 R \quad (4.1)$$

The loss tangent can be considered as measure of performance of the dielectric layer from an ideal structure with infinite resistance. For SiO_2 it is a good assumption to use the above expression for power dissipation.

Considering the multi-layered structure depicted in fig. 4.3 (a), an estimate for the power dissipated can be considered. A simple lumped circuit model of the trap is used to calculate the overall trap resistance, capacitance and hence the power dissipated for a given rf drive frequency and voltage. The capacitance and resistance of the given structures will be dominated by the buried wires. By assuming each buried wire has the same electrical characteristics, the equivalent circuit, shown in fig 4.3 (b) is the sum of the individual capacitance C and resistance R over the total number of electrodes N . Summing these elements in parallel yields a total resistance $R_T = R/N$ and capacitance $C_T = NC$. The individual buried wires are modelled as a parallel plate capacitor with capacitance

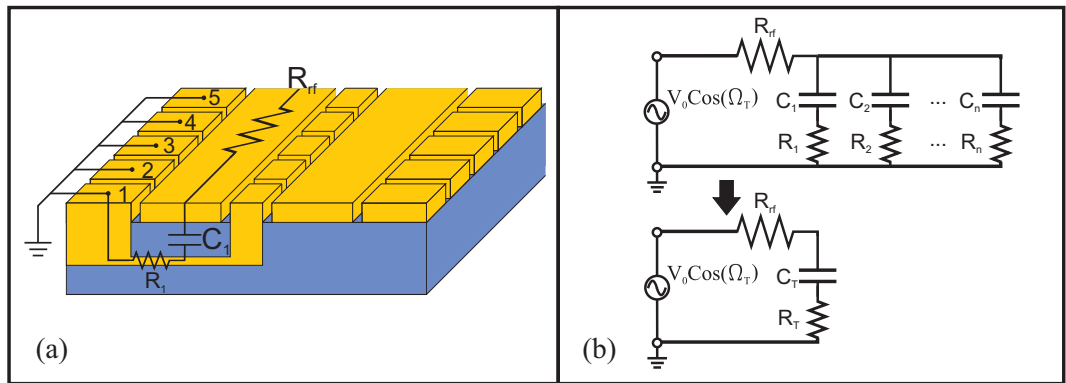


Figure 4.3: Modelled ion trap circuit to provide an estimate on the dissipated power.

$C = \epsilon_0 \epsilon_r A/d$, where A is the area, d is the dielectric thickness and ϵ_r the relative permittivity of the dielectric, with $\epsilon_r \approx 3.9$ for SiO_2 . The resistance of the wires can be estimated as $R = \rho_{Au} \frac{L}{CA}$ where L is the length, CA the cross sectional area of the buried wire and the resistivity of gold, $\rho_{Au} \approx 2.5 \times 10^{-8} \Omega\text{m}$.

4.3 Trap modelling

4.3.1 Numerical simulations

The design and numerical simulations of the ion traps was performed using AutoCAD and an open source C++ program called bemsolver [90] compiled with ROOT, together produce basis functions of the trap electrodes. Previous ion trap designs including the blade trap (section 3.6) were modelled with 3D Charged Particle Optics (CPO-3D) from CPO Ltd. This had a maximum number of 6000 segments in which to draw the electrodes. When large ion trap arrays are considered the accuracy decreases within the simulations and sometimes it is not possible to draw the whole trap.

Firstly the trap electrodes are drawn using 3D polylines within AutoCAD to produce a .dxf file. The trap electrodes are composed of closed four sided polygons shown in fig. 4.4. If drawn in any other method inaccurate calculations of the electric potentials occur. Each electrode is defined as a new layer, with the layer name matching the associate electrode name. Some key points in simulating the trap electrodes were observed in producing accurate basis functions, aim to keep the size of four sided polygons equal and avoid very acute angles.

The .dxf file is then imported into bemsolver, within the .cxx file, the electrodes are defined and imported. A *refine* factor is used to increase the accuracy, this works by filling the original object with smaller versions, this works well with cubic objects but provides problems with other shapes. The volume over which to calculate the electric potential is then considered. By defining a 3D mesh in cartesian coordinate system (x,y,z), bemsolver calculates the electric potential using a boundary element method at each point within the mesh. An output file is then generated in which the electric potential at each position is listed.

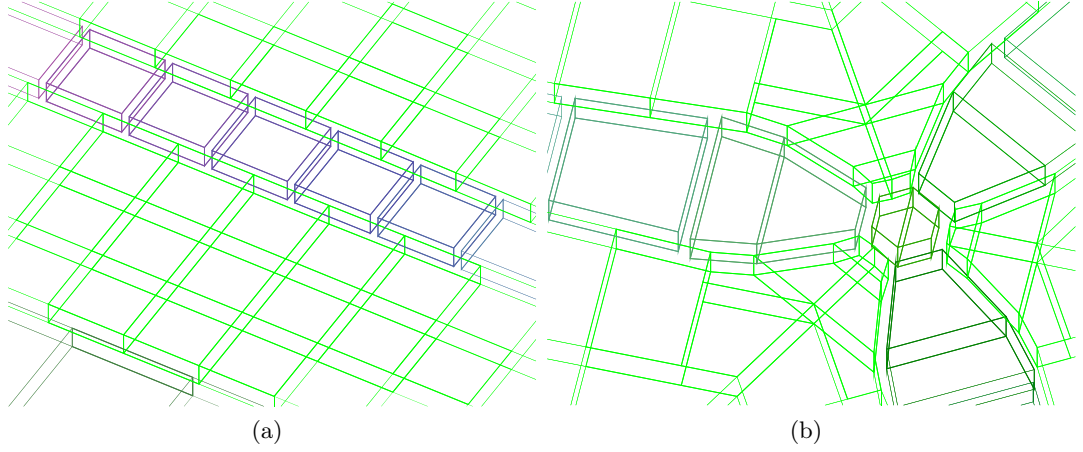


Figure 4.4: Trap electrodes drawn in AutoCAD with four sided polygons with 3D polylines. The file is then exported as a .dxf file and is used to simulate the corresponding electric fields. (a) A linear segmented section, (b) a y-junction.

By assigning one volt to the i^{th} electrode and setting the voltage applied to the other electrodes to zero, an output file can be generated and is used as a basis function. This is then repeated for all other electrodes. The accuracy of the data is dependent on the density of the 3D mesh and the refine factor. By increasing the density and lowering the refine factor generally provides more accurate data but also increases the computational time.

Next the total trapping potential can be calculated using Mathematica. The data files are imported into Mathematica and then the Interpolation function is used to produce electric fields from the electrodes. To provide trapping in all three dimensions the rf pseudopotential is applied with the sum of the static potentials [16, 63]

$$\Psi(\chi, t) = \frac{e^2 V_{rf}^2}{4m\Omega_{rf}^2} |\nabla \Theta_{rf}(\chi)|^2 + e \sum_{i=0}^n V_i(t) \Theta_i(\chi) \quad (4.2)$$

where e is the charge, m the mass and Ω_{rf} the rf drive frequency with amplitude V_{rf} . $\Theta_{rf}(\chi)$ is the basis function for the rf electrode at position vector χ . $\Theta_i(\chi)$ is the basis function for the i^{th} static control electrode when held at 1 volt and the other electrodes are grounded. $V_i(t)$ is the time varying voltage applied to the i^{th} electrode. Fig. 4.5 shows the rf pseudopotential field created from an asymmetric electrode arrangement with uneven rf electrodes.

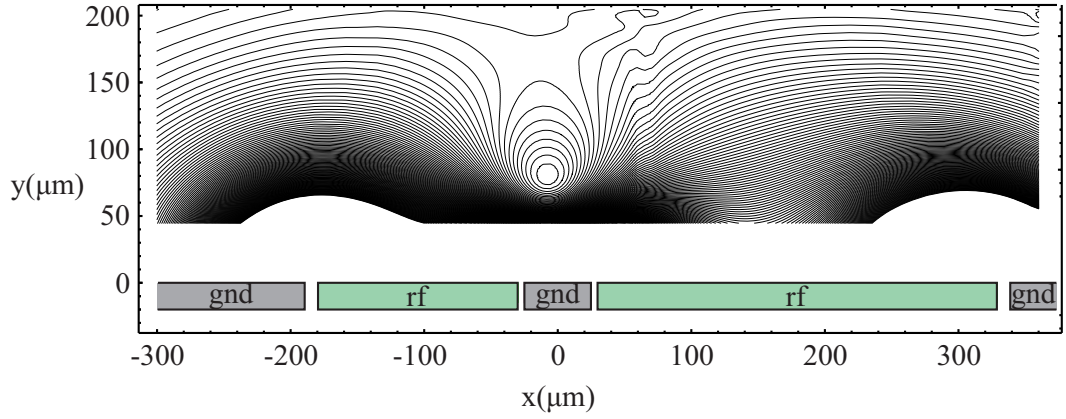


Figure 4.5: rf pseudopotential field created from an asymmetric electrode arrangement. To rotate the principal axis the symmetry of rf electrodes is broken with even rf widths having a ratio of 2:1.

4.3.2 Analytical simulations

Numerical simulations typically take a few hours to calculate the electric potential providing an impractical method in optimising geometries. There has been previous analytical studies in the optimisation of surface geometries [92–94, 152] which has allowed for faster optimisation compared to numerical simulations. House [93] has produced an analytical model to calculate electrostatics from surface geometries allowing him to calculate the rf nil, trap depth and the a and q stability parameters. Wesenberg [92] has investigated surface geometries using the Biot-Savart-like law [91] method. By solving the line integral of an electrical current around a closed loop the electric potential can be calculated. This allows for geometries to be studied that would otherwise be hard to simulate.

4.4 Asymmetric geometries

Asymmetric traps offer better scalability to large trap arrays as opposed to symmetric designs but the cost is at reduced secular frequencies and trap depths. Radial secular frequencies are one the order of one sixth for same dimensions and voltages. Trap depths are significantly reduced increasing the difficulty in loading. This can be compensated for by applying higher voltages and or reducing the ion height. But this introduces breakdown issues and increased anomalous heating. It is therefore important to optimise the electrode geometry to obtain maximum trap depth and secular frequencies for a given ion height.

Below is a summary of the work carried out by former PhD student Altaf Nizamani [82],

on the optimisation of electrode geometries for fast ion separation and combination. Combined with other studies into asymmetric geometries [93, 150], this provides a foundation for the ion traps presented. House has shown [93] that a rectangular electrode lying in the $y = 0$ plane the electrostatic potential can be defined as [93]

$$\begin{aligned} \phi(x, y, z) = \frac{V}{2\pi} \left\{ \arctan \left[\frac{(x_2 - x)(z_2 - z)}{y\sqrt{y^2 + (x_2 - x)^2 + (z_2 - z)^2}} \right] \right. \\ - \arctan \left[\frac{(x_1 - x)(z_2 - z)}{y\sqrt{y^2 + (x_1 - x)^2 + (z_2 - z)^2}} \right] \\ - \arctan \left[\frac{(x_2 - x)(z_1 - z)}{y\sqrt{y^2 + (x_2 - x)^2 + (z_1 - z)^2}} \right] \\ \left. + \arctan \left[\frac{(x_1 - x)(z_1 - z)}{y\sqrt{y^2 + (x_1 - x)^2 + (z_1 - z)^2}} \right] \right\} \end{aligned} \quad (4.3)$$

Where V is the applied voltage and x_1, x_2, x_3 and x_4 , are the corners of the electrode in the x -, z - plane. The total potential can be found by linearly summing the contribution from all the electrodes. This approximation assumes that all the electrodes lie in the $y = 0$ plane together with the gapless approximation. This is a good approximation for gaps of $5 \mu\text{m}$ and ion-electrode distance discussed within this thesis ($\sim 80\text{-}250 \mu\text{m}$), with House showing a slight perturbation within the calculated potential [93]. To maintain the highest accuracy within the analytical solutions, the electrode widths should be measured from the centre of the gaps as shown in fig. 4.6. When considering junction regions were small changes in the electrode geometry can have a large effect on the resultant pseudopotential it is advisable to use numerical methods.

By considering a 5 wire asymmetric geometry as shown in fig. 4.6, the optimisation of the trap parameters can be considered. The rf electrodes are defined to have widths b, c and are separated from each other by a static electrode of width a . Outside of the rf electrodes are additional static control electrodes that are assumed to run to infinity. House defines the coordinate system such that the origin in the x -, y - plane is on the electrode surface and at the interface between the rf and centre static electrodes, shown in fig 4.6.

Fig. 4.6 (a) shows the case when the rf electrodes have equal width. To achieve efficient laser cooling, the laser \vec{k} -vector needs a component in all three principal axes. This can be achieved by breaking the symmetry of the rf electrodes shown in fig. 4.6 (b), however in doing so results in a shift of the ion position x_d within the x -direction. Through inserting

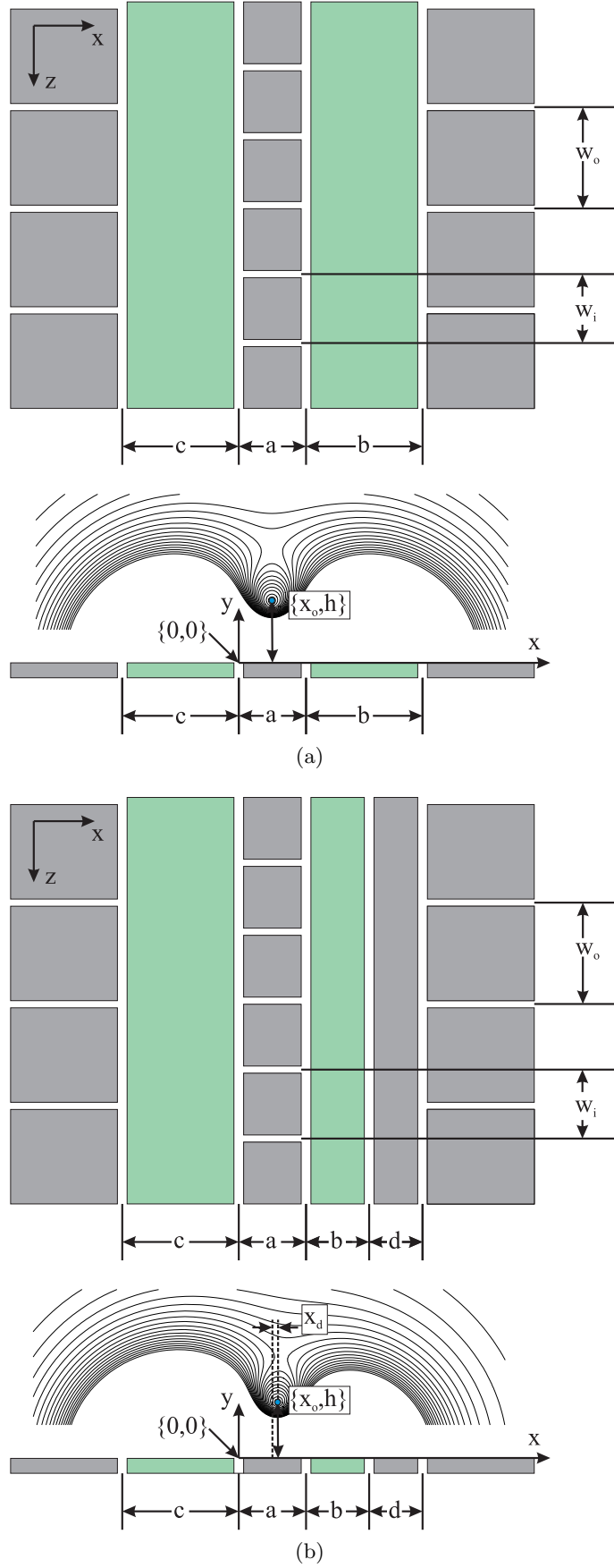


Figure 4.6: Five wire asymmetric ion trap designs with inner segmented W_i and outer segmented W_o static control electrodes. (a) Equal rf electrode widths where $b = c$. (b) Unequal electrode widths where $c = b/2$. This provides rotation of the principal axes allowing for efficient laser cooling. To provide easier compensation of the ion position a ground wire is inserted such that the outer control electrodes are symmetric about the ion position.

a ground wire the outer static control electrodes can be symmetric about the ion position.

The rf nil is calculated to be at, $x_0 = ac/(b + c)$ and $h = \sqrt{abc(a + b + c)}/(b + c)$ [93].

The trap depth can be expressed as [82, 93]

$$\Xi = \frac{e^2 V_{rf}^2}{h^2 \pi^2 m \Omega_{rf}^2} \kappa \quad (4.4)$$

where,

$$\kappa = \left[\frac{2\sqrt{abc(a + b + c)}}{(2a + b + c)(2a + b + c + 2\sqrt{a(a + b + c)})} \right]^2 \quad (4.5)$$

κ is defined as the geometric efficiency factor. By altering the various widths of the trap electrodes the trap depth can be maximised. For the case of equal rf electrodes when $c = b$ (fig. 4.6 (a)), the maximum trap depths occurs when $b \approx 3.68a$ with an ion height $h \approx 1.43a$. The case when the rf electrodes have unequal lengths when $c = b/2$ (fig. 4.6 (b)) the maximum trap depths occurs when $b \approx 4.9a$ with an ion height $h \approx 1.27a$.

4.4.1 Ion separation

Through the segmentation of the static control electrodes the control of the ion position can be performed. Most importantly the confinement within the z direction is achieved together with compensating any stray electric fields. By applying time varying voltages to the static control electrodes it is possible to shuttle the ion through various trapping zones and perform the separation of two ions within one harmonic potential. The radial secular frequencies, ω_x and ω_y are produced from the rf electrodes and ω_z , the axial secular frequency is produce from the static electrodes. The secular frequencies of the ion are typically set such that $\omega_x, \omega_y \gg \omega_z$. Home and Steane [150] carried out theoretical work on fast ion separation, the aim is to transform a single well into a double through the application of a wedge potential and to be performed with acquiring minimum kinetic energy as possible. The confinement in the axial direction (z) can be expressed using the Taylor expansion as [150]

$$V \approx 2e\alpha z^2 + 2e\beta z^4 \quad (4.6)$$

where α and β are the coefficients of quadratic and quartic terms, V is the potential in eV and e is the charge of the ion. For the case when $\alpha < 0$ a double well potential is created shown in fig. 4.7. When $\alpha = 0$ the potential is only due to the quartic term β within equation 4.6. The axial secular frequency ω_z when $\alpha < 0$, $\alpha = 0$ and $\alpha < 0$ is defined

as [150]

$$\omega_z \simeq \begin{cases} \sqrt{\frac{2e\alpha}{m}} & \text{when } \alpha > 0 \\ \sqrt{\frac{3e}{m}} \left(\frac{e}{2\pi\epsilon_o} \right)^{1/5} \beta^{3/10} & \text{when } \alpha = 0 \\ \sqrt{\frac{4e|\alpha|}{m}} & \text{when } \alpha < 0 \end{cases} \quad (4.7)$$

The axial secular frequency ω_z is a minimum when $\alpha = 0$ and sets a limit on the speed of the adiabatic separation process. The ion separation at $\alpha = 0$ is approximated as $s \simeq (\frac{e}{2\pi\epsilon_o\beta})^{1/5}$ [150] from the Coulomb repulsion in a single well.

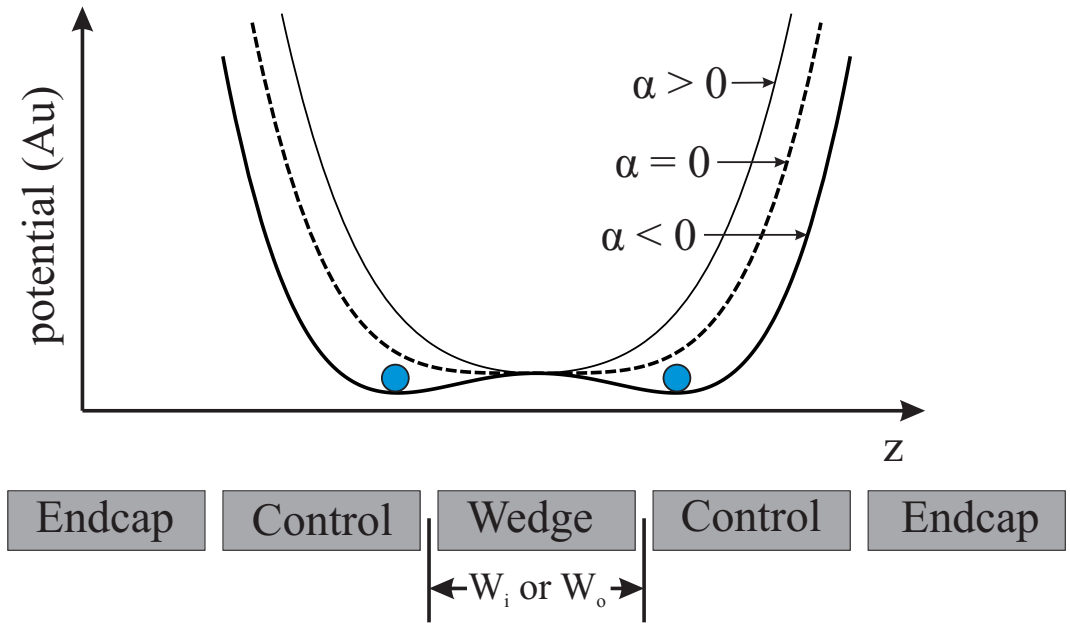


Figure 4.7: Profile of the potential for different values of α [82]. When $\alpha < 0$ a double well potential is created.

Nizamani and Hensinger [82] investigated static control electrode geometries to optimise the separation process by providing a maximum β and negative α . The static control electrodes are labelled endcap, control, or wedge as shown in fig. 4.7. Five inner segmented electrodes are used in the separation process whilst ten are used in the outer segmented design, symmetric about the ions axial position. β was shown to be maximised when the endcap, control and wedge electrode widths are approximately the same [82]. The widths of the segmented electrodes were then varied to maximise β . For the inner segmented electrodes a maximum β is obtained when $W_i \approx a$, for the outer segmented electrodes β is maximum when $W_o \approx 3.66a$. A negative α increases whilst decreasing the rf separation

a (therefore decreasing ion height) scaling as a^{-2} . The inner segmented electrode geometry produces values for α and β that are approximately 100 times greater than the outer segmented electrodes for optimum designs at the same rf electrode separation a [82].

4.4.2 Alternative geometry

Although uneven rf rails provide the opportunity to rotate the principal axes required for efficient laser cooling, it also induces a shift in the ions' position relative to the electrode geometries as shown in 4.6 (b). This complicates any compensation of the ion as the electrodes will be asymmetric about the ions' position, especially the centre static control electrodes. Allcock *et al.* [79] have shown that by splitting the centre static control electrode in an even rf electrode arrangement, thus creating an effective 'six wire' geometry, has allowed for the creation of a rotated quadrupole potential about the ions' position through applied static voltages.

Splitting the centre static control electrodes will induce a gap directly below the ion position, creating exposed dielectric in direct sight of the ion. To overcome this additional static control electrodes are added, this also has the benefit of separating the rotation voltages with other applied voltages to the electrodes. A schematic of the electrode geometry is shown in fig. 4.8.

With the optimum electrode geometries for maximum trap depth at a given ion height and efficient separation calculated, the design of various ion trap arrays can now take place.

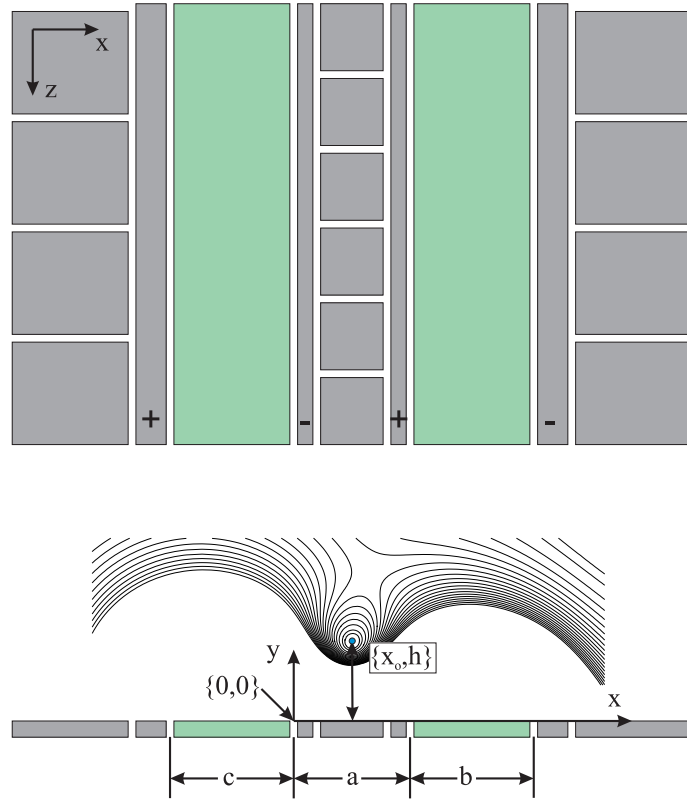


Figure 4.8: Five wire asymmetric ion trap design with equal rf electrode widths and additional static control rails to provide rotation of the principal axes allowing for efficient laser cooling. Alternating polarity of the voltages are applied to the rotation rails.

4.5 Y-junction ion trap

One of the requirements for a scalable ion trap architecture for quantum information processing (QIP) is an array consisting of storage, interaction and transport regions [14]. The ability to shuttle between different regions requires segmented electrodes, more importantly is this transport needs to be adiabatic. For the ability to create arbitrary interactions between ions needed for gate operations, junctions connecting linear arrays need to be implemented for the ability to re-order ions. The shuttling through a junction and the swapping of two ions was first demonstrated by Hensinger *et al.* [48]. Blakestad *et al.* [49] demonstrated near-adiabatic transport through a two-layer symmetric trap array with further improvements in this trap being demonstrated two years later [153]. Transport through an asymmetric ion trap junction was first demonstrated by Amini *et al.* [81] and then by Moehring *et al.* [154], however, in both cases continuous laser cooling was required and transport was non-adiabatic.

The Y-junction ion trap is based on the design by Robin Sterling [155] but with the inclusion of inner segmented electrodes to provide more control over the ion position during shuttling. The ion trap is a five-wire asymmetric arrangement with an average ion height of $80\mu\text{m}$, shown in fig 4.9. This was selected as a trade off between increased motional heating rate when moving closer to the surface and reduced trap depth and fast ion separation when moving away from the surface. For this given ion height, the electrode widths were optimised to obtain maximum trap depth as outlined in section 4.4. The separation of the rf electrodes $a \approx 55\mu\text{m}$ and the corresponding widths are $\approx 150\mu\text{m}$ and $300\mu\text{m}$. A simulation of the rf pseudopotential from this geometry is shown in fig. 4.5. Within the pseudopotential approximation the q parameter is defined in the limit as $q_i/2 \equiv \sqrt{2}\omega_i/\Omega_T \ll 1$ [16]. A limit of the applied peak rf voltage is set to 400 V, with a drive frequency of $\Omega_{rf}/2\pi = 30$ MHz, the simulated secular frequencies are $\omega_x/2\pi$, $\omega_y/2\pi \approx 5.9$ MHz, and a stability parameter q of ≈ 0.55 . This corresponds to a trap depth of ≈ 0.6 eV.

The ion trap array shown in fig. 4.9 consists of one long arm where loading of ions can be performed, and two shorter arms to form a y-junction. The control electrodes are segmented for optimum separation and combination and also allows ions to be shuttled between the arms for the ability to re order ions.

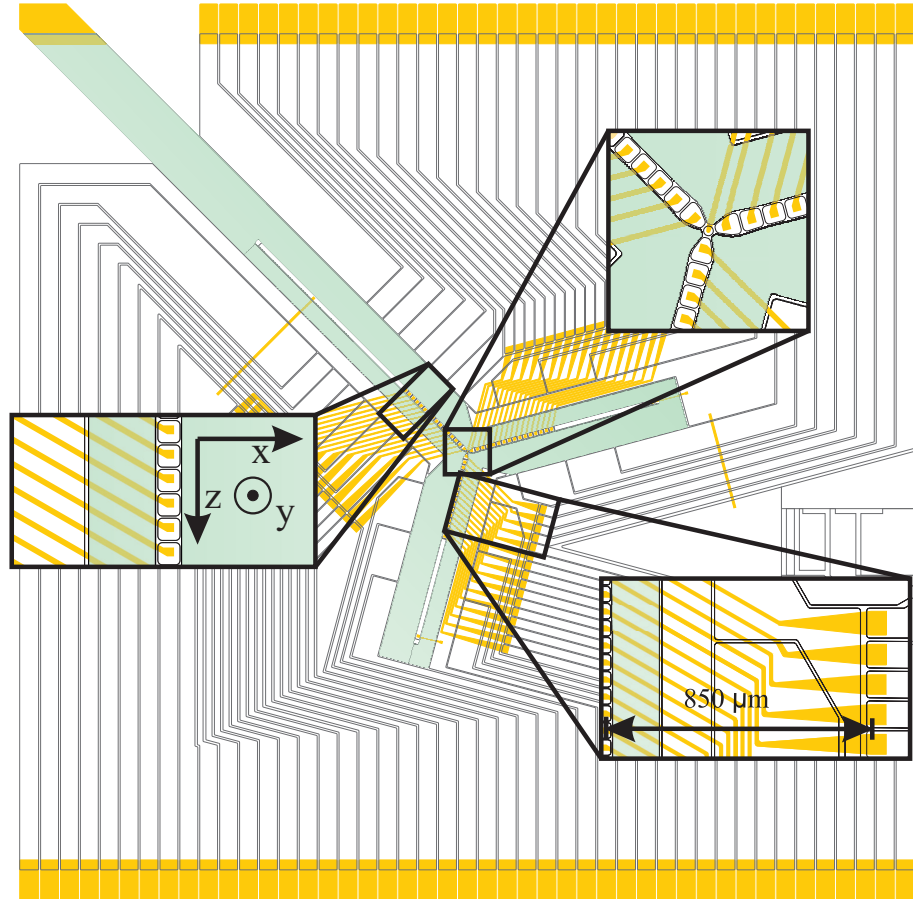


Figure 4.9: Complete design of the whole y-junction trap, the rf electrode is shaded blue and the buried wires yellow. The trap consists of 81 individual control electrodes combining both optimised inner and outer segmented electrodes for fast ion separation. A linear section and the y-junction are shown within the inserts. The geometry of the buried wires, shown in the insert tapers down to reduce the capacitance.

4.5.1 Electrical characteristics

From the finalised geometry in fig. 4.9, an estimate of the power dissipated can be made. With a total of 49 centre segmented control electrodes and the geometry of the buried wires shown within the insert of fig. 4.9 an estimated capacitance $C_y \approx 2$ pF and resistance $R_y \approx 0.4 \Omega$ of the ion trap circuit is calculated. With the previously stated applied rf voltage and drive frequency leads to a power dissipated of ≈ 4.5 mW.

4.5.2 Shuttling within the junction region

The shuttling in linear arrays has been demonstrated with little motional excitation [127, 156–158]. The current aim is to combine this with shuttling an ion through a junction region while maintained within the motional ground state. The geometry of the electrodes within the junction region is of key importance. Variations in the pseudopotential within the junction region provide more of a challenge than linear shuttling. Through the intersection of linear regions to form a junction, a non-zero pseudopotential minimum is created. Blakestad *et al.* [49, 153] have shown that the motional heating rate is proportional to the *slope* of the pseudopotential, therefore it is important to minimise oscillations within the pseudopotential when optimising the geometry of the junction region. Within asymmetric geometries an rf *barrier* exist in which the ion experiences a non zero potential along axial direction of motion, the ion's position is also displaced within the radial directions.

Through modifying the electrode geometry within the junction region, the rf *barrier* can be suppressed. A modified Y-junction designed by Robin Sterling [155] was used to provide suppression of the rf *barrier* by a factor of ≈ 6 to the unaltered electrode geometry. This was achieved by iteratively modifying the junction geometry and performing numerical simulations to achieve a reduced potential barrier and variations within the radial secular frequencies. A plot of the rf pseudopotential is shown in fig. 4.10. Variations in the ion's radial position and secular frequencies are plotted in fig. 4.11.

The time dependent voltage functions of the static control electrodes $V_i(t)$, requires the ion to be accurately transported along the rf nodal position. In steps of approximately $5\mu\text{m}$ along the axial direction, static voltages were manually obtained to maintain the ion in the rf nil and keep variations in the axial secular frequency ω_z , to a minimum. Applied static voltages $V_i(z)$ and corresponding axial secular frequency versus ion position is shown in fig. 4.12. $V_i(z)$ and ω_z were obtained by interpolating between data points using the

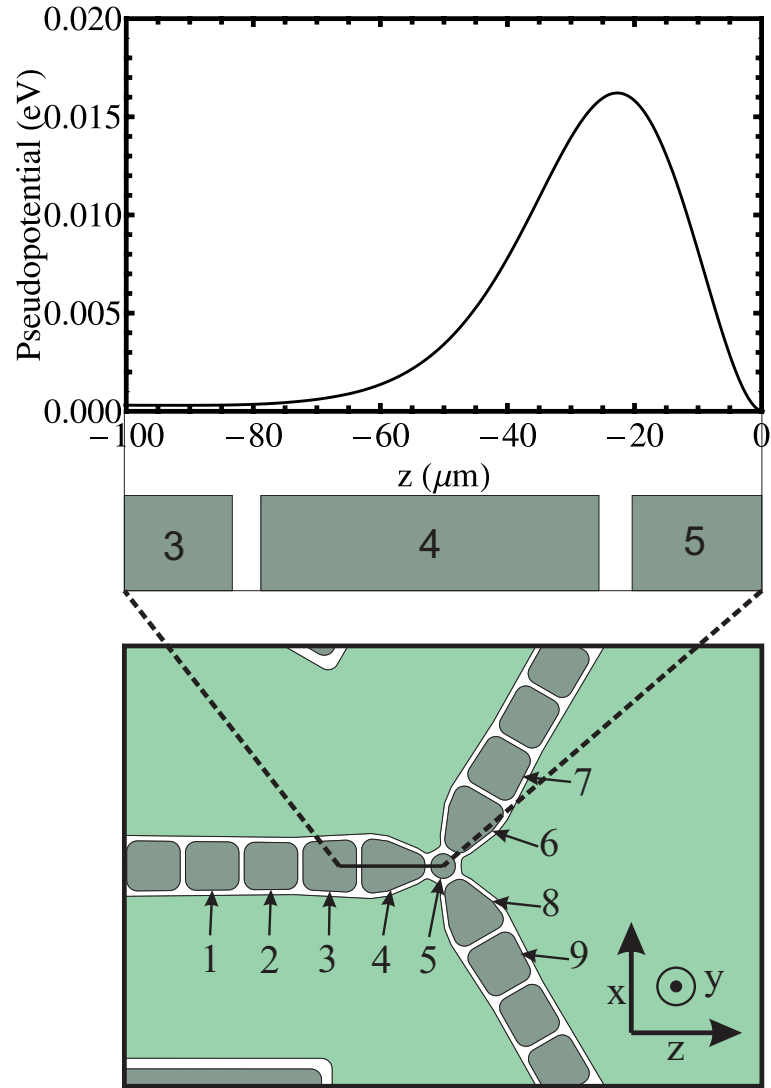


Figure 4.10: A plot of the rf pseudopotential together with the physical electrode geometry. With an applied voltage of 400 V at $\Omega_{rf}/2\pi = 30$ MHz the rf *barrier* has a maximum amplitude of ≈ 16 meV.

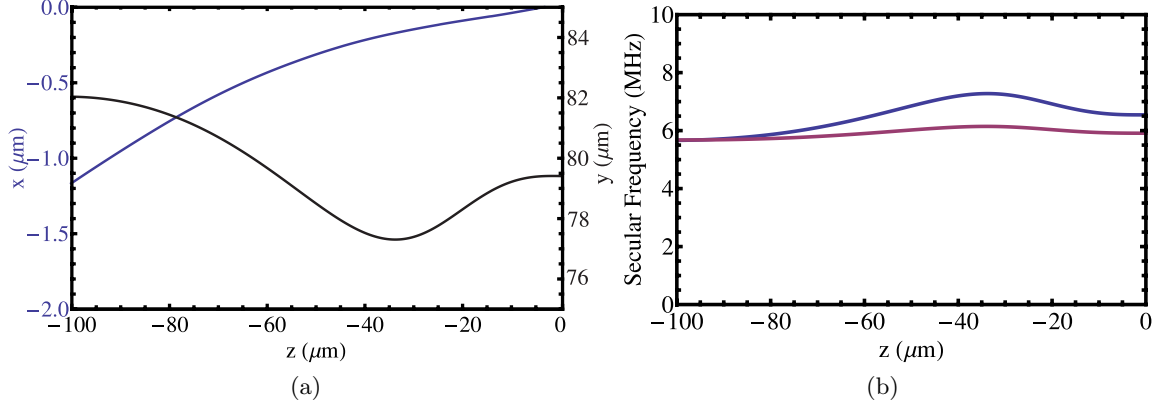


Figure 4.11: (a) Variations within the ion's radial position as a function of axial position. (b) Variation within the radial secular frequencies $\omega_x/2\pi$ (purple) and $\omega_y/2\pi$ (blue).

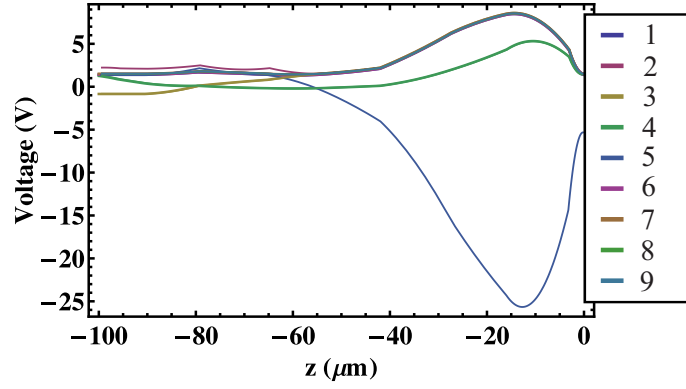
Interpolation function in Mathematica. A polynomial curve of defined order is fitted between each successive data point.

Hucul *et al.* [63] and Reichle *et al.* [89] have discussed the classical and quantum descriptions of the ion transport. Hucul *et al.* [63] also investigated different ion velocity profiles, these include linear, hyperbolic tangent and sinusoidal shown in fig. 4.13. The shuttling velocity profile requires a smooth transition at the start and end of transport as not to induce large ‘kicks’ onto the ion. The hyperbolic tangent function to shuttle ions, is defined as [63]

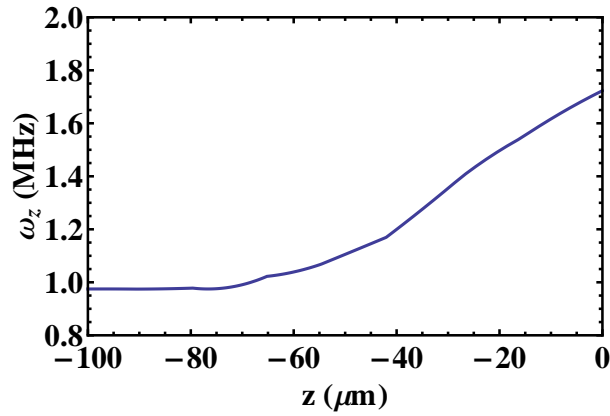
$$z_{0T}(t) = \frac{L}{2} \frac{(\tanh(N \frac{2t-T}{T}) + \tanh(N))}{\tanh(N)} (H(t) - H(t-T)) + LH(t-T) \quad (4.8)$$

where L is the total shuttling distance, t the instantaneous time, T the total shuttling time and $H(t)$ is the Heaviside step function. The hyperbolic tangent function provides a means to have a smooth start and end to the transport. The N -parameter provides a means to adjust the acceleration of the ion, values of N can be adjusted to produce similar profiles to linear ($N < 1$), sinusoidal ($N \approx 1$) and a step function ($N > 10$). The average motional state of the ion after the various velocity profiles have been analytically solved by Hucul *et al.* [63]. Their results show that a hyperbolic tangent function can shuttle an ion in the minimum amount of time for a given change in motional energy $\langle n \rangle$. The N parameter is varied according to the desired outcome.

To calculate the change in motional energy during transport I have extended the work



(a)



(b)

Figure 4.12: (a) Applied static voltages as a function of ion position $V_i(z)$ along the axial direction. The voltage on electrode 5 (centre of junction) is ramped to a negative value to ‘pull’ the ion over the rf *barrier*. (b) Variations in the axial secular frequency ω_z within the junction region from the applied voltages.

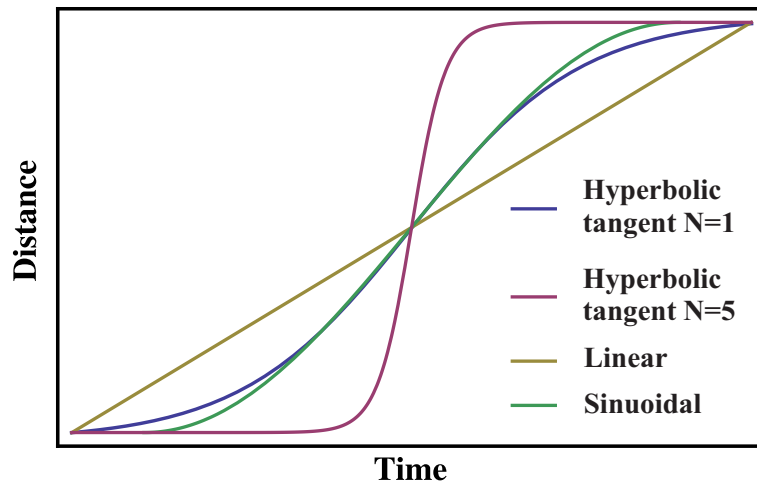


Figure 4.13: Various ion velocity profiles, hyperbolic tangent, linear and sinusoidal. The hyperbolic tangent N-parameter can be varied to achieve different profiles.

presented by Dr Altaf Nizamani [82] and have applied it to shuttling through the y-junction. The ion is considered to be cooled to ground state of motion within a quantum harmonic oscillator $\langle n \rangle = 0$. The kinetic energy of the ion is due to the secular motion in the rest frame of the pseudopotential [63]. The total gain in motional energy of the ion during transport is the sum of the change in kinetic energy and gain through anomalous heating [82].

$$\langle n \rangle = \langle n \rangle_s + \langle n \rangle_{an} \quad (4.9)$$

where

$$\langle n \rangle_s = \frac{\text{Final } K.E_{\max} - \text{Initial } K.E_{\max}}{\hbar\omega} \quad (4.10)$$

and

$$\langle \dot{n} \rangle_{an} \propto \frac{1}{\omega^2 \hbar^4} \quad (4.11)$$

Using the pseudopotential $\Psi(\chi, t)$ defined by equation 4.2 together with a classical treatment of the ion's motion, the force on the ion from the hyperbolic tangent function can be calculated [63].

$$\sum_j^3 m \ddot{\chi}_j + \nabla_j \Psi(\chi_j, t) = 0 \quad (4.12)$$

Using The NDSolve package in Mathematica, the differential equations can be solved and used to calculate the final kinetic energy of the ion. The time dependent voltage functions $V_i(t)$ is the combination of the position dependent voltages and the hyperbolic tangent velocity profile.

$$V_i(t) = V_i(z) \frac{L}{2} \frac{(\tanh(N \frac{2t-T}{T}) + \tanh(N))}{\tanh(N)} (H(t) - H(t-T)) + LH(t-T) \quad (4.13)$$

Using a hyperbolic tangent function together with $V_i(z)$ shown in 4.12 (a), theoretical shuttling protocol of the ion through the junction can be achieved. To demonstrate theoretical shuttling the ion is first confined in one of the arms, 80 μm from the junction. By applying the time dependent voltage functions $V_i(t)$ the ion is shuttled into the centre of the junction. Using the symmetry of the junction region, the voltage profiles are mapped onto the corresponding electrodes to shuttle the ion into a different arm. An N-parameter of 4 was selected together with varying the total shutting time T, the gain in kinetic energy during shuttling is then investigated. Fig. 4.14 shows the time dependent voltage functions to shuttle the ion along path *a-c-d*.

The kinetic energy of the ion is calculated using the numerical NDSolve package in Math-

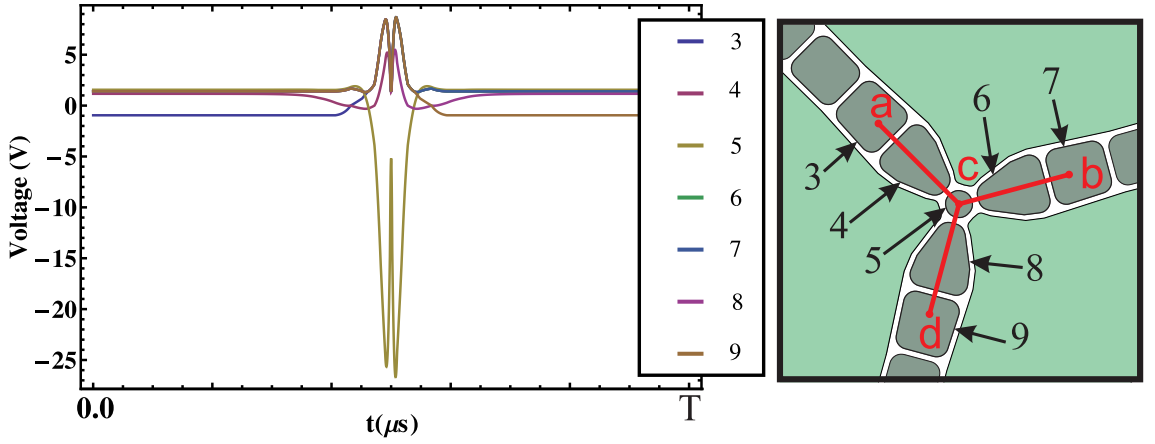


Figure 4.14: Voltage functions to shuttle the ion along path a - c - d . A hyperbolic tangent velocity profile with N-parameter of 4 was selected.

emata. The ion is assumed to be cooled to the motional ground state with $\langle n \rangle = 0.05$. The kinetic energy of the ion during transport calculated from numerical simulation is shown in fig. 4.15 for a total transport time $T = 300 \mu s$.

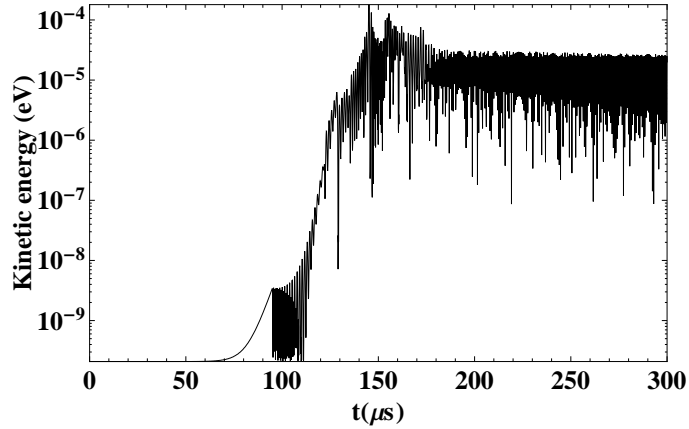


Figure 4.15: Simulated gain in kinetic energy of the ion during transport through the junction with a total shuttling time of $T = 300 \mu s$.

The gain in energy due to anomalous heating during transport will depend on many factors as shown within the spread of data from fig. 2.12. Assuming an electric field noise spectral density $S_E(\omega)$, given by the trend line in fig 2.12, provides an expression for the anomalous heating in terms of secular frequency ω_z an ion-electrode distance d given by,

$$\langle \dot{n} \rangle_{an} \simeq \frac{4.3 \times 10^{24}}{\omega_z(t)^2 d(t)^4} \mu m^4 Hz^3 \quad (4.14)$$

where d is in micrometers. By integrating the above expression over the total shuttling

time T , the gain in motional quanta $\langle n \rangle_{an}$ from anomalous heating can be calculated taking into account the variation in ion height and secular frequency during transport by,

$$\langle n \rangle_{an} = \int_0^T \langle \dot{n} \rangle_{an} dt \quad (4.15)$$

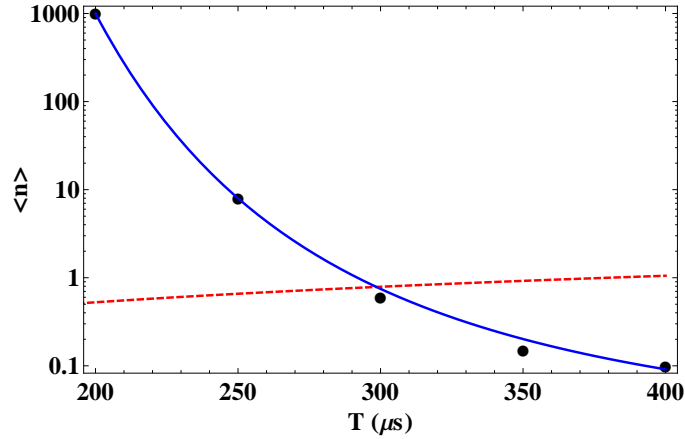


Figure 4.16: Gain in kinetic energy of the ion for various shuttling times T using an $N=4$ hyperbolic tangent velocity profile. The red dashed curve represents the gain in motional quanta from anomalous heating during the shuttling process. The crossing point between the best fit of the data and anomalous heating determines the speed of shuttling whilst minimising the total gain in motional quanta.

The gain in kinetic energy represented in terms of average motional quanta for various shuttling times T , is shown in fig. 4.16. The crossing point with the gain in motional quanta due to anomalous heating shown by the red dashed line, determines the maximum speed of shuttling whilst minimising the total gain in motional quanta during the shuttling protocol. For $T = 300 \mu s$ this produces an $\langle n \rangle \approx 1.6$.

Without the experimental implementation of the shuttling procedure, the exact gain in motional energy is unknown, with the possibility of additional motional excitation arising from the static control voltage supply [153]. However anomalous heating plays a significant role in the implementation of adiabatic shuttling through junctions and methods have been employed to reduce its effect from cryogenic cooling [120, 131] to cleaning techniques [134, 135].

As the ion passes through the centre junction there is a sudden change in the applied voltages. This will limit the speed of shuttling with the physical application of the voltages. Digital-to-analog converters (DACs) supplying the voltages will have a defined update rate

and low pass filters needed to filter out noise at the secular frequencies set a physical limit on the speed of shuttling.

4.6 Two-dimensional ion trap arrays

Ion trap architectures are an important tool in the development of quantum simulators [24, 26, 28, 55, 159, 160], especially in the investigation of complex spin systems [53, 161, 162]. To go to such systems requires the expansion from trapped linear chains of ions to two-dimensional (2D) arrays. The first steps in achieving this was demonstrated by trapping ions in a mechanically fabricated metal mesh [27] and the demonstration of a 2D triangular lattice within a Penning trap [55]. The use of microfabrication techniques [163] allows the realisation of large 2D ion trap arrays.

The design of the 2D ion trap array presented in this section is based on the optimisation of two-dimensional ion trap arrays by James Siverns *et al.* [56]. The geometry is optimised for the ratio of highest ion-ion interactions to decoherence rate in a hexagonal lattices by optimising the lattice parameters. However at the time of designing the hexagonal array presented within this section, the full optimisation method was not available and the constraints on α , (ratio of rf voltage to drive frequency) from possible coupling schemes were not considered. I will therefore present the design as an example case study in the summary of the initial optimisation method with more details presented in [56].

4.6.1 Ion-ion interactions and lattice geometry

Trapped 2D array of ions can be used to study complex spin-1/2 systems [161], the interactions between neighboring ions within a harmonic trapping potential $F_T = -m\omega_i^2$ is due to the Coulomb force $F_C = -e^2/4\pi\epsilon_0 A^2$. When this is small compared to the trapping potential, the coupling rate is given by [161]

$$J = \frac{\beta F^2}{m\omega^2} \quad (4.16)$$

where

$$\beta = \frac{e^2}{2\pi\epsilon_0 m\omega^2 A^3} \quad (4.17)$$

F is the magnitude of the state dependent force, m the mass of the ion, ω the secular

frequency and A is the ion-ion spacing. β is the ratio in the change in Coulomb force to the restoring force. When $\beta < 1$, which is possible for an array of microtraps, the interaction decays rapidly over the array allowing for short range interactions to occur.

Although an ion's internal states can be preserved for tens of seconds [164, 165] the decoherence of the motional states due to anomalous heating (section 2.5) will be an important factor with the coupling between the motional states. By defining the ratio of decoherence time to coupling time as [56]

$$K_{sim} = \frac{T_{\dot{n}}}{T_J} \quad (4.18)$$

where $T_J = 1/J$ and $T_{\dot{n}} = 4m\omega\hbar/e^2S_E(\omega)$. The case where $K_{sim} > 1$ an interaction occurs faster then the decoherence and an interaction is observable. By scaling down an array therefore bringing individual trapping sites together allows for stronger interactions between sites but in turn decreases the ion height, h . With anomalous heating scaling $\sim 1/h^4$ [119, 120] it is advantageous to trap the ion far above the surface. By varying the geometry to bring the individual trapping sites together but maintaining the ion height, causes the individual trapping regions to overlap when the separation is less than twice ion height [152]. Schmied *et al.* have created an algorithm that maximises the curvature of individual trapping sites for arbitrary ion heights and separation. The results produces non-intuitive electrode geometries [152, 166] that contain isolated electrodes. An alternative proposal [167] uses adjustable rf electrodes between trapping sites to reduce the ion-ion distance increasing the interaction, but complicates the experimental infrastructure.

A single continuous rf electrode reduces the need for many buried rf wire connections, keeping the trap capacitance low. Types of lattice geometries include square, centered rectangular and hexagonal. The lattice geometry selected within this work is a hexagonal lattice with each ion having six nearest neighbours, shown in fig 4.17. The optimisation of the all these geometries has been presented [56] and I will focus on the results obtained for the hexagonal lattice which will then be used to create a finalised design.

Through varying the parameters of the array, K_{sim} can be maximised and thus provides an optimum geometry. K_{sim} can be expressed in terms of the geometry variables as [56]

$$K_{sim} = \frac{4F^2mr^8}{\Xi\alpha^2\eta_{geo}^2\pi\epsilon_0A^3} \quad (4.19)$$

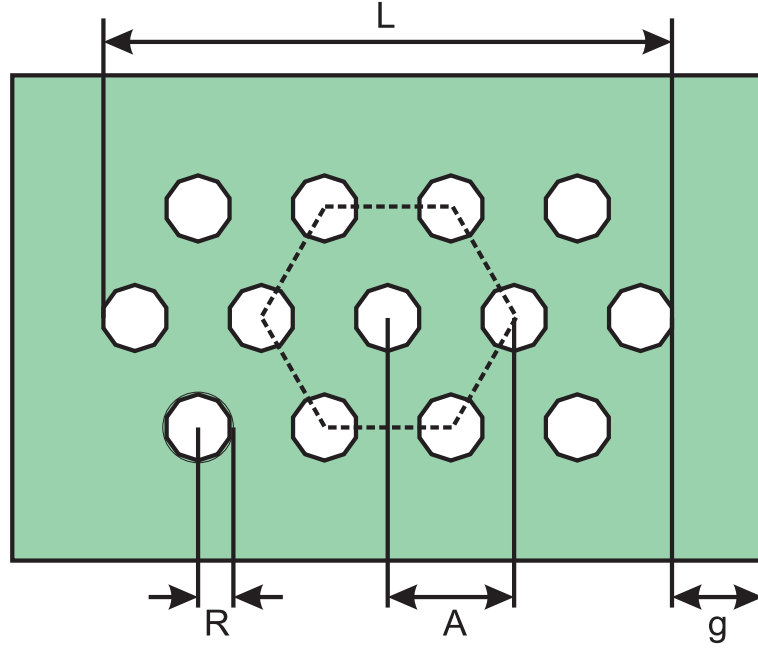


Figure 4.17: A hexagonal arrangement of an ion trap lattice. Each site is defined by a polygon of radii R , the separation between the centres of the polygons A , and g the distance to the edge of the rf from the outer ion site.

where

$$\alpha = \frac{V_{rf}}{\Omega_{rf}} \quad (4.20)$$

r is the ion height, Ξ is a scaling coefficient of the anomalous heating, η_{geo} is the geometric efficiency factor which defines how the generated potential varies from the ideal quadrupole potential [60]. α is defined as the ratio of the applied rf voltage V_{rf} to drive frequency Ω_{rf} . The secular frequency of a trapped ion can be expressed as [60]

$$\omega = \frac{e\alpha\eta_{geo}}{\sqrt{2}mr^2} \quad (4.21)$$

4.6.2 Simulation

Simulation of the electric field produced from a lattice geometry is carried out using the Biot-Savart like law by Oliveira and Miranda [91], an analytical method using a gapless plane approximation. The electric field is calculated at a given position, \bar{X} , of an arbitrary shape held at a voltage V whilst every where else is grounded through the following closed line integral [91]

$$E(\bar{X}) = \frac{V}{2\pi} \oint_C \frac{(\bar{x} - \bar{x}') \times d\bar{s}}{|\bar{x} - \bar{x}'|^3} \quad (4.22)$$

where C is the closed loop around the perimeter of the electrode, \vec{x} and \vec{x}' are the vectors to the source point and field point respectively.

Using the numerical Gauss-Newton algorithm, the trap parameters can be calculated including the ion's position, secular frequency and trap depths at each position within the array. This method was compared to analytical equations presented by House [93], it was shown using this method a maximum K_{sim} error of 10% is obtained [56]. Results were also compared to numerical BEM simulations showing similar results.

4.6.3 Optimisation method

Homogeneity of the array

The homogeneity across the array is an important parameter, spin couplings that are dependent on lattice position results in problems with the scalability of such systems [168]. By varying the distance from the outer polygon to the edge of the rf electrode g , the homogeneity across the array can be maximised. It is convenient to express g in terms of the total length of the lattice L , shown in fig. 4.17 as

$$L = (M - 1)A + 2R \quad (4.23)$$

where M is the number of lattice sites in a given row. The maximum homogeneity is dependent on the total number of lattice sites. For hexagonal lattices the optimum ratio of g/L as a function of total number of lattice sites N , is given by [56]

$$g/L = (0.39 \pm 0.01) + (3.76 \pm 1.40)N^{-(0.54 \pm 0.14)} \quad (4.24)$$

A hexagonal lattice with $N = 22$ sites is selected due to maximum number sites possible with the available static control electrodes. For $N = 22$ a maximum homogeneity occurs when $g/L \approx 1.1$.

Method

A circular geometry [92, 94, 152, 169] of each lattice site offers maximum curvature of the electric potential, required for highest K_{sim} values. But in order to reduce computational time when performing the simulations the number of sides was set to 25 to achieve approximately 95% of the maximal achievable K_{sim} [56].

For a fixed geometry the lowest K_{sim} value is obtained when α is a minimum, however in doing so the trap depth is also minimised. By setting a limit of 0.1 eV for the lowest usable trap depth provides a maximum K_{sim} for a given geometry. The trap depth given by equation 4.4 can be re-expressed in terms of alpha as

$$T_D = \frac{\zeta e^2 \alpha^2}{\pi^2 m} \quad (4.25)$$

where ζ is the geometric efficiency factor that is dependent on A and R [93]. This sets a limit on the α used for a given geometry. K_{sim} is calculated for different polygon separation, A and polygon radius R, with a resolution of 1 μm . A contour plot is produced observing how these parameters vary with the calculated K_{sim} , shown in fig. 4.18. When a particular geometry is considered there should be no inter-well barriers less than the minimum trap depth, leading to a single trapping zone [152]. By setting polygon radius to less than a third of the separation ensure this situation is avoided. For each combination of polygon separation and radius, α is calculated for a minimum trap depth and therefore K_{sim} is maximised.

From fig. 4.18 a maximum K_{sim} value is achieved when R, A and α tend towards infinity,

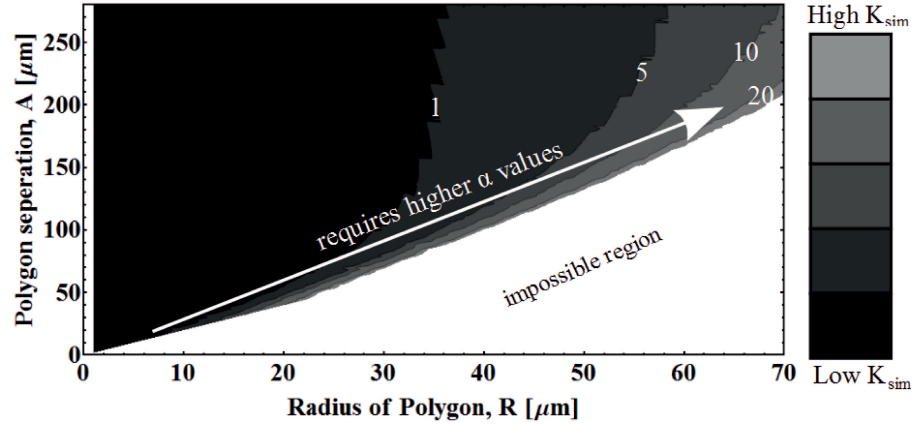


Figure 4.18: Example contour plot of K_{sim} values for various polygon separations and radii. As the polygon radius and separation increase, so does α and K_{sim} . The lower bounded impossible region describe geometries in which the individual trapping sites start to merge into a singular trapping zone. This region describes when the polygon radius, R is greater than or equal to a third of the polygon separation, A.

however there will be a limit on the α selected. For optimum geometries, the ion height, separation and radius can be expressed purely in terms of linear relationships of α as,

$$r = k_r \alpha \quad (4.26)$$

$$A = k_A \alpha \quad (4.27)$$

$$R = k_R \alpha \quad (4.28)$$

The values of k_r , k_A and k_R , are dependent on the number of trapping sites and lattice type. For an optimum geometry, which depends only on α , using equation 4.26 the secular frequency from equation 4.21 can be re-expressed as

$$\omega = \frac{e\eta_{geo}}{\sqrt{2}k_r^2 m \alpha} \quad (4.29)$$

and K_{sim} from equation 4.19 re-expressed as

$$K_{sim} = \frac{4F^2 m k_r^8 \alpha^3}{\Xi \eta_{geo}^2 \pi \epsilon_0 k_A^3} \quad (4.30)$$

For optimal geometries K_{sim} is proportional to α^3 and for a given number of lattice sites, a larger alpha in turn produces a greater ion height and separation. The heating rate scaling as $1/r^{-4}$, does not affect the geometry of an optimised array, however there will be limit on the ion height due to the coupling scheme used to drive interactions. An upper limit on α due to the error of a quantum simulator is discussed in ref [56] in more detail for a complete optimisation process.

4.6.4 Lattice design

No interaction scheme was considered in selecting a specific α and lattice geometry. Instead a proof of principle large scale hexagonal lattice is presented. To reduce the effect of anomalous heating but still provide sufficient trap depth, an ion height of $\approx 182 \mu\text{m}$ was selected. With up to 90 individual control electrodes available for the lattice to be compatible with both vacuum systems, by assigning 4 electrodes per lattice site for flexibility in control of each ion allows for an array of up to 22 sites. From the results obtained in the previous section a design was constructed to provide homogeneity across the array maximising K_{sim} for a given α . A minimum trap depth of 0.1 eV is achieved together with a q stability parameter of 0.7 with a drive frequency of $\Omega_{rf}/2\pi = 35 \text{ MHz}$ and voltage of 542.5 V, providing an α of 2.5 V/MHz. A hexagonal lattice shown in fig. 4.19 was designed with the trap parameters presented in table 4.1.

A $\beta \approx 2.9 \times 10^{-6}$ is calculated together with a $K_{sim}/F^2 \approx 2.4 \times 10^{37} \text{ N}^{-2}$. The electric field

# of sites	ion height r (μm)	ion separation A (μm)	Polygon radius R (μm)	α (V/MHz)	β	K_{sim}/F^2 (N^{-2})
22	182	386	72	2.5	2.9×10^{-6}	2.4×10^{37}

Table 4.1: List of parameters for the hexagonal ion trap lattice.

noise spectral density was estimated with the trend line in fig. 2.12 producing a motional heating rate of $\dot{n} \approx 400$ Hz. By considering interactions between lattice sites with a state dependent force F produced with lasers, a value for K_{sim} can be estimated. The state dependent force produced by a laser can be defined as [56]

$$F = \frac{2\pi\hbar P\gamma^2}{3a\Delta\lambda I_{sat}} \quad (4.31)$$

where γ is 2π times the transition linewidth, I_{sat} is the saturation intensity of the ion, λ the laser wavelength with detuning from resonance of Δ . P is the power of the laser and a , the area of the light sheet. To maximise coupling between two ions, the laser beam will be focused down to a $30 \mu\text{m}$ beam waist. A laser at 355 nm with $\Delta = 33 \text{ THz}$, minimising the effect of spontaneous emission [170] and $P = 24 \text{ W}$ is considered. This provides a $K_{sim} \approx 1.4$ and a coupling rate, $J \approx 565 \text{ Hz}$. Reducing the decoherence rate by operating at cryogenic temperatures [120, 131] and cleaning techniques [134, 135], has each shown to reduce anomalous heating by up to two orders of magnitude. Implementing these techniques would allow for a higher K_{sim} .

A BEM simulation of the hexagonal lattice is performed, with an applied voltage of $V_{rf} = 542 \text{ V}$ at a drive frequency of $\Omega_{rf}/2\pi \approx 35 \text{ MHz}$, provides a trap depth of $\approx 0.1 \text{ eV}$ and calculated stability parameter $q \approx 0.7$. This is in agreement of the optimised geometry produced with the Biot–Savart like method.

The pseudopotential within the different axes of the traps are shown in fig. 4.20. A cut through the traps y-axis at the ion height of $182 \mu\text{m}$ shows the individual trapping sites, the trap depths of the lattice is $\approx 0.1 \text{ eV}$.

Electrical characteristics

With the given geometry shown in fig.4.19 an estimate on the traps resistance and capacitance can be made. The buried wires have a diameter of $3 \mu\text{m}$ and an average length

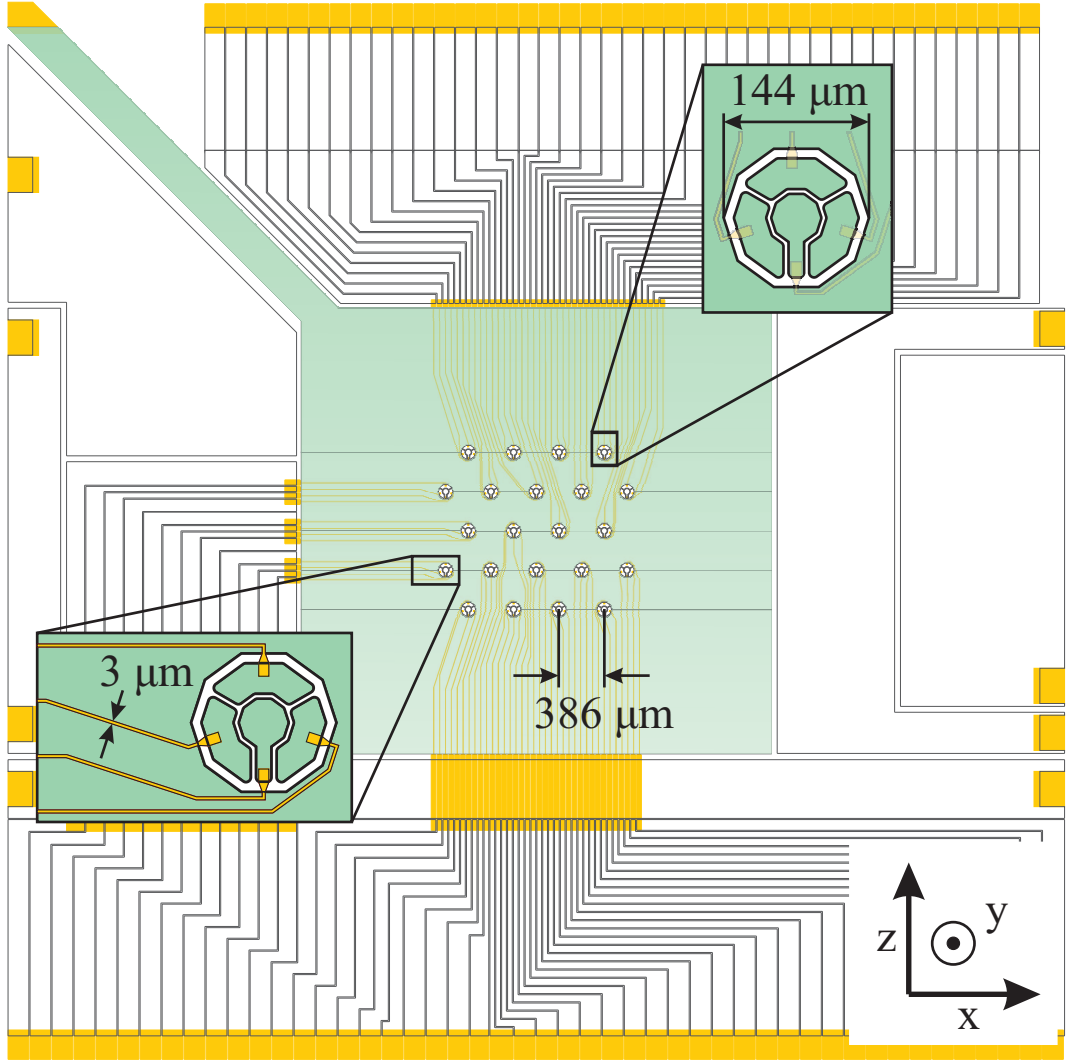


Figure 4.19: Hexagonal lattice with 22 individual trapping sites. The rf electrode is shaded blue and the buried wires yellow. Each lattice site has 4 control electrodes and is arranged such that the ion is not in direct sight of the dielectric layer. The buried wires providing electrical connections are $3\ \mu\text{m}$ and $\approx 1\ \text{mm}$ in length.

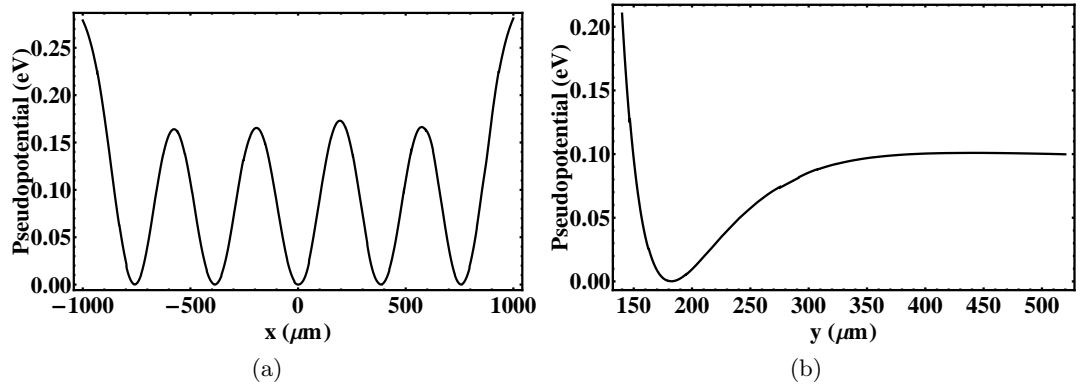


Figure 4.20: Pseudopotential of the lattice trap. (a) Cut through the trap at $z = -335\ \mu\text{m}$ at the ion height $r = 182\ \mu\text{m}$. (b) The trap depth of each lattice site is set to a minimum $\approx 0.1\ \text{eV}$ to maximise K_{sim} .

of ~ 1.0 mm with a total of $N = 88$ wires. An estimated capacitance $C_{Lattice} \approx 7$ pF resistance $R_{Lattice} \approx 0.3 \Omega$ of the trap is calculated. A dissipated power of ≈ 0.1 W is estimated with the applied voltage of $V_{rf} = 542$ V and drive frequency of $\Omega_{rf}/2\pi = 35$ MHz.

4.7 Ring ion traps

Trapped ions have demonstrated quantum simulations including the Dirac equation [171], Klein Paradox [159] and magnetic spin frustration of a few ions [28, 172], together with similar experiments extending to 16 ions within a linear chain [54, 173, 174]. Scaling up to more complex and larger ion chains within a harmonic trapping potential causes problems, as the number of ions is increased the ratio of radial to axial confinement is reduced, causing zigzag structures to form [175]. To overcome this, one may engineer anharmonic trapping potentials [176] to confine larger linear chains, another method is to consider a ring ion trap with periodic boundary conditions [177, 178].

A ring ion trap architecture can be created through wrapping a linear ion trap around on itself, this allows for true periodic boundary conditions and the creation of an effective rf nodal toroid. A higher density of ions can be achieved [179] as well as studying situations where boundary conditions provide unwanted problems including dispersion and reflections, such as spin waves [180]. Ring ion traps also provide the possibility to simulate Hawking radiation [181, 182].

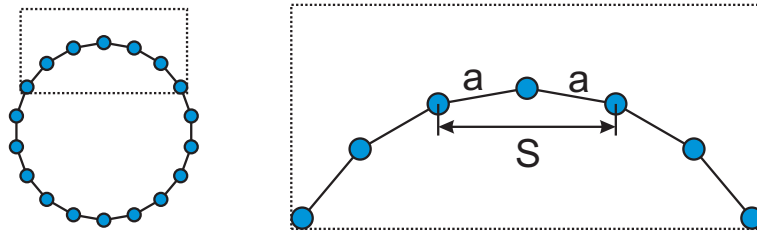


Figure 4.21: A ring arrangement of 18 ions, a is defined as the ion-ion spacing and S the spacing to the next nearest ion.

The ion-ion spacing is purely dependent on the number of ions stored and the geometry of the ring shown in fig 4.21. A constraint with ring ion traps is how small can they be designed, it is desirable to have each ion in an effective linear arrangement with interactions from nearest neighbour (NN) and next nearest neighbour (NNN) to be equivalent of a

linear ion trap [183]. The ratio of the NNN and NN interactions can be calculated from the Coulomb interaction, for more than 12 and 38 ions this interaction is less than 10% and 1% respectively bigger than the linear arrangement [183]. Defining a as the ion-ion spacing, through simple geometric analysis the distance to the next ion is defined as [183]

$$S = a \left[2 + 2\cos\left(\frac{2\pi}{n}\right) \right]^{1/2} \quad (4.32)$$

4.7.1 Ring designs

To provide greatest flexibility, two ring ion trap designs with different radii are designed, these are denoted as ‘big’ ring with a radius of 1688 μm , shown in fig. 4.22 and ‘small’ ring with a radius of 486 μm , shown in fig. 4.24.

To be compatible with the fabrication process requires buried wires to connect the two rf ring electrodes. The buried wires are designed such that there is a trade off between the increased capacitance and resistance of the ion trap circuit. It is also important to keep the impedance between the two rf ring electrodes low as not to induce a phase difference, inducing intrinsic micromotion. With the constraints on the buried wires having thickness of 0.5 μm and a dielectric thickness of 2 μm , the estimated phase difference can be calculated. The total phase difference will be the sum of the difference in impedance and path lengths given by

$$\phi_{imp} = \arctan\left(\frac{X}{R}\right) \quad (4.33)$$

and

$$\phi_{path} = 360^\circ \left(\frac{\Delta L}{\lambda} \right) \quad (4.34)$$

X is the reactance and assuming negligible inductance is defined solely by the capacitive term as $X = -\frac{1}{\Omega C}$, R is the resistance of the buried electrode. The rf phase difference of the ‘big’ ring will be higher due to the physical geometry, the estimated capacitance and resistance of the buried rf wire is ≈ 0.12 pF and ≈ 0.2 Ω respectively. With a drive frequency of $\Omega_{rf}/2\pi = 25$ MHz an estimated phase difference of $\phi_{imp} \approx (6 \times 10^{-4})^\circ$. An additional phase difference will result from the difference in path length difference between the buried wires, with a length of 215 μm will result in a phase shift of $\phi_{path} \approx 0.01^\circ$. The total phase difference is small and is not expected to produce a significant amount of intrinsic micromotion, inhibiting Doppler cooling of the ions.

‘Big’ ring

Scaling up a ring ion trap array, provides a greater approximation to a linear ion trap and greater storage capabilities. With a fixed number of control electrodes, as the ring ion trap radius is increases the ion height will increases as well. A larger ion height allows for the reduction of anomalous heating and reduced scatter from the laser beams clipping the electrode surface. The induced charging of electrode surfaces [184] will displace the ions’ position and induce micromotion. Also perturbations of the electric field from opposite electrodes in the ring will be minimised. Setting an upper limit on the ion height of 250 μm together with a maximum applied rf voltage of $V_{rf} = 400 \text{ V}$ will still allow for a sufficient trap depth for successful trapping.

The electrode geometry is based on an optimised uneven rf rail design (section 4.4) for maximum trap depth whilst being able to rotate the principal axes. An ion height of 245 μm is selected, together with 58 centre static control electrodes with a width of 175 μm . A separation of 5 μm between the centre electrodes yields an ion radius of 1688 μm and a circumference of $\approx 10.6 \text{ mm}$. The complete design is shown in fig. 4.22.

From numerical simulations, an applied rf voltage of $V_{rf} = 400 \text{ V}$ at a drive frequency of $\Omega_{rf}/2\pi = 25 \text{ MHz}$, produces a trap depth of $\approx 0.15 \text{ eV}$ and radial secular frequencies of $\omega_x/2\pi = 757 \text{ KHz}$ and $\omega_y/2\pi = 836 \text{ KHz}$ at $(x = 1688 \mu\text{m}, z = 0 \mu\text{m})$

With the given geometry shown in fig. 4.19 an estimate on the traps resistance and capacitance can be made. The buried wires have a diameter of 3 μm and an average length of $\sim 900 \mu\text{m}$ with a total of $N = 59$ wires. An estimated capacitance $C_{Bring} \approx 4 \text{ pF}$ and resistance $R_{Bring} \approx 1 \Omega$ of the trap is calculated. A dissipated power of $\approx 32 \text{ mW}$ is then estimated.

An additional consideration is the induced rf *barrier* from the outer rf connecting wire. This will not create an ideal rf nodal toroid perturbing the ions’ motion around the ring. To see the effect of the rf wire an analytical simulation using the Biot-Savart like law method [91] together with the numerical Gauss Newton algorithm is used to calculate the pseudopotential minimum around the ring. This is shown in fig 4.23. A peak potential *barrier* of $\approx 2.8 \times 10^{-6} \text{ eV}$ is simulated and is shown to be symmetric about the outer rf wire.

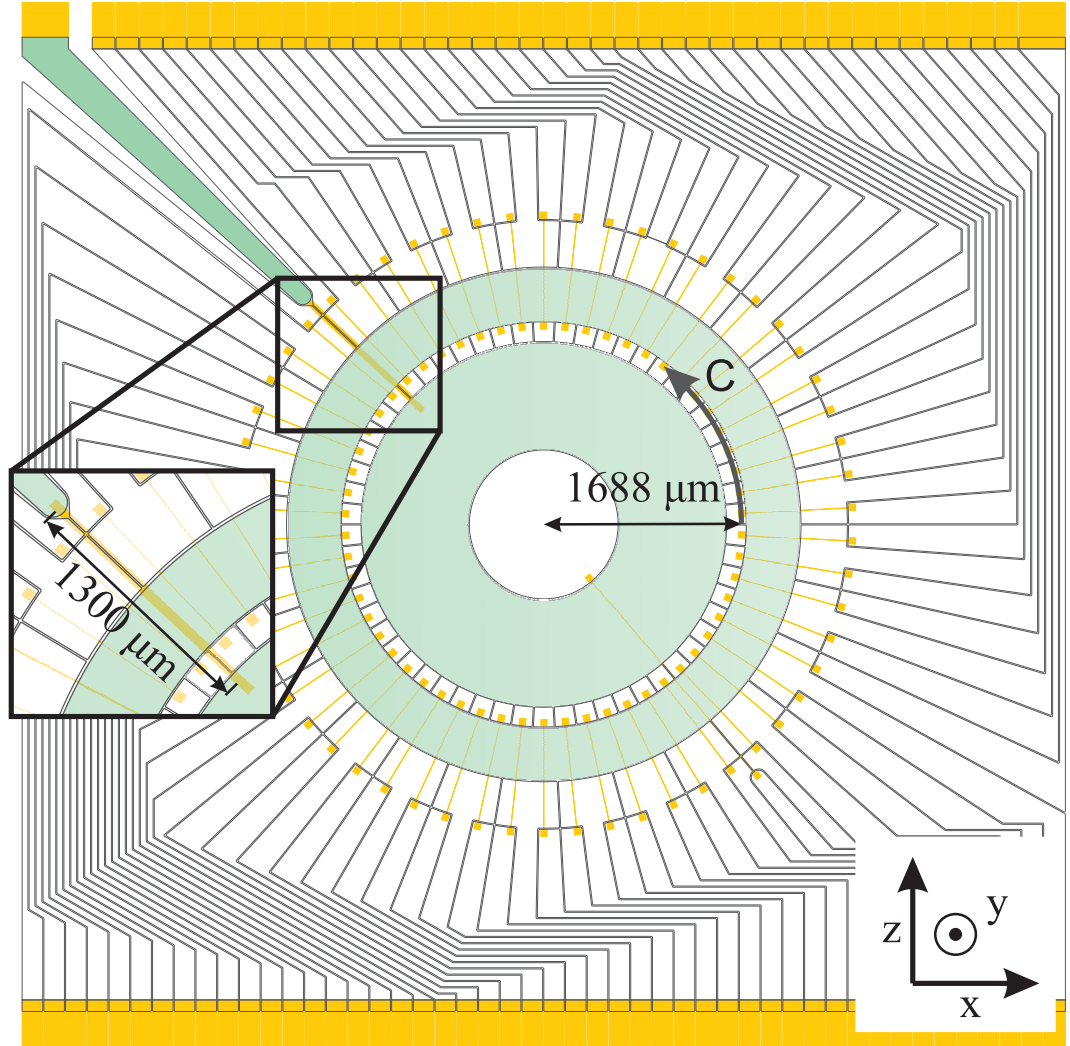


Figure 4.22: Complete design of the ‘big’ ring ion trap, the rf electrode is shaded blue and the buried wires yellow. An ion height of $\sim 250 \mu\text{m}$ is selected together with a radius of $1688 \mu\text{m}$. Shown in the insert the rf electrodes are connected via a buried wire of dimensions $(1300 \text{ by } 50) \mu\text{m}^2$.

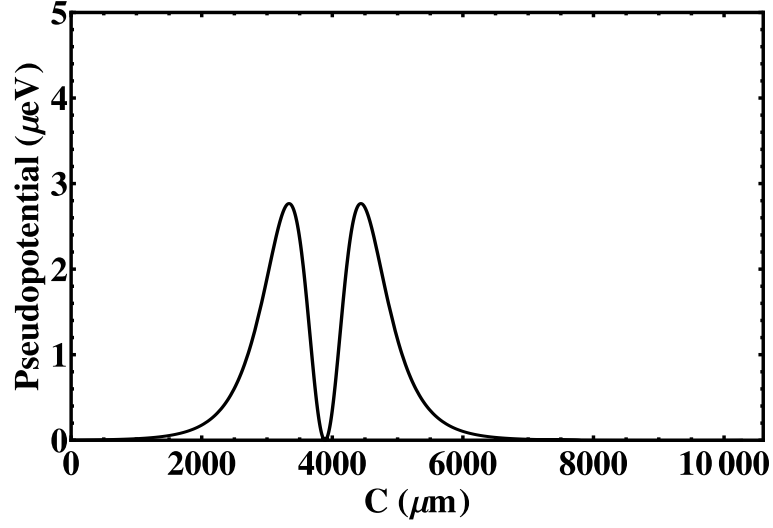


Figure 4.23: Pseudopotential minimum as a function of ion position C , around the circumference of the ring trap. An rf *barrier* is present from the outer rf wire.

‘Small’ ring

Reducing the physical dimensions of a ring trap can be advantageous, one key feature of a ring ion trap is the ability to have periodic boundary conditions within an ion chain. A smaller ring circumference allows for fewer ions to fill the ring for a given ion-ion spacing. This reduces the running of the atomic ovens when loading, reducing the coating and charging of the electrodes. A smaller ring ion trap will also allow for the imaging of the whole ring whilst maintaining a higher resolution. This enables individual detection of ions on a CCD array [185] for a smaller ion-ion spacing. Setting a lower limit on the ion height of $\sim 100 \mu\text{m}$ will enable the operation of the trap without anomalous heating and laser scatter posing a problem.

The smaller ring design is based on the design in fig. 4.8 with even rf electrodes and additional static control rails to provide rotation of the principal axes. The complete ring design is shown in fig. 4.24. From simulations and ion height of $98 \mu\text{m}$ is calculated. The width and separation of the rf electrodes is optimised for maximum trap depth, two centre rotation rails together with a bias voltage on the centre static and outer control electrodes will provide rotation of the principal axes. An applied voltage of $V_{rf} = 400 \text{ V}$ at a drive frequency of $\Omega_{rf}/2\pi = 30 \text{ MHz}$ will produce a trap depth of $\approx 0.6 \text{ eV}$.

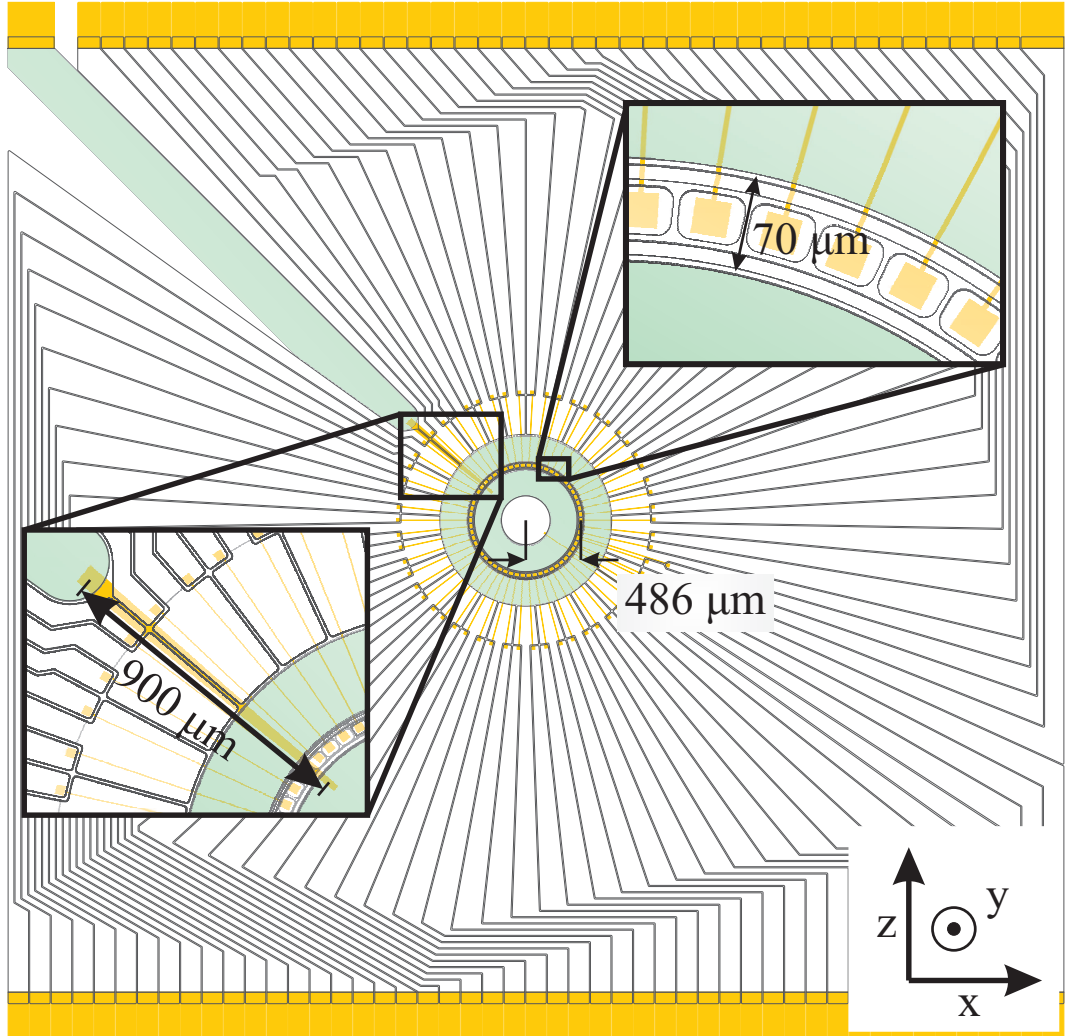


Figure 4.24: Complete design of the 'small' ring ion trap, the rf electrode is shaded blue and the buried wires yellow. An ion height of $\sim 98 \mu\text{m}$ and a radius of $486 \mu\text{m}$ is selected. Shown in the insert the rf electrodes are connected via a buried wire of dimensions $\approx (900 \text{ by } 25) \mu\text{m}^2$.

The total trap capacitance and resistance is estimated to be $C_{Sring} \approx 2$ pF and $R_{Sring} \approx 1$ Ω respectively, with half the total resistance resulting from the buried rf wire. A dissipated power of ≈ 11 mW is estimated from equation 4.1.

4.8 Linear ion trap

To achieve high fidelity gates, the anomalous heating (section 2.5) must be sufficiently suppressed. To date, asymmetric ion traps have only demonstrated entanglement with the aid of cryogenic cooling [186, 187], by going to a large ion height will help reduce anomalous heating with a scaling of $\sim 1/d^4$ [119, 120]. An ion height of ≈ 220 μm was selected and is based on the symmetric design with additional principal axes rotation electrodes [79], shown in fig. 4.8, with 41 individual trapping zones the finalised geometry is shown in fig. 4.25.

Through an applied drive voltage $V_{rf} = 400$ V and drive frequency of $\Omega_{rf}/2\pi = 25$ MHz produces a simulated trap depth of ≈ 0.15 eV, radial secular frequencies $\omega_{rad}/2\pi = 1.0$ MHz and q stability parameter of ≈ 0.1 . The total trap capacitance and resistance is estimated to be $C_{linear} \approx 2$ pF and $R_{linear} \approx 0.2$ Ω with produces a dissipated power of ≈ 2 mW.

The centre segmented electrodes allow for great flexibility, with the ability to create ions in individual harmonic wells [188] [189] and the generation of an anharmonic potential within the axial direction to produce even spacing within long ion chains [176].

4.9 Photolithography mask design

A mask set is needed in order to transfer the details of the trap electrodes during fabrication using photolithography techniques (section 5.2). After the designs are finalised, the information of each layer needs to be transferred to a photolithography mask. These are a patterned chrome layer on glass, transparent to UV light. The mask designs can be designed with AutoCAD to produce a .dxf file but the final file needs to be in gdsII format.

A collaboration with the University of Nottingham was setup to allow for the fabrica-

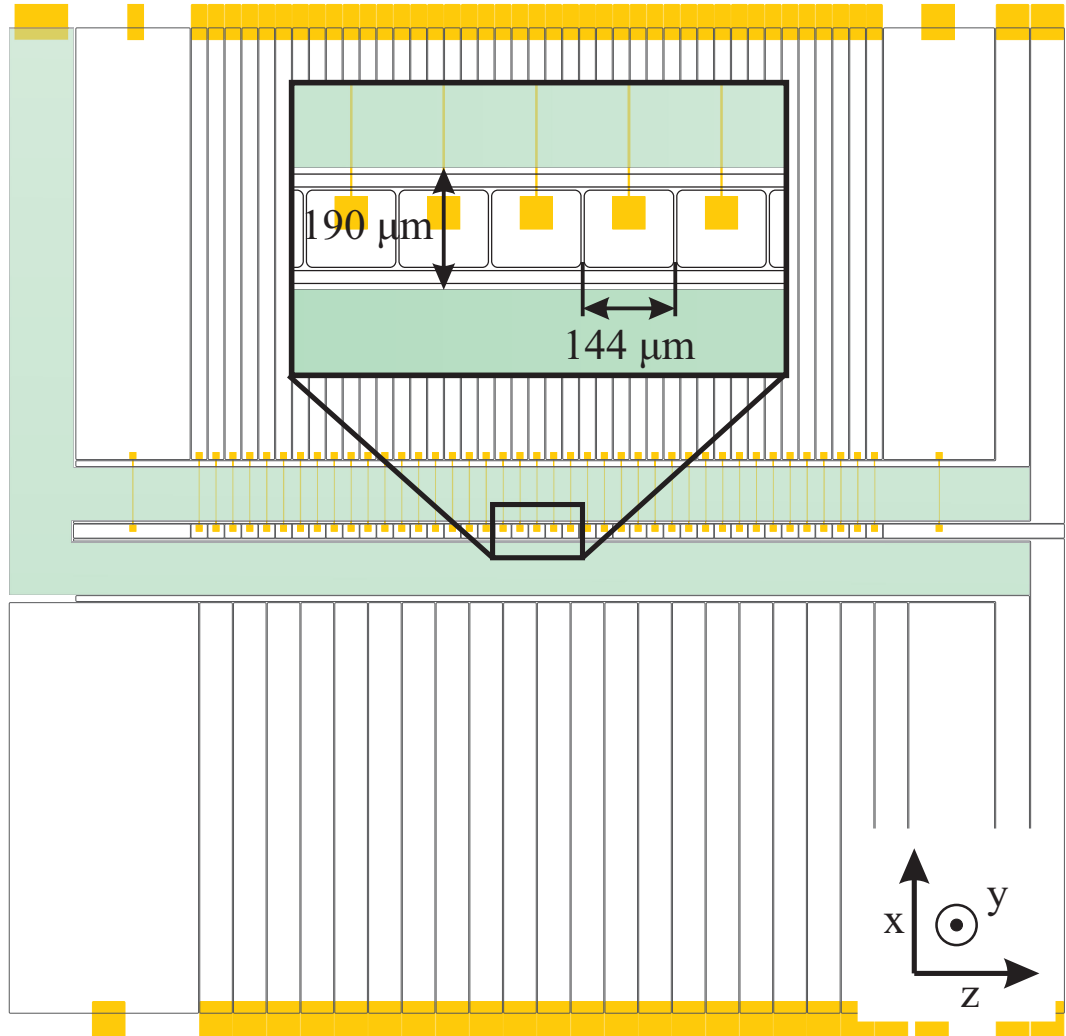


Figure 4.25: Full design of the linear ion trap, the rf electrode is shaded blue and the buried wires yellow. An ion height of $\sim 220 \mu\text{m}$ is selected to reduce the affects of anomalous heating, 70 individual control electrodes provide control of the ion in 41 individual trapping zones.

tion of the traps with initial discussions involving sending early trap designs for feedback. Barnard Microsystems Limited Wavemaker software² was used by Nottingham allowing them to import .dxf files, but guidelines with drawing had to be considered for the file to be combatable when converting gdsII format.

Within AutoCAD the following guidelines needs to be in place before drawing the mask. GDSII is an integer based format and AutoCAD is a double precision, it is therefore necessary to draw the designs to a grid. Using the ‘Snap Mode’ within AutoCAD the electrodes can be drawn to a grid. AutoCAD is dimensionless, the lengths of the objects are drawn to the desired micron scale where one unit is set to be equivalent to one micron. This eliminates the need to scale the designs when converting into gdsII format. A grid resolution of 1 nm (0.001) was selected, but a resolution of 10 nm would be more than sufficient for the required tolerances for fabrication.

The electrode shapes are drawn as closed polygons with a maximum number of vertices of 200, shapes with more than 200 vertices were segmented into smaller shapes. To improve the threshold when breakdown occurs, the corners of the electrodes are rounded to reduce the local electric field emission at the triple point, the point at which surface flashover starts [104]. This was manually performed in AutoCAD but would be possible to perform at a later step within a mask software.

Each mask defines a different step within the fabrication process and is written on a different layer in AutoCAD. Three separate masks are needed, the ‘buried wire’ layer, the pattern ‘vias’ (vertical interconnect access) layer and the ‘electrode’ layer. The finalised mask design set is shown in fig.4.26. Details of the individual mask can be found in Appendix A.9

The design of each ion trap is repeated twice on the mask, each design has an electroplating pad to provide electrical connections to all the electrodes during the electroplating step of the electrodes, described in section 5.3.2. A characterisation area has been included to test both bulk breakdown and surface flashover over various gaps of the insulating material. A square frame has also been included, by exposing a resist with the frame this provides a guide when cleaving the wafer into the finished chips ensuring all the wires are electrically

²http://www.barnardmicrosystems.com/L2_circuit_design_software.htm

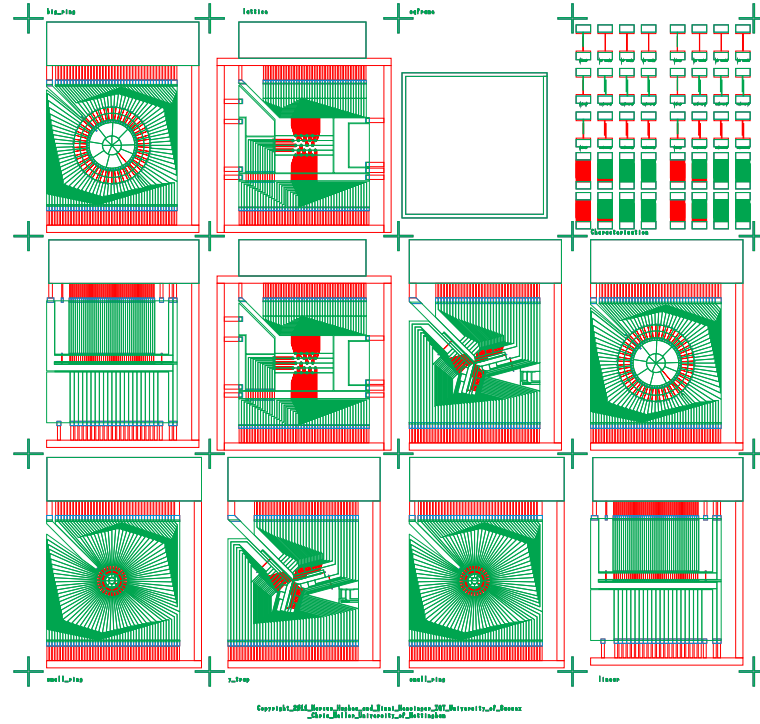


Figure 4.26: Finalised mask set. All three masks superimposed onto each other, each ion trap design is repeated twice, a characterisation area for voltage breakdown tests and a square frame for cleaving the ion traps is also included.

isolated. Alignment crosses in between each design provide a means to align each layer to within a few microns. The write field (physical area of the mask file) measures ≈ 53 mm by 50 mm allowing for a mask set 3 inch x 3 inch to be used that is compatible with the University of Nottingham mask aligner.

The masks were purchased from ML&C with each mask made from sodalime with an anti-reflective chromium coating and measuring 3" x 3". The specifications of the mask were designed to have a minimum feature size (critical dimension (CD)) of $3 \mu\text{m}$ and a tolerance of $\pm 0.1 \mu\text{m}$ together with a write grid of 50 nm. Defects on the mask can render that part of the mask useless and can affect the final operation of the chip. A density of less than 0.2 defects per cm^2 for defects bigger than $1 \mu\text{m}$ was specified to provide minimum disruption to the final chips. Each chip is approximately 1 cm^2 meaning there will be a 20% chance a defect bigger than $1 \mu\text{m}$ will exist.

Each layer is mirrored to provide the correct orientation, this is because the chrome face of the mask is in contact with the substrate a shadow which would reduce resolution. Each mask is defined as light or dark field. Light field defines the enclosed shapes on the

mask to be chrome and transparent for dark field. The ‘buried wire’ layer is defined as light field, the pattern ‘vias’ layer dark field and the ‘electrode’ layer as light field. This is dependent on the type of photoresist used within each process step and is explained in more detail within section [5.2](#).

Chapter 5

Microfabrication techniques

5.1 Introduction

One of the key requirement for a quantum computer outlined by D. P. DiVincenzo [37] is a scalable physical system with well defined qubits. The traditional design of ion traps with machined parts and mechanical alignment becomes unfeasible. By turning towards the well established area of Micro-Electro-Mechanical-Systems (MEMS) technologies, one opens up a whole new library of techniques in the development of large scale ion trap arrays. MEMS techniques allows for the miniaturisation of the trap electrodes without loss of accuracy and resolution. Also an unrivaled parallelism within the processing using photolithography techniques, allows for the construction of all the trap electrodes simultaneously. Scaling from tens of trapping zones to hundreds and thousands requires very little overhead. This has lead to a new generation of microfabricated ion traps pursuing the goal of a quantum information processor [81].

The process involved in the construction of ion traps is dependent on the geometry, asymmetric [47, 79, 86, 190] or symmetric ion trap designs [46, 191, 192]. A detailed discussion has been presented [193], detailing different processes available with the compatibility of different materials, geometries and its limitations. MEMS fabrication can transform a succession of two-dimensional processes into three-dimensional structures with the addition, subtraction and modification of materials onto a wafer.

Within the semiconductor industry silicon has become the most common and established semiconductor material used for MEMS devices and has led to the most convenient choice of material in the development of new traps [47, 86, 194]. Silicon-based materials were

selected in the design and construction of the ion traps within this thesis. Other options include III-V compounds such as Gallium arsenide (GaAs) [46].

Through scaling down ion trap dimensions, new considerations need to take place. Most notably in order of obtaining sufficient trap depths to successfully trap and hold ions, high radio-frequency voltages need to be applied. This limits both the electrode gaps and materials used so breakdown doesn't pose a problem. Other considerations include power dissipation, from the total trap capacitance and resistance. These considerations are kept in mind during the processing of the traps.

Below is an introduction to the techniques involved in the process design of the multi-layered asymmetric ion traps. This section serves as a introduction guide to microfabrication, introducing the techniques of photolithography, deposition and etching. This does not serve as a complete guide to all possible fabrication techniques, but as a guide to the relevant processes. A detailed discussion of the process sequence is then presented in chapter 6, highlighting important techniques that were used in the construction of the designs.

5.2 Photolithography

Through the use of a sacrificial layer that can be easily removed together with being photo-sensitive to UV-light, a desired pattern can be transferred from a mask onto the substrate, shown in fig. 5.1 and is used as the basis for any upcoming deposition or etching steps. Called a photoresist, the solution contains photoactive compounds that will change chemical composition when exposed to light typically $<400\text{nm}$. A Mercury lamp is often used with the i-line (365 nm), h-line (405 nm) or g-line (436 nm) stated for required exposure doses. During a development step the exposed or non-exposed areas can be removed leaving the transferred pattern from the mask. Photoresists can be classified into two types, positive and negative. When selected areas of a positive resist are exposed to UV light, these become soluble and can then be removed. For negative resist the reverse is the case where areas exposed become insoluble, shown in fig. 5.1. There are subtleties between the two types of photoresists which lend themselves to different applications such as a dry etch mask or for electroplating. The resists used are explained in more detail within chapter 6.

A general process flow for the development of a photoresist starts with a wafer that

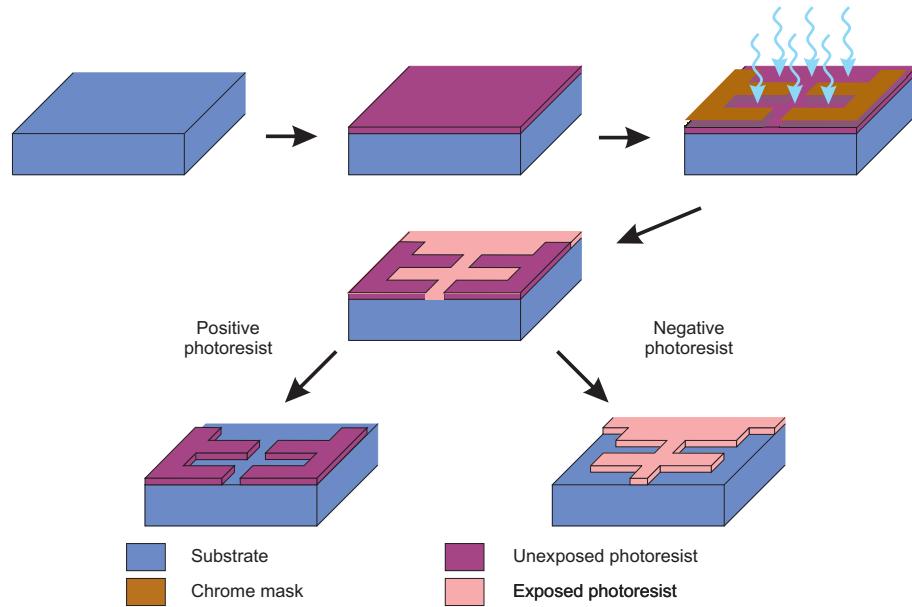


Figure 5.1: General process sequence for the use of a photoresist. A wafer is cleaned and dried before a photoresist layer is spin coated. After a soft bake the sample is then exposed to a UV light source through a patterned mask. Depending on whether the resist is positive or negative the exposed area can be removed or kept during development.

has been solvent cleaned to remove any contamination and is then heated either in a convection oven or on a hot plate to remove any moisture on the surface. To achieve an even thickness across the wafer the resist is typically spin coated. The photoresist solution is dispensed onto the wafer that has been secured to a spinner via vacuum, typical speeds of 1000-6000 rpm are used for ~30-60 seconds to produce the desired thickness.

An edge bead can develop in which the resist thickness increases at the edge of the wafer due to surface tension, depicted in fig 5.2. The size of the edge bead is mainly dependent on on the shape of the wafer and viscosity of the resist, circular wafers have the smallest edge bead due to symmetry during spin coating. This can cause reduced resolution as a gap develops between the wafer and mask during alignment. If an appreciable edge bead develops, it can be removed with the use of a bud soaked with a solvent that dissolves the resist, e.g acetone.

Next the resist is hardened by evaporating the solvents present within the resist on a hot plate, called a soft bake, to create a mechanical stable layer. To provide an accurate pattern transfer from the mask to the photoresist a mask alinger tool from Karl Suss (pt No. MJB-3) is used. This provides the ability to have accurate alignment between the mask and the wafer down to a resolution of $2\text{ }\mu\text{m}$. The UV exposure intensity is calibrated to 10 mW/cm^2 for the i-line in mercury to provide accurate and consistent exposure doses.

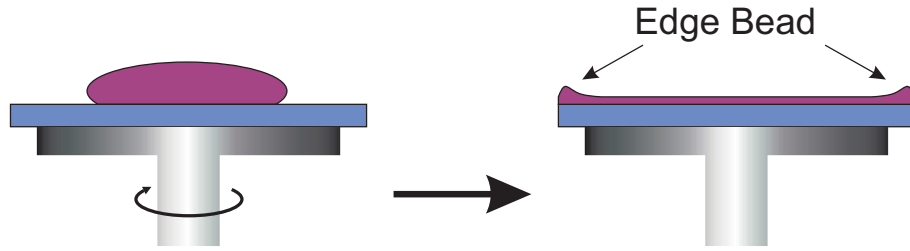


Figure 5.2: Spin coating a resist onto a wafer. An edge bead can develop

A development step then takes place in which the wafer is placed typically in an alkaline based solution to reveal the pattern. Exposure doses and concentrations of the developer affect the development rate. Data sheets from companies provide a useful guide to the parameters used in the processing of photoresists to obtain the desired outcome. The specific photoresist recipes are outlined in chapter 6.

5.3 Deposition

The deposition of materials is a fundamental step in the building of microfabricated devices. Thin films can be deposited via range of techniques from evaporation to chemical vapor deposition (CVD). Thick films $\sim 10\mu\text{m}$ can be achieved via electroplating. Outlined below are the deposition methods used within the processing of the multi-layered ion traps.

5.3.1 Thin film deposition

Thermal evaporation

The deposition of thin metallic layers ($\sim 0.5\mu\text{m}$) can be performed by the use of resistive (Joule) heating. The desired material is heated under vacuum to create a vapor that is directed to the sample, which is condensed back to a solid state on contact. Vacuum pressures are in the range of 10^{-6} mbar such that the evaporated particles can travel directly to the target without background collisions occurring. Mean free paths ~ 100 m are much greater than the source target distance. The source material is placed into a boat which can be resistivity heated to the desired temperature to allow for the desired evaporation rate. Typical rates used were 0.2-0.4nm/s.

Two Edwards E306A type evaporators were used for the evaporation of Au and Ti within my work, a schematic is shown in fig. 5.3. The samples are placed onto a sample holder and

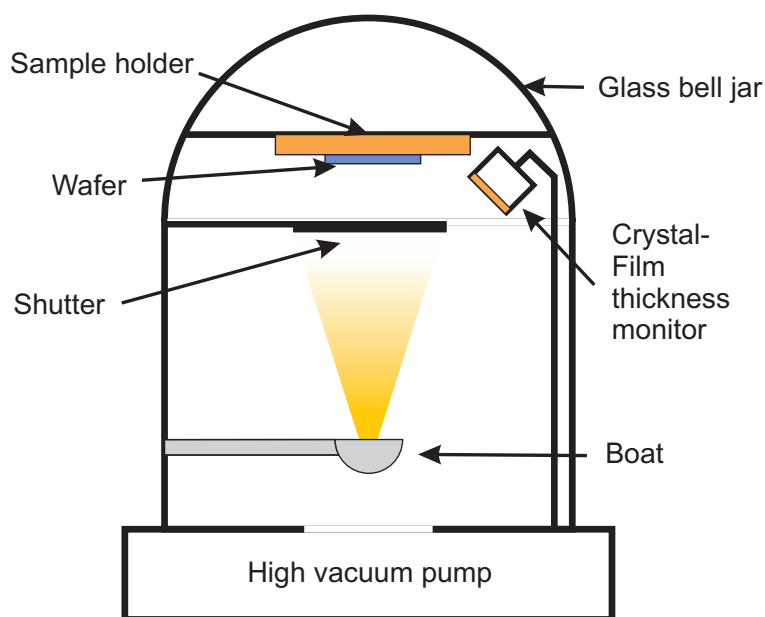


Figure 5.3: Schematic diagram of a thermal evaporator for the deposition of thin metallised films.

held in place with rare Earth magnets, this is then placed at the top of the bell jar facing the source materials below. The uniformity of the films will depend on the placement of the samples on the sample holder. Placed directly above the boat results in higher thickness than the edge of sample holder. The required amount of source materials is then placed into the associate boat. The system is then pumped out to the required vacuum pressure (10^{-7} mbar) with a rotary pump, diffusion pump and via the use of liquid N_2 . This typically takes a few hours with less contamination from lower background pressure. There is a shutter which shields the substrates from any unwanted evaporation material allowing for precise thicknesses. The evaporation rate and film thickness are recorded in situ with a crystal film thickness monitor. This works by measuring the decrease in resonant frequency though an applied rf voltage as the weight of the crystal increases from the deposited material. The density and acoustic impedance of the deposited material then allow for a rate and thickness to be measured. Table 5.1 list the properties and parameters used in the deposition of the metals used. This is an indirect measurement as the monitor is placed to one side of the vacuum chamber as not to interfere with the deposition process. An indicated film thickness and its accuracy is then checked through a direct measurement from a surface profilometer.

Metal	Melting point (°C)	Density (g cm ⁻³)	Acoustic Impedance (Z) ($\times 10^5$ g cm ⁻² s ⁻¹)	Current (A)	Deposition rate (nm s ⁻¹)
Au	1064	19.30	23.17	60	0.2-0.4
Ti	1668	4.50	14.05	50	0.2-0.4

Table 5.1: List of properties and parameters during the thermal evaporation of thin metal layers. As the metal in the boat reduces during evaporation the deposition rate increases for the same current.

Electron beam (E-beam)

Other forms of thin film deposition include electron beam (E-beam) evaporation where evaporation occurs through the acceleration and focusing of a beam of electrons onto the source material with the crucible being water cooled to reduce contamination. This method allows for localised evaporation of the source material due to the electrons being focused providing good control of the evaporation rate and materials with high melting point.

Sputtering

Through the impact of highly energetic particles onto a target material, a stream of the source material can be released. This is known as sputtering and by placing the wafer opposite the target material a thin layer can be grown. A source of ions can be supplied through an ion beam or a plasma. With a wide variety of parameters the growing films can be complex but also flexible. Noticeable feature of sputtering is the deposition of high melting point materials, which would prove problematic with evaporation, operating temperatures are less than other thin film techniques, this allows for substrates with lower thermal tolerances to be used. Due to the non-directional flux of the sputtered material, lift-off methods and shielding areas of the wafer not intended for deposition can prove difficult.

5.3.2 Thick film deposition

The deposition of thick films is an important process in the development of ion traps, high aspect ratio electrodes provides a means of shielding the dielectric as well as a means to apply high current for microwave based gates [187, 195].

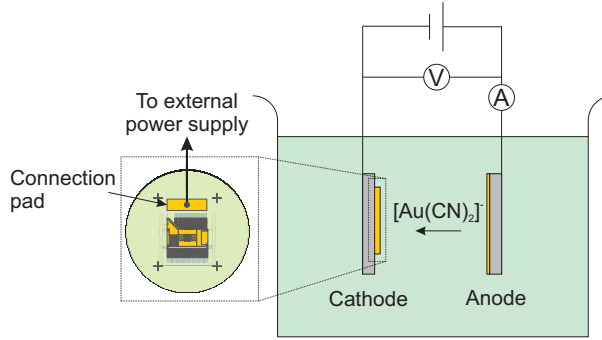
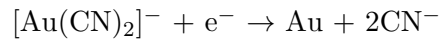


Figure 5.4: Au electroplating process, the sample is placed into an electrolyte solution and a current is created between the anode and cathode through the transport of ions allowing for the deposition of a metallic layer. The insert displays a connection pad, together with a seed layer provides a means to electrically connect all the trap electrodes.

Electroplating

The deposition of film thicknesses $\sim 10 - 20\mu\text{m}$ can be achieved by electroplating, a coating of a metallic layer is performed through the use of an electric current shown in Fig 5.4. The sample is placed in an electrolyte solution (plating bath), by creating an electric circuit between the source material (Anode) and sample (cathode) through an external power supply, deposition of a metallic layer can be achieved. An example for Au electroplating is with a gold-cyanide electrolyte solution with a $\text{pH} > 8.5$ [196]. $[\text{Au}(\text{CN})_2]^-$ ions are created at the anode through the reaction of cyanide with the source material. These ions are then attracted to the sample and through following chemical reaction deposit Au on the sample [196].



Control of the current density and known electroplating area is required to obtain accurate and reproducible film thicknesses. The purity of the deposited layer will depend on contaminants remaining on the surface of the sample prior to electroplating and within the solution. Agitation through stirring helps provide even electroplated thickness across the sample. For electroplating to occur in the desired areas requires a seed layer (150-200nm) and a connection pad from the sample to an external power supply. The wafer is attached to a carrier wafer via wax and silver dabs are used to provide electrical connection from the carrier wafer to the sample.

5.3.3 Chemical vapor deposition (CVD)

The growth of amorphous (no crystalline order) oxide and nitride layers can be performed by chemical vapor deposition (CVD), this provides a means to insulate the underlying conducting layer. This is achieved through the reaction and or decomposition of a mixture of gases resulting in deposition on the sample surface. Different layers can be grown through the mixture of different gases. The two dielectrics that are deposited within this work are silicon dioxide (SiO_2) and silicon nitride (Si_3N_4). Silicon dioxide is deposited through the combination of silane (SiH_4) and nitrous oxide (N_2O), where silicon nitride uses a combination of silane (SiH_4), ammonia (NH_3) and nitrogen (N_2).

In order to increase the deposition rate or facilitate a wider range of materials samples, extensions to the general CVD process have developed. Low pressure CVD runs at below atmospheric pressure, reducing the impurities in the grown layer. Plasma enhanced CVD (PECVD) utilises the use of a plasma, reducing the temperature required for CVD to take place.

Plasma enhanced CVD (PECVD)

Through the use of a plasma, the temperature of the sample can be significantly reduced typically from 600°C to 250°C this opens the process up to delicate semiconductor devices that are not able to withstand such high temperatures. Plasma enhanced CVD (PECVD) works by adding kinetic energy together with the thermal energy to create the chemical reactions. A schematic of the Corial D250 PECVD chamber used to grow the dielectric films is shown in fig. 5.5.

The samples are placed onto the shuttle which is kept at 250°C , closed and then pumped down to a standby pressure of 100 mT. The plasma is created by applying an rf voltage between the top plate and shuttle to ignite the gases from the inlet valve. The reactor itself is isolated at 300°C and at a higher pressure (P1) compared to the rest of the chamber (P2), this provides reduced contamination of oxygen and carbon. A laser at 670 nm is used to measure the real time film growth in situ from the interference signal between the top and bottom of the layer. Manufacture recipes are used for the growth of the silicon dioxide and nitride layers. Deposition rates of ~ 200 nm/min and ~ 70 nm/min are measured for (SiO_2) and (Si_3N_4) respectively.

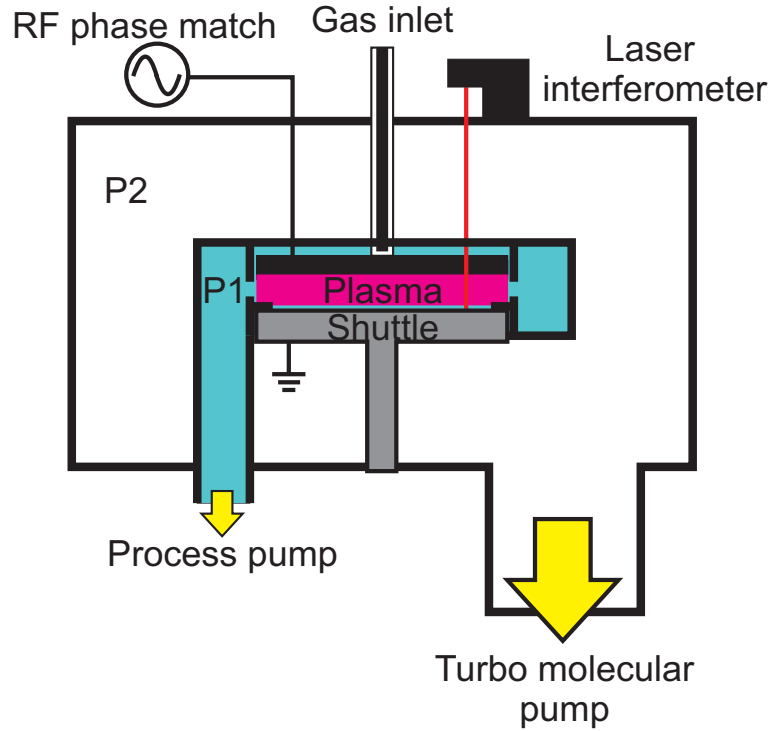


Figure 5.5: Schematic of the Corial D250 PECVD chamber used to deposit the dielectric layer.

Several properties of the grown thin films need to be considered in determining the final insulating structure. Pinholes [197] are defects in the film layer resulting in holes of a few nm. These provide the potential for metal, water or any other conducting particles to be absorbed into the layer resulting in reduce breakdown of the insulating layer. Various insulating structures were investigated and bulk breakdown measurements taken to determine the final insulating structure. The results are presented in section 7.1.1.

Conformality of the thin film describes the how the underlying surface structure affects the topography of the grown film, this is shown in fig. 5.6. The grown films were measured to be non-conformal resulting in the pattern of the underlying conducting layer to be directly transferred onto the surface of the insulator.

Residual stresses within the film provide a limit on thickness of the layer grown before cracking occurs. The compressive stresses can be reduce by adjusting the Ar flow rate and RF power, with higher values resulting in lower stresses. Initially layer thicknesses of $2\text{ }\mu\text{m}$ were thought to be the limit but structures of $3\text{ }\mu\text{m}$ (section 7.1.1) were grown without any problems in subsequent processing steps.

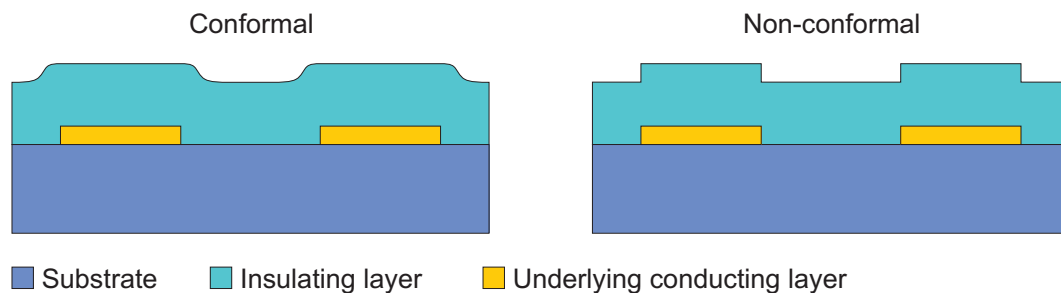


Figure 5.6: Conformality of CVD grown films. The deposited PECVD films were non-conformal transferring the underlying topography of the buried wires.

5.4 Etching

When selecting an etch the aim is to remove a desired material and create a particular etch structure whilst keeping the rest of the sample unaffected. A mask is used (e.g photoresist or silicon nitride) to protect parts of the sample that is resistant to the etchant. An important parameter is to provide sufficient selectivity between etch rates of the material and the mask. Etching can be characterised into two types, wet and dry described below.

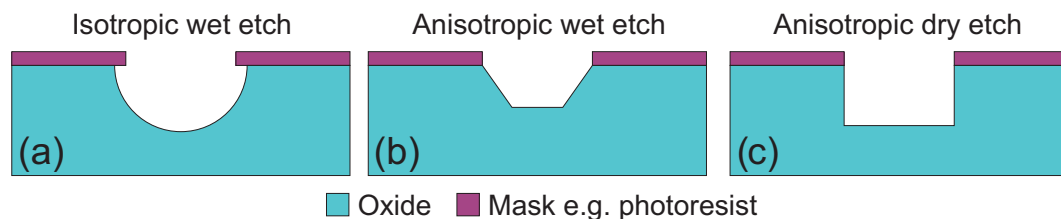


Figure 5.7: Etch profiles obtain through wet and dry etching techniques.

5.4.1 Wet etching

Wet etching immerses the sample in a chemical solution typically providing isotropic results as shown in fig. 5.7 (a). With agitation the etching occurs in all directions of the material, advantageous for undercut profiles. Anisotropic wet etches are possible by a high selectivity between different crystalline planes within the material, for example by etching silicon with potassium hydroxide (KOH) a selectivity of 400 is possible between the $\langle 100 \rangle$ and $\langle 111 \rangle$ planes, this creates sloping walls along the $\langle 111 \rangle$ plane, shown in fig 5.7 (b).

Wet etches tend to have high etching rates for example etching Au with dilute aqua regia, a mixture of nitric acid and hydrochloric acid ($\text{HCl}:\text{HNO}_3$) in a ratio of 3:1 has an etch rate of 680 nm/min [198]. This can prove difficult in etching thin films and stopping the

etch at the required time. An extensive range of different etches for various materials have been documented [198, 199] and provide a good starting point in selecting a wet etch.

5.4.2 Dry etching

Through the use of a plasma, ions and radicals are created and used as a tool for different dry etching methods. These include physical ion bombardment, reactive ion etching (RIE) and inductively coupled plasma (ICP) etching. Etch profiles are typically anisotropic shown in fig 5.7 (c). The method is similar to PECVD but with different gases used, the samples are placed inside a vacuum chamber and various gases are introduced. Through the use of a high power RF source, a plasma is ignited and the ions and other species created within the plasma are used to physically and or chemically etch the sample.

Ion bombardment

The simplest form of dry etching is through physical ion bombardment, e.g ion sputtering and ion-beam milling physically knocking out atoms on the surface. This produces highly anisotropic results but is not selective between different materials present.

Reactive ion etching (RIE)

A capacitively coupled RF source is applied between two parallel plates which creates the plasma. The RF frequency typically at 13.56 MHz is high enough such that only the electrons are affected within the plasma. The electrons are motionally driven within the RF field such that they ionise atoms and become absorbed onto the chamber wall and electrodes. Charge build up occurs on the bottom electrode creating a negative voltage bias (~ -100 V), this attracts the ions in the plasma vertically towards the sample and reactions with the surface occur. RIE produces anisotropic results and good selectivity between different materials.

Inductively coupled plasma (ICP) etching

A RF current is passed through a coil wound around the walls of the reactor. This induces a magnetic field in which the electrons present inside the reactor are set in motion creating

a plasma. Due to the helical motion of the electrons, a higher density of ions than the parallel plate arrangement is achieved, allowing for higher etching rates. An ICP is combined with a RF bias on the sample to decouple the ion generation and energy. Adjusting the RF bias allows for fine control over the etching, with anisotropic from high RF biasing and isotropic results from low RF biasing.

A Corial 200IL system is used to perform various dry etching recipe. A laser interferometer at 905 nm is used to measure the real time etch of the samples as with PECVD.

Chapter 6

Microfabrication process

The process sequence can be divided into three general steps, the deposition and patterning of the underlying conducting layer, the deposition of the insulating layer together with the creation of vertical interconnect access (vias) and finally the deposition of the electrodes, with a mask for each step. There are many intermediate steps to create the final result and will be discussed in more detail below. A diagram summarising the process flow to realise the trap structures is shown in fig 6.1, with a detailed step by step guide presented in section 6.5.

6.1 Wafer preparation

Quartz cover slips from 2Spi.com were selected, made from GE 124 fused polished quartz offering a surface roughness of <2 nm and quoted as being optically flat. Also a transmission of $>90\%$ at 369 nm is stated, providing the opportunity of integrated on chip detection without the need for a through etch of the wafer. Thicknesses of 200 nm are available allowing for the possibility of a through wafer etch opening up the options for backside loading. Round quartz cover slips are available in various diameters and thicknesses. Ten 1.0" (25.4 mm) diameter and thickness of 200 μm were initially selected and then another ten 1.300" (33.02 mm) diameter with same thickness were purchased. The 1.3" allowed two traps to be processed on each wafer simultaneously.

After receiving the quartz wafers they need to be cleaned in preparation for the forthcoming process steps. A solvent clean is performed within the cleanroom wet deck area with appropriate agitation of the samples. Agitation methods available in the cleanroom

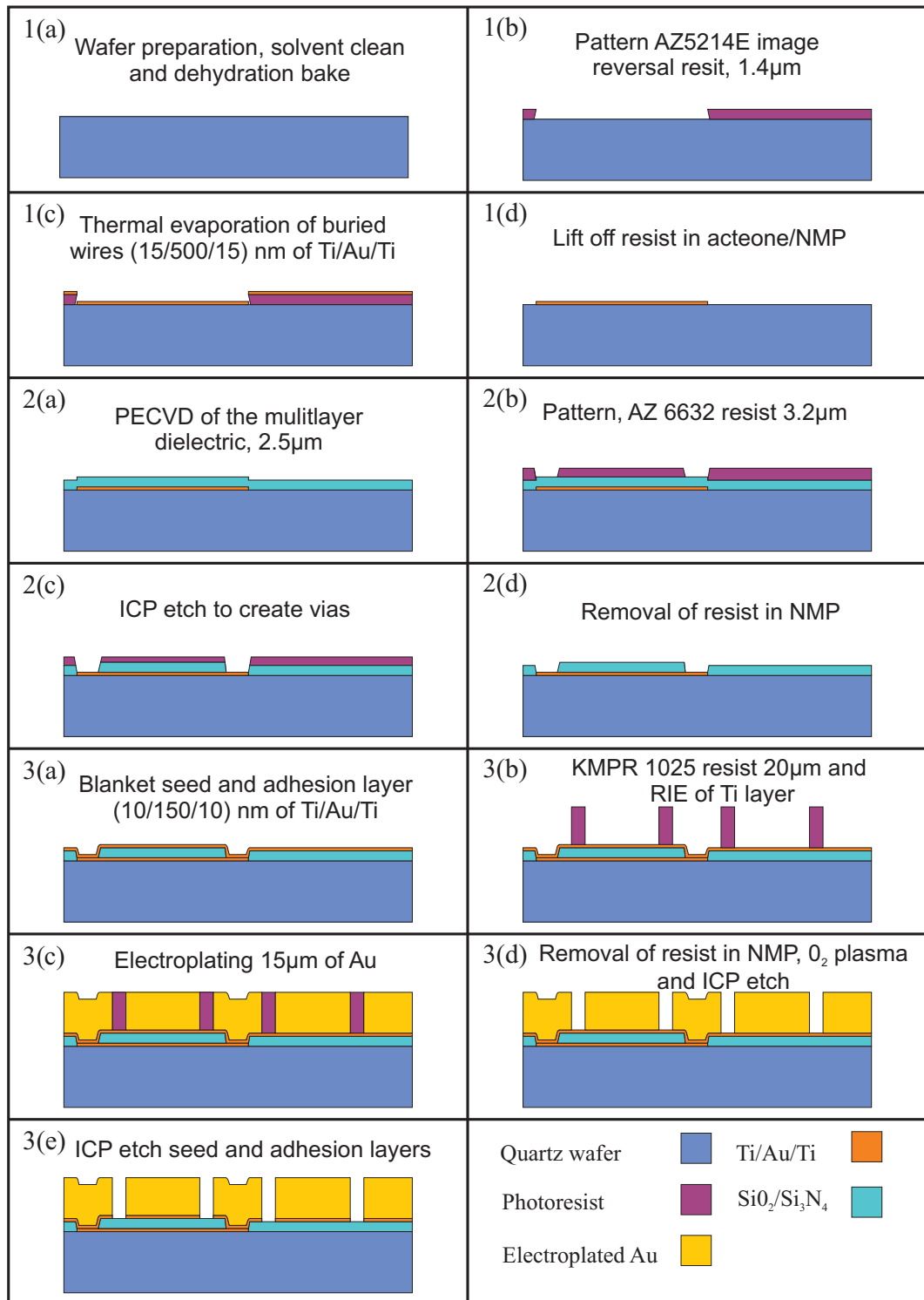


Figure 6.1: Process flow showing all the main steps involved in the realisation of the trap structures. The sequence is classified into three general steps with the intermediate steps shown.

include two ultra sonic baths, one small and a larger professional model providing more power. A stirring plate is also available to provide more gentle agitation. The selected quartz wafers with a thickness of 200 μm proved to be very delicate, especially the larger 1.3" diameter wafers which did occasionally break during in the processing. All the cleaning was either performed in the small ultra sonic bath or on the stirring plate.

For each step of the solvent clean the wafer is placed into a clean beaker of the current solvent and then placed into the small ultra sonic bath for 10 minutes. The order of the solvents used is outlined below.

Ethyl lactate \rightarrow Acetone \rightarrow Methanol \rightarrow Isopropanol

Afterwards, rinsing of the samples with clean solvent and N_2 blow drying occurs with the exception of acetone. Acetone is good at removing organic material off the substrate, but due to the high evaporation rate requires a subsequent cleaning step with Methanol or Isopropanol. This prevents any stains forming on the surface. After the solvent clean a dehydration step of the sample is performed in a convection oven at 150°C for 10 minutes to dry the sample in preparation for coating of the photoresist.

6.2 Underlying conducting layer

6.2.1 Lift-off resist

For the forthcoming thermal deposition of the underlying conducting layer requires a resist that can be easily removed leaving the patterned layer. This is achieved through the process of lift-off with a resist having a negative slope profile as shown in fig. 6.2. Negative photoresists allow for a undercut to the side wall where the opposite is true for positive resists. This prevents the side walls from being coated making the lift-off process possible.

MicroChemicals AZ 5214E image reversal resist provides another means to achieve an undercut profile. After the exposure, an additional reversal bake step is included which cross links exposed areas within the resist. A flood exposure without the mask is performed to make the unexposed areas soluble within the development step. The final result is a negative image from the mask. Below is the recipe for the AZ 5214E image reversal photoresist for a thickness of 1.40 μm .

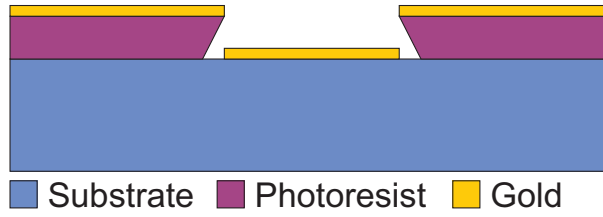


Figure 6.2: Negative profile of a resist for lift-off process. The deposited gold layer on the substrate remains separated making the process of lift-off possible.

- Spin coat resist at 4 krpm for 30sec.
- 3 min air dry.
- Soft bake at 90°C for 5 min.
- Exposure with mask layer 1 for 2.0 sec.
- Reversal bake at 120°C for 120 sec.
- Flood exposure without mask for 22 sec.
- Development in AZ 726 MIF for 60 sec.

The samples are then visually inspected under the microscope for any defects which could result in electrically isolated electrodes. The thickness of the resist required is dependent on the thickness of the deposited layer. A ratio of $\approx 3:1$ of resist to deposited layer thickness was used to provide successful lift-off results.

6.2.2 Thermal deposition

Underlying gold wires are used due to low resistivity ($\rho \sim 2.5 \times 10^{-8} \Omega m$), however due to poor adhesion of gold to other materials a Ti adhesion layer is used. The metal wires consists of a 15 nm Ti adhesion layer, 500 nm Au Layer and another 15 nm Ti layer. An Edwards E306A thermal evaporator is used in the deposition of thin metal films. The samples are placed onto the sample holder with rare earth magnets round the edge of the wafer and then pumped down to 10^{-7} mbar by a rotary and diffusion pump with the aid of liquid N₂ taking ~ 3 hours. Due to the relatively small size of the boats the 500 nm Au layer is performed in two evaporation steps, depleting the Au, bringing the evaporator back to atmospheric pressure and then re filling the Au boat before being pumped out again. The boats are able to hold enough Au for for the deposition of ~ 350 nm in one go,

however overloading the crucibles resulted in spitting from the boat, this can be seen in fig. 6.3. The result was the deposition of large grains of gold often shorting adjacent electrodes.

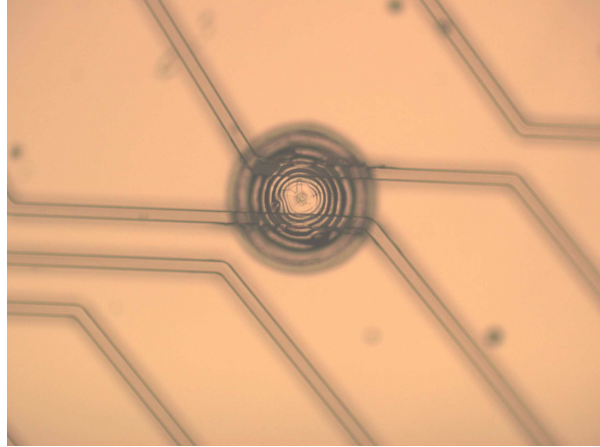


Figure 6.3: Microscope image showing a spit of gold shorting adjacent electrodes.

To provide reproducible film thicknesses the indicated thickness film monitor values were compared to actual measurements recorded with a KLA Tencor stylus profiler. As the thickness of the layer increased, a discrepancy was observed between the indicated and measured layer thicknesses, with an underestimate of the actual film thickness. Overtime data was collected to correct for this difference and produce more accurate results.

6.2.3 Resist removal

The final step in the lift-off process is to remove the gold coated resist. The samples are placed into acetone heated to 70°C in which the resist can be dissolved and the overlying gold layer lifted off. Agitation of the sample was used to encourage lift-off from stirring of the sample, using an indirect stream of solvent from a bottle and ultrasound. Care had to be taken not to agitate the sample too much as the wires had the tendency to rip rendering the electrical connections to the electrodes useless. This is due to the long and thin profile and was only observed with the 3 μm wide wires, shown in fig. 6.4

The samples are lifted out of the acetone and then instantly rinsed with isopropanol. Acetone can provide a difficult median during the lift-off process due to the trend for particles to be reabsorbed onto the surface. In later lift-off processes NMP (1-methyl-

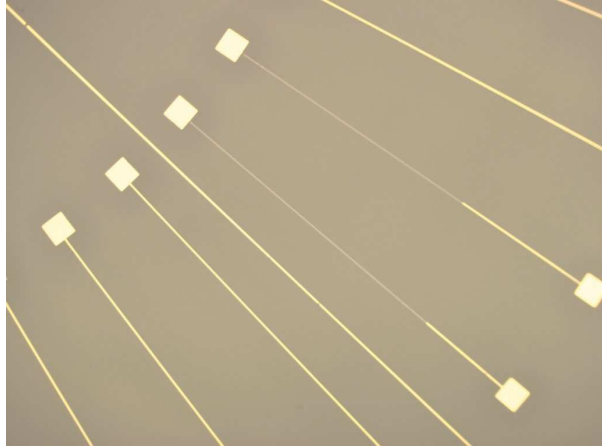


Figure 6.4: Microscope image showing detaching of two underlying wires during the lift-off process.

2-pyrrolidone) was used, with a lower vapour pressure and the ability to heat to higher temperatures (85°C).

6.3 Insulating Layer and vias

6.3.1 Plasma enhanced CVD

Dielectric layers were grown by Dr Chris Mellor with a corial D250 via plasma enhanced chemical vapour deposition (PECVD). Operating temperatures of 250°C are used to grow the SiO_2 and Si_3N_4 layers at a deposition rate of $\sim 200 \text{ nm/min}$ and $\sim 70 \text{ nm/min}$ respectively.

Three structures were grown to test their structural integrity and breakdown properties before finalising the insulating structure. The test samples, together with the results are outlined in more detail within section 7.1.1. Results show that thicknesses of $2 \mu\text{m}$ are more than sufficient in the prevention of bulk breakdown. The final structure shown in fig. 6.5 consists of $1.5 \mu\text{m}$ of SiO_2 sandwich between two multi-layered structures $0.5 \mu\text{m}$ thick, comprising of six alternating layers of SiO_2 and Si_3N_4 with individual thicknesses of $\sim 80 \text{ nm}$. The multi-layered structure is to limit the effect of pinholes whilst a total thickness of $2.5 \mu\text{m}$ was chosen to limit the effect of the vias in the final electroplated structure due to no planarisation steps.

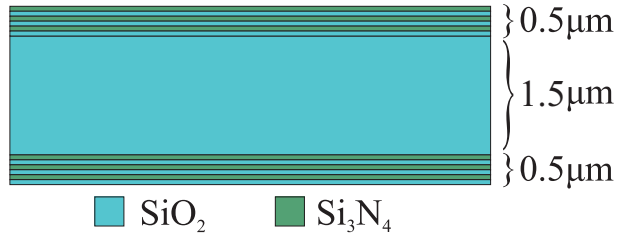


Figure 6.5: Finalised insulating structure after performing breakdown measurements.

6.3.2 ICP etch resist

During ICP etching, high temperatures on the surface of the sample are experienced, a photoresist that can withstand high temperatures during plasma etching is therefore required. MicroChemicals AZ 6632 positive photoresist was selected also offering a steep sidewall profile of the resist makes it a good choice for dry etching. With an expected etch rate selectivity of 3:1 between the dielectric and the photoresist will allow all the exposed areas to be fully etched without affecting the masked areas.

Initial processing of the resist resulted in bubbling from N_2 forming during the exposure, shown in fig. 6.6. This was due to insufficient evaporation of the solvents within the resist during the soft bake. By increasing the soft bake time solved the problem of bubbling within the resist.

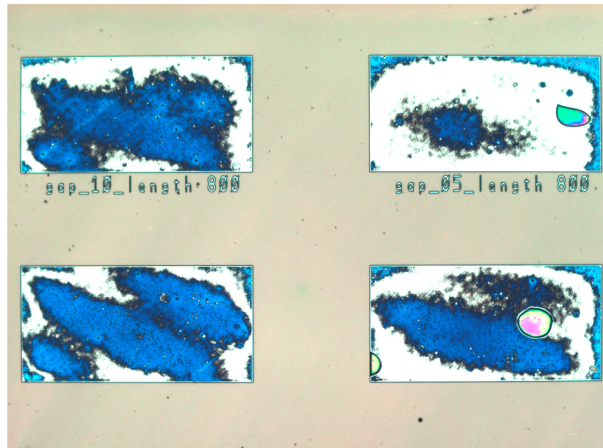


Figure 6.6: Bubbling of the AZ 6632 resist due to insufficient evaporation of the solvents during the soft bake step.

The final recipe for the processing of AZ 6632 positive photoresist for a thickness of $3.2 \mu\text{m}$.

- Spin coat resist at 4 krpm for 30sec.
- Soft bake at 110°C for 5 min.
- Exposure with mask layer 2 for 15 sec.
- Development in AZ 400K:DI water (1:4) for 60 sec.

Overdevelopment of the resist was performed to produce positive sloping sidewalls, this was performed to assist in the deposition of the seed layer for electroplating. The samples are inspected under the microscope for full development and good alignment with the underlying wires.

6.3.3 ICP etch

During dry etching, the samples can get hot and to avoid burning of the resist the samples are attached to the shuttle which is cooled via Helium. First the samples are attached to a Si carrier wafer with wax and then to the shuttle with Y Vac 3 vacuum grease. The samples aren't directly attached to the shuttle as the Y Vac 3 vacuum grease is expected to produce more contamination than the wax. To attach the samples, the Si wafer is placed onto a hot plate at 70°C, the wax is then melted on the Si wafer and the sample is then carefully placed on top ensuring an even coating.

The etching step was performed by Dr Chris Mellor and Dr Jessica Maclean with a corial 200IL dry etcher. The etching of (SiO₂) and (Si₃N₄) is performed with a CHF₃ plasma and a graphite shuttle in place. After attaching the samples to the Si carrier wafer the system is pumped down to a working pressure of a few mT. Manufacture recipes are used to perform an ICP etch with Fluoroform (CHF₃) and Ethylene (C₂H₄) gases present. Etch rates of ≈ 230 nm/s were measured during the etch step, with a total duration of ~ 11 minutes. The etch step was split into two with a 5 minute pause in between. This allowed the sample to cool down and prevent the burning of the resist. Using the stylus profiler the resist thickness was measured before and after etching resulting in a selectivity of $\approx 2.8:1$. A slight over etch is performed to ensure all the dielectric layer is removed. The exposed Ti adhesion layer is also etched away due to the presence of fluorine.

6.3.4 Resist removal

Firstly the samples are detached from the carrier wafers by heating sample to melt the wax. A bud soaked in Trichlorethylene is used to remove the wax off the back of the sample, next the samples are then placed in Microposit Stripper 1165 (NMP) heated to 85°C. Agitation with the small ultra sonic bath is used approximately every hour to encourage the removal of the resist. After a few hours the samples are then transferred to a fresh beaker of acetone and isopropanol before being inspected under the microscope to check for no remaining residual of resist.

6.4 Electrode layer

6.4.1 Seed and adhesion layer

To allow for the electroplating across the whole sample an electrical connection needs to be made to all areas that are going to be electroplated. Originally the buried wires were to provide electrical connections to the isolated electrodes but the resistance was too high to produce an even thickness across the whole chip. A blanket seed layer was then employed as an alternative method. A seed layer of 150-200 nm was chosen to provide sufficient conductance for electroplating. A thinner layer allows for easier removal in the later etching step where a thicker layer allows for more control during electroplating. After loading and pumping down the evaporator, a thermal evaporation of 10 nm of Ti, 150-200 nm of Au and 10 nm of Ti was performed. As well as an adhesion layer, Ti also serves the purpose as a diffusion barrier between the dielectric layer and the gold electrodes [200].

6.4.2 Electroplating resist

To provide shielding of the dielectric layer from the ion, a thick electroplated layer is required. MicroChem KMPR 1025¹ i-line epoxy based negative photoresist is used, designed for electroplating provides an aspect ratio of up to 5:1. With electrode gaps of 5 μm electroplated thicknesses of 25 μm should be possible. The data sheet² provided a starting point in the optimisation of the resist. After following these guidelines the delamination of the resist occurred during the electroplating trials, resulting in electroplating within the

¹<http://www.microchem.com/Prod-KMPR.htm>

²<http://microchem.com/pdf/KMPRDataSheetver4.2a.pdf>

gaps, this is shown in fig. 6.7.

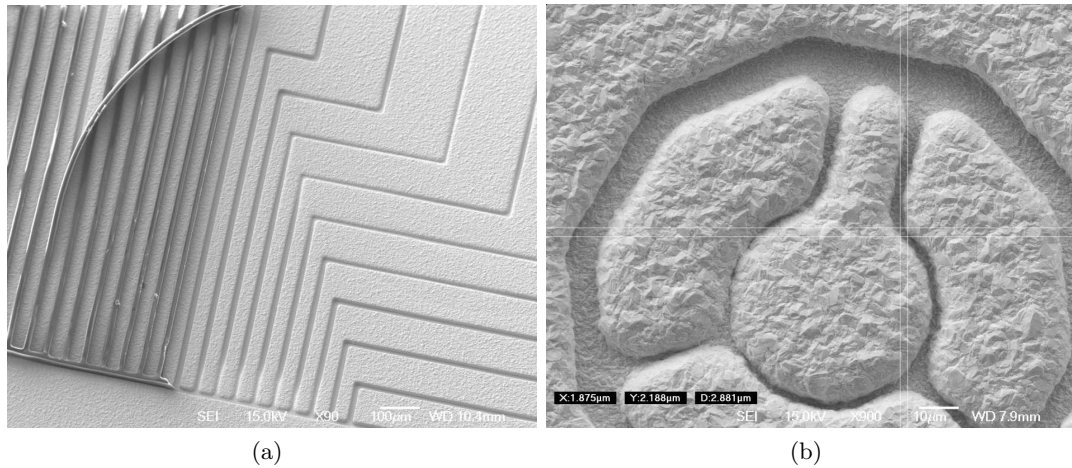


Figure 6.7: (a) SEM picture showing delamination of the resist during electroplating. (b) Electroplating occurred within the gaps due to delamination.

Many resist processing and electroplating trials took place in which different parameters were varied, an optimized recipe is outlined together with the progress in achieving these results. MicroChem SU-8 is another thick resist for MEMS applications, online resources^{3,4} of this resist have helped with the optimisation of the KMPR resist process.

High film thicknesses are possible with the resist, but as a consequence is a high viscosity of 4800 cSt and solid content of 63.8% which makes handling the resist more challenging. Dispensing the resist is performed directly from the bottle across the sample in one motion, this is to prevent air bubbles forming in the resist, which creates areas where the resist will not be present. To achieve an even coating over the sample a Brewer Scientific Cee 100 spin coater is used to apply a programable spin cycle. The spin cycle starts by ramping up to 500 rpm at an acceleration of 100 rpm/sec, this is to stop the resist initially “flying” off the sample and creating an uneven coverage. A second acceleration phase ramps up to 5000 rpm at 300 rpm/sec and is then held for 25 seconds. This results in a resist thickness of $\approx 18 \mu\text{m}$. The profile of the spin cycle is shown in fig. 6.8.

After spin coating of the resist there is a noticeable edge bead that formed. Initial trials showed the edge bead remained tacky after the soft bake, resulting in the masks and sample to stick during exposure. Also with a gap present between the mask and the substrate,

³<http://memscyclopedia.org/su8.html>

⁴ <https://www.memsnet.org/memstalk/>

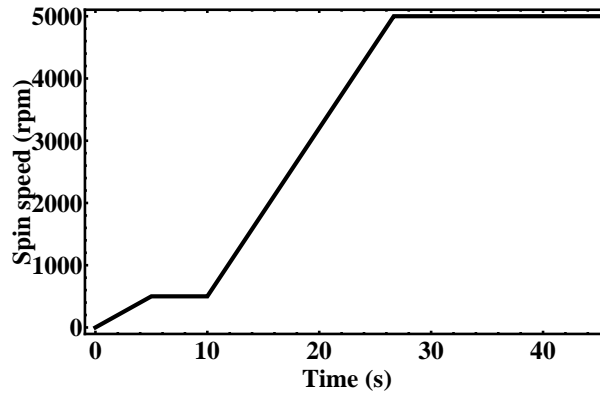


Figure 6.8: Spin program of the KMPR 1025 resist to achieve a thickness of $\approx 18 \mu\text{m}$.

the resolution during exposure is reduced. Therefore the edge bead is manually removed with a swab rinsed with acetone, a slow spin cycle of 500 rpm for 15 seconds to level off any variations in the thickness at the edge of the sample.

An initial soft bake was performed at 100°C for 7 minutes on a level hotplate, this was then altered to a ramped soft bake to reduce the stresses within the resist and increase the adhesion, shown in fig. 6.9. The sample is placed on the hot plate at room temperature and heated to 65°C . After 10 minutes the sample is ramped up to 100°C , held for 15 minutes after which the hot plate is turned off and the sample is allowed to cool back down to room temperature. The samples were typically allowed to cool overnight.

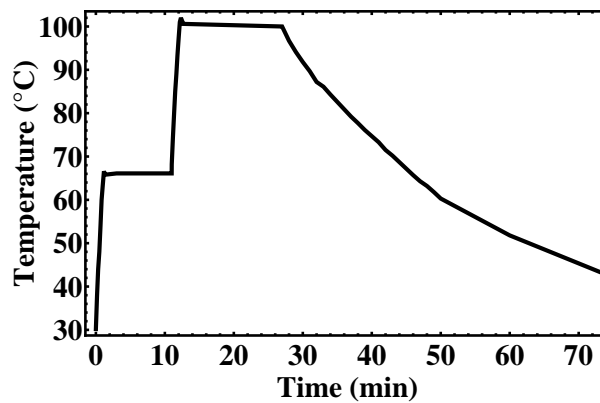


Figure 6.9: Soft bake profile

Next the exposure step defining the electrodes is performed. The exposure dose is dependent on the thickness and the reflectance of the underlying material. The correct exposure dose had to be found by exposing a variety of batch of test samples. This was

first optimised for a Au seed layer and then a Ti seed layer for later samples. There should be a visible latent image after being placed on the hot plate for the post exposure bake (PEB) and not before. With the Karl Suss mask aligner calibrated to 10 mW/cm^2 for the i-line in mercury, an exposure dose of 120 seconds was used. This might have been a slight overexposure but using a negative resist this did not have a major impact and can improve the structural integrity. By exposing the substrate in one go, it was observed after development that there was “nibbling” of the corners of the structures due to high dose exposure (1200 mJ/cm^2), shown in fig. 6.10 (a). Segmenting the total exposure into six 20 second exposures with a 90 second relaxation time in between resulted in a higher resolution of the resist after development, shown in fig. 6.10 (b). This is to reduce the top layer of resist from getting too hot due to the UV absorption. To help reduce stresses in the resist a relaxation step of one hour was introduced into later sample trials.

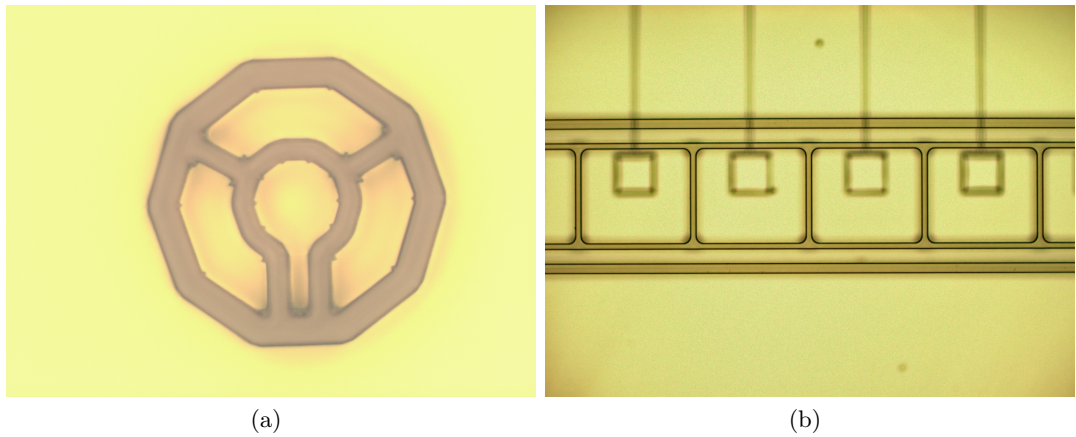


Figure 6.10: (a) Nibbling of the resist structure from one continuous exposure. (b) Segmenting the exposure and adding in time delays between exposures improved the resolution.

The post exposure bake (PEB) like the soft bake is ramped to improve adhesion and reduce the stresses within the resist. Firstly the samples are placed on the hot plate at room temperature and ramped to an intermediate temperature of 65°C , it is then held for 1 minute before being ramped to 100°C . Once the hot plate has reached 100°C , the temperature is then held for 30 seconds before being turned off and letting the residual heat slowly cool the sample. To create a profile more inline with the datasheet, a beaker of water to placed onto the hotplate after 2 minutes from turning off the hot plate to increase cooling rate back to room temperature. The profile of the PEB is shown in fig. 6.11. Once the temperature of the hotplate is below 30°C the samples are taken off ready

for development.

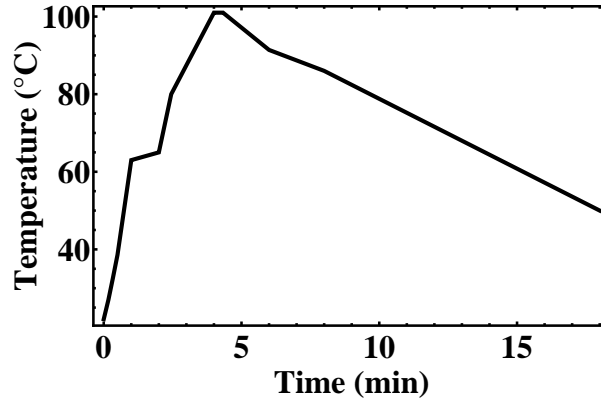


Figure 6.11: Post exposure bake (PEB) profile

KMPR resist can be developed in TMAH based solution however ethyl lactate was used as an alternative. The samples are immersed in a solution of ethyl lactate and gentle agitation is provided from the stirring plate. A development time of 4 minutes 30 minutes was sufficient for the given thickness of the resist ($\approx 18 \mu\text{m}$). The samples are then rinsed in deionised (DI) water and blow dried with N_2 before being inspected under the optical microscope.

6.4.3 Removal of exposed adhesion layer

Within the exposed areas, the Ti adhesion layer is removed to expose the gold in preparation for electroplating. A Sulfur hexafluoride (SF_6) RIE etch is used with an etch rate of 18 nm/min . The etch can easily be monitored by observing the reflectance signal increase and level off as the underlying gold layer becomes exposed.

6.4.4 Electroplating

The electroplating step was performed by Dr Jessica Maclean in the e2v cleanroom at the University of Nottingham, separate to the Schools cleanroom. The final electroplated thickness is an important factor for shielding the dielectric and needs to be accurately estimated. The thickness is dependent on the electroplating area, current density and process time. After developing the resist the exposed area is often hard to estimate. By attaching the sample to a carrier wafer with a known area, the relative uncertainty of

the total electroplating area is reduced. This provides a smaller uncertainty in the final measured electrode thickness. The current density is then set to a value which will create a slow deposition rate ($\sim 3\text{-}4\ \mu\text{m}/\text{hour}$), decreasing surface roughness.

As previously mentioned, the original design on the mask had an electroplating pad and a pattern seed layer was going to be deposited. Electrical connections for electroplating to the segmented electrodes was via the buried wires, but it was determined that the resistance was too high to obtain reliable plating in terms of overall thickness and same deposition thickness of the substrate. The process was then altered with a blanket seed layer to provide electrical connection across the whole sample. The revised process made estimating the plating area difficult and led to variations between the estimated and actual thickness. An estimated area of $\sim 40\%$ of the wafers area is electroplated.

Thicknesses of $25\ \mu\text{m}$ were originally trialled, but to improve reliability and increase yield, successful electroplating thickness from $3\text{-}20\ \mu\text{m}$ were achieved. A successful electroplating trial is shown in fig. 6.12 with a thickness of $18\ \mu\text{m}$.

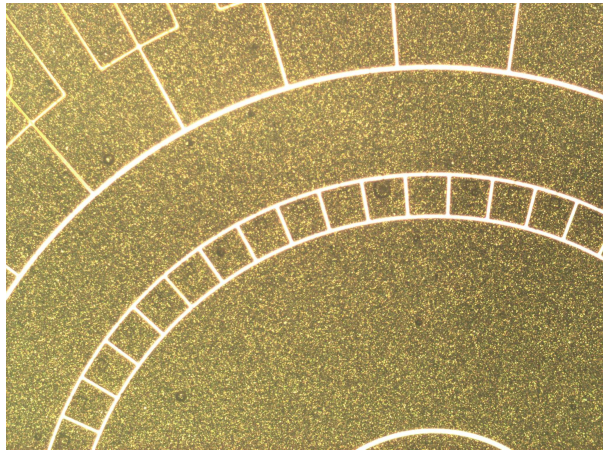


Figure 6.12: Electroplating of big ring design to a thickness of $18\ \mu\text{m}$.

6.4.5 Resist removal

Immediately once the sample was removed from the electrolyte solution the resist started to swell and delaminate in parts around the edge of the wafer. Working quickly the samples are detached and cleaned from the carrier wafer, through melting the wax on a hot plate at 70°C and swabbing the back of the wafer with Trichlorethylene. Next the sample

is placed into NMP heated to 85°C, agitation in the form of the small ultra sonic bath was used to help remove the resist.

Through the optimisation in processing the KMPR resist resulted in improved adhesion and required more cleaning steps in later process runs. Soaking the samples in NMP typically lasted for 8 hours heated and then left to soak overnight. An O₂ plasma asher step was introduced which improved cleaning of the remaining resist. This was performed by an in-house built O₂ plasma asher, with the temperature set to 100°C and a duration of 30 minutes. After these clean steps most of the resist had been removed but a small residue was still present at the bottom of the tracks.

An ICP etch step was introduced to remove the remaining photoresist, after 90 seconds there was no presence of photoresist under the microscope, however the time required varied between samples.

6.4.6 Etching of the seed and adhesion layer

The final etch step was to remove the adhesion and seed layers within the tracks to electrically isolate the electrodes. Different options in etching the Au seed layer exist, wet and dry etching as well as reverse plating are possible options, Paul Werbaneth *et al.* [201] have discussed there experiences with these different methods.

As mentioned earlier wet etching gold in dilute aqua regia results in etch rates of 680 nm/min [198], this would result in etch times on the order of ~ 13 seconds for a 150 nm seed layer. Quick etch times will result in a uncontrollable process, together with an isotropic etch profile that will cause under cutting of the electrodes, reducing structural integrity. Even with sufficient agitation, etching of the electroplated gold will occur at a faster rate than the evaporated gold reducing the height of the electrodes and increasing surface roughness.

Reverse plating can be employed, following the same steps as electroplating but reversing the current flow allows gold to be stripped from the sample. This needs an underlying conduction layer of sufficient thickness below seed layer to provide electrical connection. Once the electrodes become isolated they continue to be electrochemically etched which

poses a problem with the non uniformity of the reverse plating across the sample.

Dry etching techniques can be employed with anisotropic results possible. This will limit any possible undercutting of the electrode structures resulting from wet etching. The process is easily controllable by stopping the process through turning off the plasma.

Gold being a noble metal and therefore resistant to oxidation makes it hard for any chemical reactions to occur. Another concern with the gold etch chosen is the selectivity between the electroplated and evaporated gold. With the high aspect ratio of the electrodes, etches that are highly directional are required to etch evaporated seed layer whilst minimising the etching to the electroplated gold. Dry etching using mainly physical ion bombardment was selected to keep the etch anisotropic, but did not provide high selectivity between different materials.

A chlorine (Cl_2) based ICP etch [202] together with Argon (Ar) was used in the etching of the Au seed layer. Firstly the characterisation of the etch took place by measuring the etch rates of evaporated Au, PECVD SiO_2 layer and an electroplated trial sample. Etching 160 nm of Au and Ti adhesion layer took 47 seconds from observing the drop in reflectance signal of the laser, providing an etch rate of ≈ 204 nm/min. Next a 100 nm PECVD SiO_2 layer was etched in ≈ 100 s resulting in an etch rate of ≈ 60 nm/min. A selectivity of $\approx 3.4:1$ between the seed plus adhesion layer and dielectric layer was obtained.

A gold etch trial on an electroplated structure was performed to observe the characteristics of the etch on a realistic trap structure. The laser was positioned over the seed layer on an exposed area of the wafer, where the fastest etching occurs. The etch was manually stopped after reflectance signal dropped and the sample was visually checked under the microscope. Images were taken of the remaining gold within the tracks of the electrodes, shown in fig. 6.13 (a) and (b). It was observed that gold still remained around the bottom of the electrodes, leading into the narrower ($10\text{ }\mu\text{m}$) gaps. After a further 60 seconds of etching, the removal of the seed layer was observed in all exposed areas of the sample.

All the successfully electroplated samples were individually processed. An initial etch time was calculated to remove the seed and adhesion layers, after which the samples were then visually checked under the microscope. Additional etch times, typically in steps of 15 sec-

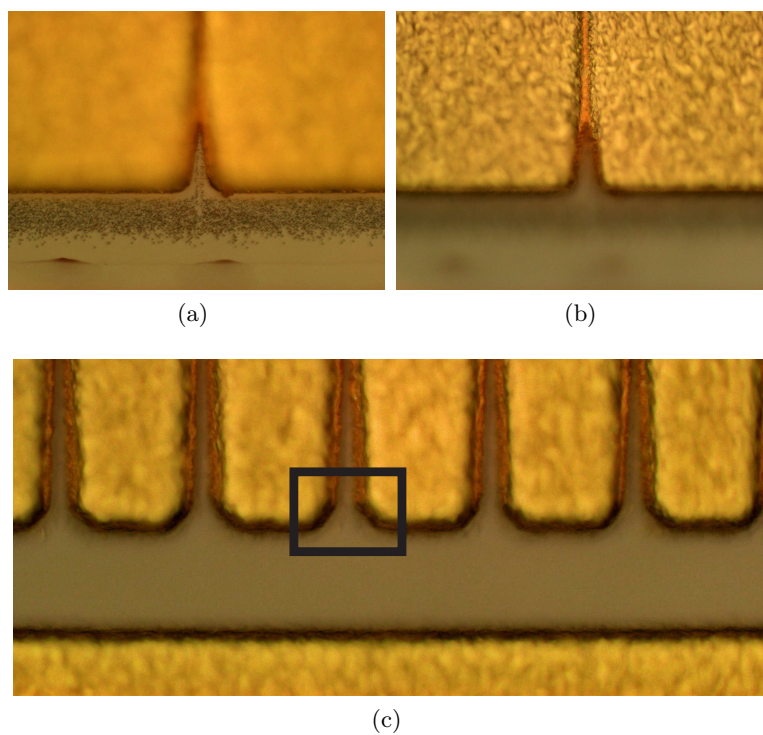


Figure 6.13: Au etch trail on an electroplated structure. (a) Microscope focused on the quartz wafer showing residual Au remaining after an initial etch. (b) Microscope focused on the tracks showing seed layer still present after the initial etch. (c) After a second etch step the Au seed layer was removed in the tracks.

onds were then estimated to remove the remaining Au within the tracks. Once it had been determined that all the Au within the tracks has been removed, the individual traps can be cleaved from the wafer.

6.4.7 Wafer dicing

The final step in the process is to cleave the trap structures from the wafer ready to be mounted on the chip carriers. To protect the samples whilst being cleaved, MicroChemicals AZ 6632 photoresist is spun onto the samples at 2.5 krpm for 30 seconds. This will produce an expected thickness of $\sim 4 \mu\text{m}$. A soft bake at 110°C for 10 minutes then hardens the resist. The wafers are manually scribed and cleaved to separate the traps. A solvent clean as described in section 6.1 then removes the resist and any residual quartz dust ready for mounting onto chip carriers.

Due to the number of individual electrodes each individual trap is documented under the microscope for possible defects. Shorting of adjacent electrodes can occur during the processing from spits of Au during the thermal evaporation steps. Areas of the chip limiting breakdown due to reduced electrode gaps from misalignment of masks or distortion of the resist during electroplating. The chips are then ready to be taken back to Sussex, packaged onto the chip carriers and mounted into the vacuum system.

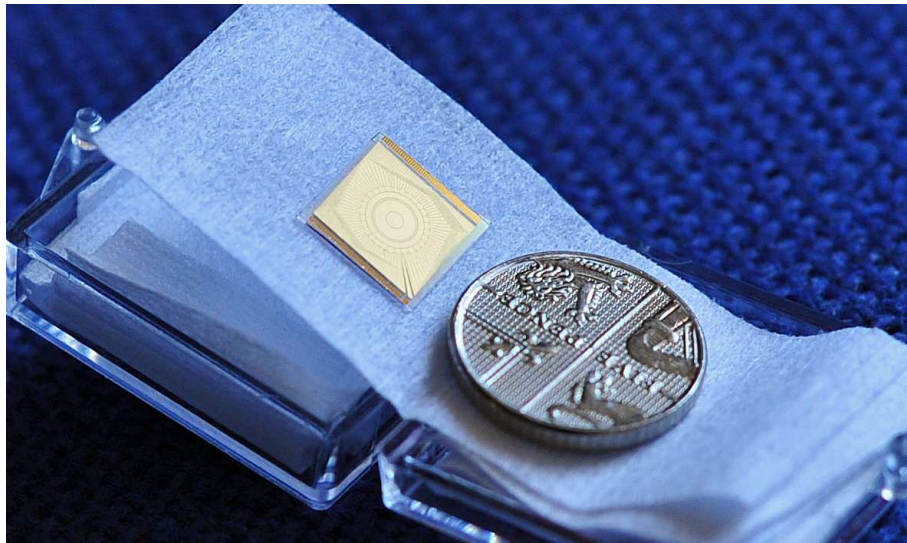


Figure 6.14: Picture of a ‘Big’ ring ion trap after the whole process sequence.

6.5 Process sequence for multi-layered ion traps

Quartz wafer  Photoresist  Ti/Au/Ti  SiO₂/Si₃N₄  Electroplated Au 

1 Underlying conducting layer

1(a) Wafer preparation

Scribe back of the wafer with sample number.

Solvent clean sample for 10 min each step with ultrasound in the following order.

- Ethyl lactate, rinse and N₂ blow dry.
- Acetone, just rinse.
- Methanol, rinse and N₂ blow dry.
- Isopropanol, rinse and N₂ blow dry.

Dehydration bake at 150°C for 10 min in convection oven.

1(a) Wafer preparation, solvent clean and dehydration bake



1(b) Pattern image reversal lift-off resist: MicroChemical AZ 5214E

Recipe for 1.4 μm thick photoresist.

- Spin coat at 4 krpm for 30 sec.
- 3 min air dry.
- Soft bake at 90°C for 5 min.
- Exposure with 1st layer mask for 2.0 sec.
- Post exposure bake (PEB) at 120°C for 120 sec.
- Exposure without mask for 22 sec.
- Development in MicroChemicals AZ 726MIF neat for 60 sec.

Inspect sample under optical microscope for defects in resist defining the long ‘buried’ wires causing electrically isolated electrodes.

1(b) Pattern AZ5214E image reversal resist, 1.4μm



1(c) Thermal evaporation of metallised layers

Solvent clean enough Au for 500 nm deposition and Ti (if required), 10 min each step with ultrasound.

- Acetone, just rinse.
- Isopropanol, rinse and N₂ blow dry.

Place sample into thermal evaporator with half the Au and pump down to 10⁻⁶ mbar.

Melt any metals that have been replace.

Deposit 10 nm Ti adhesion layer.

Deposit Au layer until the boat has been depleted. Note indicated thickness of the deposited Au.

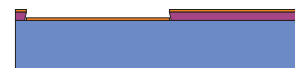
Open up the thermal evaporator, place the remaining Au into the boat and pump down to 10⁻⁶ mbar.

Deposit additional Au totalling 500 nm.

Deposit 10 nm Ti adhesion layer.

Remove sample from thermal evaporator.

1(c) Thermal evaporation of buried wires (15/500/15) nm of Ti/Au/Ti



1(d) Lift-off

Place sample into hot (70°C) acetone/NMP. Monitor the progress of the lift-off process providing gentle agitation with stirring and/or ultrasound if needed.

Solvent clean, 5 min for each step with ultrasound.

- Acetone, just rinse.

1(d) Lift off resist in acetone/NMP



- Isopropanol, rinse and N₂ blow dry.
- Inspect sample under optical microscope.
Measure total thickness with stylus profiler.

2 Insulating layer and vias

2(a) PECVD insulating layer

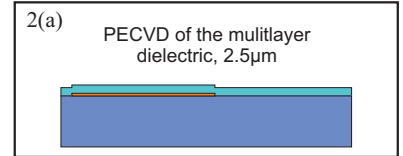
Prepare PECVD chamber and load sample onto shuttle with ceramic tweezers.

Close and pump down chamber to standby pressure.

Blanket deposition.

- Multi-layered dielectric layer 0.5 μm thick, alternating Si₃N₄ and SiO₂ layers each ≈ 80 nm thick.
- SiO₂ layer 1.5 μm thick.
- Repeat multi-layered dielectric layer step 0.5 μm thick.

Unload sample from chamber.

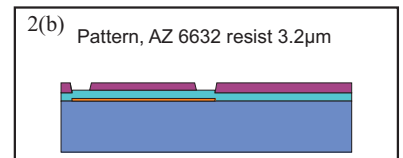


2(b) Pattern dry etch photoresist: MicroChemical AZ 5214E

Recipe for 3.2 μm thick photoresist.

- Spin coat at 4 krpm for 30 sec.
- Soft bake at 110°C for 5 min.
- Exposure with 2nd layer mask for 15.0 sec.
- Development in DI water:MicroChemicals AZ 400K diluted 4:1 for 60 sec.

Inspect sample under optical microscope before next step.



2(c) ICP etch

Attach sample to Si carrier wafer.

- Place Si wafer with wax onto a hot plate at 70°C.
- When wax is melted, place sample on top ensuring even coverage of wax.
- Remove and allow to cool.

Apply Y Vac 3 vacuum grease to backside of Si wafer and place onto shuttle.

Close and pump down chamber to standby pressure.

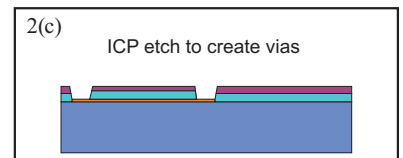
CHF₃ base ICP etch.

- Run etch for 5 min.
- Pause for a minimum of 5 min allowing the sample to cool.
- Resume etch until the reflectance signal saturates from Au layer (≈ 6 min).

Unload sample and wipe back of the Si wafer with isopropanol to remove the Y Vac 3 vacuum grease.

Remove sample from Si carrier wafer.

- Place sample and carrier wafer onto hot plate at 70°C to melt the wax.
- Detach sample and swab underside with trichlorethylene to remove the wax.



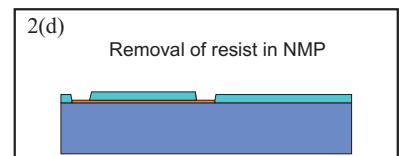
2(d) Strip photoresist

Place sample into hot (85°C) Microposit remover 1165 (NMP). Apply ultrasound to improve the process.

After 1 hour rinse sample and place into fresh NMP.

Solvent clean after another hour, 5 min each step with ultrasound.

- Acetone, just rinse.
- Isopropanol, rinse and N₂ blow dry.



Inspect under optical microscope for full development of resist before next step.

3 Electrode layer

3(a) Blanket deposition of adhesion and seed layers

Solvent clean enough Au for a 150 nm deposition and Ti (if required), 10 min each step with ultrasound.

- Acetone, just rinse.
- Isopropanol, rinse and N₂ blow dry.

Place sample into thermal evaporator with metals and pump down to 10⁻⁶ mbar.

Melt any metals that have been replace.

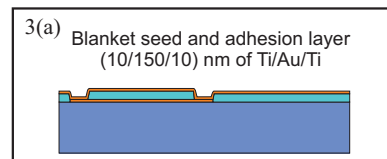
Deposit 10 nm Ti adhesion layer.

Deposit 150 nm Au layer.

Deposit 10 nm Ti adhesion layer.

Remove sample from thermal evaporator.

Measure total thickness with stylus profiler.



3(b) pt1 Pattern electroplating photoresist: KMPR 1025

Mount sample onto chuck and centre.

Apply resist directly from bottle.

Spin resist with ramped profile.

Remove edge bead with acetone swab.

Level edge bead with spin cycle at 500 rpm for 15 sec.

Soft bake on level hot plate.

- Ramp from room temperature to 65°C, hold for 10min.
- Ramp to 100°C, hold for 15min.
- Turn off hot plate, allow residual heat to cool down sample.
- Relaxation step minimum 4 hours, typically overnight.

Exposure with 3rd layer mask, 6×(20 sec exposure plus 1 min 30 sec pause).

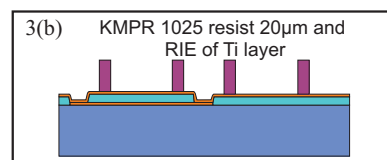
Relaxation step minimum of 1 hour.

Post exposure bake (PEB) on hot plate.

- Ramp from room temperature to 65°C, hold for 1min.
- Ramp to 100°C, hold for 20 sec.
- Turned off hot plate, ramp down quicker with beaker of water used as a heat sink.
- Remove sample when temperature reached below 30°C.

Relaxation step minimum of 10 min.

Development in ethyl lactate on vibration mount for 4 min 30 sec.



3(b) pt2 RIE Ti adhesion layer

Load sample onto shutter, close and pump down chamber to standby pressure.

Run SF₆ base RIE for ≈70 sec.

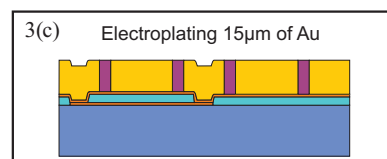
Stop etch when reflectance signal saturates from Au layer.

3(c) Electroplate sample. Performed in e2V cleanroom

Mount sample with wax to carrier wafer.

Attach electrical connections with silver dabs.

Set current density and time to electroplate 15-20 μm .



3(d) Strip photoresist

place sample onto hot plate, remove wax and silver dab with trichloroethylene.

Place sample into hot (85°C) Microposit remover 1165 (NMP) and apply ultrasound every hour for 2 hours.

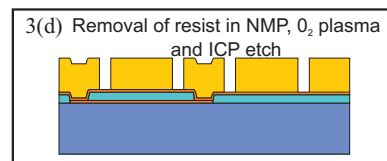
Rinse sample and place into fresh NMP.

After 4 hours perform solvent clean.

- Acetone, just rinse.
- Isopropanol, rinse and N₂ blow dry.

Inspect under optical microscope.

Perform additional cleaning if required, O₂ plasma step and further soaking with NMP.

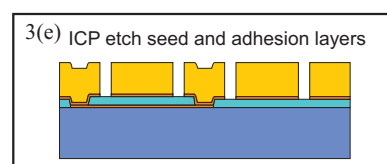


3(e) Dry etch adhesion and seed layers

Calculate initial etch time from adhesion and seed layer thickness from step 3(a) with an etch rate of ≈ 204 nm/min. Cl₂ based ICP etch.

- Load sample onto shutter, close and pump down chamber to standby pressure.
- Initial etch time typically 60 sec.
- Remove sample and inspect under optical microscope.

Repeat above etch in steps of 15 sec until residual gold within the electrode tracks is removed.



4 Wafer dicing

Cover sample with resist for cleaving, MicroChemicals AZ 6632.

- Spin at 2 krpm for 30 sec.
- Soft bake for 10 min at 110°C.

Dice up wafer for individual traps by scribing around the traps and cleaving.

Remove resist in acetone, then perform full solvent clean 10 min each step with ultrasound.

- Ethyl lactate, rinse and N₂ blow dry.
 - Acetone, just rinse.
 - Methanol, rinse and N₂ blow dry.
 - Isopropanol, rinse and N₂ blow dry.
-

6.6 Conclusion

Using MEMS based fabrication techniques at the University of Nottingham, multi-layered asymmetric ion traps were created. Using a thick negative photoresist, high aspect ratio electroplated electrodes are created. This provides shielding of the dielectric from the ion reducing the affects of stray charge. Improvements in the design and fabrication process can still be made. The buried wires were $3\text{ }\mu\text{m}$ wide to reduce capacitance of the ion trap, together with the length of up to 1 mm on some designs resulted in the wires to occasionally rip during lift-off. By increasing the width to $5\text{ }\mu\text{m}$ will help to alleviate the problem. The alignment between layers was made more difficult with the vias being the same size as other layers at the bond pads, this allowed for zero tolerance when aligning the mask. With alignment possible down to $2\text{ }\mu\text{m}$, the gaps at the edge of the chip will be reduced. By reducing the size of the vias at the edge will eliminate this problem and save time when aligning.

The next generation of the fabrication process will be to introduce planarisation steps that will provide a smooth surface to the electrodes. This can be achieved through chemical mechanical polishing techniques and developing etches that provide an equal selectivity between the resist and material to be etch. Other changes to the fabrication process are likely after the operation of the traps.

Chapter 7

Characterisation and testing of microfabricated ion traps

The operation of microfabricated ion traps requires electrical testing of the structures to determine the maximum applied voltage before breakdown and packaging of the traps before being mounted into the vacuum system and successfully operated. I will first discuss the voltage breakdown measurements performed in order to determine a final dielectric structure and then focus on the progress towards trapping of individual ions in a ring ion trap.

7.1 Voltage breakdown measurements

To apply sufficient voltage to the trap necessary for desired trap depths and secular frequencies, requires the ion trap structures outlined in section 4 to withstand more than the designed operating voltage of 400 V. Both bulk breakdown and surface flashover measurements were performed under vacuum to quantify the maximum applied voltage.

Bulk breakdown was performed on various dielectric structures, shown in fig. 7.4 and surface flashover across gaps of 5, 10 and 20 μm . Test samples were grown using the characterisation area of the mask (appendix A.9). Fabrication started with a reclaimed Si wafer on which a thermally evaporated 10 nm Ti adhesion layer, and a Au layer of ≈ 150 nm and another 10 nm Ti adhesion layer were deposited. Three different dielectric structures were then grown using plasma enhanced chemical vapour deposition (PECVD) within an isothermal PECVD reactor (Corial D250). A final thermally evaporated layer of

10 nm of Ti and 150-200 nm of Au was then added. Both patterned conducting layers were performed using lift-off with Microchemicals AZ514E image reversal resist, as described in section 6.2.1. An optical image of the final structures is shown in fig. 7.1.

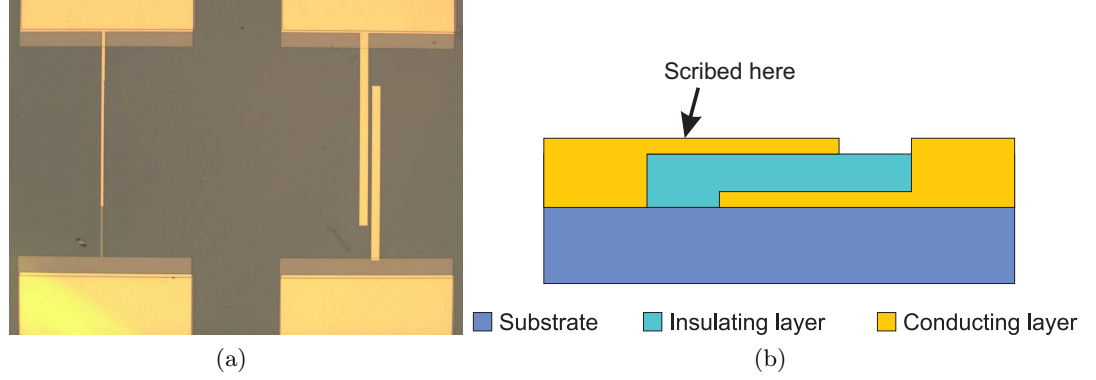


Figure 7.1: (a) Optical microscope image of two test samples. The sample on the left has two overlapping wires from different conducting layers to test bulk breakdown. The sample on the right has a gap of 20 μm to test surface flashover. (b) Side view schematic of a bulk breakdown sample.

After fabrication the samples are superglued to a ceramic chip carrier and wire bonded using 30 μm gold wire between the electrodes and chip carrier. A high power vacuum feedthrough was then attached and then encased in a glass belljar before being pumped down using a turbomolecular pump to 1×10^{-6} mbar. Breakdown measurements were performed with a 5 kV static voltage supply with an in built voltage divider producing 0-10 V. Using a calibrated voltmeter with an error of ± 10 mV the output voltage can be monitored resulting in an experimental error of ± 5 V. The setup is shown in fig. 7.2.

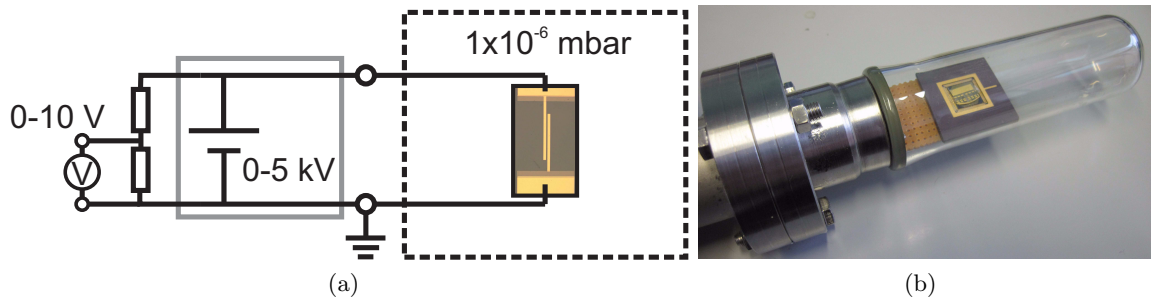


Figure 7.2: (a) Circuit diagram for voltage breakdown measurements, the breakdown voltage is measured from an in built voltage divider. (b) The test samples are mounted to a chip carrier and wire bonded before being placed under vacuum in a glass belljar.

Unfortunately after wire bonding up the test samples a finite resistance of ~ 10 K Ω was

measured as a result of the test samples being grown on a reclaimed Si wafer. Shown in fig. 7.1 (b) both electrodes make contact with the wafer due to the vias, causing the Si wafer to create an electrical connection between the electrodes. The top conducting wires were electrically isolated by manually scribing the sample (as shown in fig 7.1 (b)) whilst trying to keep the dielectric layer unaffected in the breakdown area. The samples were then checked to verify the correct breakdown process had occurred. Fig. 7.3 displays SEM images of surface flashover and bulk breakdown of the test samples, there is significant damage to both samples which would render the ion traps unusable if breakdown was to occur.

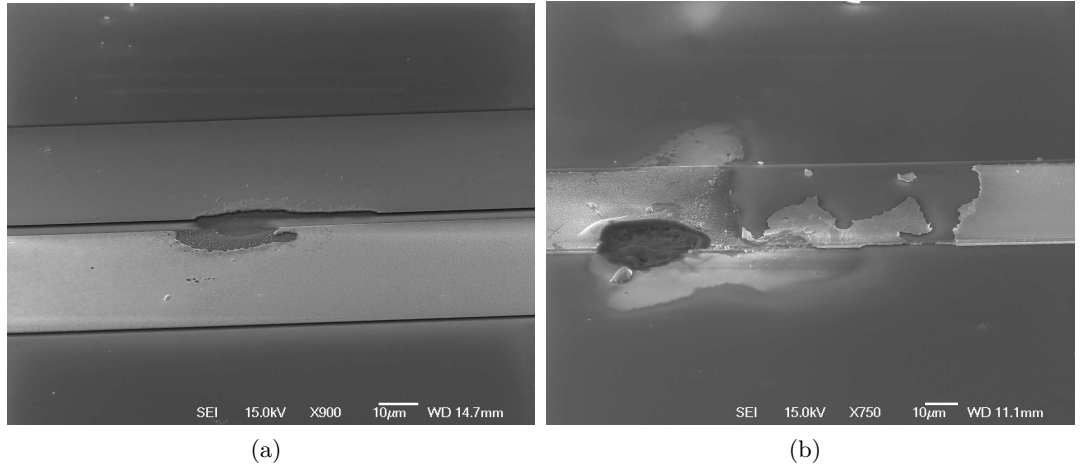


Figure 7.3: (a) SEM image of surface flashover over a 20 μm gap. (a) SEM image of bulk breakdown over a 2 μm SiO_2 layer showing the formation of a hot spot.

7.1.1 Bulk breakdown

With the limited number of samples and the need to manually scribe the samples for breakdown to occur, provided only four results. Therefore no conclusions comparing different dielectric structures could be obtained. Instead a minimum breakdown voltage was measured.

Three different structures shown in fig. 7.4 were tested, sample A consists of 2.0 μm of SiO_2 , sample B has the addition of two $\approx 80\text{nm}$ Si_3N_4 layers. Sample C has 2.0 μm of SiO_2 sandwich between a multi-layered structure of six alternating SiO_2 and Si_3N_4 layers of $\approx 80\text{nm}$ thick with a total thickness of 0.5 μm .

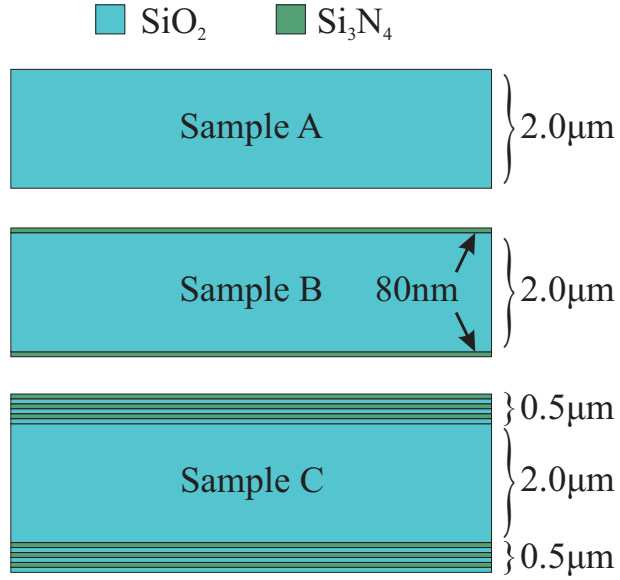


Figure 7.4: Dielectric structures of the samples used for bulk breakdown measurements. Sample A consists of $2.0 \mu\text{m}$ of SiO_2 . Sample B has the addition of two 80 nm Si_3N_4 layers. Sample C the addition of six $\sim 80 \text{ nm}$ alternating SiO_2 and Si_3N_4 layers totalling $0.5 \mu\text{m}$.

Table 7.1: Bulk breakdown measurements for different dielectric structures.

Sample	Breakdown voltage (V)	Thickness (μm)
A	2705 ± 5	2.0
B	$1679, 1740 \pm 5$	2.16
C	692 ± 5^a	3.0

^a The sample was damaged during isolation of the top conducting layer.

A list of the results is shown in table 7.1, all samples displayed a far greater breakdown voltage than required. The final dielectric structure was determined through a compromise between decreased trap capacitance through a thicker layer and limiting the variations in the electrode topography from the plasma etch of the vias. The final structure was based on sample C with the exception of a 1.5 μm thick SiO_2 layer in the centre.

7.1.2 Surface flashover

The electric field strength for surface flashover has been measured to be a factor of 2.5 less than that for bulk breakdown of the same material, dimensions and deposition process [101]. Surface flashover is therefore expected to be the limiting factor in the electrical breakdown of the ion traps presented in this thesis.

Previous surface flashover work of gold electrodes on polished quartz was carried out by Dr Robin Sterling [151]. In his work mean surface flashover measurements occurred at ≈ 480 V across a $5\mu\text{m}$ gap, shown in fig. 7.5. This is the minimum gap size of the micro-fabricated traps presented in this thesis and would be advantageous if surface flashover voltage could be increased. Measurements across silicon nitride were investigated to see if the voltage threshold before surface flashover occurred could be increased and therefore increase the reliability of the traps.

The process of surface flashover presented in ref [151] is repeated here for clarity and provides a fit to the data. Surface flashover is described by secondary electron emission avalanche (SEEA) across the dielectric surface. Electrons emitted at the triple point, the interface between the electrode (denoted cathode), dielectric and vacuum are accelerated towards the anode. Upon impact with the dielectric surface desorbed gas molecules are emitted leading to a gas layer above the electrodes. The desorbed gas molecules are ionised from emitted electrons and accelerated towards the cathode leading to a build up of charge. Further increase in electron emission occurs, leading to a Townsend-like breakdown through the gas layer [104, 203, 204]. The voltage when flashover occurs is given by [104]

$$V_b = \left[\frac{\varphi de}{2\epsilon_0} \right]^{\frac{1}{2}} \quad (7.1)$$

where d is the electrode separation, e is the electron charge and ϵ_0 is the permittivity of

free space. The constant φ is defined as

$$\varphi = \frac{v_0 M_{cr} A_1}{\gamma v_e \tan \theta} \quad (7.2)$$

and is composed of parameters describing the flashover process. M_{cr} , the amount of desorbed gas per m^2 at the point of flashover, γ , the efficiency of electron stimulated gas desorption, v_0 the molecule ejection velocity, v_e the electron velocity, given by $v_e = 5.94 \times 10^5 \sqrt{A_1} \text{ ms}^{-1}$ [104] and θ , the angle of the emitted electrons from the triple point, given by $\tan \theta = [2A_0/(A_1 - A_0)]^{\frac{1}{2}}$, where A_1 and A_0 are the electron impact and emission energies [104].

Difficulty in accurately measuring M_{cr} , γ and v_0 exists, with a large spread of several orders of magnitude for different dielectric materials and experimental setups [104, 203–205] and A_1 only known for a few dielectrics [104]. This has lead us to treat φ as a fitting parameter between results from different fabrication processes.

As previously mentioned, surface flashover measurements across silicon nitride were investigated to see if the voltage threshold before surface flashover occurred could be increased. To gather enough results and compare flashover measurements a second batch of test samples were made with just the dielectric and top electrode layer. The finalised dielectric structure was grown onto a Si wafer ending with a nitride layer. 200 nm Au electrodes were patterned on top of the dielectric via lift off. Static voltage flashover measurements were performed with electrode separations of 5, 10 and 20 μm . The results are shown in fig. 7.5. Individual measurements are shown as empty diamonds with the mean as solid diamonds. An uncharacteristic dip at 10 μm is observed, thought to be due to a defect on the mask. Two fits to the data were performed, the first includes the mean values of all three electrode gaps providing a $\varphi = (18.1 \pm 4.4 \times) 10^{18} \text{ eV m}^{-2}$. Compared to the previous results of Au on quartz shown by the solid triangles, surface flashover is increased approximately by a factor of two. The second fit using the mean values at 5 and 20 μm gaps provides an increase of approximately of 2.5 times in flashover voltage with a $\varphi = 29.2 \pm 2.6 \times 10^{18} \text{ eV m}^{-2}$.

To confirm that the fabrication process did not change the increase in flashover and was due to the dielectric material, gold electrodes on quartz using a lift-off process was compared to initial measurements fabricated using wet etching. Five measurements at 10 μm

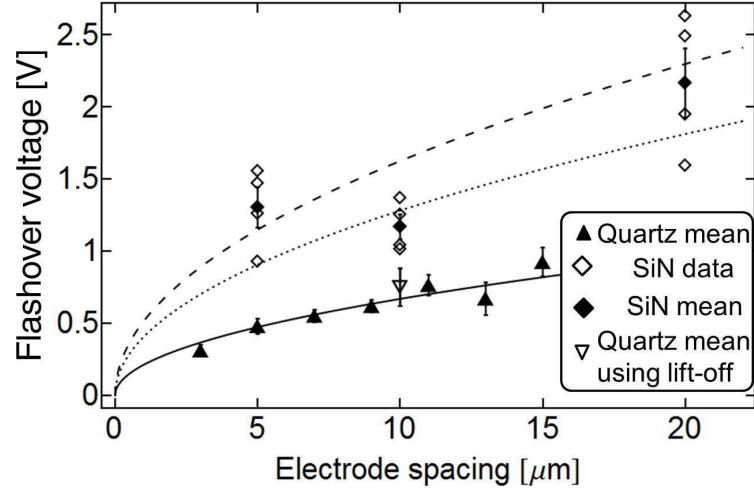


Figure 7.5: Comparison between Au on PECVD nitride and Au on quartz flashover measurements. PECVD nitride data are shown as empty diamonds with the average shown as a solid diamond. The dotted line is a fit to all the data whilst the dashed line to 5 and 20 μm gaps using equation 7.1. Au on quartz measurements are shown as solid triangles, an average from rf and static measurements. The average of the second set of Au on quartz measurements is shown as an empty inverted empty triangle and shows good agreement with the first set of data. Equation 7.2 is used to provide a fit to the data.

electrode separation were performed. The results show to be within agreement of each other. The mean flashover voltage for gold on quartz using lift-off fabrication process is shown in fig. 7.5 by the inverted triangle.

Using a PECVD multi-layered dielectric layer, both bulk breakdown and surface flashover measurements presented are more than required for the desired operation of the ion traps presented in this thesis. Surface flashover, typically the limiting process was significantly increased using a PECVD Silicon nitride layer over gold on quartz wafer. Reduced electrode gaps can be implemented resulting in reduced exposed dielectrics as seen from the ion.

7.2 Vacuum System

To allow more flexibility and a faster turn around time in the testing and operation of chips, a third vacuum system was created. Based on the second vacuum system as described in section 3.3.2 a couple of adjustments were performed to the design. The removal of a 5-way cross piece was performed to reduce the volume of the system allowing for more

efficient pumping. A new recessed window shown in fig. 7.6, designed by Bjoern Lekitsch, allowing for the integration of an Argon ion gun for in situ cleaning of the ion chips. Previous studies have shown a reduction in anomalous heating by a factor of 100 [135]. This has great impact on the coherence time of gate operations and allows for reduced ion heights.

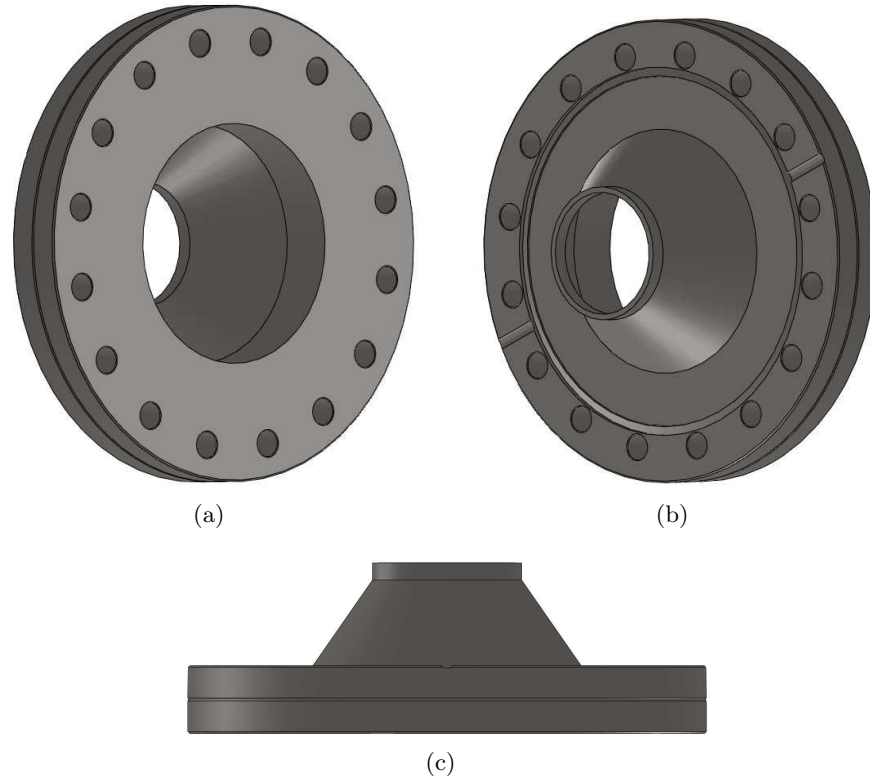


Figure 7.6: Custom recessed viewport designed by Bjoern Lekitsch. (a) Atmosphere side (b) Vacuum side (c) Side view.

7.2.1 Assembly

Careful assembly of the vacuum system needs to take place to achieve ultra high vacuum (UHV) down to 10^{-12} mbar, resulting in reduced background collisions and increased ion lifetime. A clean area with personal protective equipment (PPE) consisting of overalls and gloves is used to ensure no contamination in the assembly procedure of the vacuum system.

The first step was cleaning and pre baking the stainless steel vacuum parts. Each part was submerged in acetone and ultrasound was applied for 10 minutes. A methanol rinsed was then employed to remove any residual acetone causing stains. The vacuum parts were

then wrapped in aluminium foil and pre baked in an oven at 200° for a week. This creates a layer of chromium oxide, reducing the outgassing of hydrogen [206].

All other parts of the vacuum system including the wires, chip bracket, screws and fixings were then solvent cleaned. The viewports were only cleaned in isopropanol with results using methanol showing damage to the coatings [207].

Starting from the pump end of the vacuum system the parts are assembled by placing a copper gasket between the ConFlat (CF) flanges of each vacuum part and tightening of the bolts in a star pattern to create an even seal. The 6 pin oven feedthrough (Kurt J Lesker pt No. EFT0265063) is attached to oxygen free copper wire using a barrel connecting and threaded with ceramic beads to provide electrical insulation. Microwave feedthroughs (Vacom pt No. CF16-SMA50-SH-DE-CE-INC) are attached to RG-405 high frequency coaxial cable. Both the oven wires and microwave coaxial cables are then passed through the custom elbow and before attaching the combined spherical octagon weldable cluster (Kurt J Lesker pt No. MCF600-SphOct-F2C8 and MCF450-WldClstr-E1A4 respectively).

The chip bracket is assembled by pressing each male pin receptacle (Mill Max pt No. 0133-0-15-15-30-27-04-0) through the top PEEK plate and into the bottom plate, this was then repeated for all 100 pins. The static control voltages are supplied through two 50 pin D-type feedthrough welded to a 6" CF flange (Kurt J Lesker pt No. IFDGG501056AX). Kapton coated wires are then stripped and crimped to the female pin receptacle (Mill Max pt No. 0672-4-15-15-30-27-10-0). Each wire is pressed mounted with a male pin from the rear side of the chip bracket. After connecting all the wires a map documenting each pin receptacle to an associate D-type feedthrough pin is made by testing for an electrical connection. Full details of the map together with the respective bond pad on the ceramic pin grid array (CPGA) chip carrier (Global Chip Materials pt No. PGA20855101) is presented in appendix B. The rf and ground pins are attached to rf feedthrough directly above the octagon.

Construction of the atomic ovens was performed by spot welding a piece of constantan foil with a stainless steel tube and copper wire. The stainless steel tubes are then filled with a piece of solid Yb, the enriched $^{171}\text{Yb}^+$ ovens are filled with 90% enriched Yb from Oak Ridge National Laboratory (pt No. OA0036). The natural ovens are filled with Yb from

from Goodfellow Cambridge Limited (pt No. GO0196). Four ovens are mounted within the vacuum system, an enriched and natural oven on the front side of the chip bracket for asymmetric traps and two on the back side for symmetric traps and backside loading. Each atomic oven is attached to a beaded wire and electrically tested to determine the associate oven feedthrough pin. Layout and pin arrangement of the ovens is shown in fig. 7.7.

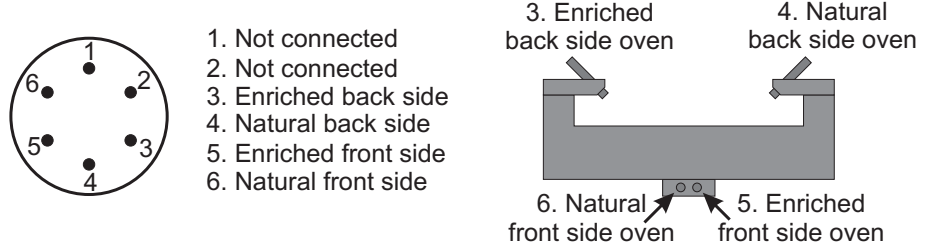


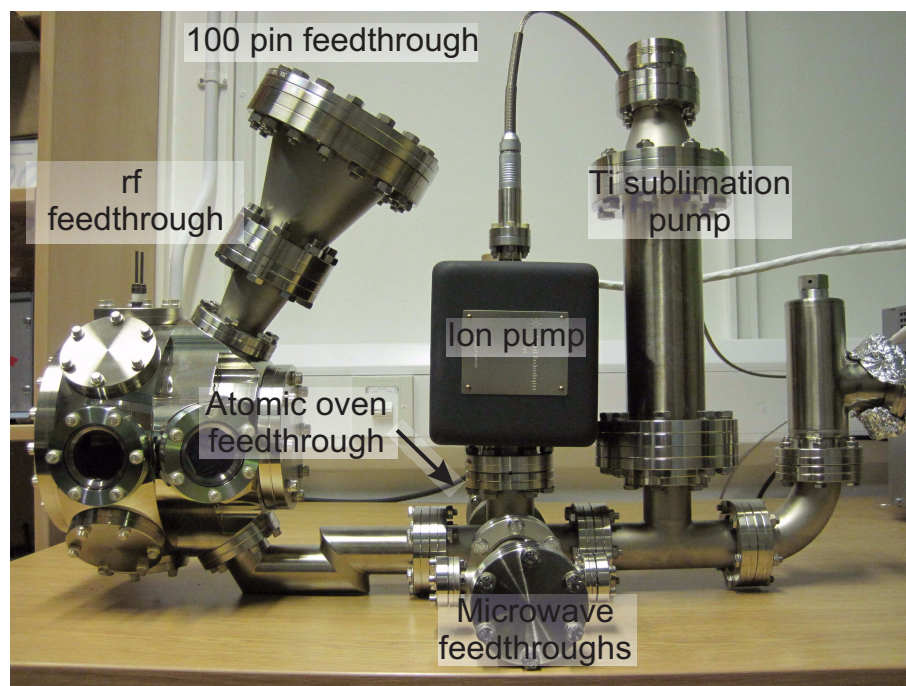
Figure 7.7: Layout and pin arrangement of the frontside and backside ovens.

The viewports are then attached together with the ion pump and titanium sublimation pump (TSP) to close the vacuum system. An initial pumping down and bake procedure was employed to clean the system before inserting a trap into the system. A turbo molecular pump evacuated the system down to 1×10^{-5} mbar where leak testing is then performed. Using helium (He) gas and a residual gas analyser (RGA), helium is sprayed around each flange with a rise in signal showing a leak. Each flange is tightened until no more leaks are visible at the current pressure.

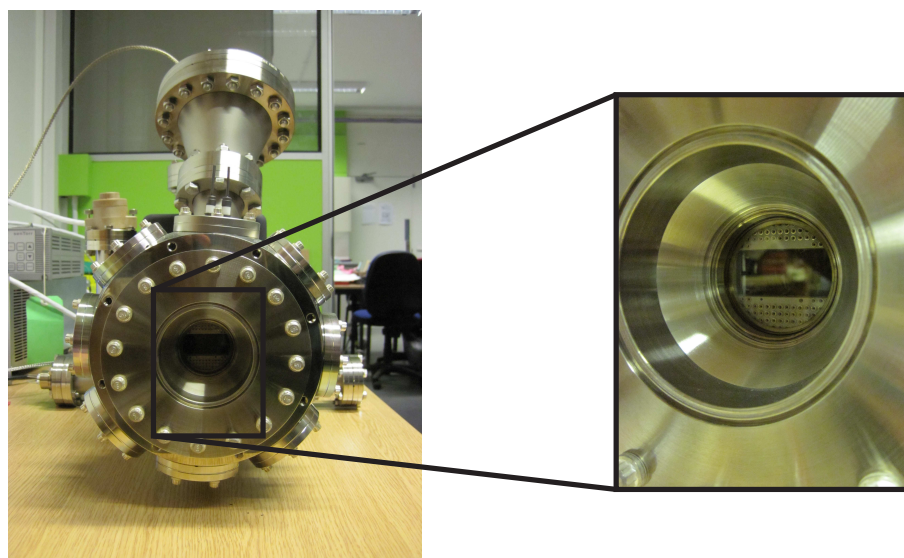
Outgassing of certain vacuum components is then performed. Each oven was fired for 5 minutes at 6.5 A, the expected operating current. Each TSP filament was then outgassed by ramping the current at 5 A per minute up to 35 A and then held for an hour. The vacuum system is then baked in an oven at 200°C for two weeks. The temperature is ramped at $\approx 10^\circ\text{C}$ per hour determined by the viewports. During baking the external and internal ion pumps are turned on, after a few days the system is isolated by tightening the internal valve before ramping the pressure back to room temperature.

7.3 Trap packaging

The traps will be mounted onto a 204-pin ceramic pin grid array (CPGA) chip carrier (Global Chip Materials pt No. PGA20855101). Silver epoxy (EPO-TEK H21) is used to



(a)



(b)

Figure 7.8: (a) Picture of the assembled vacuum system (b) Front view of the hemisphere and custom recessed window.

attach a trap to a 3 mm aluminum spacer to bring the ion trap surface in alignment with the front side ovens. Each electrode will be wire bonded using 127 μm gold ribbon to an associate bond pad on the chip carrier. A picture of a ‘big’ ring ion trap before wire bonding is shown in fig. 7.9.

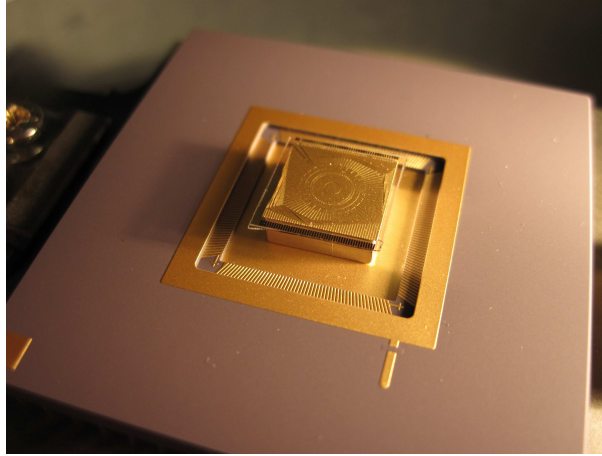


Figure 7.9: Photo of a ‘Big’ ring ion trap before being wire bonded.

Currently the development of in vacuum filtering [47, 153] is taking place to reduce the noise pickup inside the vacuum of the static control wires and provide a low impedance path to ground for the rf [79]. Unfortunately there is not enough space on the conducting gold ring surrounding the bond pads to accommodate filters for all the electrodes.

7.4 Further work

The next stages in the testing of the chips is to package the chip carriers with low pass filters from surface mount components. In order to accommodate all the filter components an evaporated gold layer to extend the ground plane is currently under progress before the filter components can be mounted onto the chip carrier and wire bonding of the electrodes. Once mounted into the vacuum system the traps can then be pumped down and baked to achieve the required operating pressure.

Initial experiments with the ring trap will be the characterisation of the ion trap through ion secular frequency measurements and heating rate measurements. Mapping out the potential around the ring will be important in demonstration of shuttling around the ring showing periodic boundary conditions.

Chapter 8

Conclusion

In this thesis I have described the development towards trapping in multi layered asymmetric ion traps. Firstly the implementation of an Yb ion trap experiment was achieved. Details of the experimental setup is presented, vacuum systems capable of housing both symmetric and asymmetric traps with at least 90 individual static control electrodes. Laser stabilisation for efficient Doppler cooling, the application of high voltages via a helical resonator and an imaging system for the detection of single ions are presented. Using a macroscopic two-layer symmetric ion trap, different Yb^+ isotopes were successfully trapped and transition wavelengths measured. The characterisation of the trap through a heating rate measurement was performed, the result obtained was consistent with previously published measurements.

Scaling up to larger ion trap arrays requires high number of control electrodes. The design of multi-layered asymmetric ion trap designs allows for isolated control electrodes providing a high density of individual trapping zones. Several designs are presented incorporating optimised electrode geometries for maximum trap depth at a given ion height and optimised control electrodes for fast ion separation and combination. Trapping ions in a two-dimensional array allows the ability to study more complex spin systems. Utilising isolated electrodes, a two-dimensional hexagonal lattice is presented with individual control above each lattice site. The geometry of the lattice has been optimised to maximise the ion-ion interaction rate to decoherence rate across the array. Ring ion traps are presented, through connecting the ends of a linear ion trap periodic boundary conditions can be created and any component of the pseudopotential within the axial direction can be eliminated. This opens up ring trap architectures to study the implementation of quantum simulations [181].

Fabrication of the ion trap arrays was performed. Through electroplating, thick electrodes an aspect ratio of 4:1 between the electrode height and gap was achieved. This allows for shielding of the dielectric from the ion necessary in reducing stray electric field due to charge build on dielectric surfaces. Thick electrodes will also allow for the application of high currents with reduced power to the ion trap, required for creating high magnetic field gradients in the generation microwave quantum logic gates [208, 209].

Characterisation of the ion trap structures was performed by performing bulk breakdown and surface flashover measurements. Results show the application of high voltages more than sufficient for the operation of the ion traps. Surface flashover voltage measurements over PECVD silicon nitride showed an improvement of 2.5 compared to polished quartz. This allows for the next generation of ion traps to be scaled down allowing for faster gate operations. The progress is now focused on successful trapping and characterisation the ion traps.

Bibliography

- [1] Lov K. Grover. Quantum mechanics helps in searching for a needle in a haystack. *Phys. Rev. Lett.*, 79:325–328, Jul 1997. [2](#)
- [2] P. W. Shor. Algorithms for quantum computation: Discrete logarithms and factoring. In *Proceedings, 35th Annual Symposium on Foundations of Computer Science, IEEE Computer Soc. Press*, pages 124–134, 1994. [2](#)
- [3] E. Knill, R. Laflamme, and G. J. Milburn. A scheme for efficient quantum computation with linear optics. *Nature*, 409:46–52, 2001. [2](#)
- [4] Neil A. Gershenfeld and Isaac L. Chuang. Bulk spin-resonance quantum computation. *Science*, 275:350–356, 1997. [2](#)
- [5] David G. Cory, Amr F. Fahmy, , and Timothy F. Havel. Ensemble quantum computing by nmr spectroscopy. *Proc. Natl Acad. Sci. USA*, 94(5):1634–1639, 1997. [2](#)
- [6] Y. Nakamura, Yu. A. Pashkin, and J. S. Tsai. Coherent control of macroscopic quantum states in a single-cooper-pair box. *Nature*, 398:786–788, 1999. [2](#)
- [7] John M. Martinis, S. Nam, J. Aumentado, and C. Urbina. Rabi oscillations in a large josephson-junction qubit. *Phys. Rev. Lett.*, 89:117901, Aug 2002. [2](#)
- [8] I. Chiorescu, Y. Nakamura, C. J. P. M. Harmans, and J. E. Mooij. Coherent quantum dynamics of a superconducting flux qubit. *Science*, 299:1869–1871, 2003. [2](#)
- [9] T. D. Ladd, D. Maryenko, Y. Yamamoto, E. Abe, and K. M. Itoh. Coherence time of decoupled nuclear spins in silicon. *Phys. Rev. B*, 71:11401, 2005. [2](#)
- [10] M. V. Gurudev Dutt, L. Childress, L. Jiang, E. Togan, J. Maze, F. Jelezko, A. S. Zibrov, P. R. Hemmer, and M. D. Lukin. Quantum register based on individual electronic and nuclear spin qubits in diamond. *Science*, 316:1312–1316, 2007. [2](#)

- [11] Oliver Morsch and Markus Oberthaler. Dynamics of bose-einstein condensates in optical lattices. *Rev. Mod. Phys.*, 78:179–215, Feb 2006. [2](#)
- [12] Marco Anderlini, Patricia J. Lee, Benjamin L. Brown, Jennifer Sebby-Strabley, William D. Phillips, and J. V. Porto. Controlled exchange interaction between pairs of neutral atoms in an optical lattice. *Nature*, 448:452–456, 2007. [2](#)
- [13] J. I. Cirac and P. Zoller. A scalable quantum computer with ions in an array of microtraps. *Nature*, 404:579–581, 2000. [2](#), [3](#), [11](#)
- [14] D. Kielpinski, C.R. Monroe, and D.J. Wineland. Architecture for a large-scale ion-trap quantum computer. *Nature*, 417:709–711, 2002. [2](#), [3](#), [68](#)
- [15] Wolfgang Paul. Electromagnetic traps for charged and neutral particles. *Rev. Mod. Phys.*, 62(3):531–540, Jul 1990. [2](#)
- [16] H G Dehmelt. Radiofrequency spectroscopy of stored ions i: Storage. *Adv. At. Mol. Phys.*, 3:53, 1967. [2](#), [9](#), [60](#), [68](#)
- [17] Wolfgang Paul. Electromagnetic traps for charged and neutral particles. *Rev. Mod. Phys.*, 62(3):531–540, Jul 1990. [2](#)
- [18] P. K. Ghosh. Oxford University Press, New York, 1995. [2](#), [8](#)
- [19] G. Zs. K. Horvath, R. C. Thompson, and P. L. Knight. Fundamental physics with trapped ions. *Contemporary Physics*, 38(1):25–48, 1997. [2](#)
- [20] R. C. Thompson. Spectroscopy of trapped ions. *Adv. At. Mol. Phys.*, 31:63–136, 1993. [2](#)
- [21] D. J. Wineland, C. Monroe, W. M. Itano, D. Leibfried, B. E. King, and D. M. Meekhof. Experimental issues in coherent quantum-state manipulation of trapped atomic ions. *J. Res. Nat. Inst. Stand. Tech.*, 103(3):259–328, 1998. [2](#), [24](#), [27](#)
- [22] M. Keller, B. Lange, K. Hayasaka, W. Lange, and H. Walther. Deterministic cavity quantum electrodynamics with trapped ions. *J. Phys. B: At. Mol. Opt. Phys.*, 36(3):613–622, 2003. [2](#)
- [23] Peter F. Herskind, Aurélien Dantan, Joan P. Marler, Magnus Albert, and Michael Drewsen. Realization of collective strong coupling with ion coulomb crystals in an optical cavity. *Nature Phys.*, 5:494–498, 2009. [2](#)

- [24] Marisa Pons, Veronica Ahufinger, Christof Wunderlich, Anna Sanpera, Sibylle Braungardt, Aditi Sen(De), Ujjwal Sen, and Maciej Lewenstein. Trapped ion chain as a neural network: Error resistant quantum computation. *Phys. Rev. Lett.*, 98(2):023003, Jan 2007. [2](#), [77](#)
- [25] A. Friedenauer, H. Schmitz, J. T. Glueckert, D. Porras, and T. Schaetz. Simulating a quantum magnet with trapped ions. *Nature Phys.*, 4:757–761, 2008. [2](#), [3](#)
- [26] M. Johanning, A. F. Varón, and C. Wunderlich. Quantum simulations with cold trapped ions. *J. Phys. B*, 42(15):154009, 2009. [2](#), [77](#)
- [27] R. J. Clark, T. Lin, K. R. Brown, and I. L. Chuang. A two-dimensional lattice ion trap for quantum simulation. *J. Appl. Phys.*, 105:013114, 2009. [2](#), [3](#), [77](#)
- [28] K. Kim, M.-S. Chang, S. Korenblit, R. Islam, E. E. Edwards, J. K. Freericks, G.-D. Lin, L.-M. Duan, and C. Monroe. Quantum simulation of frustrated ising spins with trapped ions. *Nature*, 465:590–593, 2010. [2](#), [3](#), [77](#), [85](#)
- [29] Th. Udem, S. A. Diddams, K. R. Vogel, C. W. Oates, E. A. Curtis, W. D. Lee, W. M. Itano, R. E. Drullinger, J. C. Bergquist, and L. Hollberg. Absolute frequency measurements of the hg^+ and ca optical clock transitions with a femtosecond laser. *Phys. Rev. Lett.*, 86(22):4996–4999, May 2001. [2](#)
- [30] S. A. Webster, P. Taylor, M. Roberts, G. P. Barwood, and P. Gill. Kiloherzt-resolution spectroscopy of the $^2s_{1/2} - ^2f_{7/2}$ electric octupole transition in a single $^{171}yb^+$ ion. *Phys. Rev. A*, 65(5):052501, Apr 2002. [2](#)
- [31] Chr. Tamm, S. Weyers, B. Lipphardt, and E. Peik. Stray-field-induced quadrupole shift and absolute frequency of the 688-thz $^{171}yb^+$ single-ion optical frequency standard. *Phys. Rev. A*, 80(4):043403, Oct 2009. [2](#)
- [32] M. Chwalla, J. Benhelm, K. Kim, G. Kirchmair, T. Monz, M. Riebe, P. Schindler, A. S. Villar, W. Hänsel, C. F. Roos, R. Blatt, M. Abgrall, G. Santarelli, G. D. Rovera, and Ph. Laurent. Absolute frequency measurement of the $^{40}ca^+ 4s^2s_{1/2} - 3d^2d_{5/2}$ clock transition. *Phys. Rev. Lett.*, 102(2):023002, Jan 2009. [2](#)
- [33] J. I. Cirac and P. Zoller. Quantum computations with cold trapped ions. *Phys. Rev. Lett.*, 74(20):4091–4094, May 1995. [2](#), [3](#)
- [34] H. Häffner, C. F. Roos, and R. Blatt. Quantum computing with trapped ions. *Phys. Rep.*, 469(4):155–203, 2008. [2](#)

- [35] R. C. Thompson, S. Donnellan, D. R. Crick, and D. M. Segal. Applications of laser cooled ions in a penning trap. *J. Phys. B: At. Mol. Opt. Phys.*, 42:154003, 2009. [3](#), [6](#)
- [36] J. R. Castrejón-Pita, H. Ohadi, D. R. Crick, D. F. A. Winters, D. M. Segal, and R. C. Thompson. Novel designs for penning ion traps. *J. Mod. Opt.*, 54(11):1581–1594, 2007. [3](#)
- [37] D. P. DiVincenzo. Quantum computation. *Science*, 270:255–261, 13 October 1995. [3](#), [96](#)
- [38] D. Leibfried, D. M. Meekhof, B. E. King, C. Monroe, W. M. Itano, and D. J. Wineland. Experimental determination of the motional quantum state of a trapped atom. *Phys. Rev. Lett.*, 77(21):4281–4285, Nov 1996. [3](#)
- [39] D. Leibfried, D. M. Meekhof, B. E. King, C. Monroe, W. M. Itano, and D. J. Wineland. Experimental preparation and measurement of quantum states of motion of a trapped atom. *J. Mod. Opt.*, 44:2485, 1997. [3](#)
- [40] D. Leibfried, B. DeMarco, V. Meyer, D. Lucas, M. Barrett, J. Britton, W. M. Itano, B. Jelenkovic, C. Langer, T. Rosenband, and D. J. Wineland. Experimental demonstration of a robust, high-fidelity geometric two ion-qubit phase gate. *Nature*, 422:412–415, 2003. [3](#)
- [41] Anders Sørensen and Klaus Mølmer. Quantum computation with ions in thermal motion. *Phys. Rev. Lett.*, 82(9):1971–1974, Mar 1999. [3](#), [11](#)
- [42] J. Benhelm, G. Kirchmair, C. F. Roos, and Rainer Blatt. Towards fault-tolerant quantum computing with trapped ions. *Nature Phys.*, 4:463–466, 2008. [3](#)
- [43] D. M. Lucas, B. C. Keitch, J. P. Home, G. Imreh, M. J. McDonnell, D. N. Stacey, D. J. Szwer, and A. M. Steane. A long-lived memory qubit on a low-decoherence quantum bus. *arXiv:0710.4421v1*, 2007. [3](#)
- [44] A. H. Myerson, D. J. Szwer, S. C. Webster, D. T. C. Allcock, M. J. Curtis, G. Imreh, J. A. Sherman, D. N. Stacey, A. M. Steane, and D. M. Lucas. High-fidelity readout of trapped-ion qubits. *Phys. Rev. Lett.*, 100(20):200502, May 2008. [3](#), [44](#)
- [45] M. Acton, K.-A. Brickman, P.C. Haljan, P.J. Lee, L. Deslauriers, and C. Monroe. Near-perfect simultaneous measurement of a qubit register. *Quantum Inf. Comp.*, 6(6):465—482, 2006. [3](#)

- [46] D. Stick, W. K. Hensinger, S. Olmschenk, M. J. Madsen, K. Schwab, and C. Monroe. Ion trap in a semiconductor chip. *Nature Phys.*, 2:36–39, 2006. [3](#), [20](#), [24](#), [96](#), [97](#)
- [47] S. Seidelin, J. Chiaverini, R. Reichle, J. J. Bollinger, D. Leibfried, J. Britton, J. H. Wesenberg, R. B. Blakestad, R. J. Epstein, D. B. Hume, W. M. Itano, J. D. Jost, C. Langer, R. Ozeri, N. Shiga, and D. J. Wineland. Microfabricated surface-electrode ion trap for scalable quantum information processing. *Phys. Rev. Lett.*, 96(25):253003, Jun 2006. [3](#), [24](#), [96](#), [142](#)
- [48] W. K. Hensinger, S. Olmschenk, D. Stick, D. Hucul, M. Yeo, M. Acton, L. Deslauriers, and C. Monroe. T-junction ion trap array for two-dimensional ion shuttling, storage, and manipulation. *Appl. Phys. Lett.*, 88:034101, 2006. [3](#), [17](#), [18](#), [68](#)
- [49] R. B. Blakestad, C. Ospelkaus, A. P. VanDevender, J. M. Amini, J. Britton, D. Leibfried, and D. J. Wineland. High-fidelity transport of trapped-ion qubits through an x -junction trap array. *Phys. Rev. Lett.*, 102(15):153002, Apr 2009. [3](#), [17](#), [18](#), [68](#), [70](#)
- [50] A. Steane. The ion trap quantum information processor. *Appl. Phys. B*, 64:623–642, 1997. [3](#)
- [51] R. Feynman. Simulating physics with computers. *Int. J. Theor. Phys*, 21(6/7):467–488, 1982. [3](#)
- [52] Matthias Troyer and Uwe-Jens Wiese. Computational complexity and fundamental limitations to fermionic quantum monte carlo simulations. *Phys. Rev. Lett.*, 94:170201, May 2005. [3](#)
- [53] Anders W. Sandvik. Ground states of a frustrated quantum spin chain with long-range interactions. *Phys. Rev. Lett.*, 104:137204, Mar 2010. [3](#), [77](#)
- [54] R. Islam, E.E. Edwards, K. Kim, S. Korenblit, C. Noh, H. Carmichael, G.-D. Lin, L.-M. Duan, C.-C. Joseph Wang, J.K. Freericks, and C. Monroe. Onset of a quantum phase transition with a trapped ion quantum simulator. *Nature Commun*, 2:377, 2011. [3](#), [85](#)
- [55] Joseph W. Britton, Brian C. Sawyer, Adam C. Keith, C.-C. Joseph Wang, James K. Freericks, Hermann Uys, Michael J. Biercuk, and John. J. Bollinger. Engineered 2d ising interactions on a trapped-ion quantum simulator with hundreds of spins. *Nature*, 484:489–492, 2012. [3](#), [77](#)

- [56] James D. Siversns, Seb Weidt, Kim Lake, Bjoern Lekitsch, Marcus D. Hughes, and Winfried K. Hensinger. Optimization of two-dimensional ion trap arrays for quantum simulation. *New J. Phys.*, 14, 2012. [3](#), [77](#), [78](#), [80](#), [82](#), [83](#)
- [57] D. J. Griffiths. Benjamin Cummings, 3rd edition, 1999. [6](#)
- [58] F. M. Penning. Die glimmentladung bei niedrigem druck zwischen koaxialen zylindern in einem axialen magnetfeld. *Physica*, 3(9):873–894, 1936. [6](#)
- [59] M. Abramowitz and I. A. Stegun. Dover Publications, 1965. [9](#)
- [60] M. J. Madsen, W. K. Hensinger, D. Stick, J. A. Rabchuk, and C. Monroe. Planar ion trap geometry for microfabrication. *App. Phys. B*, (78):639–651, 2004. [10](#), [13](#), [15](#), [79](#)
- [61] D. J. Berkeland, J. D. Miller, J. C. Bergquist, W. M. Itano, and D. J. Wineland. Minimization of ion micromotion in a paul trap. *Journal of Applied Physics*, 83(10):5025–5033, 1998. [10](#), [11](#), [49](#)
- [62] A. Steane, C. F. Roos, D. Stevens, A. Mundt, D. Leibfried, F. Schmidt-Kaler, and R. Blatt. Speed of ion-trap quantum-information processors. *Phys. Rev. A*, 62(4):042305, Sep 2000. [11](#)
- [63] D. Hucul, M. Yeo, W. K. Hensinger, J. Rabchuk, S. Olmschenk, and C. Monroe. On the transport of atomic ions in linear and multidimensional ion trap arrays. *Quant. Inf. Comp.*, 8:501–578, 2008. [11](#), [17](#), [18](#), [60](#), [72](#), [74](#)
- [64] D. Kielpinski, M. Cetina, J. A. Cox, and F. X. Kärtner. Laser cooling of trapped ytterbium ions with an ultraviolet diode laser. *Opt. Lett.*, 31(6):757–759, 2006. [12](#)
- [65] Chr. Balzer, A. Braun, T. Hannemann, Chr. Paape, M. Ettler, W. Neuhauser, and Chr. Wunderlich. Electrostatically trapped yb^+ ions for quantum information processing. *Phys. Rev. A*, 73:041407, Apr 2006. [12](#)
- [66] S. Olmschenk, K. C. Younge, D. L. Moehring, D. N. Matsukevich, P. Maunz, and C. Monroe. Manipulation and detection of a trapped yb^+ hyperfine qubit. *Phys. Rev. A*, 76:052314, Nov 2007. [12](#), [29](#)
- [67] A. S. Bell, P. Gill, H. A. Klein, A. P. Levick, Chr. Tamm, and D. Schnier. Laser cooling of trapped ytterbium ions using a four-level optical-excitation scheme. *Phys. Rev. A*, 44:R20–R23, Jul 1991. [12](#)

- [68] D. M. Lucas, C. J. S. Donald, J. P. Home, M. J. McDonnell, A. Ramos, D. N. Stacey, J.-P. Stacey, A. M. Steane, and S. C. Webster. Oxford ion-trap quantum computing project. *Phil. Trans. R. Soc. Lond. A*, 361(1808):1401–1408, 2003. [12](#)
- [69] D.J. Wineland, C. Monroe, W.M. Itano, B.E. King, D. Leibfried, D.M. Meekhof, C. Myatt, and C. Wood. Experimental primer on the trapped ion quantum computer. *Fortschr. Phys*, 46(4-5):363–390, 1998. [12](#)
- [70] L. Deslauriers, P. C. Haljan, P. J. Lee, K-A. Brickman, B. B. Blinov, M. J. Madsen, and C. Monroe. Zero-point cooling and low heating of trapped $^{111}\text{Cd}^+$ ions. *Phys. Rev. A*, 70:043408, Oct 2004. [12](#)
- [71] M. D. Barrett, B. DeMarco, T. Schaetz, V. Meyer, D. Leibfried, J. Britton, J. Chiaverini, W. M. Itano, B. Jelenković, J. D. Jost, C. Langer, T. Rosenband, and D. J. Wineland. Publisher’s note: Sympathetic cooling of $^9\text{Be}^+$ and $^{24}\text{Mg}^+$ for quantum logic [phys. rev. a **68** , 042302 (2003)]. *Phys. Rev. A*, 68:059904, Nov 2003. [12](#)
- [72] G. Leschhorn, S. Kahra, and T. Schaetz. Deterministic delivery of externally cold and precisely positioned single molecular ions. *Appl. Phys. B*, 108:237–247, 2012. [12](#)
- [73] R. J. Hughes, D. F. V. James, J. J. Gomez, M. S. Gulley, M. H. Holzscheiter, P. G. Kwiat, S. K. Lamoreaux, C. G. Peterson, V. D. Sandberg, M. M. Schauer, C. M. Simmons, C. E. Thorburn, D. Tupa, P. Z. Wang, and A. G. White. The los alamos trapped ion quantum computer experiment. *Fortschr. Phys*, 46(329-261), 1998. [12](#)
- [74] M. R. Dietrich, A. Avril, R. Bowler, N. Kurz, J. S. Salacka, G. Shu, and B. B. Blinov. Barium ions for quantum computation. *arXiv:0905.2701v1*, 2009. [12](#)
- [75] V. Letchumanan, G. Wilpers, M. Brownnutt, P. Gill, and A. G. Sinclair. Zero-point cooling and heating-rate measurements of a single $^{88}\text{Sr}^+$ ion. *Phys. Rev. A*, 75:063425, Jun 2007. [12](#), [24](#)
- [76] M. Johanning, A. Braun, N. Timoney, V. Elman, W. Neuhauser, and Chr. Wunderlich. Individual addressing of trapped ions and coupling of motional and spin states using rf radiation. *Phys. Rev. Lett.*, 102:073004, Feb 2009. [12](#)
- [77] C. Monroe, D. M. Meekhof, B. E. King, S. R. Jefferts, W. M. Itano, D. J. Wineland, and P. Gould. Resolved-sideband raman cooling of a bound atom to the 3d zero-point energy. *Phys. Rev. Lett.*, 75(22):4011–4014, Nov 1995. [12](#)

- [78] B. E. King, C. S. Wood, C. J. Myatt, Q. A. Turchette, D. Leibfried, W. M. Itano, C. Monroe, and D. J. Wineland. Cooling the collective motion of trapped ions to initialize a quantum register. *Phys. Rev. Lett.*, 81(7):1525–1528, Aug 1998. [12](#)
- [79] D. T. C. Allcock, J. A. Sherman, D. N. Stacey, A. H. Burrell, M. J. Curtis, G. Imreh, N. M. Linke, D. J. Szwer, S. C. Webster, A. M. Steane, and D. M. Lucas. Implementation of a symmetric surface-electrode ion trap with field compensation using a modulated raman effect. *New J. Phys.*, 12:053026, 2010. [13](#), [16](#), [24](#), [66](#), [91](#), [96](#), [142](#)
- [80] J. Britton, D. Leibfried, J. A. Beall, R. B. Blakestad, J. H. Wesenberg, and D. J. Wineland. Scalable arrays of rf paul traps in degenerate si. *Appl. Phys. Lett.*, 95:173102, Oct 2009. [13](#), [14](#), [17](#), [19](#), [24](#)
- [81] J. M. Amini, H. Uys, J. H. Wesenberg, S. Seidelin, J. Britton, J. J. Bollinger, D. Leibfried, C. Ospelkaus, A. P. VanDevender, and D. J. Wineland. Toward scalable ion traps for quantum information processing. *New J. Phys.*, 12:033031, 2010. [13](#), [15](#), [17](#), [18](#), [24](#), [55](#), [68](#), [96](#)
- [82] Altaf H. Nizamani and Winfried K. Hensinger. Optimum electrode configurations for fast ion separation in microfabricated surface ion traps. *Appl Phys B*, 106(2):327–338, 2012. [13](#), [16](#), [55](#), [61](#), [64](#), [65](#), [66](#), [74](#)
- [83] James J. McLoughlin, Altaf H. Nizamani, James D. Siversns, Robin C. Sterling, Marcus D. Hughes, Bjoern Lekitsch, Björn Stein, Seb Weidt, and Winfried K. Hensinger. Versatile ytterbium ion trap experiment for operation of scalable ion-trap chips with motional heating and transition-frequency measurements. *Phys. Rev. A*, 83(1):013406, Jan 2011. [13](#), [14](#), [24](#)
- [84] J. D. Siversns, L. R. Simkins, S. Weidt, and W. K. Hensinger. On the application of radio-frequency voltages to ion traps via helical resonators. *Appl Phys B*, 107(4):921–924, 2012. [13](#), [41](#)
- [85] L. Deslauriers, M. Acton, B. B. Blinov, K.-A. Brickman, P. C. Haljan, W. K. Hensinger, D. Hucul, S. Katnik, R. N. Kohn, P. J. Lee, M. J. Madsen, P. Maunz, S. Olmschenk, D. L. Moehring, D. Stick, J. Sterk, M. Yeo, K. C. Younge, and C. Monroe. Efficient photoionization loading of trapped ions with ultrafast pulses. *Phys. Rev. A*, 74(6):063421, Dec 2006. [14](#)
- [86] J. Britton, D. Leibfried, J. A. Beall, R. B. Blakestad, J. J. Bollinger, J. Chiaverini, R. J. Epstein, J. D. Jost, D. Kielpinski, C. Langer, R. Ozeri, R. Reichle, S. Seidelin,

- N. Shiga, J. H. Wesenberg, and D. J. Wineland. A microfabricated surface-electrode ion trap in silicon. *arXiv:quant-ph/0605170v1*, Feb 2008. [17](#), [96](#)
- [87] J. H. Wesenberg. Ideal intersections for radio-frequency trap networks. *Phys. Rev. A*, 79(1):013416, Jan 2009. [17](#)
- [88] F. Splatt, M. Harlander, M. Brownnutt, F. Zaehringer, R. Blatt, and W. Haensel. Deterministic reordering of 40Ca^+ ions in a linear segmented paul trap. *New J. Phys.*, 11:103008, Oct 2009. [17](#)
- [89] R. Reichle, D. Leibfried, R. B. Blakestad, J. Britton, J. D. Jost, E. Knill, C. Langer, R. Ozeri, S. Seidelin, and D. J. Wineland. Transport dynamics of single ions in segmented microstructured Paul trap arrays. *Fortschritte der physik-progress of physics*, 54(8-10):666–685, AUG-OCT 2006. [17](#), [72](#)
- [90] Kilian Singer, Ulrich Poschinger, Michael Murphy, Peter Ivanov, Frank Ziesel, Tommaso Calarco, and Ferdinand Schmidt-Kaler. Colloquium: Trapped ions as quantum bits: Essential numerical tools. *Rev. Mod. Phys.*, 82(3):2609–2632, Sep 2010. [17](#), [59](#)
- [91] Mário H. Oliveira and José A. Miranda. Biot-savart-like law in electrostatics. *Eur. J. Phys.*, 22(1):31–38, 2001. [18](#), [61](#), [79](#), [87](#)
- [92] J. H. Wesenberg. Electrostatics of surface-electrode ion traps. *Phys. Rev. A*, 78(6):063410, Dec 2008. [18](#), [61](#), [80](#)
- [93] M. G. House. Analytic model for electrostatic fields in surface-electrode ion traps. *Phys. Rev. A*, 78(3):033402, Sep 2008. [18](#), [61](#), [62](#), [64](#), [80](#), [81](#)
- [94] R. Schmied. Electrostatics of gapped and finite surface electrodes. *New J. Phys.*, 12:023038, 2010. [19](#), [61](#), [80](#)
- [95] V. K. Agarwal and V. K. Srivastava. Thickness dependence of breakdown field in thin films. *Thin Solid Films*, 8:377–381, 1971. [19](#)
- [96] V. K. Agarwal and V. K. Srivastava. Thickness dependent studies of dielectric breakdown in langmuir thin molecular films. *Solid State Communications*, 12:829–834, 1973. [19](#)
- [97] D. Mangalaraj, M. Radhakrishnan, and C. Balasubramanian. Electrical conduction and breakdown properties of silicon nitride films. *Journal of Materials Science*, 17:1474–1478, 1982. [19](#)

- [98] H. K. Kim and F. G. Shi. Thickness dependent dielectric strength of a low-permittivity dielectric film. *IEEE Transactions on Dielectrics and Electrical Insulation*, 8(2):248–252, 2001. [19](#)
- [99] H. Zhou, F.G. Shi, and B. Zhao. Thickness dependent dielectric breakdown of pecvd low-k carbon doped silicon dioxide dielectric thin films: modeling and experiments. *Microelectronics Journal*, 34:259–264, 2003. [19](#)
- [100] H. Bartzsch, D. Glöß, B. Böcher, P. Frach, and K. Goedicke. Properties of SiO_2 and Al_2O_3 films for electrical insulation applications deposited by reactive pulse magnetron sputtering. *Surface and Coatings Technology*, 174-175:774–778, 2003. [19](#)
- [101] J. Mueller, D. Pyle, I. Chakraborty, R. Ruiz, W. Tang, and R. Lawton. Feasibility study of mems-based accelerator grid systems for micro-ion engines: Electric breakdown characteristics. *AIAA Journal of Propulsion and Power U.S.A.*, 1999. [19](#), [20](#), [135](#)
- [102] H. C. Miller. Flashover of insulators in vacuum: review of the phenomena and techniques to improved holdoff voltage. *IEEE Transactions on Electrical Insulation*, 28(4):512–527, 1993. [19](#), [20](#)
- [103] A. S. Pillai and Reuben Hackam. Surface flashover of solid insulators in atmospheric air and in vacuum. *J. Appl. Phys.*, 58:146–153, 1985. [19](#), [20](#)
- [104] A. Sivathanu Pillai and Reuben Hackam. Surface flashover of solid dielectric in vacuum. *J. Appl. Phys.*, 53(4):2983–2987, 1982. [20](#), [93](#), [135](#), [136](#)
- [105] J. D. Kraus and D. A. Fleisch. McGraw-Hill Science/Engineering/Math, 5th edition, 1999. [21](#)
- [106] Dök İlbilge, Şemsettin Altındal, and Muharrem Gökçen. Frequency and gate voltage effects on the dielectric properties of $\text{Au/SiO}_2/\text{n-Si}$ structures. *Microelectron. Eng.*, 85:1910–1914, September 2008. [21](#), [22](#)
- [107] Stephen C. Thierauf. Artech House Publishers, 2004. [21](#)
- [108] Howard Johnson and Martin Graham. Prentice Hall, 2003. [21](#)
- [109] Paul Horowitz and Winfield Hill. Cambridge University Press, 1989. [21](#)
- [110] Jerzy Krupka, Jonathan Breeze, Anthony Centeno, Neil Alford, Thomas Claussen, and Leif Jensen. Measurements of permittivity, dielectric loss tangent, and resistivity

- of float-zone silicon at microwave frequencies. *IEEE Transactions on microwave theory and techniques*, 54(11), 2006. [22](#)
- [111] A. Tataroğlu. Electrical and dielectric properties of mis schottky diodes at low temperatures. *Microelectron. Eng.*, 83:2551–2557, November 2006. [22](#)
- [112] M. M. Bülbül. Frequency and temperature dependent dielectric properties of al/si₃n₄/p-si(100) mis structure. *Microelectron. Eng.*, 84:124–128, January 2007. [22](#)
- [113] Sükrü Karataş. Studies on electrical and the dielectric properties in ms structures. *Journal of Non-Crystalline Solids*, 354:3606–3611, 2008. [22](#)
- [114] A. Birkan Selçuk. On the dielectric characteristics of *au/sno₂/n – si* capacitors. *Physica B*, 396:181–186, 2007. [22](#)
- [115] N. Tomozeiu. Electrical conduction and dielectric relaxation of *a – sio_x* ($0 < x < 2$) thin films deposited by reactive rf magnetron sputtering. *Thin Solid Films*, 516:8199–8204, 2008. [22](#)
- [116] Klaus Mølmer and Anders Sørensen. Multiparticle entanglement of hot trapped ions. *Phys. Rev. Lett.*, 82(9):1835–1838, Mar 1999. [23](#)
- [117] P. J. Lee, K.-A. Brickman, L. Deslauriers, P. C. Haljan, L.-M. Duan, and C. Monroe. Phase control of trapped ion quantum gates. *Journal of Optics B*, 7(10):S371–S383, 2005. [23](#)
- [118] J. J. García-Ripoll, P. Zoller, and J. I. Cirac. Speed optimized two-qubit gates with laser coherent control techniques for ion trap quantum computing. *Phys. Rev. Lett.*, 91(15):157901, Oct 2003. [23](#)
- [119] Q. A. Turchette, Kielpinski, B. E. King, D. Leibfried, D. M. Meekhof, C. J. Myatt, M. A. Rowe, C. A. Sackett, C. S. Wood, W. M. Itano, C. Monroe, and D. J. Wineland. Heating of trapped ions from the quantum ground state. *Phys. Rev. A*, 61(6):063418, May 2000. [23](#), [24](#), [78](#), [91](#)
- [120] L. Deslauriers, S. Olmschenk, D. Stick, W. K. Hensinger, J. Sterk, and C. Monroe. Scaling and suppression of anomalous heating in ion traps. *Phys. Rev. Lett.*, 97(10):103007, Sep 2006. [23](#), [24](#), [25](#), [76](#), [78](#), [83](#), [91](#)

- [121] F. Diedrich, J. C. Bergquist, Wayne M. Itano, and D. J. Wineland. Laser cooling to the zero-point energy of motion. *Phys. Rev. Lett.*, 62(4):403–406, Jan 1989. [24](#)
- [122] Ralph G. DeVoe and Christian Kurtsiefer. Experimental study of anomalous heating and trap instabilities in a microscopic ^{137}Ba ion trap. *Phys. Rev. A*, 65(6):063407, Jun 2002. [24](#)
- [123] Ch. Roos, Th. Zeiger, H. Rohde, H. C. Nägerl, J. Eschner, D. Leibfried, F. Schmidt-Kaler, and R. Blatt. Quantum state engineering on an optical transition and decoherence in a paul trap. *Phys. Rev. Lett.*, 83(23):4713–4716, Dec 1999. [24](#)
- [124] Stephan A. Schulz, Ulrich Poschinger, Frank Ziesel, and Ferdinand Schmidt-Kaler. Sideband cooling and coherent dynamics in a microchip multi-segmented ion trap. *New J. Phys.*, 10(045007):15, 2008. [24](#)
- [125] N. Daniilidis, S. Narayanan, S. A. Möller, R. Clark, T. E. Lee, P. J. Leek, A. Wallraff, St. Schulz, F. Schmidt-Kaler, and H. Häffner. Fabrication and heating rate study of microscopic surface electrode ion traps. *New J. Phys.*, 13(013032):17, 2011. [24](#)
- [126] Chr. Tamm, D. Engelke, and V. Bühner. Spectroscopy of the electric-quadrupole transition $^2s_{1/2}(f=0) \rightarrow ^2d_{3/2}(f=2)$ in trapped $^{171}\text{Yb}^+$. *Phys. Rev. A*, 61(5):053405, Apr 2000. [24](#)
- [127] M. A. Rowe, A. Ben-Kish, B. DeMarco, D. Leibfried, V. Meyer, J. Beall, J. Britton, J. Hughes, W. M. Itano, B. Jelenkovic, C. Langer, T. Rosenband, and D. J. Wineland. Transport of quantum states and separation of ions in a dual rf ion trap. *Quant. Inf. Comp.*, 2(4):257–271, 2002. [24](#), [70](#)
- [128] J. Britton. *Microfabrication techniques for trapped ion quantum information processing*. Ph.d. thesis, arxiv:1008.2222v1, Boulder, 2008. [24](#)
- [129] R. J. Epstein, S. Seidelin, D. Leibfried, J. H. Wesenberg, J. J. Bollinger, J. M. Amini, R. B. Blakestad, J. Britton, J. P. Home, W. M. Itano, J. D. Jost, E. Knill, C. Langer, R. Ozeri, N. Shiga, and D. J. Wineland. Simplified motional heating rate measurements of trapped ions. *Phys. Rev. A*, 76(3):033411, Sep 2007. [24](#)
- [130] Shannon X. Wang, Yufei Ge, Jaroslaw Labaziewicz, Eric Dauler, Karl Berggren, and Isaac L. Chuang. Superconducting microfabricated ion traps. *Appl. Phys. Lett.*, 97:244102, 2010. [24](#), [25](#)

- [131] J. Labaziewicz, Y. Ge, P. Antohi, D. Leibbrandt, K. R. Brown, and I. L. Chuang. Suppression of heating rates in cryogenic surface-electrode ion traps. *Phys. Rev. Lett.*, 100(1):013001, 2008. [24](#), [25](#), [76](#), [83](#)
- [132] J. Labaziewicz, Y. Ge, D. R. Leibbrandt, S. X. Wang, R. Shewmon, and I. L. Chuang. Temperature dependence of electric field noise above gold surfaces. *Phys. Rev. Lett.*, 101(18):180602, 2008. [25](#)
- [133] A. Safavi-Naini, P. Rabl, P. F. Weck, and H. R. Sadeghpour. Microscopic model of electric-field-noise heating in ion traps. *Phys. Rev. A*, 84:023412, Aug 2011. [25](#)
- [134] D. T. C. Allcock, L. Guidoni, T. P. Harty, C. J. Ballance, M. G. Blain, A. M. Steane, and D. M. Lucas. Reduction of heating rate in a microfabricated ion trap by pulsed-laser cleaning. *New J. Phys.*, 13:123023, 2011. [25](#), [76](#), [83](#)
- [135] D. A. Hite, Y. Colombe, A. C. Wilson, K. R. Brown, U. Warring, R. Jördens, J. D. Jost, K. S. McKay, D. P. Pappas, D. Leibfried, and D. J. Wineland. 100-fold reduction of electric-field noise in an ion trap cleaned with *In Situ* argon-ion-beam bombardment. *Phys. Rev. Lett.*, 109:103001, Sep 2012. [25](#), [76](#), [83](#), [138](#)
- [136] Erik W. Streed, Benjamin G. Norton, Andreas Jechow, Till J. Weinhold, and David Kielpinski. Imaging of trapped ions with a microfabricated optic for quantum information processing. *Phys. Rev. Lett.*, 106:010502, Jan 2011. [26](#)
- [137] W. Neuhauser, M. Hohenstatt, P. Toschek, and H. Dehmelt. Optical-sideband cooling of visible atom cloud confined in parabolic well. *Phys. Rev. Lett.*, 41:233–236, Jul 1978. [27](#)
- [138] M. Johanning, A. Braun, D. Eiteneuer, C. Paape, C. Balzer, W. Neuhauser, and C. Wunderlich. Resonance-enhanced isotope-selective photoionization of ybi for ion trap loading. *Applied Physics B: Lasers and Optics*, 103:327–338, 2011. 10.1007/s00340-011-4502-7. [27](#), [29](#)
- [139] Harold J. Metcalf and Peter Van Der Straten. Springer-Verlag New York, Inc., 1999. [28](#)
- [140] Altaf H. Nizamani, James J. McLoughlin, and Winfried K. Hensinger. Doppler-free yb spectroscopy with the fluorescence spot technique. *Phys. Rev. A*, 82:043408, Oct 2010. [29](#), [30](#)

- [141] D. J. Berkeland and M. G. Boshier. Destabilization of dark states and optical spectroscopy in zeeman-degenerate atomic systems. *Phys. Rev. A*, 65:033413, Feb 2002. [30](#)
- [142] A. S. Arnold, J. S. Wilson, and M. G. Boshier. A simple extended-cavity diode laser. *Rev. Sci. Instrum.*, 69:1236, 1998. [31](#)
- [143] R. W. P. Drever, J. L. Hall, F. V. Kowalski, J. Hough, G. M. Ford, A. J. Munley, and H. Ward. Laser phase and frequency stabilization using an optical resonator. *Applied Physics B*, 31:97–105, 1983. 10.1007/BF00702605. [33](#)
- [144] E. D. Black. An introduction to pound-drever-hall laser frequency stabilization. *American Journal of Physics*, 69:79, 2001. [33](#)
- [145] S. Kraft, A. Deninger, C. Trück, J. Fortágh, F. Lison, and C. Zimmermann. Rubidium spectroscopy at 778–780 nm with a distributed feedback laser diode. *Laser Physics Letters*, 2(2):71–76, 2005. [34](#)
- [146] A. P. VanDevender, Y. Colombe, J. Amini, D. Leibfried, and D. J. Wineland. Efficient fiber optic detection of trapped ion fluorescence. *Phys. Rev. Lett.*, 105:023001, Jul 2010. [44](#), [55](#)
- [147] J. H. Wesenberg, R. J. Epstein, D. Leibfried, R. B. Blakestad, J. Britton, J. P. Home, W. M. Itano, J. D. Jost, E. Knill, C. Langer, R. Ozeri, S. Seidelin, and D. J. Wineland. Fluorescence during doppler cooling of a single trapped atom. *Phys. Rev. A*, 76:053416, Nov 2007. [51](#), [52](#)
- [148] J. True Merrill, Curtis Volin, David Landgren, Jason M. Amini, Kenneth Wright, S. Charles Doret, C.-S. Pai, Harley Hayden, Tyler Killian, Daniel Faircloth, Kenneth R. Brown, Alexa W. Harter, , and Richard E. Slusher. Demonstration of integrated microscale optics in surface-electrode ion traps. *New J. Phys.*, 13:103005, 2011. [55](#)
- [149] D. Allcock, T. Harty, H. Janacek, N. Linke, C. Ballance, A. Steane, D. Lucas, R. Jarecki, S. Habermehl, M. Blain, D. Stick, and D. Moehring. Heating rate and electrode charging measurements in a scalable, microfabricated, surface-electrode ion trap. *Applied Physics B: Lasers and Optics*, 107:913–919, 2012. 10.1007/s00340-011-4788-5. [55](#)

- [150] J. P. Home and A. M. Steane. Electrode configurations for fast separation of trapped ions. *Quant. Inf. Comp.*, 6(4&5):289–325, 2006. [55](#), [62](#), [64](#), [65](#)
- [151] R. C. Sterling, M. D. Hughes, C. J. Mellor, and W. K. Hensinger. Increased surface flashover voltage in microfabricated devices. *arXiv:1208.5672*, 2012. [57](#), [135](#)
- [152] Roman Schmied, Janus H. Wesenberg, and Dietrich Leibfried. Optimal surface-electrode trap lattices for quantum simulation with trapped ions. *Phys. Rev. Lett.*, 102:233002, Jun 2009. [61](#), [78](#), [80](#), [81](#)
- [153] R. B Blakestad, C. Ospelkaus, A. P VanDevender, J. H Wesenberg, M. J Biercuk, D. Leibfried, and D. J Wineland. Near-ground-state transport of trapped-ion qubits through a multidimensional array. *Phys. Rev. A*, 84:032314, Sep 2011. [68](#), [70](#), [76](#), [142](#)
- [154] D. L. Moehring, C. Highstrete, D. Stick, K. M. Fortier, R. Haltli, C. Tigges, and M. G. Blain. Design, fabrication and experimental demonstration of junction surface ion traps. *New J. Phys.*, 14, 2012. [68](#)
- [155] R. C. Sterling. *Ytterbium ion trapping and microfabrication of ion trap arrays*. Ph.d. thesis, Brighton, 2011. [68](#), [70](#)
- [156] M. D. Barrett, J. Chiaverini, T. Schaetz, J. Britton, W. M. Itano, J. D. Jost, E. Knill, C. Langer, D. Leibfried, R. Ozeri, and D. J. Wineland. Deterministic quantum teleportation of atomic qubits. *Nature*, 429:737–739, 2004. [70](#)
- [157] G. Huber, T. Deuschle, W. Schnitzler, R. Reichle, K. Singer, and F. Schmidt-Kaler. Transport of ions in a segmented linear paul trap in printed-circuit-board technology. *New J. Phys.*, 10(013004), 2008. [70](#)
- [158] R. Bowler, J. Gaebler, Y. Lin, T. R. Tan, D. Hanneke, J. D. Jost, J. P. Home, D. Leibfried, and D. J. Wineland. Coherent diabatic ion transport and separation in a multi-zone trap array. *arXiv:1206.0780*, 2012. [70](#)
- [159] R. Gerritsma, B. P. Lanyon, G. Kirchmair, F. Zähringer, C. Hempel, J. Casanova, J. J. García-Ripoll, E. Solano, R. Blatt, and C. F. Roos. Quantum simulation of the klein paradox with trapped ions. *Phys. Rev. Lett.*, 106:060503, Feb 2011. [77](#), [85](#)
- [160] Ch Schneider, Diego Porras, and Tobias Schaetz. Experimental quantum simulations of many-body physics with trapped ions. *Rep. Prog. Phys.*, 75:024401, 2012. [77](#)

- [161] D. Porras and J. I. Cirac. Effective quantum spin systems with trapped ions. *Phys. Rev. Lett.*, 92:207901, May 2004. [77](#)
- [162] Peter A. Ivanova, Diego Porras, Svetoslav S. Ivanov, and Ferdinand Schmidt-Kaler. Simulation of jahn-teller-dicke magnetic structural phase transition with trapped ions. *arXiv:1207.0452*, 2012. [77](#)
- [163] Marc. J. Madu. *Fundamentals of Microfabrication: The Science of Miniaturization, Second Edition*. Taylor & Francis, 2002. [77](#)
- [164] C. Langer, R. Ozeri, J. D. Jost, J. Chiaverini, B. DeMarco, A. Ben-Kish, R. B. Blakestad, J. Britton, D. B. Hume, W. M. Itano, D. Leibfried, R. Reichle, T. Rosenband, T. Schaetz, P. O. Schmidt, and D. J. Wineland. Long-lived qubit memory using atomic ions. *Phys. Rev. Lett.*, 95:060502, Aug 2005. [78](#)
- [165] H. Häffner, F. Schmidt-Kaler, W. Hänsel, C. F. Roos, T. Körber, M. Chwalla, M. Riebe, J. Benhelm, U. D. Rapol, C. Becher, and R. Blatt. Robust entanglement. *Applied Physics B: Lasers and Optics*, 81:151–153, 2005. 10.1007/s00340-005-1917-z. [78](#)
- [166] Roman Schmied, Janus H. Wesenberg, and Dietrich Leibfried. Quantum simulation of the hexagonal kitaev model with trapped ions. *New J. Phys.*, 13(115011), 2012. [78](#)
- [167] Muir Kumph, Michael Brownnutt, and Rainer Blatt. Two-dimensional arrays of radio-frequency ion traps with addressable interactions. *New J. Phys.*, 13(073043), 2011. [78](#)
- [168] D. Mc Hugh and J. Twamley. Quantum computer using a trapped-ion spin molecule and microwave radiation. *Phys. Rev. A*, 71:012315, Jan 2005. [80](#)
- [169] Tony Hyun Kim, Peter F. Herskind, Taehyun Kim, Jungsang Kim, and Isaac L. Chuang. Surface-electrode point paul trap. *Phys. Rev. A*, 82:043412, Oct 2010. [80](#)
- [170] W. C. Campbell, J. Mizrahi, Q. Quraishi, C. Senko, D. Hayes, D. Hucul, D. N. Matsukevich, P. Maunz, and C. Monroe. Ultrafast gates for single atomic qubits. *Phys. Rev. Lett.*, 105:090502, Aug 2010. [83](#)
- [171] R. Gerritsma, G. Kirchmair, F. Zähringer, E. Solano, R. Blatt, , and C. F. Roos. Quantum simulation of the dirac equation. *Nature*, 463:68–71, 2010. [85](#)

- [172] E. E. Edwards, S. Korenblit, K. Kim, R. Islam, M.-S. Chang, J. K. Freericks, G.-D. Lin, L.-M. Duan, and C. Monroe. Quantum simulation and phase diagram of the transverse-field ising model with three atomic spins. *Phys. Rev. B*, 82:060412, Aug 2010. [85](#)
- [173] K. Kim, S. Korenblit, R. Islam, E. E. Edwards, M.-S. Chang, C. Noh, H. Carmichael, G.-D. Lin, L.-M. Duan, C. C. Joseph Wang, J. K. Freericks, and C. Monroe. Quantum simulation of the transverse ising model with trapped ions. *New J. Phys.*, 13(105003), 2011. [85](#)
- [174] W. C. Campbell S. Korenblit J. Smith A. Lee E. E. Edwards C.-C. J. Wang J. K. Freericks R. Islam, C. Senko and C. Monroe. Emergence and frustration of magnetic order with variable-range interactions in a trapped ion quantum simulator. *arXiv:1210.0142*, 2012. [85](#)
- [175] Daniel H. E. Dubin. Theory of structural phase transitions in a trapped coulomb crystal. *Phys. Rev. Lett.*, 71:2753–2756, Oct 1993. [85](#)
- [176] G.-D. Lin, S.-L. Zhu, R. Islam, K. Kim, M.-S. Chang, S. Korenblit, C. Monroe, and L.-M. Duan. Large-scale quantum computation in an anharmonic linear ion trap. *Europhys. Lett.*, 86(6):60004, 2009. [85](#), [91](#)
- [177] I. Waki, S. Kassner, G. Birkel, and H. Walther. Observation of ordered structures of laser-cooled ions in a quadrupole storage ring. *Phys. Rev. Lett.*, 68:2007–2010, Mar 1992. [85](#)
- [178] G. Birkel, S. Kassner, and H. Walther. Multiple-shell structures of laser-cooled $^{24}\text{Mg}^+$ ions in a quadrupole storage ring. *Nature*, 357:310–313, 1992. [85](#)
- [179] T. Schätz, U. Schramm, and D. Habs. Crystalline ion beams. *Nature*, 412:717–720, 2001. [85](#)
- [180] X.-L. Deng, D. Porras, and J. I. Cirac. Effective spin quantum phases in systems of trapped ions. *Phys. Rev. A*, 72:063407, Dec 2005. [85](#)
- [181] B. Horstmann, B. Reznik, S. Fagnocchi, and J. I. Cirac. Hawking radiation from an acoustic black hole on an ion ring. *Phys. Rev. Lett.*, 104:250403, Jun 2010. [85](#), [143](#)
- [182] Birger Horstmann, Ralf Schützhold, Benni Reznik, Serena Fagnocchi, and J Ignacio Cirac. Hawking radiation on an ion ring in the quantum regime. *New J. Phys.*, 13(069601), 2011. [85](#)

- [183] J. Chiaverini and W. E. Lybarger. Laserless trapped-ion quantum simulations without spontaneous scattering using microtrap arrays. *Phys. Rev. A*, 77:022324, Feb 2008. [86](#)
- [184] Shannon X. Wang, Guang Hao Low, Nathan S. Lachenmyer, Yufei Ge, Peter F. Herskind, , and Isaac L. Chuang. Laser-induced charging of microfabricated ion traps. *J. Appl. Phys.*, 110:104901, 2011. [87](#)
- [185] A. H. Burrell, D. J. Szwer, S. C. Webster, and D. M. Lucas. Scalable simultaneous multiqubit readout with 99.99% single-shot fidelity. *Phys. Rev. A*, 81:040302, Apr 2010. [89](#)
- [186] Shannon X. Wang, Jaroslaw Labaziewicz, Yufei Ge, Ruth Shewmon, and Isaac L. Chuang. Demonstration of a quantum logic gate in a cryogenic surface-electrode ion trap. *Phys. Rev. A*, 81:062332, Jun 2010. [91](#)
- [187] C. Ospelkaus, U. Warring, Y. Colombe, K. R. Brown, J. M. Amini, D. Leibfried, and D. J. Wineland. Microwave quantum logic gates for trapped ions. *Nature*, 476:181–184, 2011. [91](#), [101](#)
- [188] K. R. Brown, C. Ospelkaus, Y. Colombe, A. C. Wilson, D. Leibfried, and D. J. Wineland. Coupled quantized mechanical oscillators. *Nature*, 471:196–199, 2011. [91](#)
- [189] M. Harlander, R. Lechner, M. Brownnutt R. Blatt, and W. Hänsel. Trapped-ion antennae for the transmission of quantum information. *Nature*, 471:200–203, 2011. [91](#)
- [190] D. Stick, K. M. Fortier, R. Haltli, C. Highstrete, D. L. Moehring, C. Tigges, and M. G. Blain. Demonstration of a microfabricated surface electrode ion trap. *arXiv:1008.0990*, 2010. [96](#)
- [191] M. Brownnutt, G. Wilpers, P. Gill, R. C. Thompson, and A. G. Sinclair. Monolithic microfabricated ion trap chip design for scaleable quantum processors. *New. J. Phys.*, 8:232, 2006. [96](#)
- [192] Guido Wilpers, Patrick See, Patrick Gill, and Alastair G. Sinclair. A monolithic array of three-dimensional ion traps fabricated with conventional semiconductor technology. *Nature Nano.*, 7:572–576, 2012. [96](#)
- [193] Marcus D. Hughes, Bjoern Lekitsch, Jiddu Broersma, and Winfried K. Hensinger. Microfabricated ion traps. *Contemporary Physics*, 52:6(6):505–529, 2011. [96](#)

- [194] W. K. Hensinger, D. Stick, J. Sterk, M. Madsen, W. Noonan, M. Pedersen, S. Gross, M. Huff, and C. Monroe. Mems fabrication of silicon ion trap arrays workshop on trapped ion quantum computing (boulder, co), <http://tf.nist.gov/ion/workshop2006/t11.pdf>. 2006. 96
- [195] N. Timoney, I. Baumgart, M. Johanning, A. F. Var´on, M. B. Plenio, A. Retzker, and Ch. Wunderlich. Quantum gates and memory using microwave-dressed states. *Nature*, 476:185–188, 2011. 101
- [196] Mordechai Schlesinger and Milan Paunovic. *Modern Electroplating, 5th Edition*. Wiley, 2010. 102
- [197] Young-Shig Choi and Insup Lee. Pinholes on thermally grown oxide under polysilicon layer after plasma etching. *Metals and Materials*, 5(4):377–380, 1999. 104
- [198] K.R. Williams, K. Gupta, and M. Wasilik. Etch rates for micromachining processing—part ii. *Journal of microelectromechanical systems*, 12(6), 2003. 105, 106, 122
- [199] K.R. Williams and R. S. Muller. Etch rates for micromachining processing. *Journal of microelectromechanical systems*, 5(4), 1996. 106
- [200] B. Okkerse. Self-diffusion of gold. *Phys. Rev.*, 103:1246–1249, Sep 1956. 116
- [201] Paul Werbaneth, Tim Lester, and Jadwiga Pakulska. Removing gold seed-layer materials using reactive ion etch. <http://micromagazine.fabtech.org/archive/03/07/werbaneth.html>. 122
- [202] R. M. Ranade, S. S. Ang, and W. D. Brown. Reactive ion etching of thin gold films. *J. Electrochem. Soc.*, 140(12):3676–3678, 1993. 123
- [203] A. Neuber, M. Butcher, L. L. Hatfield, and H. Krompholz. Electric current in dc surface flashover in vacuum. *J. Appl. Phys.*, 85(6):3084, 1999. 135, 136
- [204] R. A. Anderson and J. P. Brainard. Mechanism of pulsed surface flashover involving electron-stimulated desorption. *J. Appl. Phys.*, 51(3):1414, 1980. 135, 136
- [205] A. A. Avdienko and M. D. Malev. Flashover in a vacuum. *Vacuum*, 27(12):643, 1977. 136
- [206] K Odaka and S Ueda. Dependence of outgassing rate on surface oxide layer thickness in type 304 stainless steel before and after surface oxidation in air. *Vacuum*, 47(6-

- 8):689 – 692, 1996. Proceedings of the 13th International Vacuum Congress and the 9th International Conference on Solid Surfaces. [139](#)
- [207] A. H. Nizamani. *Yb⁺ ion trapping and optimum planar trap geometries for scalable quantum technology*. Ph.d. thesis, Brighton, 2011. [139](#)
- [208] Florian Mintert and Christof Wunderlich. Ion-trap quantum logic using long-wavelength radiation. *Phys. Rev. Lett.*, 87:257904, Nov 2001. [144](#)
- [209] C. Ospelkaus, C. E. Langer, J. M. Amini, K. R. Brown, D. Leibfried, and D. J. Wineland. Trapped-ion quantum logic gates based on oscillating magnetic fields. *Phys. Rev. Lett.*, 101:090502, Aug 2008. [144](#)

Appendix A

Mask set

A.1 First layer ‘buried wires’ mask

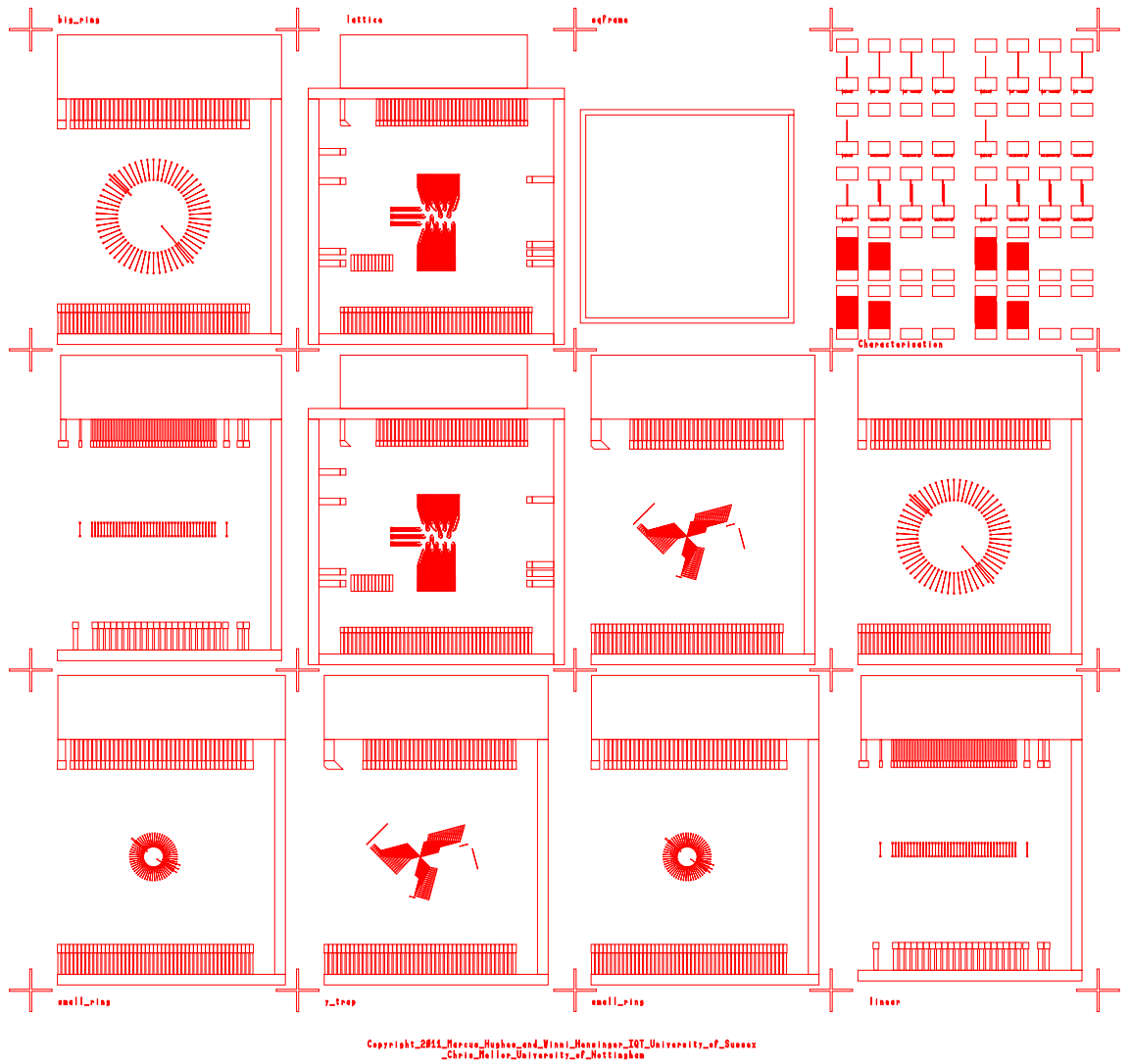
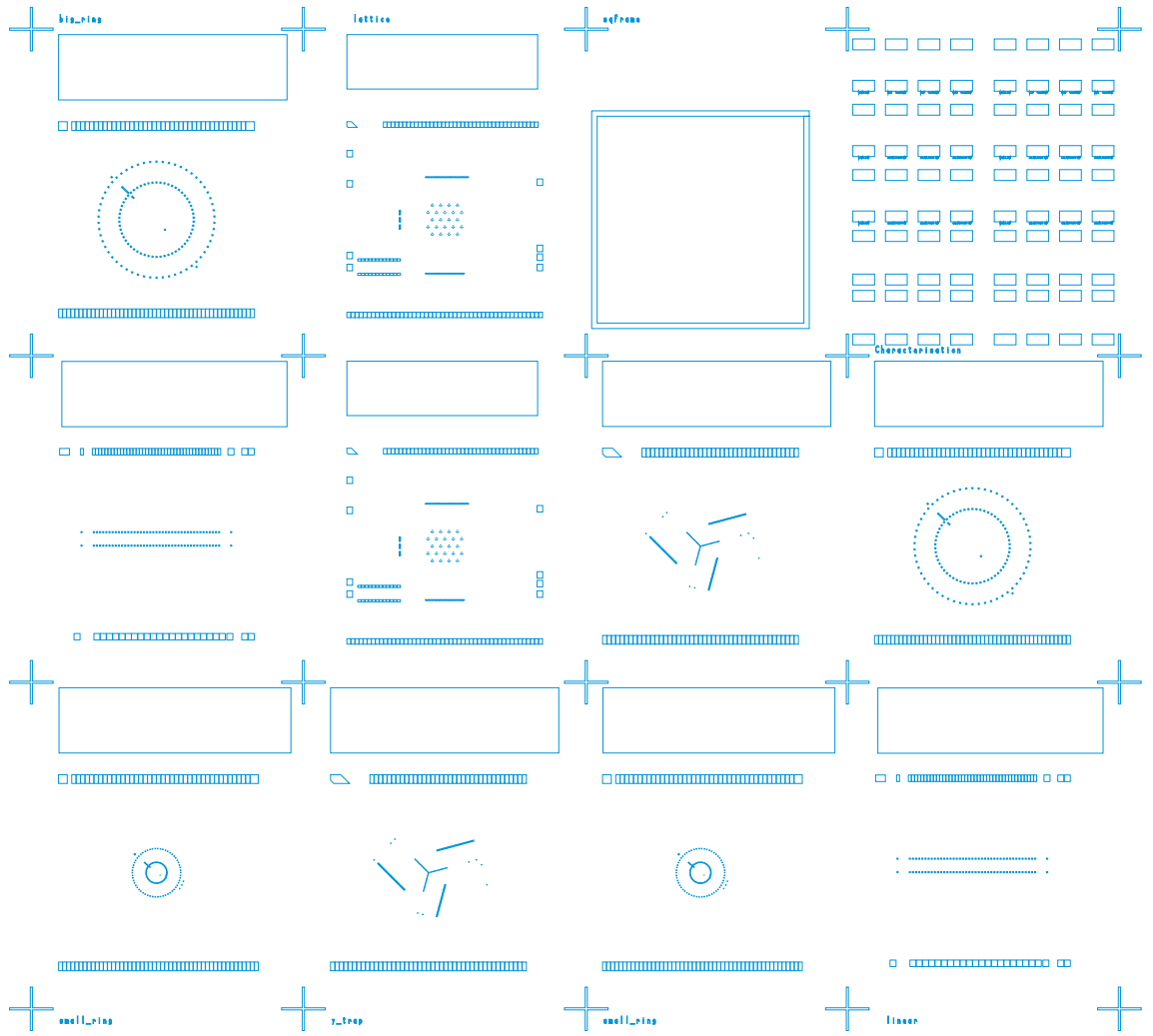


Figure A.1: Mask layout to pattern the first conducting layer.

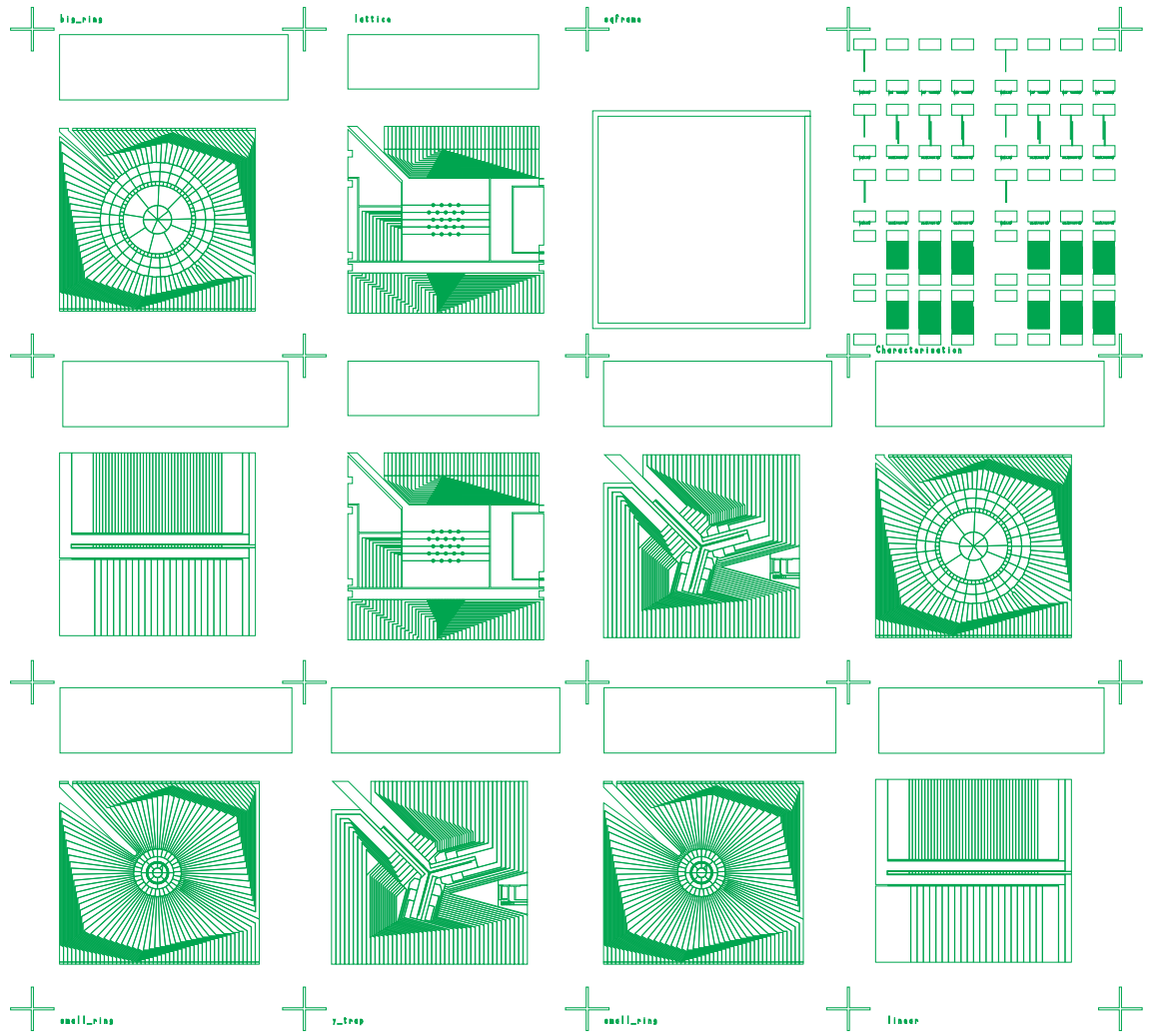
A.2 Second layer ‘vias’ mask



Copyright 2015, Marcus Hughes and Vinni Hanninen, IOT, University of Sussex
 Chris Heller, University of Nottingham

Figure A.2: Mask layout to create vias to the buried conducting wires.

A.3 Third layer ‘electrodes’ mask



Copyright 2014, Marcus Hughes and Vinni Hanstmann, IOT, University of Sussex
Chris Hoffer, University of Nottingham

Figure A.3: Mask layout for the electrode layer of the trap designs.

A.4 Y-junction ion trap

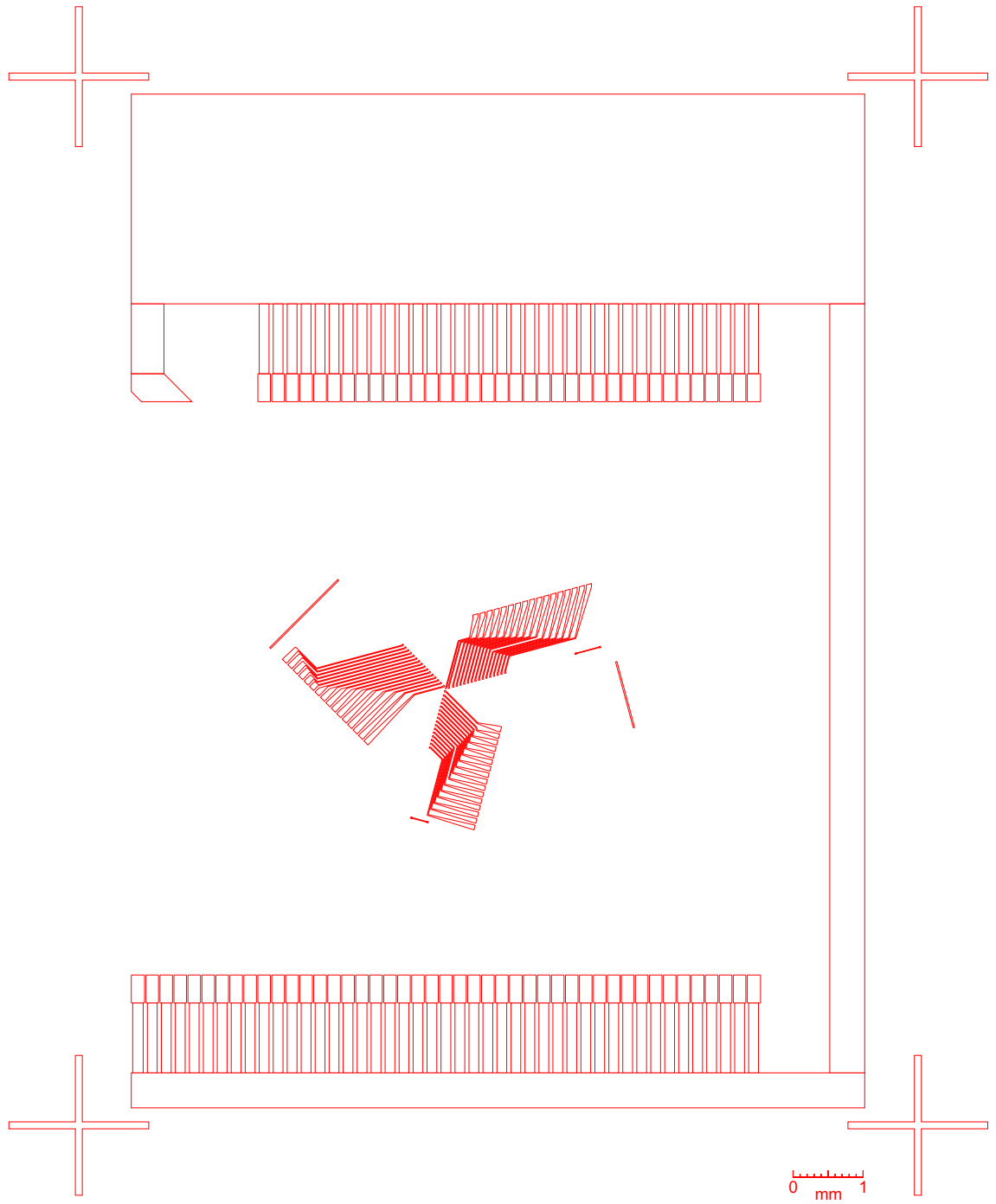


Figure A.4: Y-junction first layer mask.

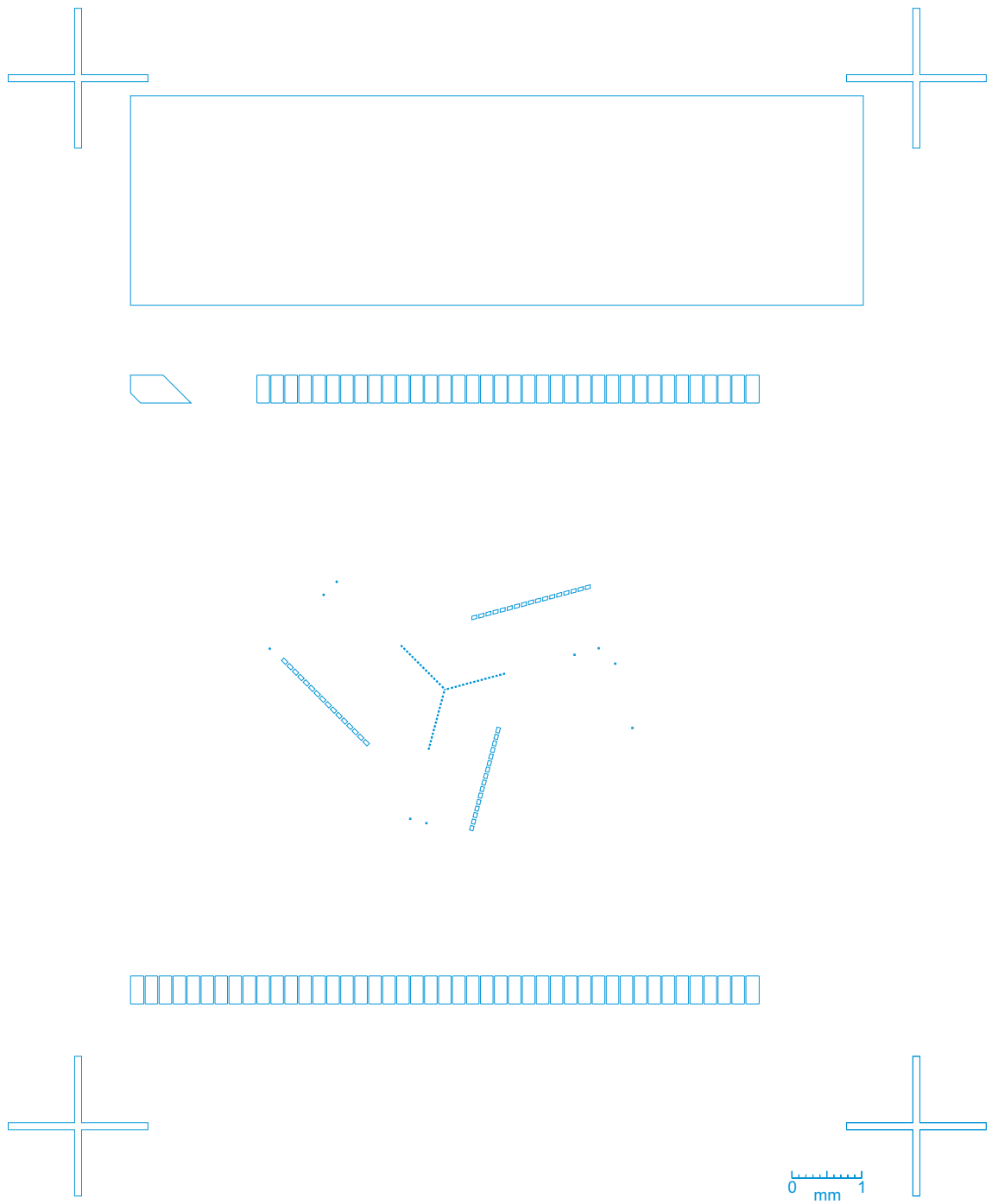


Figure A.5: Y-junction second layer mask.

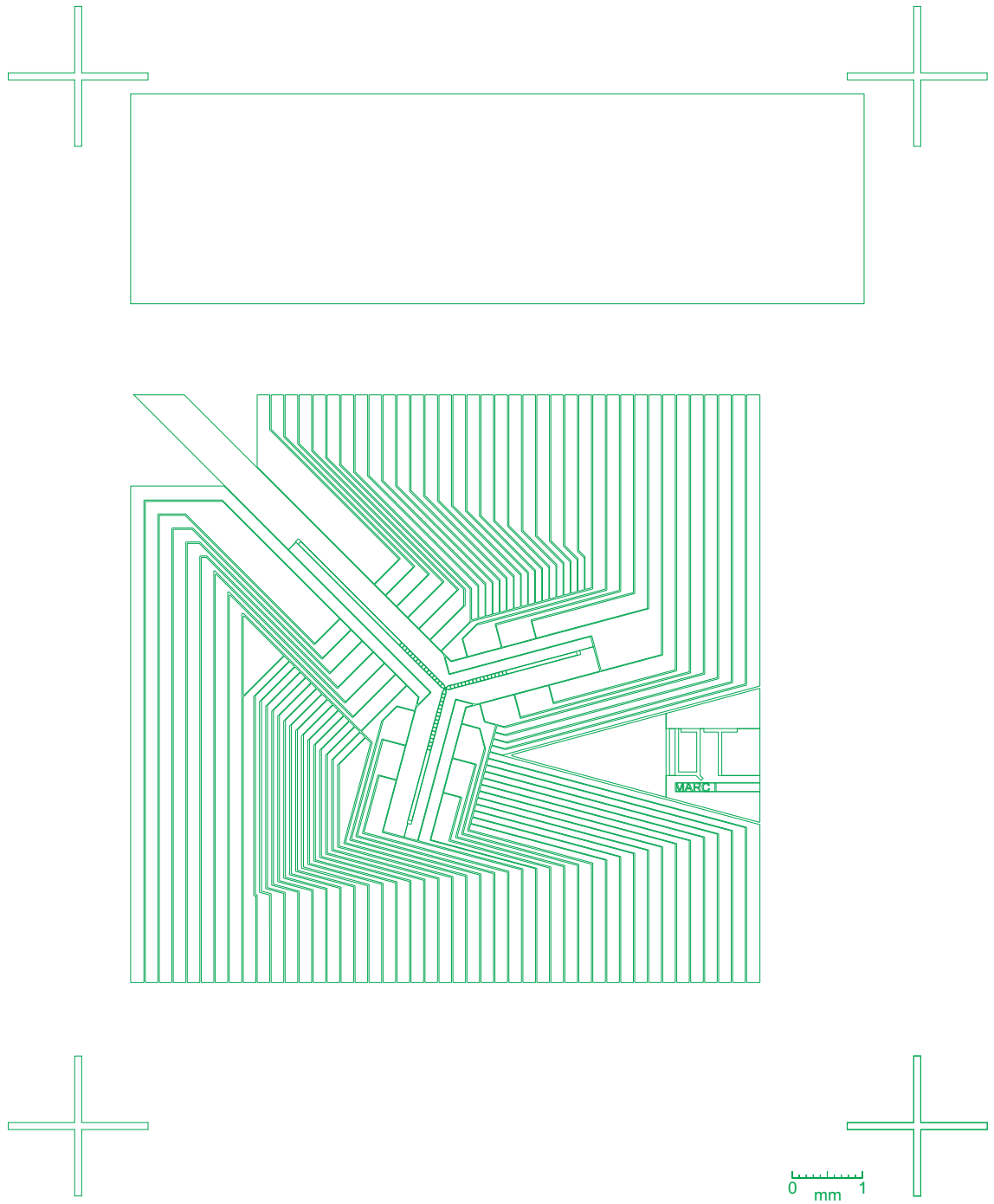


Figure A.6: Y-junction third layer mask.

A.5 Lattice ion trap

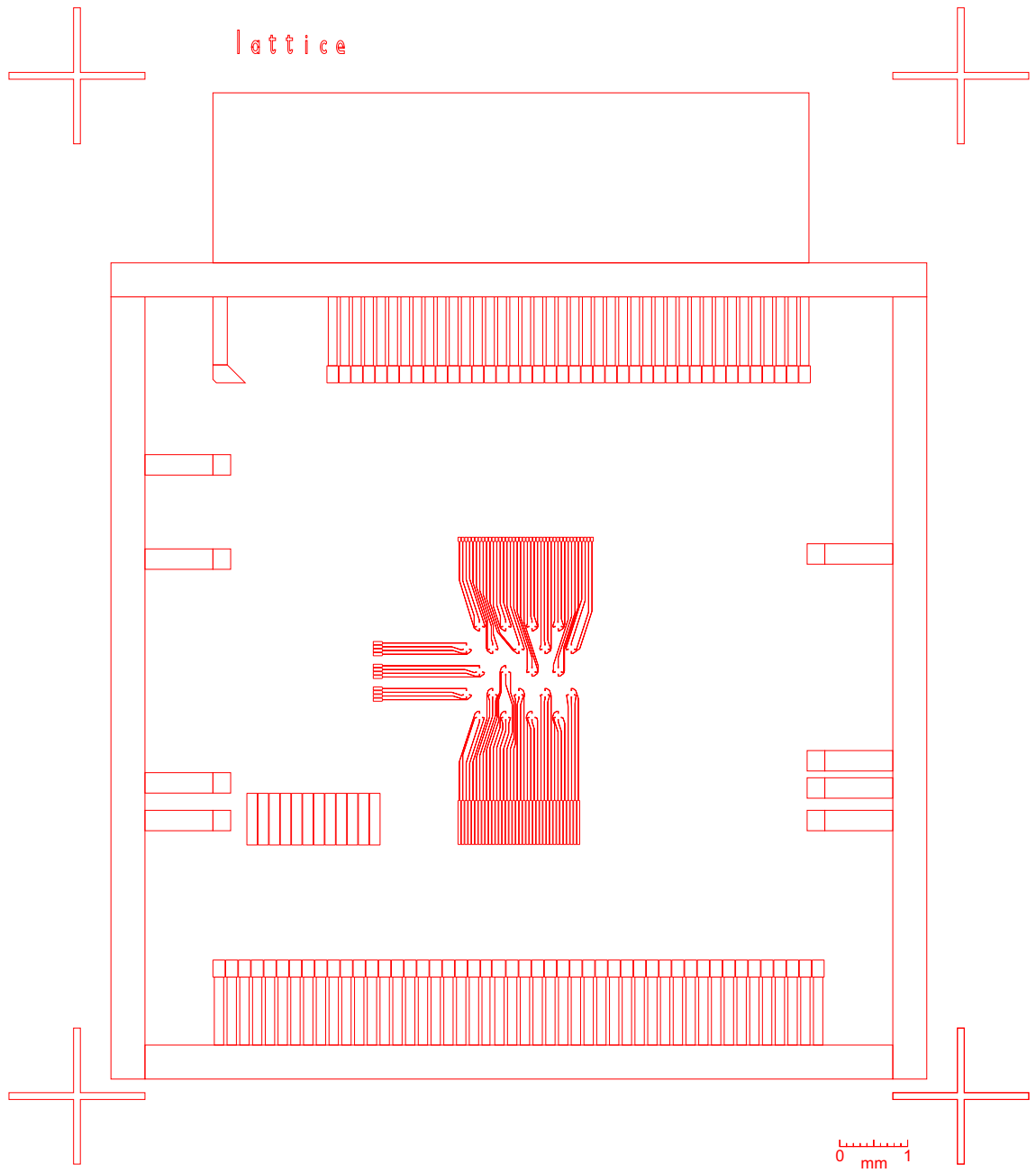


Figure A.7: Lattice first layer mask.

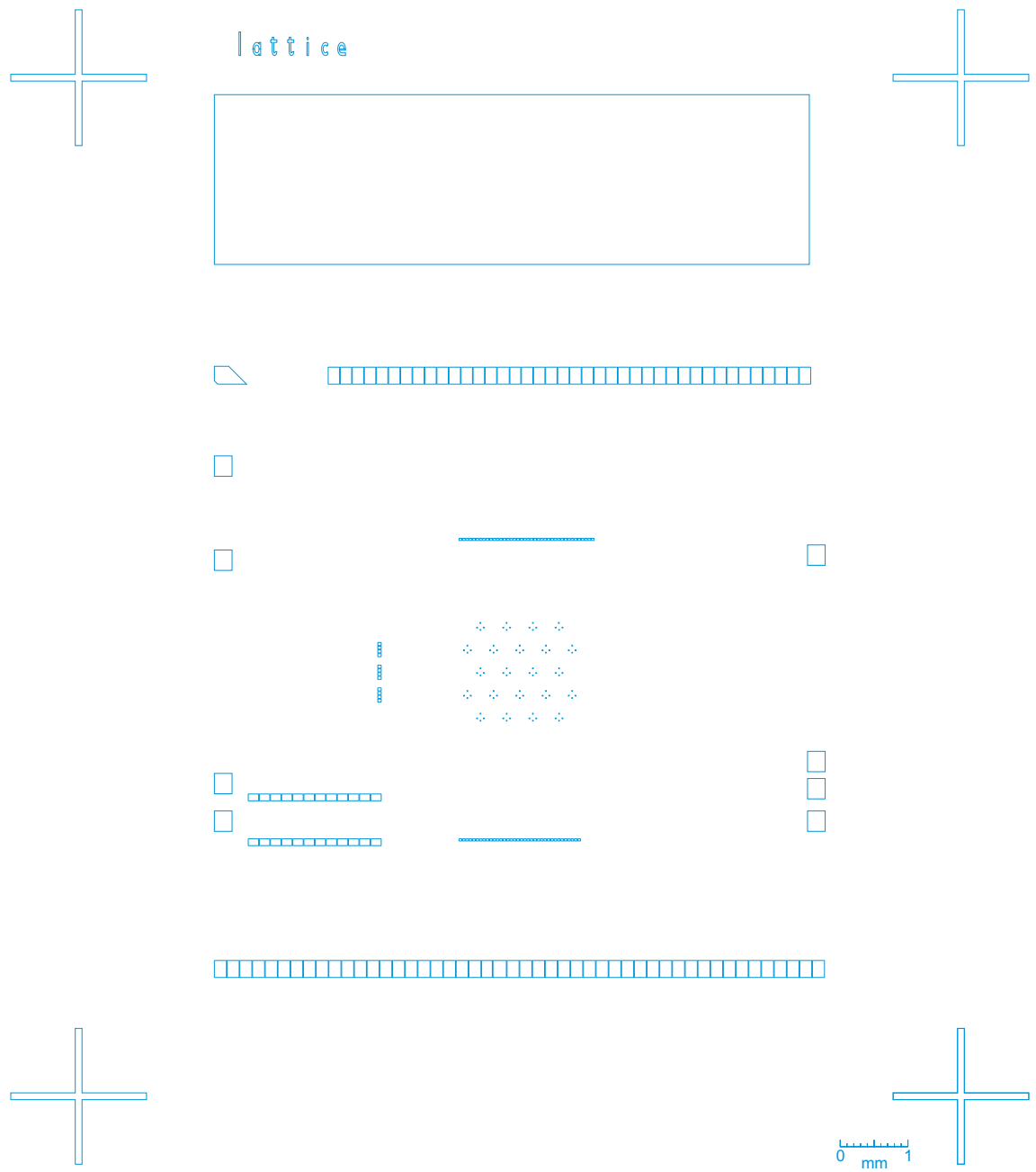


Figure A.8: Lattice second layer mask.

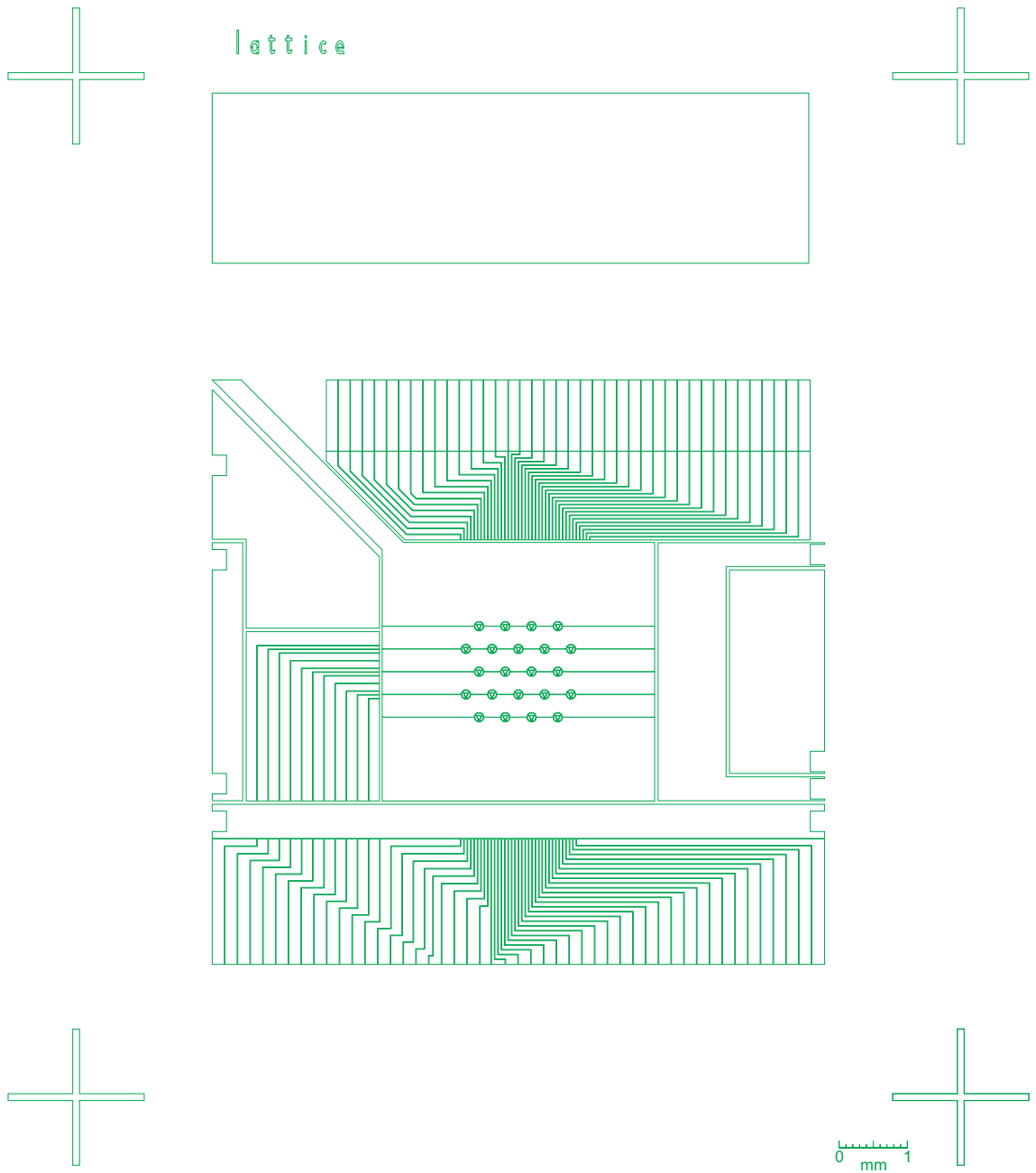


Figure A.9: Lattice third layer mask.

A.6 ‘Big’ ring ion trap

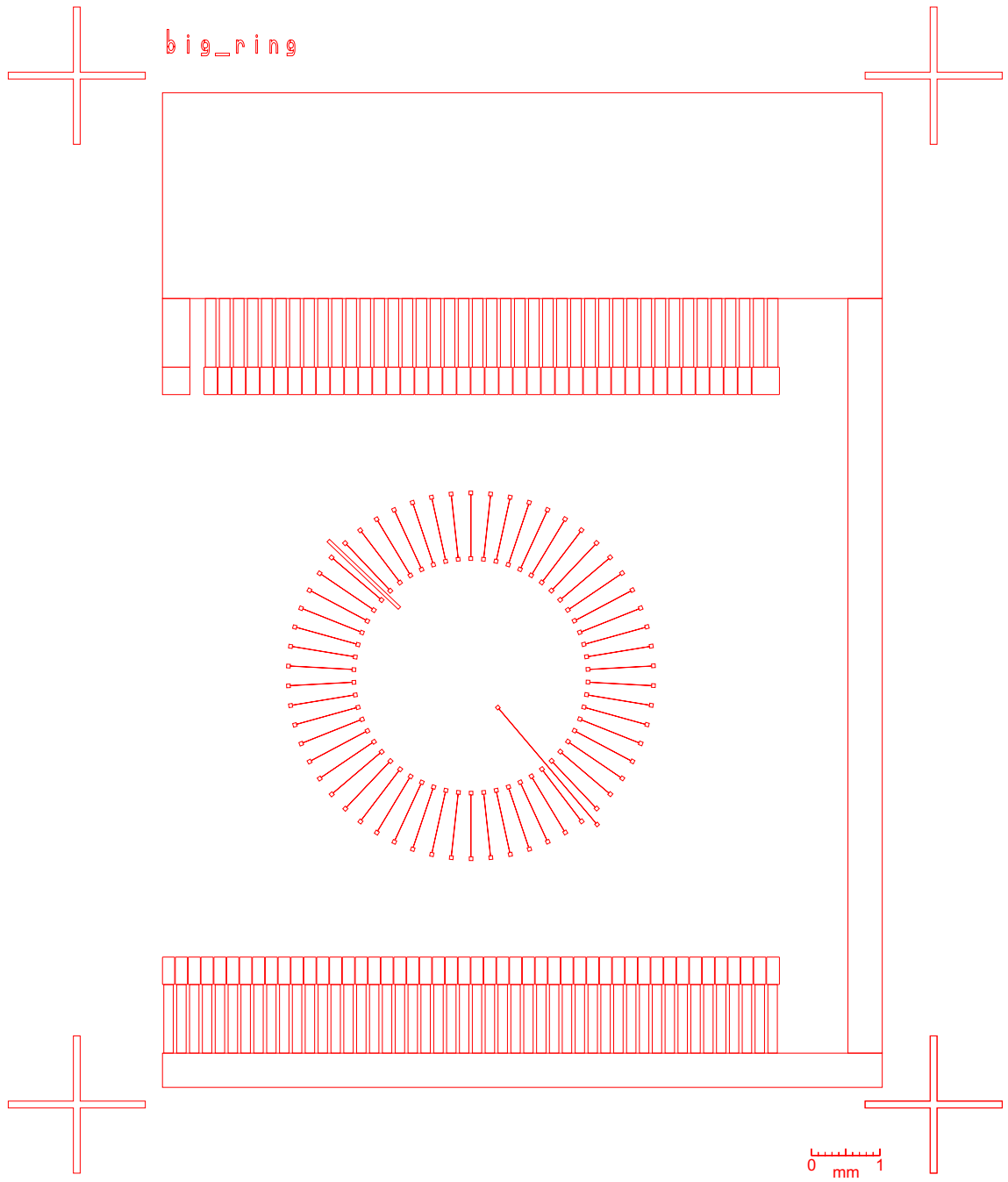


Figure A.10: ‘Big’ ring first layer mask.

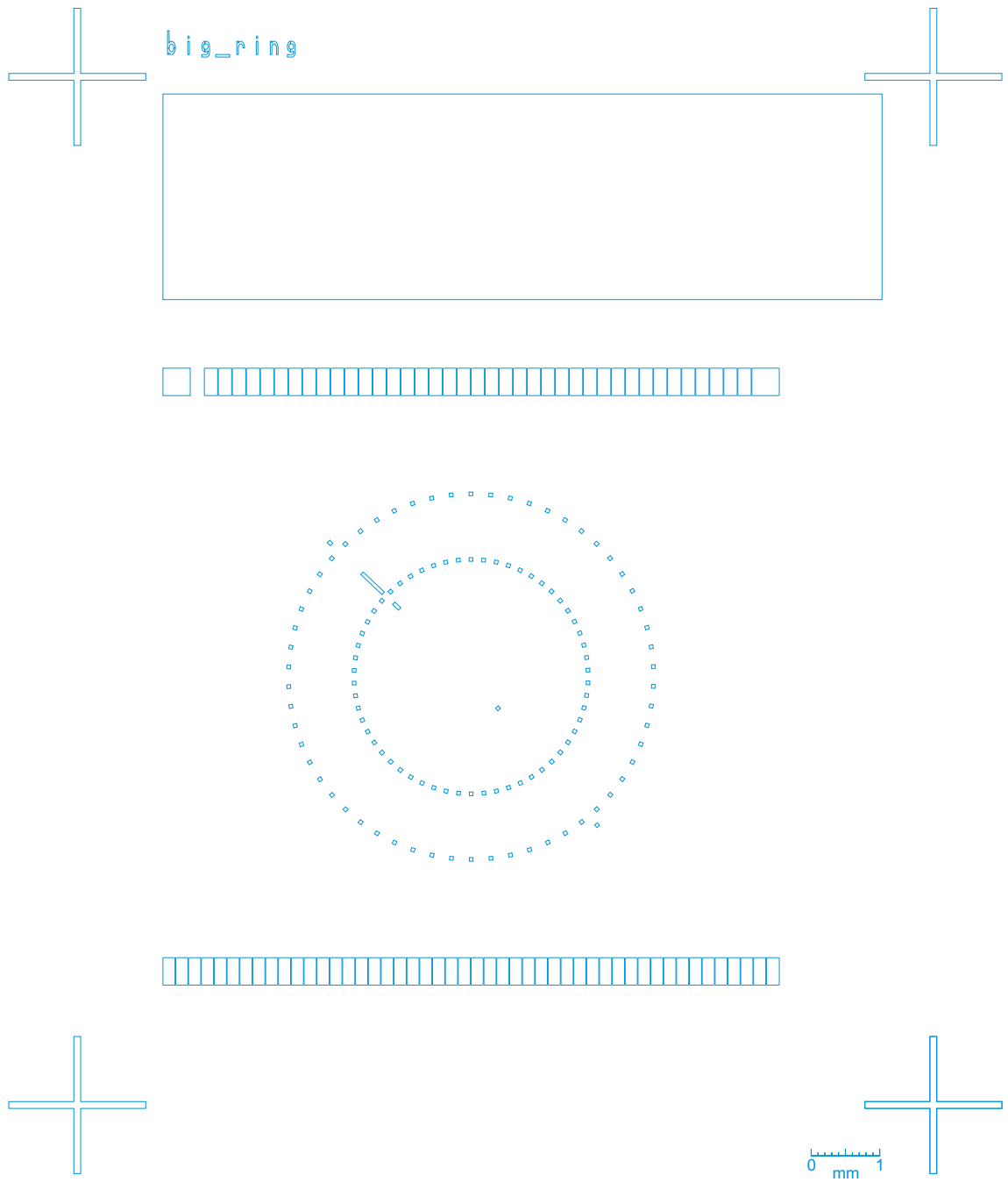


Figure A.11: 'Big' ring second layer mask.

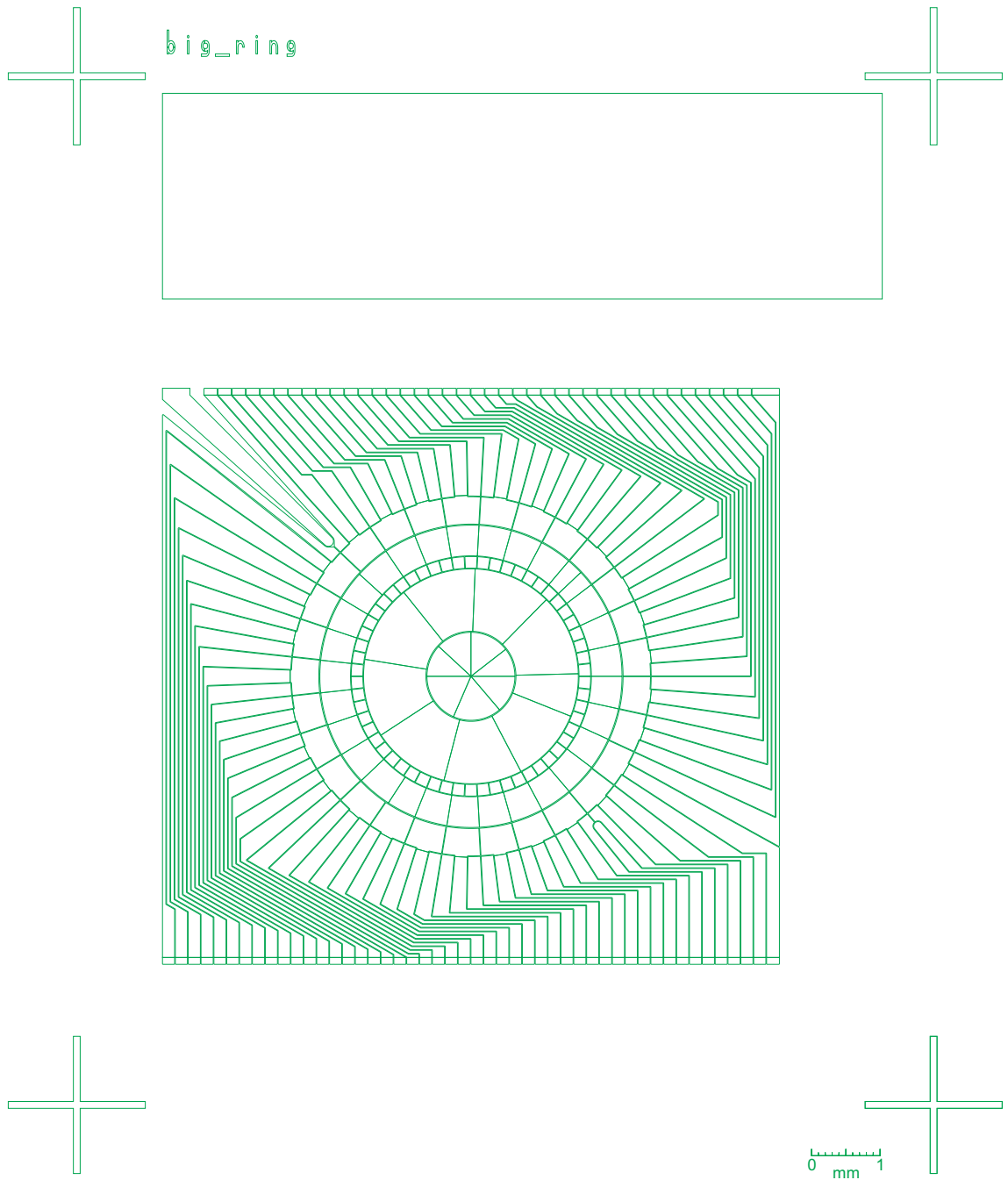


Figure A.12: 'Big' ring third layer mask.

A.7 ‘Small’ ring ion trap

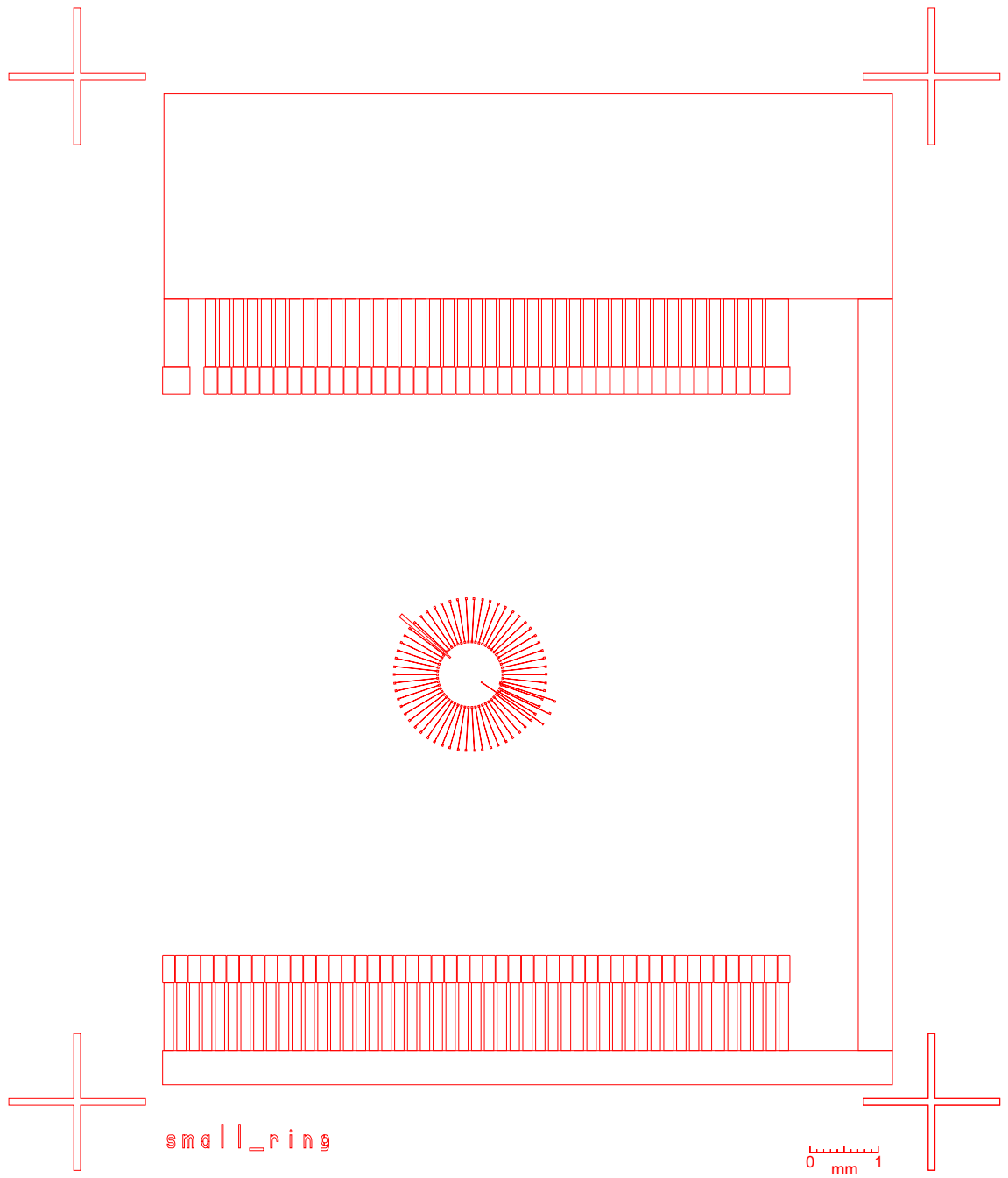


Figure A.13: ‘Small’ ring first layer mask.

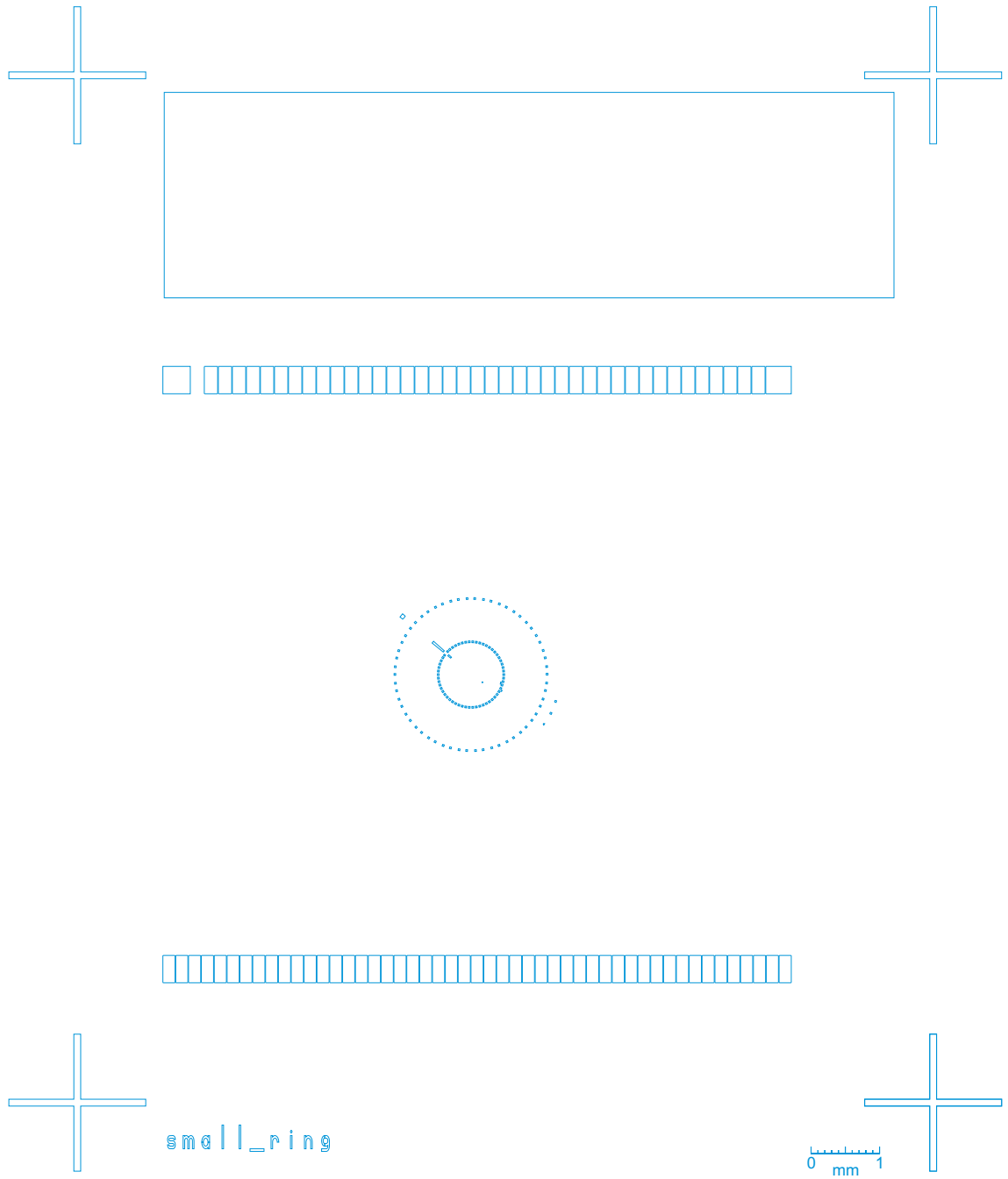


Figure A.14: 'Small' ring second layer mask.

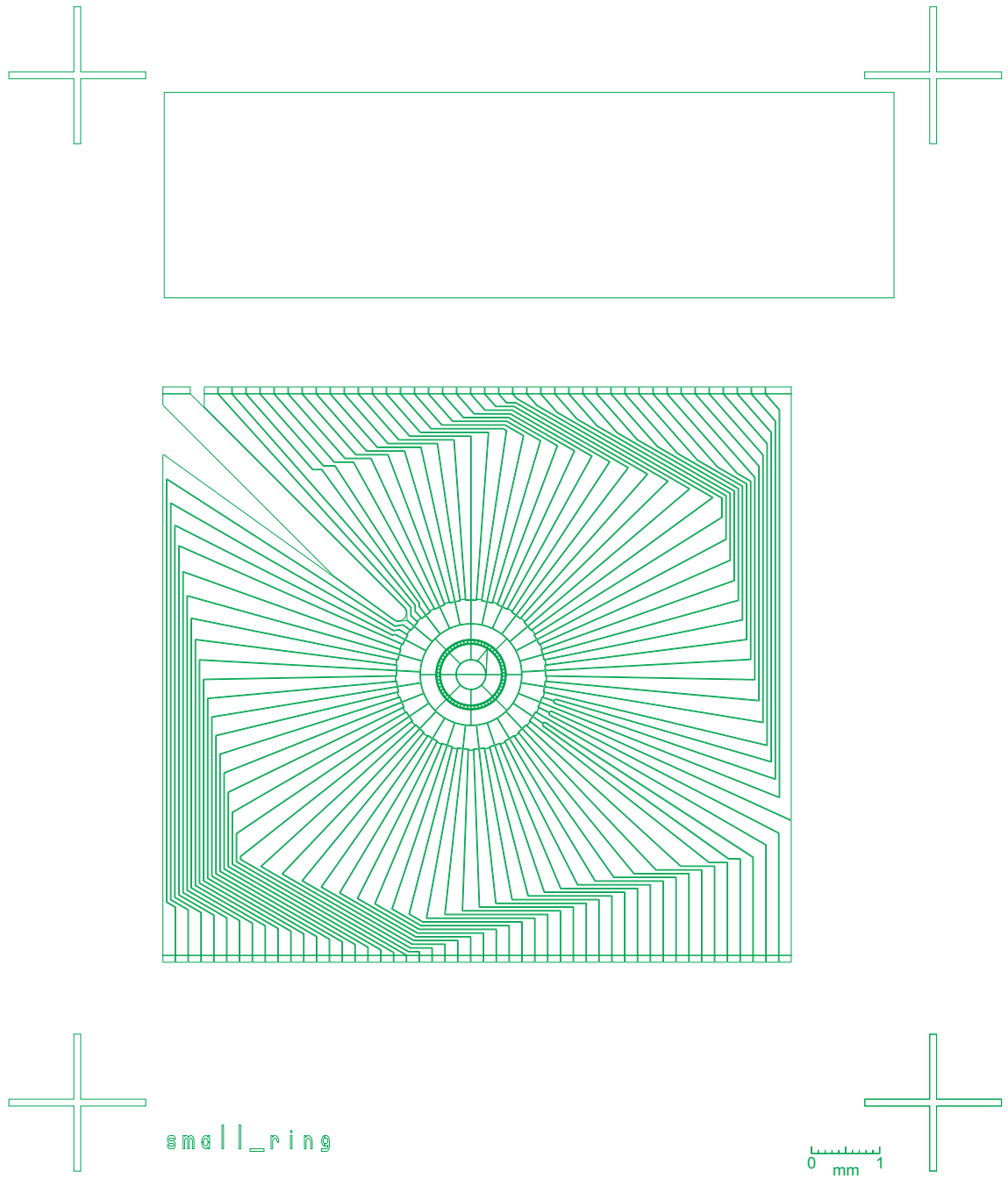


Figure A.15: 'Small' ring third layer mask.

A.8 Linear ion trap

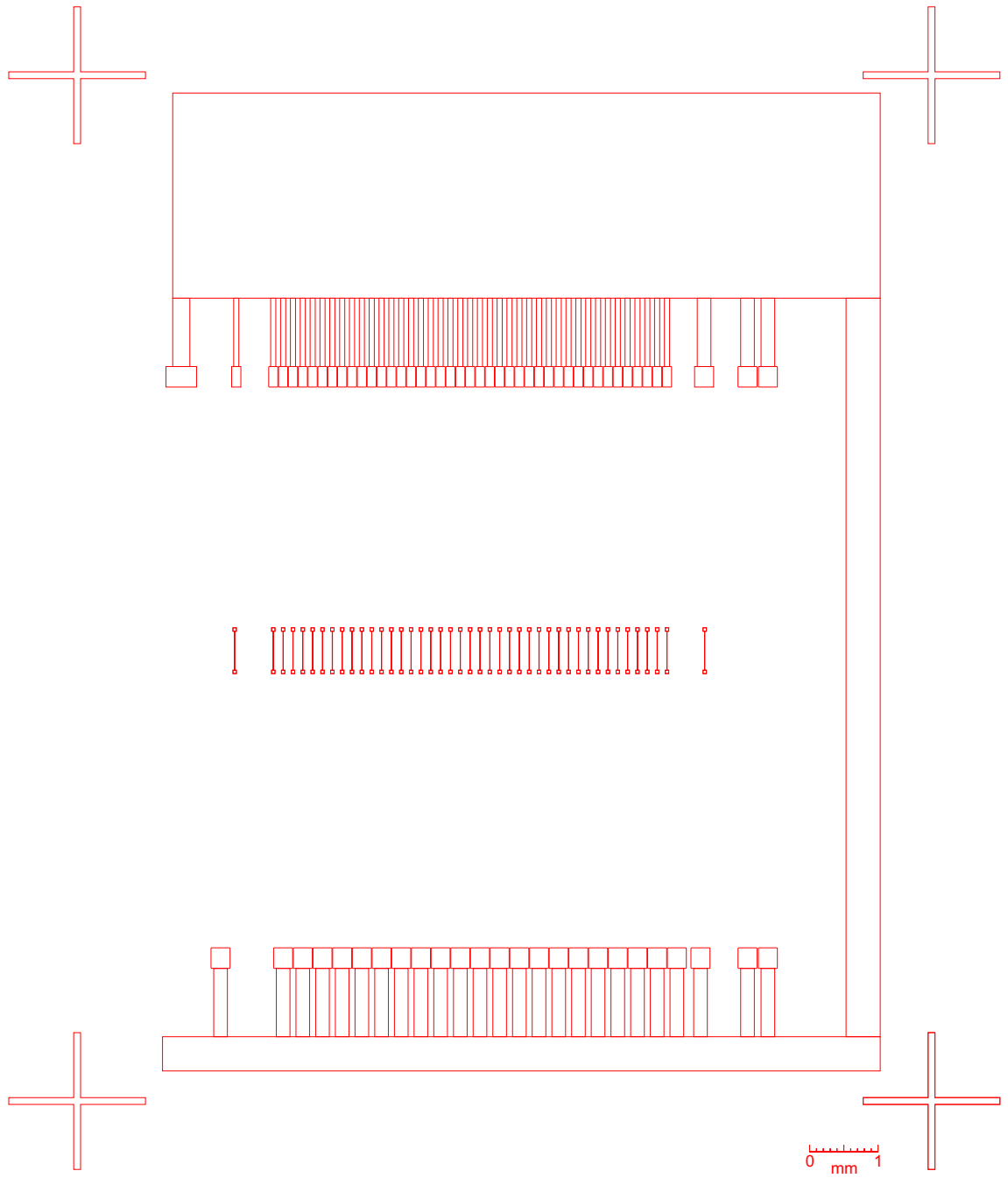


Figure A.16: Linear first layer mask.

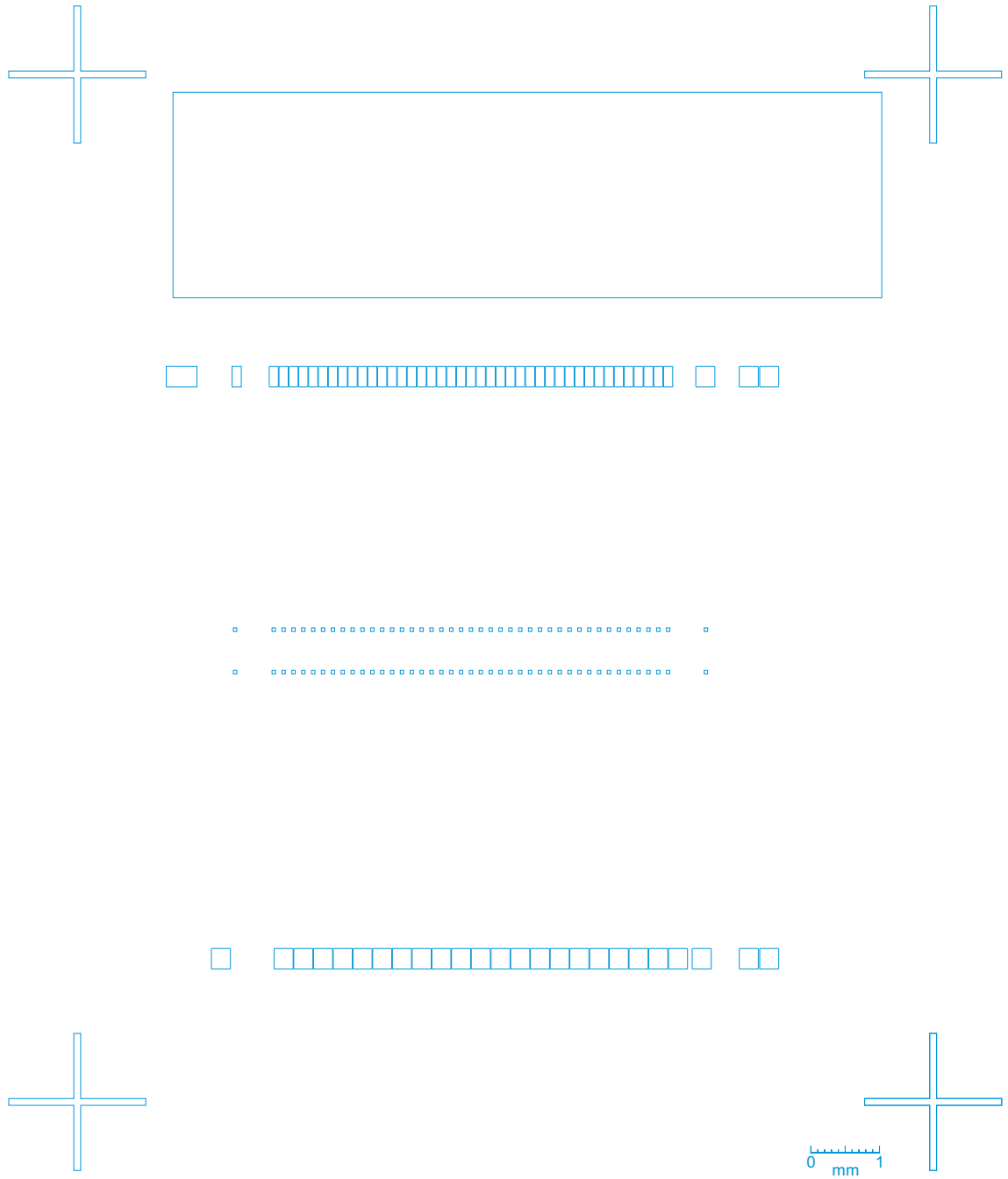


Figure A.17: Linear second layer mask.

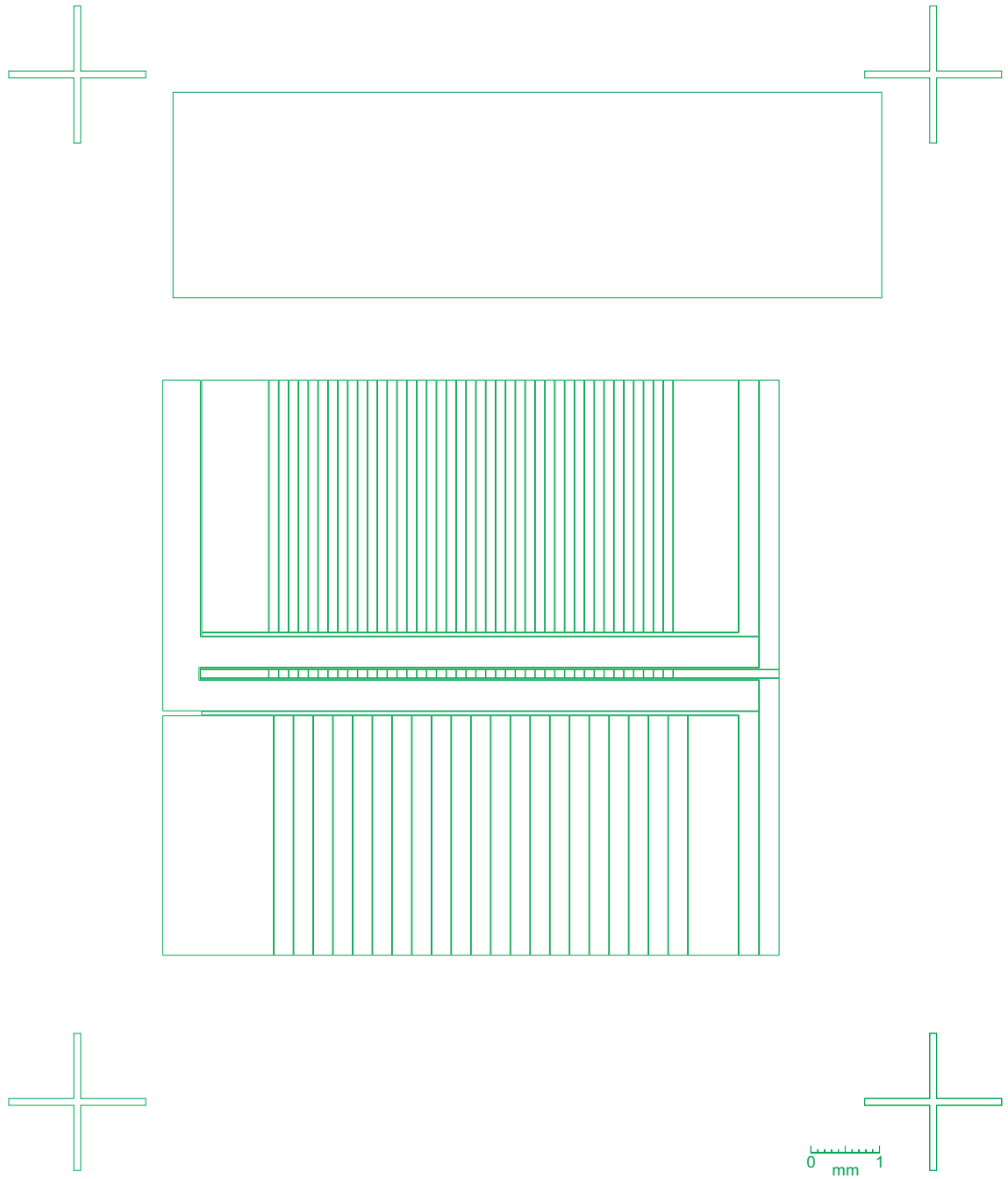


Figure A.18: Linear third layer mask.

A.9 Characterisation area

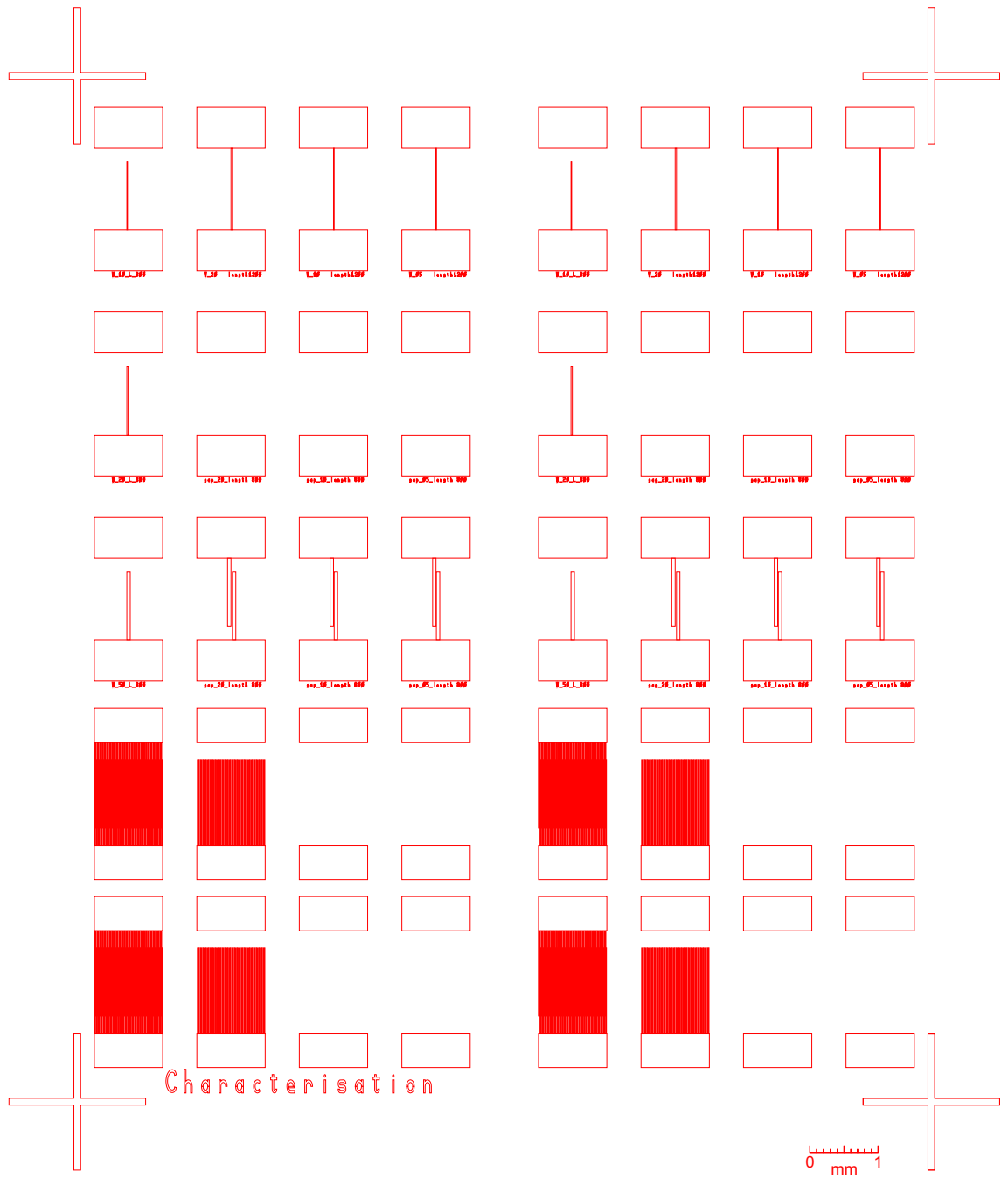


Figure A.19: Characterisation first layer mask.

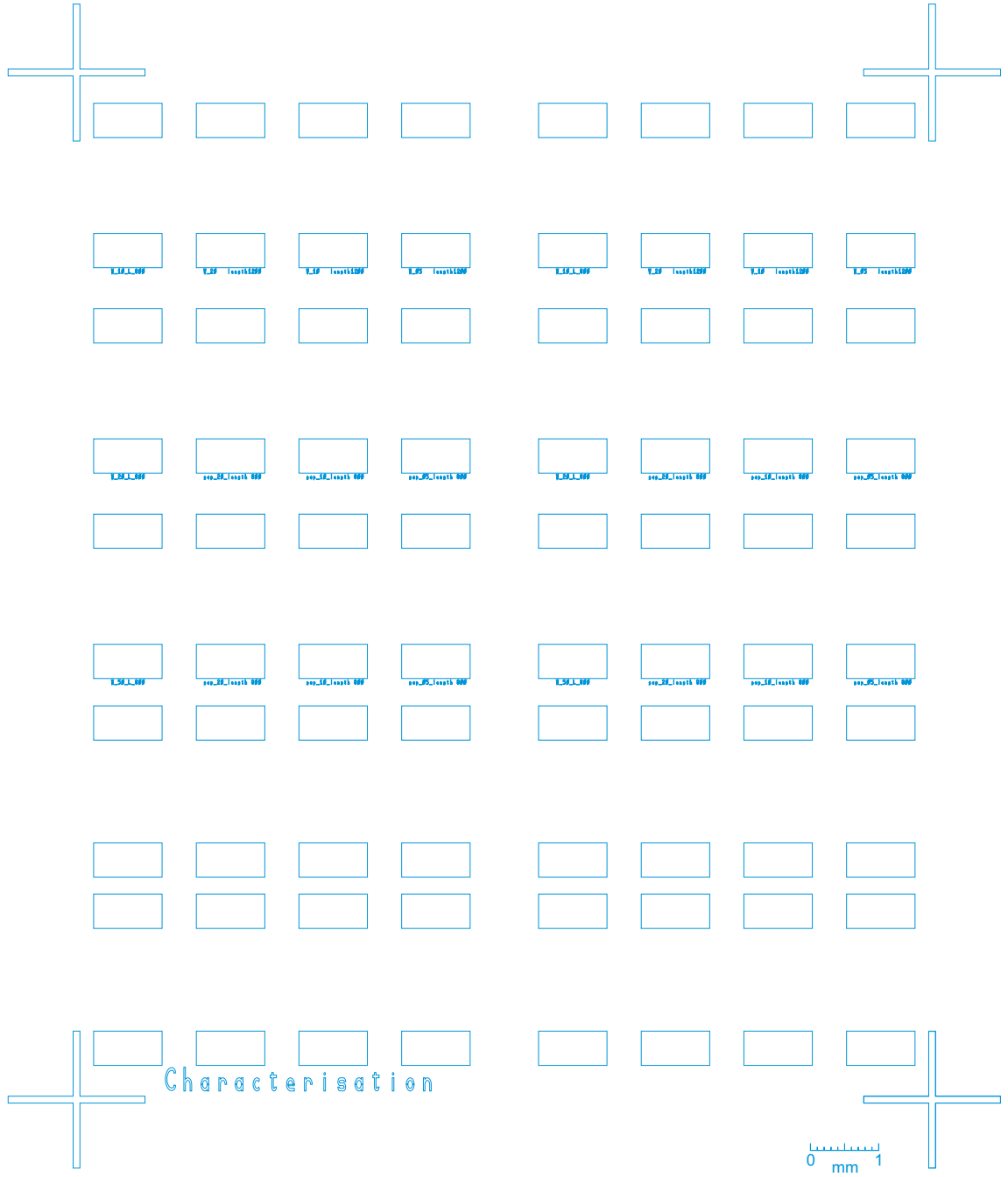


Figure A.20: Characterisation second layer mask.

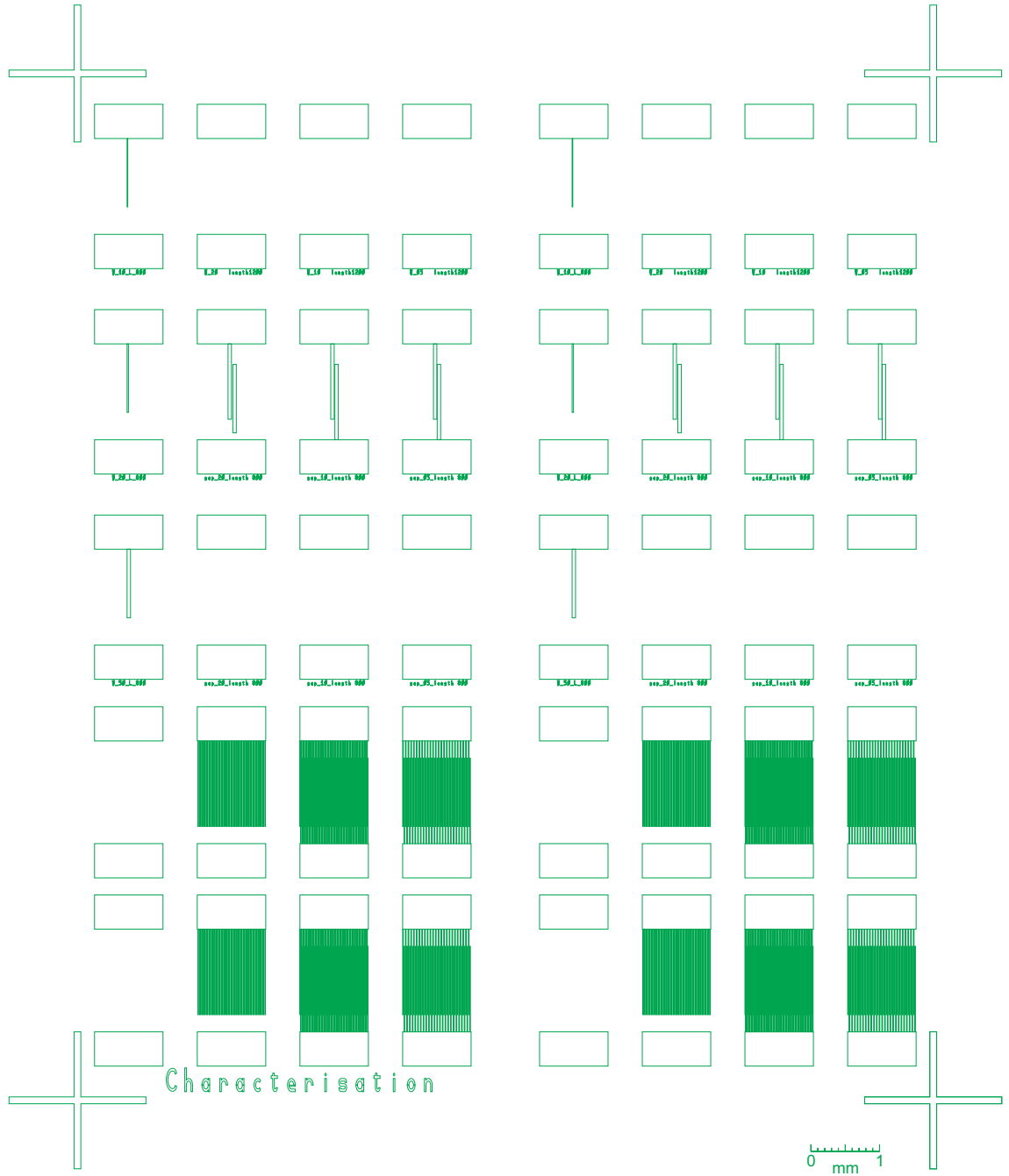


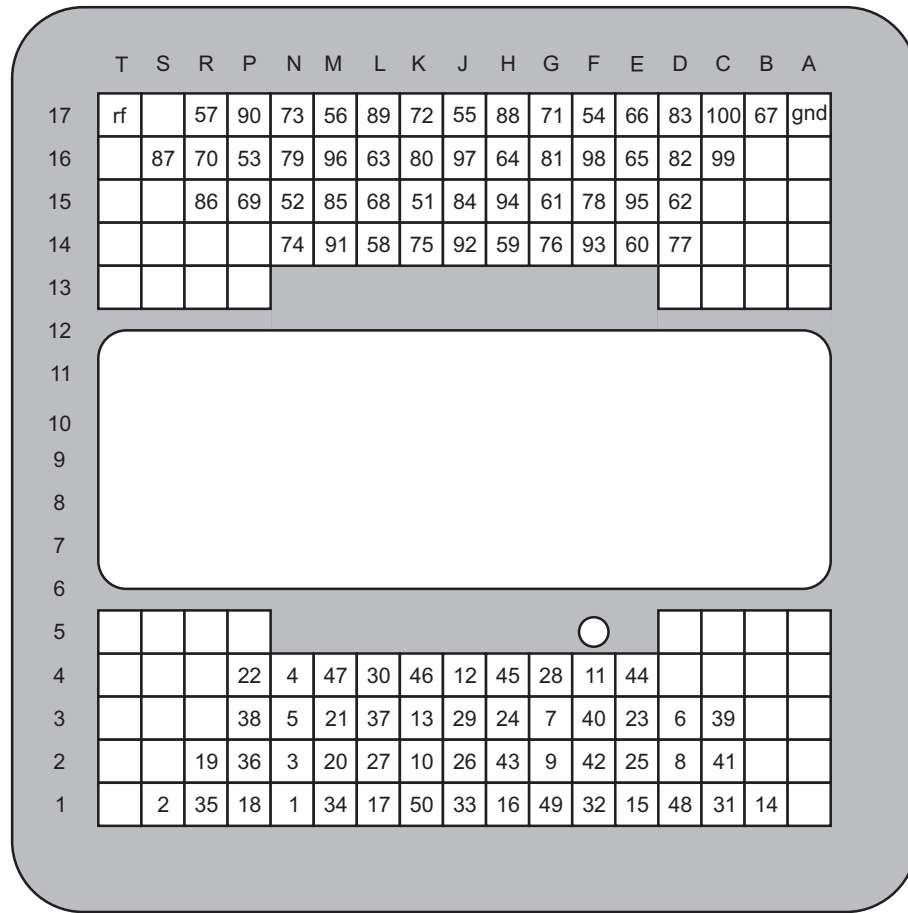
Figure A.21: Characterisation third layer mask.

Appendix B

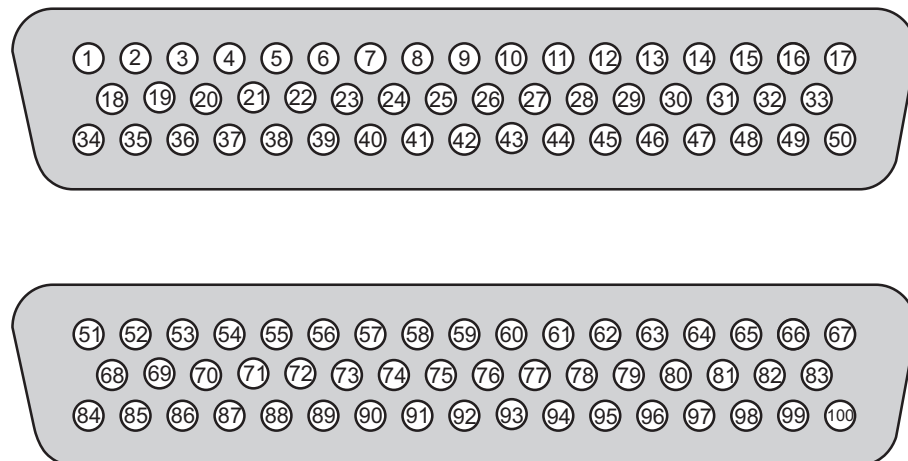
Electrical feedthrough map

Bond pad No.	D-type feedthrough No.	Bond pad No.	D-type feedthrough No.	Bond pad No.	D-type feedthrough No.
1	22	38	15	125	59
2	38	39	42	126	94
3	19	40	48	127	64
4	Not connected	41	40	128	88
5	36	42	11	129	97
6	4	43	31	130	92
7	5	44	25	131	84
8	35	45	14	132	55
9	2	46	23	133	72
10	3	47	8	134	80
11	47	48	44	135	75
12	21	49	41	136	51
13	18	50	6	137	89
14	20	51	Not connected	138	63
15	1	52	39	139	56
16	30	53-104	Not connected	140	68
17	37	105	77	141	58
18	34	106	62	142	73
19	27	107	99	143	96
20	17	108	Ground	144	90
21	46	109	82	145	85
22	13	110	60	146	91
23	10	111	95	147	57
24	50	112	67	148	79
25	26	113	100	149	Not connected
26	12	114	65	150	52
27	29	115	93	151	53
28	33	116	78	152	74
29	16	117	83	153	70
30	43	118	98	154	69
31	45	119	66	155	87
32	24	120	76	156	86
33	49	121	61	157	Not connected
34	9	122	54	158	Not connected
35	32	123	81	159	Not connected
36	7	124	71	160	RF
37	28			161-208	Not connected

Table B.1: Mapping of bond pad number to corresponding D-type electrical feedthrough pin.



(a)



(b)

Figure B.1: Mapping of the chip bracket pins to the corresponding pins on the 2×50 D-type electrical feedthroughs.

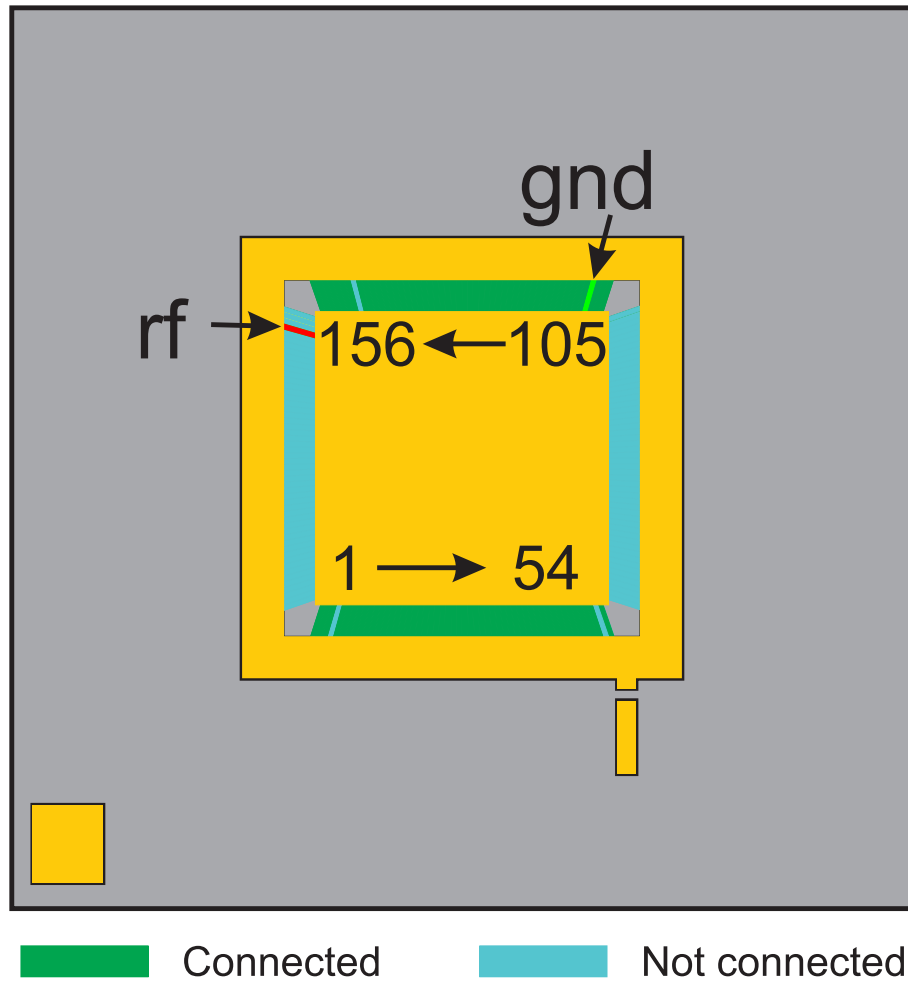


Figure B.2: Schematic of the ceramic pin grid array (CPGA) chip carrier from Global Chip Materials (pt No. PGA20855101). 102 of the 208 pins on the chip are connected via the chip bracket. The bond pads are numbered from the bottom left corner in a anticlockwise direction. The rf and ground pins are highlighted. A mapping of the bond pad to feedthrough pin number is presented in table B.1.